

Turboelectric Distributed Propulsion Test Bed Aircraft

LEARN Phase I

FINAL REPORT

Contract Number NNX13AB92A

**Principal Investigator: Michael Kerho
Rolling Hills Research Corporation
November 11th, 2013**

Any opinions, findings, and conclusions or recommendations expressed in this material are those of the author(s) and do not necessarily reflect the views of the National Aeronautics and Space Administration.

1 **PROJECT SUMMARY**

In order to meet future goals for aircraft efficiency for proposed large reductions in fuel burn, emissions, and noise, next generation aircraft will have to employ new technologies for both the aerodynamics and propulsion. One configuration which shows significant promise is the Hybrid Blended Wing Body (HBWB) coupled with a turboelectric distributed propulsion (TeDP) system. The revolutionary TeDP propulsion concept uses electric motor driven fans to provide propulsive thrust, with the gas turbine generators providing electric power for the system.

The TeDP concept has several distinct advantages, including boundary layer ingestion (BLI), re-energizing the wake of the airframe with the fan thrust stream, decoupling the propulsion from the power source, a very high effective bypass ratio, ultimate redundancy for increased safety, and differential thrust control for directional stability and trim. There are also significant challenges associated with TeDP, including increased inlet distortion due to BLI. The TeDP concept also leads to very close coupling between the aerodynamics and propulsion of the airframe. Significant interactions exist between the sectional aero performance and thrust level. Changes in thrust and mass flow through the fan affect circulation, spillage, blockage, and stagnation point movement, producing changes in sectional lift and moment. Changes in individual fan thrust can affect adjacent fan inlet conditions, distortion, and performance.

RHRC proposes the development of a distributed propulsion system for a small test bed aircraft. The development of a flying demonstrator for TeDP concepts, systems, and technologies allows early investigation of complex aerodynamics, propulsion, and systems vital to the success of a TeDP configuration. The flying demonstrator reduces development risk of a larger, dedicated TeDP configuration by testing concepts, performance, and technologies at a smaller, and relatively cheaper scale. The subscale test bed can be used to study the effects of BLI, aerodynamic/ thrust coupling, angle-of-attack, differential thrust effects on adjacent fan performance and distortion, inlet area design, and power generation topology.

The main goal of the Phase I program was to design and test a multi-fan boundary layer ingesting model based on a conceptual test bed aircraft TeDP installation. The test measured installed fan thrust, inlet distortion, surface pressures, boundary layer profiles, and required fan power for a three fan model based on a full scale test bed aircraft design. The test examined the effects of adjacent fan thrust level on neighboring fan performance and distortion.

The major tasks of the Phase I effort included the selection of a proposed test bed aircraft, the evaluation of the required performance of a TeDP system to replace the baseline IC/propeller propulsion system, followed by the selection of an available electric ducted fan (EDF) and design of the BLI inlet, s-duct, and exhaust. A preliminary model of the propulsion system was designed. Prior to testing, a 3D CFD model of the wind tunnel test article was developed. Finally, a wind tunnel test of the multi-fan model was performed and the results compared to the CFD predictions. All proposed tasks and milestones for the Phase I program were met and achieved. A very unique CFD and experimental data set was generated for a distributed array of boundary-layer ingesting propulsors.

2 TABLE OF CONTENTS

1	Project Summary	1
2	Table of Contents.....	3
3	Introduction	4
3.1	Identification and Significance of Innovation	4
3.2	TeDP Advantages and Challenges	5
3.3	Subscale Test Bed	6
3.4	Scaling.....	7
4	Phase I Technical Objectives.....	8
5	Phase I Results.....	8
5.1	Initial Program Kick-off Discussions.....	8
5.2	Test Bed Aircraft Propulsion Requirements	11
5.3	Airfoil and Inlet Boundary Layer Estimate.....	13
5.4	Choice of COTS Ducted Fan and Fan Power Source	17
5.4.1	COTS EDF Unit.....	17
5.4.2	Power For EDF Units.....	20
5.4.3	Thrust Test Stand Development and Preliminary Results	22
5.4.4	Preliminary Static Test Stand Results.....	23
5.5	Preliminary Wind Tunnel Model Design and Inlet Sizing.....	24
5.6	Notional Test Bed Aircraft Layout.....	26
5.7	CFD Model.....	27
5.7.1	Preliminary Hump Model	27
5.7.2	Full EDF Hump Model	30
5.7.3	Differential Thrust Results.....	42
5.7.4	CFD Results Summary	47
5.8	Wind Tunnel Test.....	48
5.8.1	Model Construction and Experimental Set-Up.....	48
5.8.2	Instrumentation	50
5.8.3	Wind Tunnel Test Results.....	55
6	Summary and Conclusions	69
7	Phase II Objectives	72

8	References	73
9	Appendix #1	74
10	Appendix # 2.....	99
11	Appendix #3.....	127

3 **INTRODUCTION**

3.1 **Identification and Significance of Innovation**

In order to meet future goals for aircraft efficiency and performance for proposed large reductions in fuel burn, emissions, and noise, next generation aircraft will have to employ new technologies for both the aerodynamics and propulsion. The NASA Subsonic Fixed Wing (SFW) project has identified ambitious goals for the next three generations of aircraft, N+1, N+2, and N+3. For the N+3 generation (2025 timeframe), these include a -52 dB noise reduction¹ relative to stage 4 noise limit, and -80% reduction in NOx emissions, and a -60% reduction in total mission energy consumption relative to the base in class current aircraft.² For a current state-of-the-art Boeing 777-200LR Baseline, this represents a -70% reduction in fuel burn³. These large reductions will require exploring new, radical configurations, materials, and propulsion technologies. One configuration which shows significant promise is the Hybrid Blended Wing Body (HBWB). The HBWB provides high cruise L/D with some noise shielding with upper surface mounted engines. With pylon mounted ultra high bypass ratio (UHB) engines, the HBWB provides a possible 52% fuel burn reduction.³ In order to meet N+3 goals, however, an additional 18% fuel burn reduction is required. HBWB fuel burn can be further reduced -18% to -20% using a turbo electric distributed propulsion (TeDP) concept, bringing the total fuel burn reduction to -70% to -72%. The revolutionary TeDP propulsion concept uses electric motor driven fans to provide propulsive thrust, with the gas turbine generators providing electric power for the system. The fans, generators, and transmission network are superconducting to reduce the propulsion mass fraction. Instead of several individual UHB engines, ten to fifteen fans are distributed in a line across the upper surface of the HBWB near the trailing-edge and ingest the boundary layer. Gas turbine generators provide power to the propulsive fans and are mounted near the wing tips to provide optimal efficiency by ingesting free-stream air.

A successful TeDP implementation poses significant challenges, even for an N+3 2025 timeframe. RHRC proposes the development of a distributed propulsion system for a small test bed aircraft. The development of a flying demonstrator for TeDP concepts, systems, and technologies allows early investigation of complex aerodynamics, propulsion, and systems vital to the success of a TeDP configuration. The flying demonstrator reduces development risk of a larger, dedicated TeDP configuration by testing concepts, performance, and technologies at a smaller, and relatively cheap scale. Although significant differences in vehicle size, thrust level,

Reynolds number and cruise speed exist, several key technologies and concepts scale well from the subscale test bed to the full scale aircraft.

3.2 TeDP Advantages and Challenges

The TeDP concept has several distinct advantages. These include boundary layer ingestion (BLI), re-energizing the wake of the airframe with the fan thrust stream, decoupling the propulsion from the power source, a very high effective bypass ratio, ultimate redundancy for increased safety, and differential thrust control for directional stability, trim, and possible yaw control. The use of BLI reduces the average inlet velocity increasing thrust, and also reduces the drag of the inlet, reducing fuel burn as compared to a pylon mounted design. By decoupling the propulsion from the power, each can be placed at optimum locations on the airframe, with the rpm of the power generating turbine independent of the fan rpm, allowing each to be operated at their highest efficiency. There are also significant challenges associated with TeDP, including increased inlet distortion due to BLI and inlet geometry leading to reduced fan performance and increased blade fatigue. The TeDP concept also leads to very close coupling between the aerodynamics and propulsion of the airframe. Nonlinear interactions may exist between the sectional aero performance and thrust level. Changes in thrust level and mass flow through the fan can affect circulation, spillage induced blockage, and stagnation point movement, producing significant changes in sectional lift and moment. Figure 1 shows a 2D CFD based representation of the effect of different thrust levels on the integrated lift and pitching moment for a generic airfoil with an aft mounted ducted fan unit. The calculations were made using the OVERFLOW CFD code. A baseline thrust/mass flow was chosen and the thrust then varied to 20% above and below the baseline case. Below the baseline thrust, or mass flow, the duct creates blockage, or spillage, locally retarding the flow. As a result, the pressure distribution is observed to decrease (become more positive) upstream of the fan. This diffusive effect is felt by the entire airfoil, resulting in a -33% reduction in C_l , accompanied by a +25% nose up change in C_m . Above the baseline thrust, the fan is drawing more mass flow, increasing the local velocity and creating more negative pressures. These effects are again felt by the entire section as the circulation changes and the stagnation point moves. The 20% increase in thrust creates a +13% increase in C_l , and a -10% nose down change in C_m . Clearly, changing thrust level can, and will, affect the integrated force characteristics of the section.

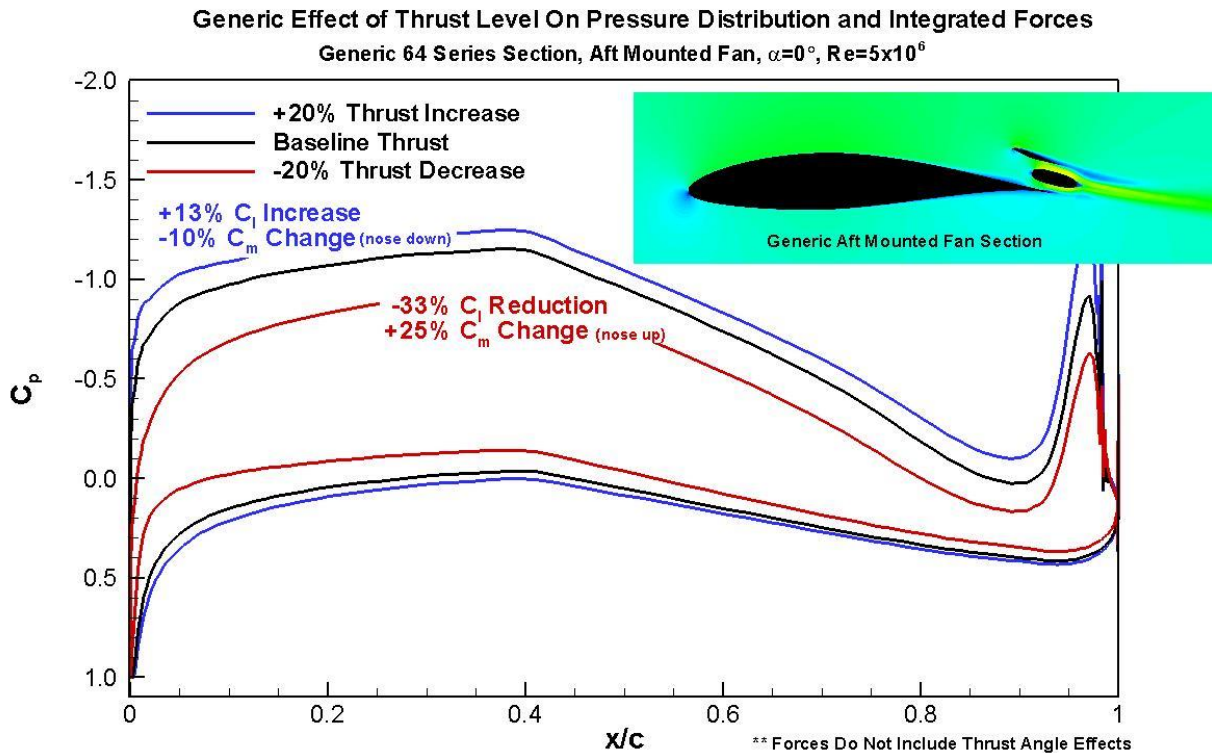


Figure 1: Generic effect of thrust level on sectional airfoil pressure distribution and integrated forces.

Additionally, the changes in thrust level will affect the electric power demands on the generators. Finally, changes in individual fan thrust can affect adjacent fan inlet conditions, distortion, and performance. Also, reliance on superconducting materials adds risk and complexity to the system.

3.3 Subscale Test Bed

RHRC proposes to design a distributed propulsion system for a small, single engine aircraft that NASA already owns (to be selected in coordination with NASA), which could be converted to become a test bed for TeDP. As previously stated, in order to reduce risk and provide an early assessment of multiple TeDP technologies and systems, the subscale test bed can be used to study the effects of BLI, aerodynamic/thrust coupling, angle-of-attack, differential thrust effects on adjacent fan performance and distortion, inlet area design, and power generation topology. It is not suggested that a TeDP installation on a small aircraft is a practical and efficient propulsion solution, but rather that it will provide an extremely valuable research tool. The test bed is a flying wind tunnel mean to study TeDP concepts and technologies.

The subscale test bed, for example, can be used to investigate BLI actual efficiencies, and the possible distortion challenges it creates. The test bed can also be used to study the effect of sectional aerodynamic and thrust coupling. Specifically, the effect of thrust levels and mass flow on sectional aerodynamic characteristics such as lift, drag, pitching moment, trim, and trim drag.

As thrust changes, mass flow increases or decreases above or below the design mass flow for the inlet, changing blockage and resulting spillage, pressure distributions, and circulation effects. The changes in thrust level and aero/propulsive coupling will be especially important for approach and landing configurations, high angle-of-attack, approach to stall, and stall. The test bed can also be used to investigate the effects of spanwise differential thrust, and the effect of changing mass flow and spillage on adjacent fan thrust, performance, and distortion. Inlet area design can also be studied using the subscale test bed. This includes design of the inlet to minimize losses due to changes in local inflow angles as a result of neighboring fan spillage, and reducing the effects of spillage through design or the possible inclusion of a moveable inlet lip. Finally, although vastly different in power levels, the power distribution topology for the subscale test bed is similar to the full scale aircraft. Power must be produced, rectified and transmitted efficiently from one or multiple sources to multiple fans. The key to the successful implementation and use of the test bed is to study and focus on technologies which will scale appropriately to the full scale transport aircraft.

3.4 Scaling

Although the subscale test bed is significantly smaller in size, thrust level, Reynolds number, and cruise speed, key technologies and concepts scale well from the test bed to the full scale aircraft. Technologies which scale well include BLI effects, aerodynamic and propulsive coupling effects, inlet lip geometry effects, and power distribution topology.

Although the Reynolds number is significantly different, matching the ratio of the boundary-layer height to the inlet height, and matching the shape factor at the inlet entrance to the full scale vehicle will allow BLI effects on the subscale test bed to reflect those on the full scale aircraft. The effect of aerodynamic and propulsive coupling will also scale well between the test bed and full scale aircraft. This includes the effect of fan thrust and mass flow on circulation, lift, drag, pitching moment, and trim. As thrust changes and mass flow through the fan increases or decreases above and below the design mass flow of the inlet, the sectional blockage and circulation will change, as well as the pressure distribution. These changes will affect the sectional performance. These changes with thrust level will need to be well understood for approach and landing configurations. The effects of angle-of-attack on thrust due to changes in boundary layer thickness, and the effects of thrust level on approach to stall and stall characteristics can also be studied. Although the configuration effects will be different due to the different vehicle shapes (conventional aircraft versus HBWB), the trends with thrust level should be similar. The effect of an adjacent fan's thrust and spillage level on neighboring fan performance and distortion characteristics will be similar. Also scalable are the inlet design choices relating to design mass flow. These include the possible need for a movable inlet lip to adjust for off-design flight conditions to minimize spillage effects. Finally, the power distribution topology of the subscale test bed compares well to the full scale. Although power levels are substantially different, the basic components and their function are similar.

Areas that do not scale well include the inlet duct shape, the electric power levels generated and required, and the effects of possible transonic shocks upstream of the inlets. Since the test bed aircraft operates at low subsonic speeds, the inlet is a converging s-duct, and not a diffusing s-

duct required by transonic fans. The diffusing duct is required at transonic free-stream Mach numbers to keep the fan tip speeds subsonic and to provide increased pressure at the compressor inlet for a turbofan. As a result, distortion levels at the fan face will be less for the converging duct. The distortion levels will also be lower due to the lower free-stream Mach number.

Overall, the majority of the technologies critical to the success of a TeDP configuration can be studied using the subscale test bed. Other than the transonic shock effects, aerodynamics external to the inlet and fan should scale well, while those internal to the fan do not.

4 PHASE I TECHNICAL OBJECTIVES

The main goal of the Phase I program was to design and test a multi-fan, boundary layer ingesting model based on a conceptual test bed aircraft TeDP installation. The test measured installed fan thrust, inlet distortion, surface pressures, boundary layer profiles, and required fan power for a three fan model based on a full scale test bed aircraft design. The test examined the effects of adjacent fan thrust level on neighboring fan performance and distortion.

The major tasks of the Phase I effort included:

- Selection of a proposed test bed aircraft
- Evaluation of the required performance of a TeDP system to replace the baseline internal combustion/propeller based propulsion system
- Selection of a commercially available electric ducted fan (EDF) and motor
- Sizing and design of the BLI Inlet, s-duct, and exhaust
- Preliminary wind tunnel test model design
- Generation of a 3D CFD model of the wind tunnel test article
- Wind tunnel test of the multi-fan model

All proposed tasks and milestones for the Phase I program were met and achieved. Although only a single fan model was proposed in the original program, the scope of the effort was increased to examine multiple fans. This increase in scope was pursued as it significantly increased the immediate usefulness and applicability of the Phase I results to the full scale TeDP effort.

5 PHASE I RESULTS

5.1 Initial Program Kick-off Discussions

Prior to beginning an in depth study of the embedded propulsor, several concepts were discussed with the program technical monitor in an attempt to maximize the applicability of the program results to NASA's overall goals for distributed electrical propulsion. Whereas the overall goal for NASA is a large scale transport aircraft utilizing a distributed electric propulsion system, the

primary thrust of the current project is the development of a small test bed aircraft utilizing many of the same concepts and technologies to be incorporated in the large transport version. The small test bed aircraft approach is being pursued in an attempt to reduce the development risk of the larger system by first studying the system in a smaller, more manageable and cost effective package.

The first topic of discussion was the type of inlet for the embedded fan system (mail slot, flush, etc.). From a review of the publications on the Glenn TeDP effort for a large HBWB type configuration, the inlet geometry has been focused on a mail slot type inlet for the embedded fan. A “flush” scalloped s-duct design was also proposed. NASA Dryden personnel also discussed a reverse mail slot design with RHRC. The reverse mail slot design attempts to alleviate some of the distortion issues of a diffusing s-duct by transferring some of the diffusing duct adverse gradient to the wall opposite the boundary-layer ingesting wall. Below is a quick cartoon of these three inlets.

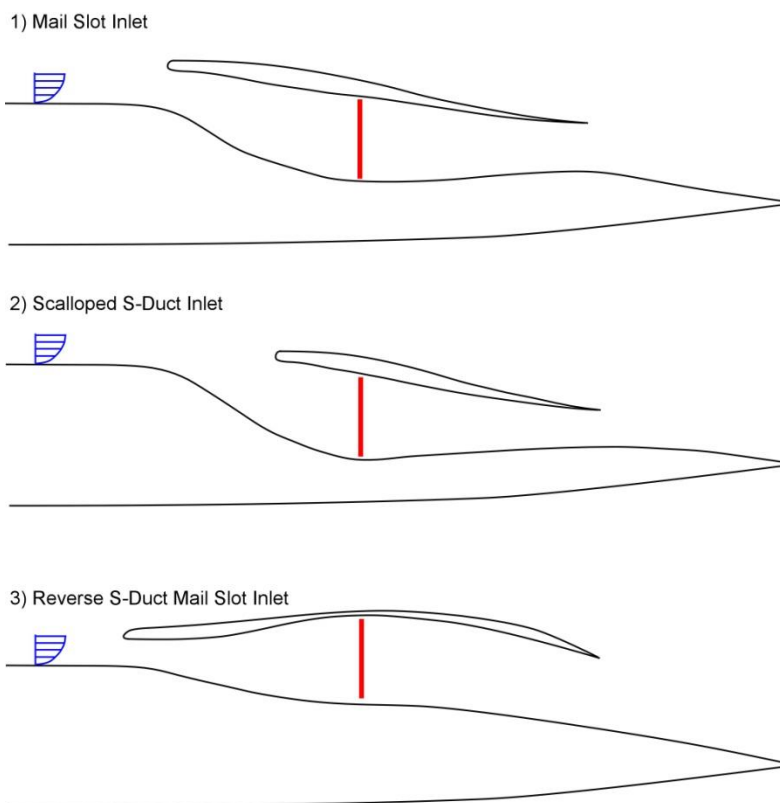


Figure 2: Three types of inlet/duct designs considered.

After discussion of the above inlet types with the program technical monitor, the traditional mail slot type of inlet was chosen as it provides the configuration with the largest crossover applicability to both the small test bed design and the larger commercial transport configuration. Based on the mail slot type inlet, multiple wind tunnel test configurations were discussed.

The model, duct, and propulsion system was tested in the University of Illinois at Urbana-Champaign’s 3’x4’ low speed wind tunnel. Due to the tunnel size, the maximum chord length

for a traditional 2D airfoil model is about 24". This limits the size of the fan installation available, and makes testing the duct distortion more difficult. Alternatively, the duct and fan could be designed in a 2D floor mounted hump model that approximates the upper surface of the airfoil. A third set-up discussed was that of a simple flat plate with the duct mounted on the plate surface and the fan below the plate. Schematics of these three set-ups are shown below in Figure 3.

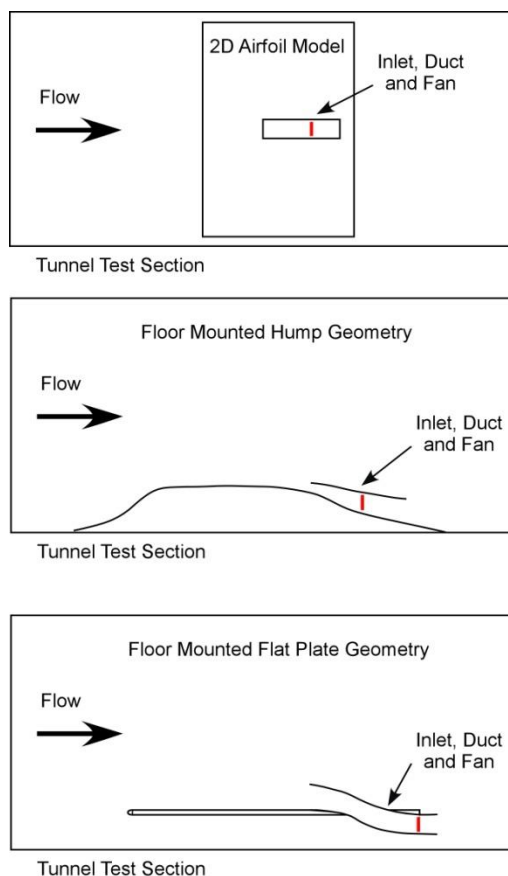


Figure 3: Proposed wind tunnel test geometries.

Each of the proposed test set-ups has advantages and disadvantages. The 2D airfoil model is the most realistic geometry and allows the effect of changing angle-of-attack on the boundary-layer and duct system to be studied, as well as providing lift, drag, and pitching moment. Due to size constraints of the tunnel, however, this option makes for a complicated model, increasing cost and test complexity and reducing the size of the fan and duct. The floor mounted hump geometry allows for a much larger model, duct, and fan, easing testing difficulties and reducing model cost. The disadvantage lies in being unable to varying the incoming boundary-layer by changing the angle-of-attack. The boundary-layer can be manipulated by adding various levels of roughness to the hump geometry upstream of the duct inlet. The simplest and cheapest option is the flat plate based geometry. The boundary layer can be manipulated in the same manner as the hump using roughness upstream of the inlet, but the aft body flow and pressure recovery do not represent the airfoil flow field well. Thrust for these cases would be determined from a rake

based pressure measurement system, or a thrust balance mounted directly to the fan. Additionally, the 2D airfoil model has the advantage of using an available floor balance for overall lift, drag, and pitching moment.

Based on discussions with the technical monitor, the 2D floor mounted hump geometry was chosen. Again, this geometry allowed the greatest crossover applicability to both the small test bed design and the larger commercial transport configuration. For the 2D floor hump, as opposed to the original plan of just a single fan, multiple spanwise inlet/fan combinations were incorporated into the model. The multiple duct/fan system allowed investigation of the effect that changes in neighboring duct mass flow rates have upon a given duct's inlet flow distortion and fan efficiency. As previously discussed, this increase in scope was pursued as it significantly increased the immediate usefulness and applicability of the Phase I results to the full scale TeDP effort.

5.2 Test Bed Aircraft Propulsion Requirements

The test bed aircraft identified for the project is one of NASA Dryden's TG-14A motor gliders. The TG-14A motor glider was previously selected as an excellent candidate for conversion to an electric aircraft test bed under a previous SBIR Phase I study (Contract # NNX11CI08P). The TG-14A was chosen for a combination of factors including aerodynamic performance, available space for batteries and instrumentation, maximum take-off gross weight, and ease of modification. A table showing basic information for the TG-14A is shown in Table 1 with a three-view CAD model rendering of the TG-14A shown in Figure 4.

Aircraft	Manufacturer	Type	# of Seats	Motor
TG-14A	Grupo Aeromot	Motor Glider	2	Rotax 912, 100 Hp
				Propeller
Wingspan	57.3 ft	Max Speed (V_{NE})	132 kts	Hoffman HO-V62R-1/170FA
Length	26.5 ft	Maneuver (V_A)	97 kts	
Height	6.3 ft	Stall	39 kts	Endurance 5 hrs
Width	42.5"			
		Glide Ratio	31-1	
Empty Wt	1334 lbs	Airfoil	NACA 64 ₃ -618	
Takeoff Wt	1874 lbs			




Table 1: TG-14A general information.

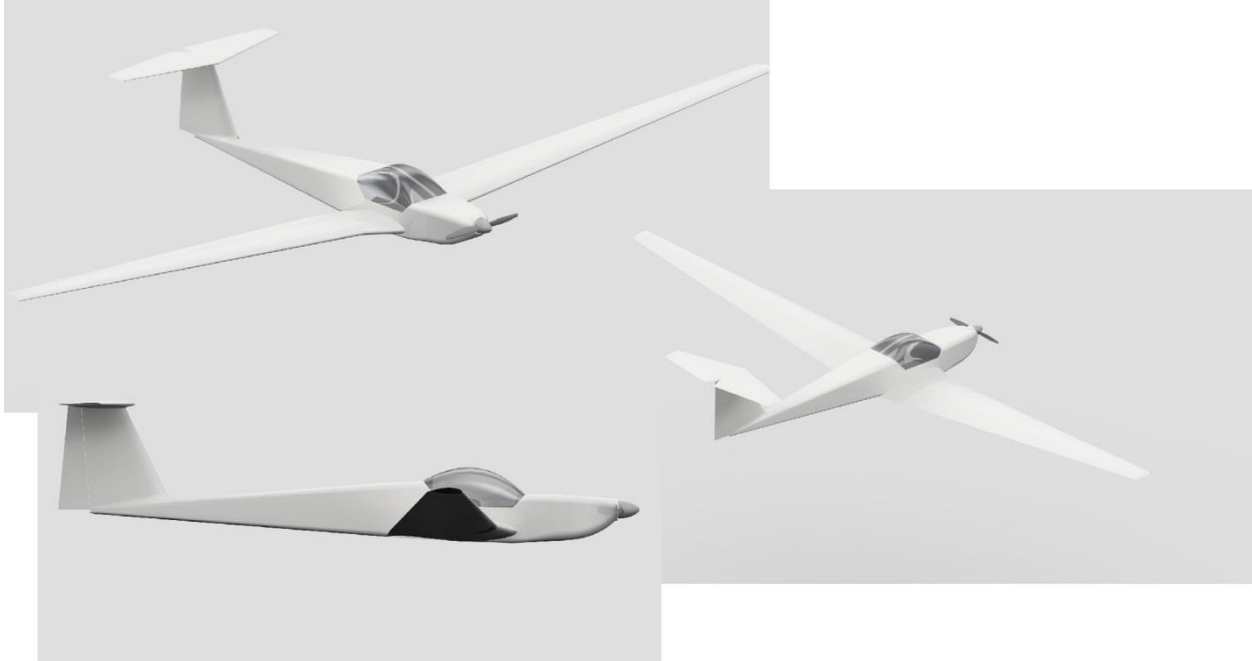


Figure 4: Three-View CAD model rendering of the TG-14A.

Under the Phase I SBIR electric aircraft conversion study, a detailed performance model of the TG-14A was developed. This performance model of the TG-14A was used to develop an understanding of the thrust performance required for the converted TG-14A platform. A plot showing the thrust available and required for the TG-14A for a take-off weight of 1,830 lbs and a cruise altitude of 1,000 ft is shown in Figure 5. The baseline engine for the TG-14A is a 100 Hp Rotax 912 with a Hoffman HO-V62R-1/170FA propeller, which provides approximately 550 lbs static thrust. From the TG-14A flight manual, maximum cruise speed at 75% power is approximately 97 kts. From Figure 5, to replicate the TG-14A power available at 97 kts, an alternative propulsion system would have to produce 270 lbs of thrust. For the purposes of this study, any embedded propulsion system designed to replace the baseline TG-14A power plant will be sized for a static thrust of approximately 550 lbs with a cruise thrust available at 97 kts of 270 lbs.

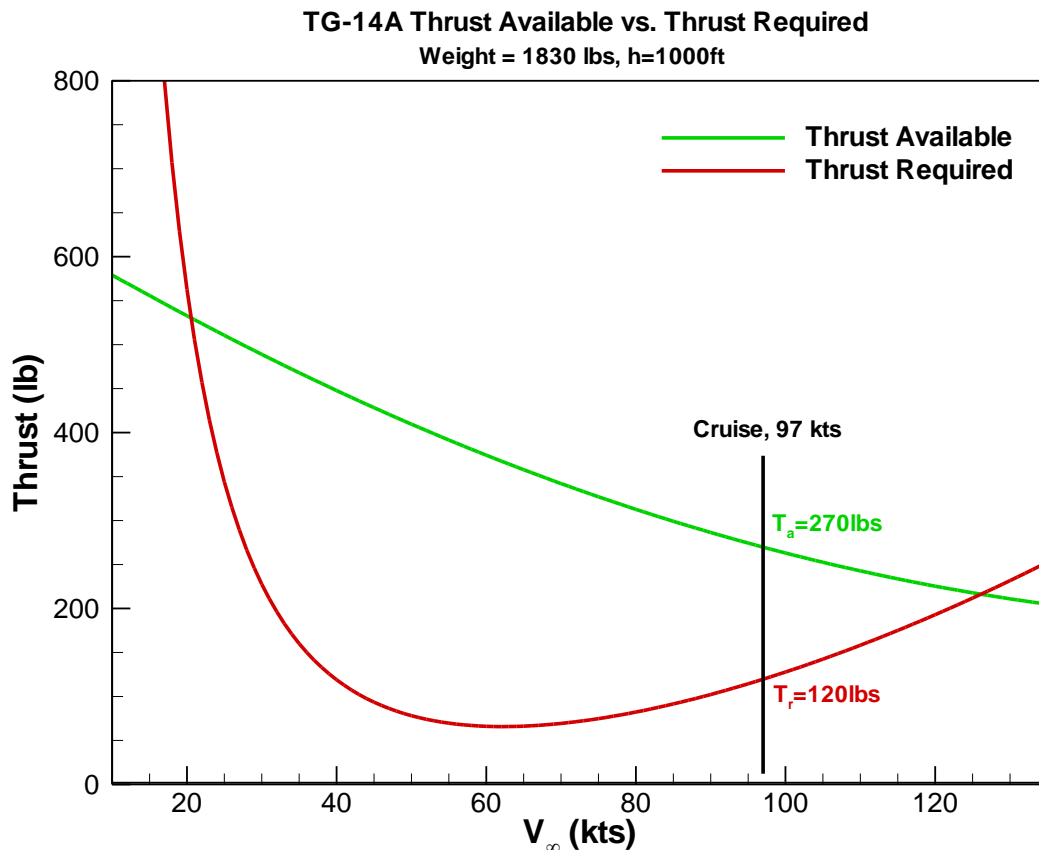


Figure 5: Calculated thrust available and thrust required for the TG-14A aircraft with a take-off weight of 1830 lbs for an altitude of 1000ft.

5.3 Airfoil and Inlet Boundary Layer Estimate

The airfoil section used on the TG-14A is the NACA 64₃-618. The NACA 64₃-618 is an 18% thick section with max thickness at $x/c=0.35$ and max camber at $x/c=0.55$. The root chord of the TG-14A is approximately 57.25 in. Based on the root chord and a cruise speed of 97 kts, the Reynolds number of the wing root sections is 4.96×10^6 .

The XFOIL analysis and design code was used to obtain preliminary predictions of transition location and boundary layer parameters for the airfoil section at zero degrees incidence. The zero degrees incidence case would be the simplest to imitate in the 2D hump wind tunnel test. At $\alpha=0^\circ$, $Re=4.96 \times 10^6$, XFOIL predicts a lift and drag coefficient of $C_l=0.496$, $C_d=0.00817$, respectively. Transition was fixed at $x/c=0.01$ on the upper surface. The XFOIL predicted pressure distribution for the section is given in Figure 6.

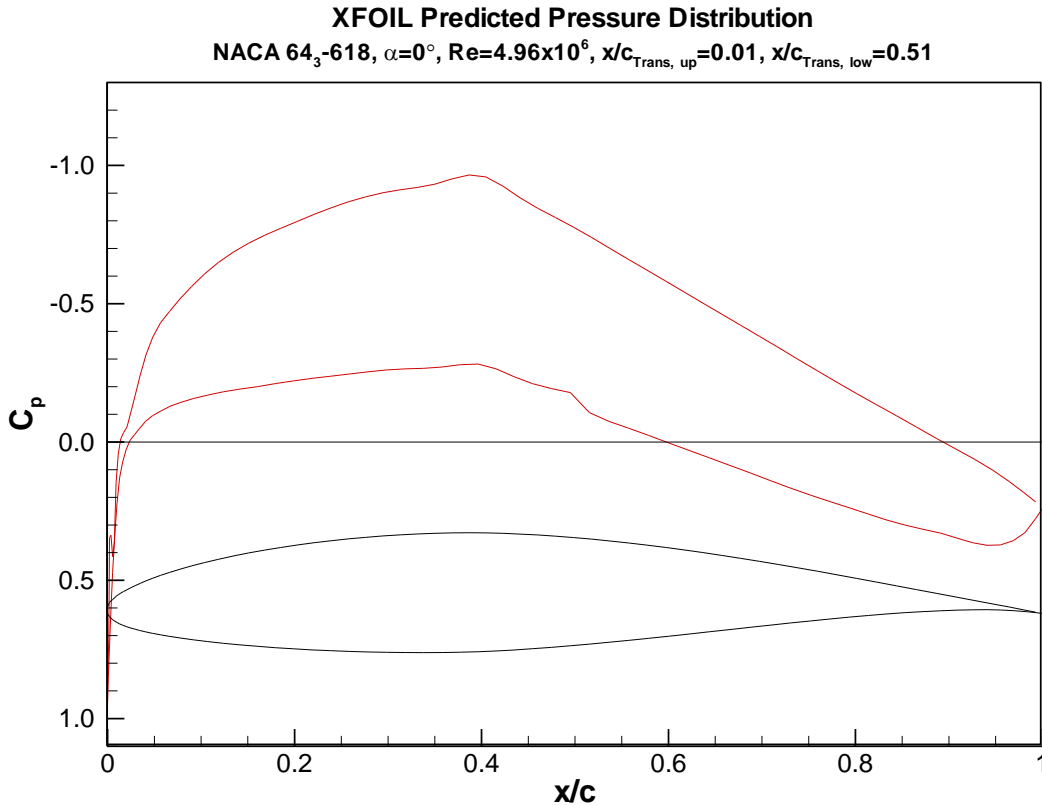


Figure 6: XFOIL predicted pressure distribution for the NACA 64₃-618 section at $\alpha=0^\circ$, $Re=4.96 \times 10^6$.

From Figure 6, the chordwise location on the upper surface of the embedded EDF should be far enough aft so that the local velocity is as near to free-stream velocity as possible to maximize the fan thrust. The boundary-layer edge velocity does not approach free-stream until $x/c=0.90$ on the upper surface. In order to maximize the BLI benefit, the inlet should therefore be placed at $x/c=0.90$.

After obtaining the baseline XFOIL simulation, the boundary-layer thickness as a function of chord length for the model upper surface was estimated. The baseline XFOIL integral boundary-layer calculates transition location, skin friction and momentum and displacement thickness as a function of surface length from the leading-edge stagnation point. Using these values, the boundary-layer thickness and profile shape can be estimated at any point.

Based on the local boundary-layer parameters, δ^* , θ , and C_f , a boundary-layer profile generation routine was written to calculate a boundary-layer profile for a given x/c location. For laminar attached flows the Falkner-Skan profile family is used; the same family used to generate the current XFOIL integral parameters. The Falkner-Skan profiles allow for both favorable and adverse pressure gradients. The Falkner-Skan equation is given below⁴:

$$f''' + ff'' + \beta(1 - f'^2) = 0$$

Equation 1

where: $f' = u/U_{\text{edge}}$ and $\beta = (2s/U_{\text{edge}})(dU_{\text{edge}}/ds)$

The parameter β is related to the pressure gradient and can be correlated to the shape factor H . For a given shape factor, the Falkner-Skan equation can be solved to generate a velocity profile $u(y/\delta)/U_{\text{edge}}$. The Falkner-Skan family of profiles is only valid, however, for attached laminar flows. Solutions are difficult to obtain in a region with a separation bubble. For separated flows, Karman-Pohlhausen profiles are generated.

The Karman-Pohlhausen method is an approximate method which also takes pressure gradient into account and is valid for attached and separated flows. The Karman-Pohlhausen equation is given below⁵:

$$\frac{u}{U_{\text{edge}}} = a\eta + b\eta^2 + c\eta^3 + d\eta^4$$

Equation 2

$$\text{where: } a = 2 + \frac{\lambda}{6}; b = -\frac{\lambda}{2}; c = -2 + \frac{\lambda}{2}; d = 1 - \frac{\lambda}{6}; \lambda = \frac{\delta^2}{\nu} \frac{dU_{\text{edge}}}{ds}$$

As with the Falkner-Skan solution, the λ parameter is related to the pressure gradient and can be correlated to the shape factor. Pohlhausen profiles are generated for all separated flow regions.

Finally, attached turbulent flows are approximated by a Cole's wake solution. Cole's wake solution is an approximate form of the law of the wake. Again, the method is suitable for both favorable and adverse pressure gradients. The Cole's wake solution is given below⁶:

$$\frac{u}{U_{\text{edge}}} = 1 + \frac{\sqrt{C_f/2}}{\kappa} \ln\left(\frac{y}{\delta}\right) - \frac{2\Pi}{\kappa} \sqrt{\frac{C_f}{2}} \left[1 - 3\left(\frac{y}{\delta}\right)^2 + 2\left(\frac{y}{\delta}\right)^3 \right]$$

Equation 3

where: $\Pi = \Pi\left(\frac{\delta^*}{\tau_w} \frac{dP}{dx}\right)$, which is related to Clauser's equilibrium parameter, and $\kappa = \text{constant}$.

For turbulent profiles, from Drela and Giles⁷:

$$\delta = \theta \left(3.15 + \frac{1.72}{H_k - 1} \right) + \delta^*$$

Equation 4

where: H_k is the kinematic shape factor. All three methods produce realistic velocity profiles, especially the Falkner-Skan solutions. The following logic is used to determine which profiles are used:

Flow	Profile Family
Laminar	Falkner-Skan
Separated, $C_f < 0$	Pohlhausen
Turbulent	Cole's Wake

Using the above relationships, the boundary-layer thickness on the model upper surface was calculated as a function of x/c and is shown in Figure 7. From Figure 7, at $x/c=0.90$, the predicted boundary-layer thickness is approximately 1.38 in. The Cole's Wake turbulent boundary-layer profile calculated for $x/c=0.90$ is shown in Figure 8.

The XFOIL predicted results provide a good first estimate of the boundary-layer characteristics of the proposed airfoil section at the test conditions. The boundary-layer profile shown in Figure 8 will be used in the next section in order to estimate the inlet height and area based on the required fan mass flow rate.

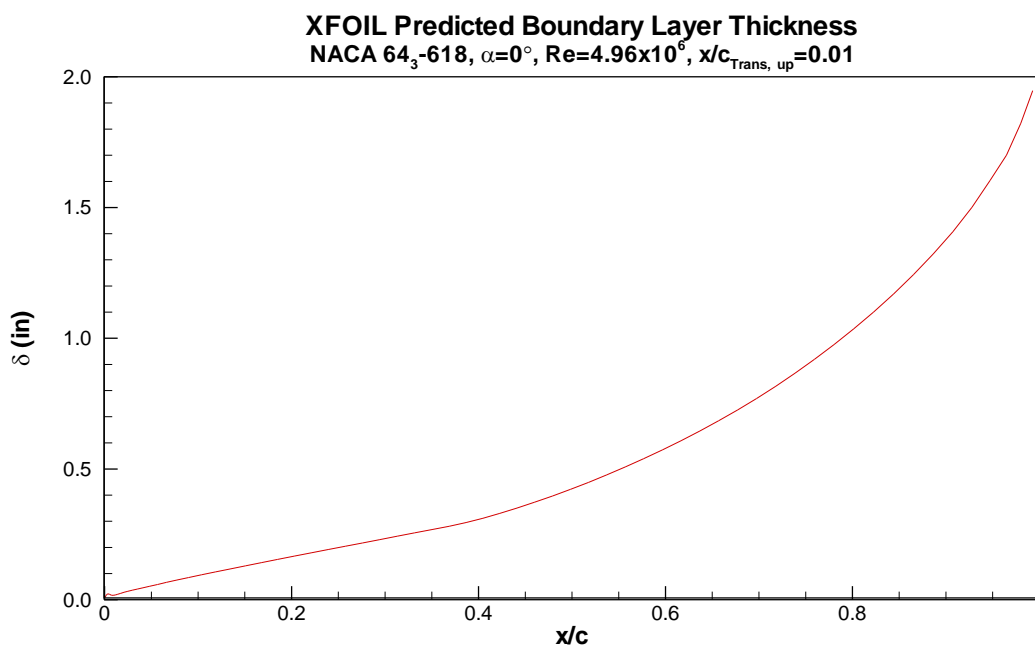


Figure 7: Predicted upper surface boundary-layer thickness versus x/c for the NACA 64₃-618 section at $\alpha=0^\circ$, $Re=4.96 \times 10^6$.

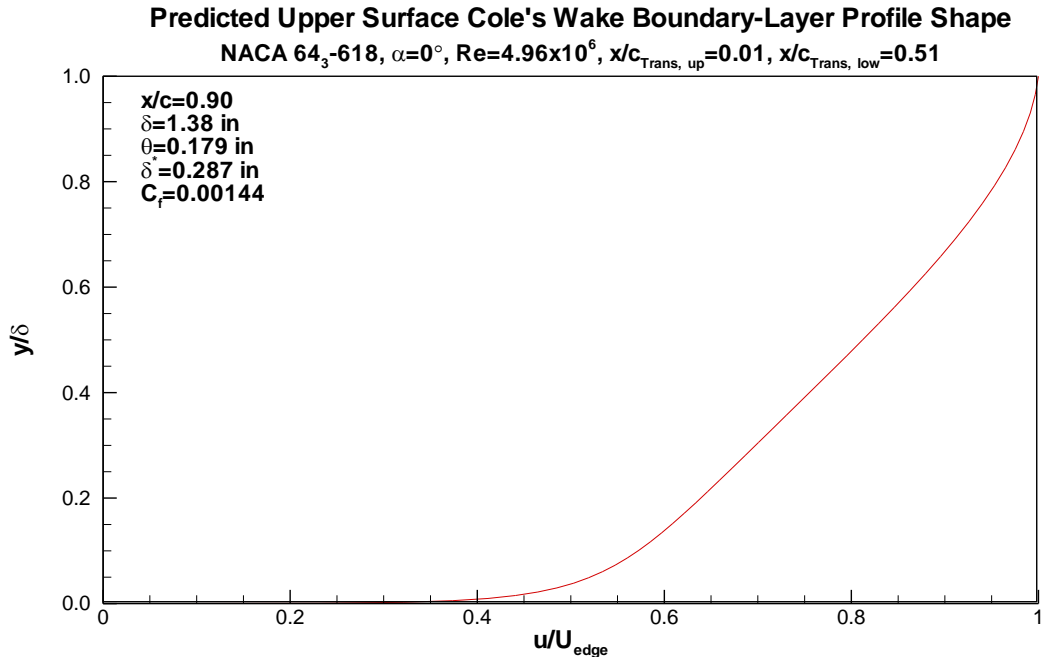


Figure 8: Predicted boundary-layer profile at $x/c=0.90$ on the upper surface of the NACA 64₃-618 section at $\alpha=0^\circ$, $Re=4.96 \times 10^6$

5.4 Choice of COTS Ducted Fan and Fan Power Source

5.4.1 COTS EDF Unit

After determining the thrust required for the alternate propulsion system (≈ 550 lbs static thrust and 270 lbs at 97 kts cruise), available currently off-the-shelf electric ducted fans were investigated. Since the system envisioned is a distributed propulsion system, multiple EDFs are required. Several EDFs were found which could possibly work for a TG-14A based test bed.

COTS EDFs come in several “standard” sizes. These “standard” sizes generally refer to the fan core inner diameter. These include 70 mm, 90 mm, and 128 mm sizes, or classes of EDFs. In addition, a 140 mm size also exists. The 128 mm fan sizes can produce static thrusts up to 29 lbs, with the 140 mm size producing up to 46 lbs of thrust. For a 29 lb static thrust EDF, 18 individual fans would produce 522 lbs static thrust. For the 46 lb thrust EDF, 12 individual fans would produce 552 lbs static thrust. These individual fans would most likely be divided equally per wing, and placed near the wing roots. These static thrust numbers are for the fan as tested on a thrust stand and do not include any inlet duct losses. A table showing the individual fans considered, their thrust, power required, and required number of fans is shown in Table 2.

Manufacturer	Model	Class	Fan Diam. (in)	Fan Swept Area (in ²)	Max Thrust (lbs)	Power Req. (kW)	Eff.	# of Fans Req. *	Inlet Size WxH (in)	% BL Ingestion	Total Power Required	
											Take-Off (kW)	Cruise** (kW)
Aero-Naut	TF-8000	140mm	5.65	20.84	46	17.5	0.65*	12	6.99x6.99	19.8	210.0	178.8
JMP/Extreme Power Sys.	XPS Dynamax Extreme	120mm	5.00	15.44	29	12.1	0.55*	18	6.00x5.62	24.5	217.8	207.0
Schuebeler	DS-94-DIA HST DSM6745-700	120mm	5.04	14.57	29	9.8	0.70	18	6.00x5.47	25.2	175.5	162.9
Schuebeler	DS-77-DIA HST DSM6745-700	120mm	4.72	11.93	25	8.6	0.70	21	5.25x5.25	26.2	180.6	162.7
Schuebeler	DS-51-DIA HST DSM4640-950	90mm	3.66	7.91	11	3.4	0.70	48	3.96x3.96	34.8	160.8	158.4

* Estimation based on Power Required For Max Thrust

** Estimated Power Required To Match Baseline Propeller/IC Engine Available Cruise Thrust

+ Based on required take-off thrust

Table 2: Commercially available off-the-shelf EDF units considered for TG-14A TeDP system.

Also included in Table 2 are the individual fan efficiencies, an estimation of the appropriate inlet size for a mail slot type inlet, and the associated percentage of boundary layer ingestion based on the inlet height, an inlet location of $x/c=0.90$, and an airfoil chord based Reynolds number of 4.96×10^6 which corresponds to a cruise velocity of 97 kts. The percentage boundary layer ingestion assumes a boundary layer height calculated from the XFOIL based estimation discussed in the previous section (Section 5.3). For a fully turbulent boundary layer at $x/c=0.90$ and $Re_c=4.96 \times 10^6$, the estimated boundary layer thickness is $\delta \approx 1.38$ in. The inlets sized are approximately square.

From Table 2, the thrust range of the fans investigated range from 46 lbs for the TF-8000 to 11 lbs for the 90 mm class Schuebeler. These thrust levels do not account for any installation losses. Based on the maximum static thrust for each EDF unit, the number of units required to produce a net thrust of 525 lbs was calculated. The smallest 90 mm class Schuebeler fan would require 48 individual fans to match this thrust level, whereas the largest TF-8000, would only require 12 fans. The total power required to produce this thrust level was also estimated. Again, while this power required includes the fan efficiency, it does not include any installation efficiency losses. As would be expected, as the fan size increases, and the maximum attainable thrust increases, the power required also increases. For the 12 TF-8000's EDF units, the power required to match the static thrust of the TG-14A would be approximately 210 kW, which drops to 160.8 kW for the 48 small 90 mm class Schuebeler fans.

From a systems and integration standpoint, 48 fans seems a sub-optimal solution. The power hungry, lower efficiency TF-8000 also would appear to be a sub-optimal solution. The three remaining 120 mm fans would appear to provide a good compromise between size, thrust, and power. The XPS Dynamax Extreme was eliminated due to its relatively low efficiency as compared to the Schuebeler fans. Elimination of the Dynamax extreme left the DS-94-DIA HST and the DS-77-DIA HST fans. The DS-94-DIA HST has a larger fan swept area of 14.57 in^2 as compared to the 11.92 in^2 for the DS-77-DIA HST, providing a maximum thrust of 29 lbs and 25 lbs, respectively. The slightly larger DS-94-DIA HST would appear to be the better choice, requiring fewer fans at a slightly lower power required.

Also included in Table 2 is an estimation of the power required to match the baseline TG-14A power plant thrust available at cruise. This estimation of power required for max cruise thrust takes into account the ingested boundary layer. The result being that the power required to match the maximum cruise thrust provided by the baseline TG-14A power plant is less for the embedded propulsors (as compared to the power required for maximum static thrust) due to the boundary layer ingestion lowering the effective free-stream velocity.

Based on the above analysis, the Schuebeler DS-94-DIA HST DSM6745-700 appears to provide the best combination of thrust level, efficiency, power required, and the number of required units to match the baseline TG-14A power plant performance. As a result, the Schuebeler DS-94-DIA HST DSM6745-700 was chosen as the primary fan for testing during the Phase I effort. Although three fans were planned for the wind tunnel investigation, a single fan was ordered from Schuebeler for preliminary testing. A photograph of the EDF unit is shown in Figure 9, with a photograph of the electronic speed control shown in Figure 10. The electronic speed control (ESC) is an MGM Compro TMM 25063-3 X series controller and allows smooth throttability of the EDF unit. The ESC was controlled through a LabVIEW generated PWM signal.

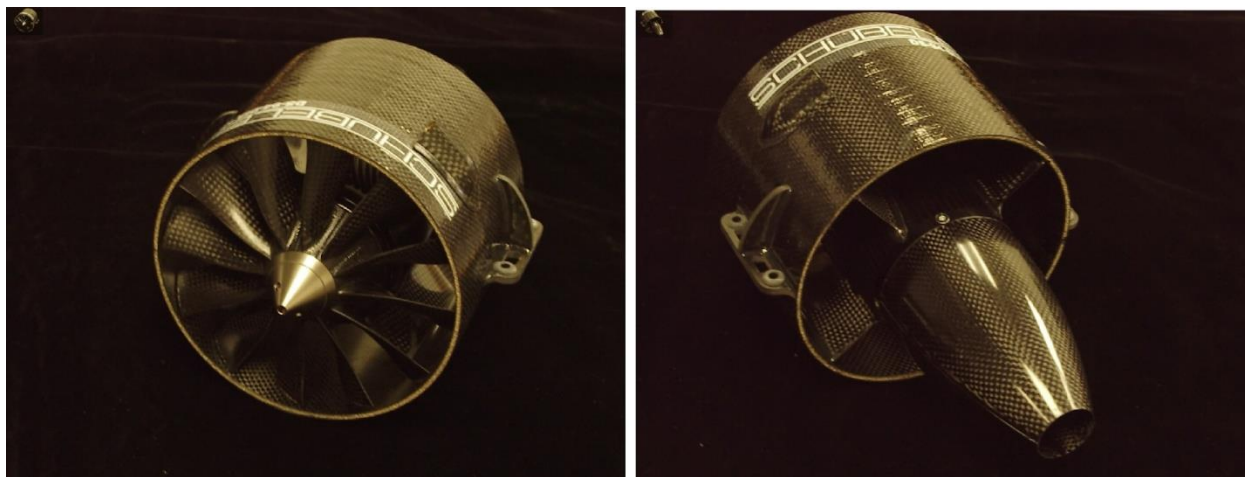


Figure 9: Photograph of new Schuebeler DS-94-DIA HST DSM6745-700 EDF unit at RHRC.

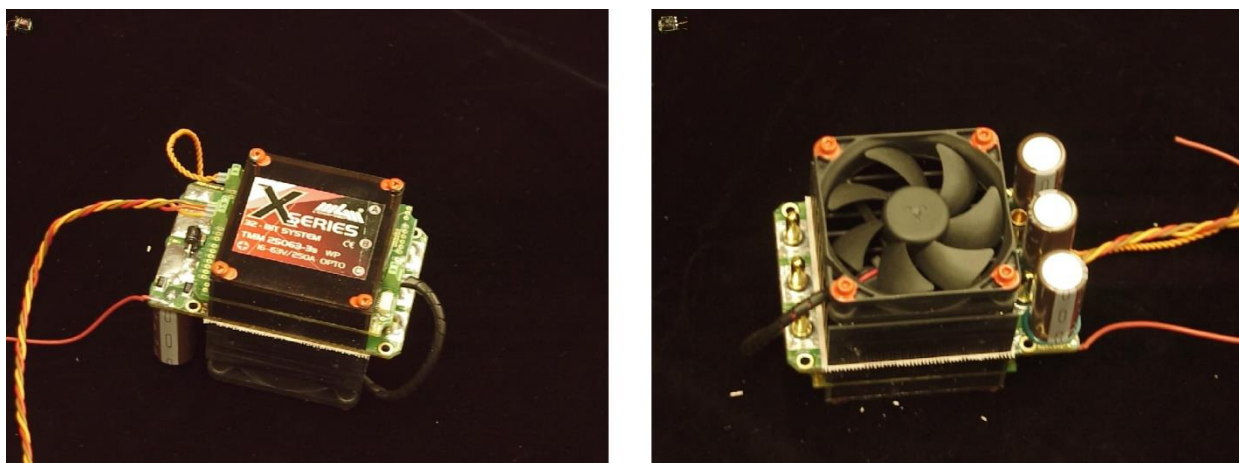


Figure 10: Electronic speed control for the new Schuebeler DS-94-DIA HST DSM6745-700 EDF unit.

5.4.2 Power For EDF Units

The EDF units chosen are primarily used for scale radio control jet aircraft models. They are typically powered by lithium polymer batteries, giving short run times of approximately 2-3 minutes at full power. The Schuebeler DS-94-DIA HST DSM6745-700 draws at 192 A at 52 V for 29 lbs maximum static thrust. Powering the fans with DC power supplies would be optimal for control, ease of set-up, and extended run times. Power supplies capable of providing 52 V at 192 A however, are prohibitively expensive.

In order to increase run time and keep cost down, it was first envisioned that the fans for the wind tunnel test could be powered by multiple deep cycle marine batteries wired in series. RHRC has access to several Optima marine deep cycle batteries. The batteries have a C/20 rating of 55 Ah, which means they are rated to provide 55 Ah of current over 20 hours. They have a maximum cranking amperage of 870 A, and a cold cranking amperage of 750 A. Four batteries in series should provide an operating voltage of 51 V. Peukert's equation⁸ can be used to estimate the amount of available runtime for the battery pack at full static thrust. Peukert's equation relates a battery's capacity and discharge rate to the amount of life, or time available at that discharge rate. Peukert's equation is given as:

$$I^{\dot{\eta}}t = C$$

Equation 5

Where I = Load in amperes

$\dot{\eta}$ = Peukert's constant

C = Capacity of the battery (Amp hours)

t = total time required to discharge battery

For the Optima deep cycle batteries, Peukert's constant was found to be 1.04. At the full static thrust setting, Equation 5 predicts a runtime of 13.2 minutes before the battery is 90% discharged. Predicted runtimes for the motors are assumed to be approximately 2-3 minutes. For a 2-3 minute runtime, the battery discharge depth would be 14% to 21%. A plot showing estimated runtime versus discharge depth is shown in Figure 11. It is acknowledged that the battery voltage will also drop with runtime. Keeping the runtime short and the discharge depth to around 20% or below significantly helps keep the output voltage, and therefore the thrust, constant.

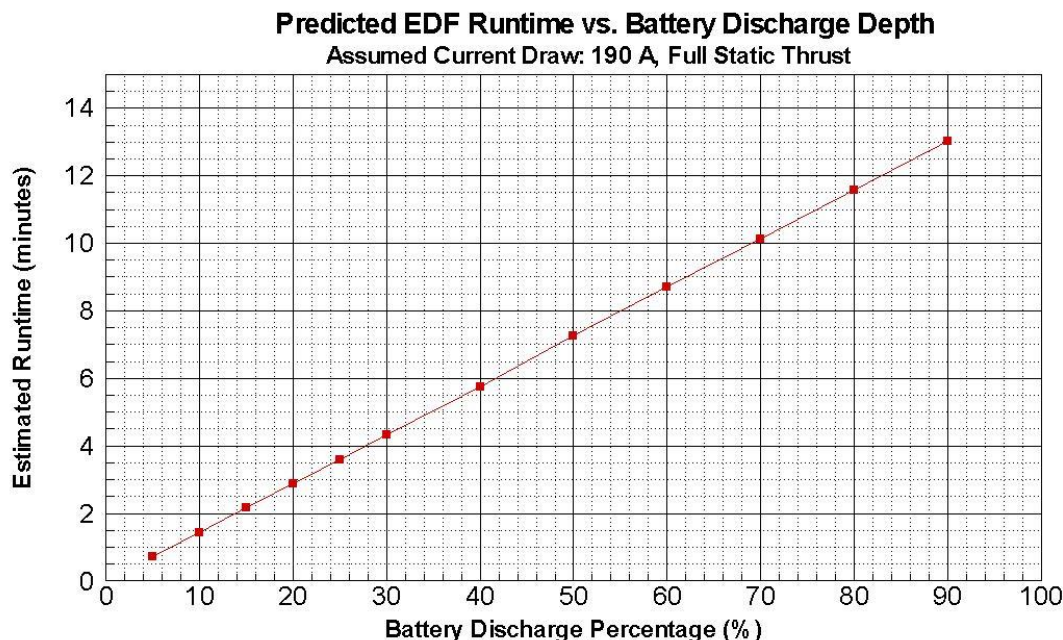


Figure 11: Predicted EDF runtime at full static thrust versus battery discharge depth.

After each individual run, the batteries will need to be recharged before another run can be made. Since three EDF units will be used, 12 individual batteries will need to be recharged. Since a 52 V charger would be prohibitively expensive, the batteries will have to be charged individually. A “smart” battery charger was identified that should provide high charge rates in a package economical enough to allow multiple chargers to be purchased. The charger in question, the Black & Decker model VEC1093DBD charger, can charge at 4, 10, 20, or 40 amp rates. The charger is fully automatic, with a digital microprocessor control for selecting charging rate. For a 25% discharge rate, 13.75 Ah would need to be recharged per battery. Assuming a 20% charging efficiency loss, at 20 A, each individual battery would require approximately 49 minutes. With three chargers, all 12 batteries could be recharged in approximately 3 hours and 15 minutes. At the 40 amp rate, all 12 batteries could be recharged in 1 hour and 40 minutes.

Unfortunately, after initial testing, the deep cycle marine batteries were unable to provide the required power at high thrust/rpm levels. The power required at full thrust for the fans is approximately 52 volts at 190 amps. At high thrust/rpm levels, the voltage of the 4 deep cycle marine batteries would drop to between 40 and 44 volts, significantly reducing the thrust of the fan.

As a result, the battery choice was changed from the deep cycle marine batteries to R/C hobby lithium polymer packs. Specifically, two 7800 mAh 7s packs in series for a 14s pack. At the nominal run voltage of 3.7 volts per cell, the 14s pack will provide 51.8 volts at 190 amps, allowing full thrust from the fan to be produced. Three sets of the 7800 mAh 14s packs were obtained from the fan manufacturer, Schuebeler.

5.4.3 Thrust Test Stand Development and Preliminary Results

For the wind tunnel test, the centerline fan thrust was to be measured. Measurement of thrust for the centerline fan was a significant challenge. The preferred method of thrust measurement would be to have a strain gage based measurement of the thrust. This would require the EDF unit to “float” in the inlet. In order for this type of “floating” set-up to work, the tolerances are exacting. The surrounding structure must not interfere with the EDF metric surface, yet any flow outside of the EDF inner core should be negligible. For the proposed wind tunnel hump model set-up, a strain gaged balance for the EDF unit could be located under the tunnel floor. Although the preferred set-up for thrust measurement, the difficulty with this method is the proper aerodynamic sealing around the fan to minimize flow leakage, yet allowing the EDF unit to float to obtain the most accurate and sensitive thrust measurement.

If a method and set-up could not be determined for a strain gage based thrust measurement, a pressure rake downstream of the fan could be used to measure the EDF thrust. This type of measurement would require the careful placement of a large number of individual tubes in a rake near the jet exit plane. These individual rake ports would then be used to integrate the exit velocity of the jet. If this type of measurement system were used, the CFD results could be used to help locate the tubes in order to estimate and minimize the measurement error. After careful examination of the two above approaches, a thrust balance was devised to measure the thrust directly during the test entry.

As previously stated, in order for a “floating” thrust balance set-up to work, the surrounding structure must not interfere with the EDF metric surface. Also any flow outside of the EDF inner core should be negligible. The thrust balance designed utilizes a compact fan attachment structure that mounts to a 1D ultra-low friction linear slide. The slide allows the attachment structure and fan to move freely in the thrust/drag direction. A single load cell attached to the attachment fixture is used to measure the thrust. The thrust stand design is simple and stout. For the wind tunnel hump model set-up, the thrust balance for the EDF unit is located under the tunnel floor. A photograph showing the thrust balance with an EDF unit mounted is shown in Figure 12. In addition to thrust, the test stand measures motor temperature, voltage, and amperage.

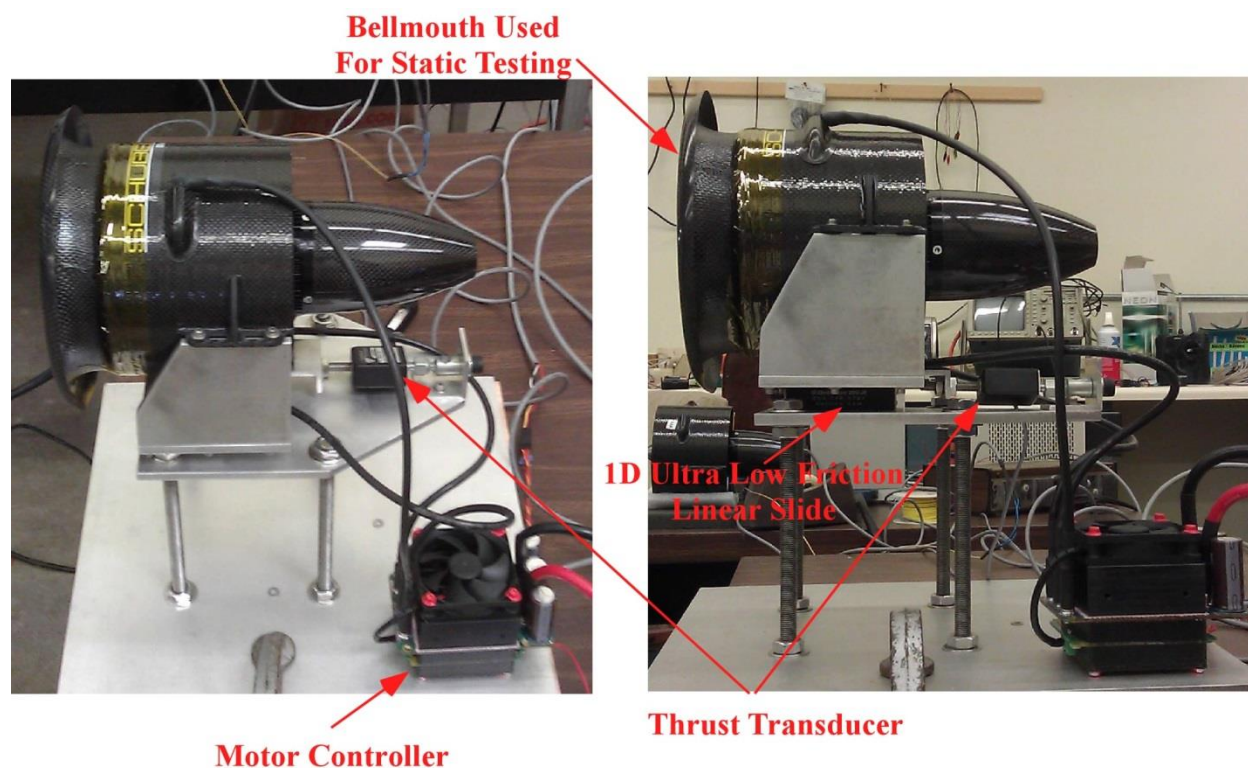


Figure 12: Photographs showing EDF thrust test stand.

5.4.4 Preliminary Static Test Stand Results

Preliminary results from the thrust test stand for one of the Schuebeler DS-94-DIA HST DSM6745-700 fans using the lithium polymer batteries is shown in Figure 13. From Figure 13, thrust, voltage, amperage, and motor temperature are plotted versus % maximum RPM. At the max thrust level, the EDF produced just over 26 lbs thrust, at 50.1 V and 146.9 A. The 26 lbs thrust is 10% below the manufacturer quoted maximum static thrust of 29 lbs. The fan manufacturer was contacted in order to determine the cause of the low thrust. After speaking with the manufacturer, it was determined that of the three pounds of missing thrust, one pound was a result of the inlet bell mouth not being as efficient as the one used by the manufacturer for static testing, and the remaining two pounds being a result of the batteries not providing the voltage. The battery voltage dropped to 50.1 V, instead of holding at 52 V as per the manufacturer. At full charge (4.2 V per cell), the 14s packs have a nominal voltage of 58.8 V. At full power, the fans pull this voltage down to 52 V. The manufacturer was asked several times if the two 7s 7800mAh packs would provide sufficient power. The manufacturer repeatedly promised that the 14s packs would be sufficient. Unfortunately, they were slightly below specification, providing 7.3 kW to the motors instead of the required 9.75 kW. Since the manufacturer is used to dealing with R/C hobbyists, they believed that the battery performance was sufficient, although they did not meet their quoted performance. Since RHRC did not have sufficient budget or time to seek an alternative, the 14s 7800mAh lithium polymer packs were used for the wind tunnel investigation.

EDF Thrust Test Stand Results

Fan: Schuebeler DS-94-DIA HST DSM6745-700, Batteries: Lipo 7800HDHE 14S

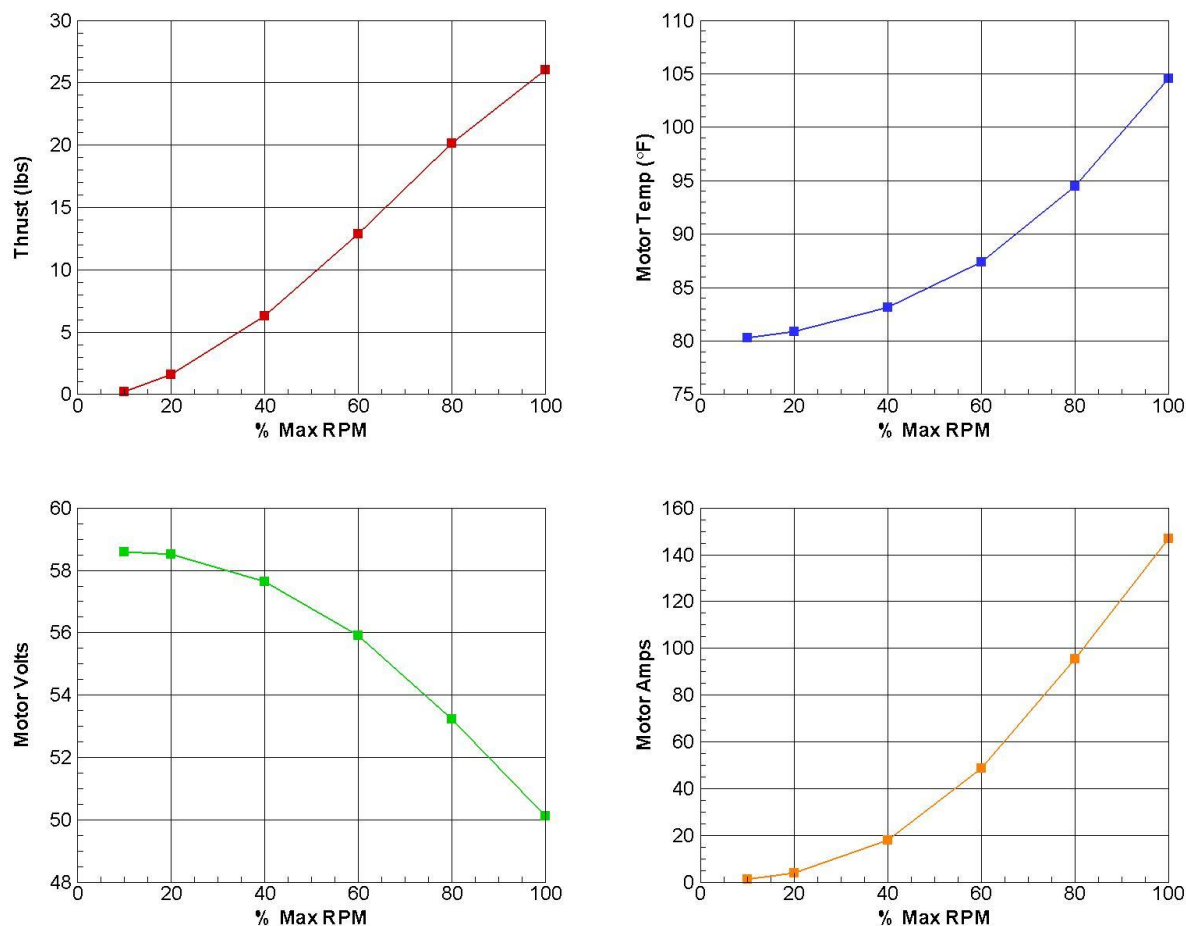


Figure 13: Preliminary thrust test stand results for the Schuebeler DS-94-DIA HST DSM6745-700 fan with 7800HDHE 14s lithium polymer batteries.

5.5 Preliminary Wind Tunnel Model Design and Inlet Sizing

The 2D hump model was designed to be tested in the University of Illinois 3'x4' low speed, low turbulence wind tunnel. The tunnel is an open-return type with a rectangular 3-ft by 4-ft by 8 ft test section. The tunnel width expands in the streamwise direction through the test section to account for the wall boundary-layer growth. The maximum speed of the tunnel is approximately 235 ft/sec.

The 2D hump model envisioned was the full scale TG-14A root chord length of the NACA 64₃-618 upper surface (chord length of 57.25 in). The model spans the tunnel width, 43.8 in at the test section inlet, growing to 44.25 in at the test section exit. Since the cruise speed of the TG-14A is 97 kts (163.6 ft/s), the model was able to be run at full scale Reynolds numbers. Due to its floor mount, the model boundary layer will be fully turbulent. Three separate side-by-side inlet/fan combinations were incorporated into the model. The multiple duct/fan system allows investigation of the effects that changes in neighboring duct mass flow rates have upon a given ducts inlet flow distortion and fan efficiency.

The Schuebeler DS-94-DIA HST fan shroud has an inner diameter of 5.039 in, with a motor diameter of 2.62 in, for an FSA = 14.57 in². In order to size the fan inlet, an estimate of the required mass flow rate was computed based on the static thrust and the thrust available at cruise (97 kts). Assuming an individual static thrust of 29 lbs, 18 of the individual Schuebeler fans would be required. For the required thrust available at cruise (270 lbs), this would equate to 15 lbs thrust from each individual fan. Assuming that the fan exit pressure is equal to free-stream pressure, the fan thrust is related to the mass flow and the difference in velocity between the free-stream and fan exit as given by:

$$T = \dot{m}(v_{exit} - v_{\infty})$$

Equation 6

From continuity, the free-stream capture area mass flow, inlet mass flow, and fan exit mass flow must be equal ($\dot{m} = \rho v A$). Knowing the thrust and free-stream velocity, and fan exit area, an estimate of the required mass flow can be calculated:

$$\dot{m} = \frac{\rho A_{exit}}{2} \left\{ v_{\infty} + \sqrt{v_{\infty}^2 + \frac{4T}{\rho A_{exit}}} \right\}$$

Equation 7

For the case of static thrust, $v_{\infty} = 0$, the calculated mass flow rate is 0.0835 slugs/s, with an exit velocity of 347.25 ft/s. The manufacturer measured fan exit velocity is reported as 354 ft/s. For the cruise speed of 97 kts with a thrust of 15 lbs, the calculated mass flow rate is 0.0823 slugs/s. Based on the mass flow rate of 0.0823 slugs/s, and the estimated boundary-layer profile shown in Figure 8 for model upper surface at $x/c=0.90$, $Re=4.96 \times 10^6$, $\alpha=0^\circ$, the required inlet area was calculated to be 32.8 in². The inlet area was calculated by integrating the velocity profile mass flow contribution and then determining the added height required to match the mass flow for a given inlet width. The inlet area was sized for the full cruise thrust available condition.

As previously stated in Section 5.3, in order to maximize the benefits of boundary layer ingestion, the EDF inlet should be placed at or downstream of $x/c=0.90$. Of significant note, is that since this is a low speed test/EDF system, the duct is a converging s-duct, and not a diffusing s-duct required by transonic turbofans. The diffusing duct is required at transonic free-stream Mach numbers to keep the large diameter fan tip speeds subsonic and to provide increased pressure at the compressor inlet for a turbofan. This difference in inlet design, converging versus diffusing, is one area where the scaling between a smaller, lower speed test bed does not translate directly to the larger commercial transport. Since the inlet duct is a converging, the inlet L/D can most likely be aggressive. For initial design purposes, a value of $L/D \approx 1.0$ was chosen. Since the fan unit has a finite length of about 4 inches, with an $L/D \approx 1.0$, the total length of inlet/fan unit will be approximately 9 inches, including an inch for the inlet distortion rake. If the inlet face sits at $x/c=0.90$, this places the fan exit plane approximately 3.5 inches aft of the trailing-edge at $x/c=1.06$. For installation on the aircraft, having the EDF units sit slightly aft of the trailing-edge does not pose any significant concerns at this time. Since the duct is converging, a lower L/D might also be possible.

Based on an inlet location of $x/c=0.90$ and an inlet width of 6.0 inches, an inlet height of 5.47 inches is required. The 6.0 inch width of the inlet was arrived at as the minimum distance between fans (6 inches on center between fans) to allow for mounting considerations in the model. After fixing the 6 inch width, the 5.47 inch height is arrived at to provide the correct mass flow into the fan, which transitions to a round duct with a 5.04" diameter. Based on an inlet height of 5.47 inches, at cruise, a boundary layer thickness of $\delta=1.38$ inches implies 25% of the inlet height is occupied by the boundary layer.

An initial ProENGINEER CAD model of the wind tunnel set-up with the three individual inlet/fans was developed. Several views of the ProE model developed are shown in Figure 14. From Figure 14, the three EDF units are faired together. Although the rear fairing is not optimal from an aerodynamic point of view for the flight vehicle, the fairing should work well for the wind tunnel investigation since overall lift and drag of the 2D hump will not be measured.

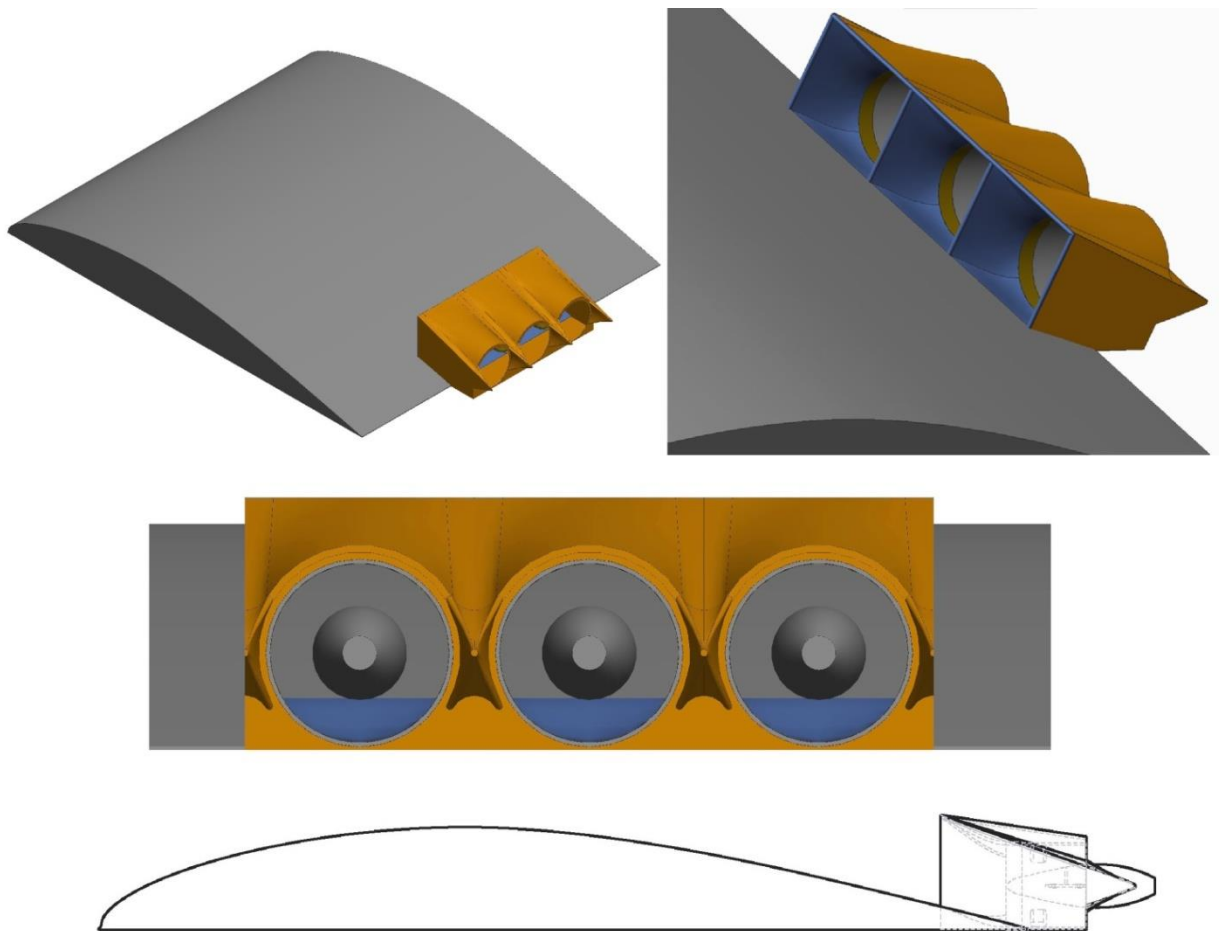


Figure 14: Preliminary ProE model of wind tunnel model showing three EDF units.

5.6 Notional Test Bed Aircraft Layout

After choosing the DS-94-DIA HST DSM6745-700 Schuebeler fan and designing the basic inlet and fairing system, a notional layout of the fans on the TG-14A aircraft was performed. Based

on the assumed thrust level of the chosen EDF unit, as previously stated, 18 individual fans would be required to replace the TG-14A 100 Hp Rotax 912 engine. The 18 fans would be split between the two wings, 9 on each side. A ProE mock-up of the notional test bed aircraft with the 9 fans per wing is shown in Figure 15.

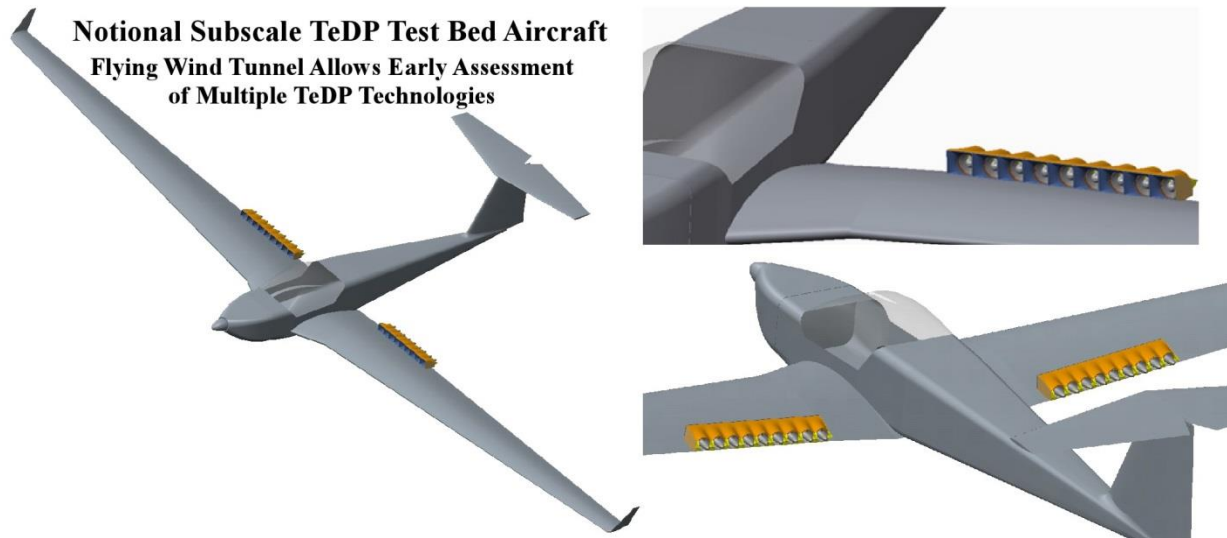


Figure 15: CAD mock-up of notional TG-14A based subscale TeDP test bed aircraft.

5.7 CFD Model

After the initial ProE CAD design of the wind tunnel model was complete, a CFD study was undertaken to evaluate the wind tunnel hump model to help design the converging s-duct inlet and provide a better understanding of the overall EDF flow field. Prior to the full EDF wind tunnel hump model, a model of just the airfoil upper surface mounted in the wind tunnel was studied. The CFD code used was the OVERFLOW⁹ 2.2g solver. OVERFLOW is a Reynolds averaged Navier-Stokes flow solver for structured grid systems. OVERFLOW can use single block grids or Chimera overset (structured) grid systems, allowing accurate assessment of complex aerodynamic geometries. OVERFLOW has been used extensively in the design and analysis of s-ducts.

5.7.1 Preliminary Hump Model

The preliminary CFD model includes the 2D hump model for the airfoil and the wind tunnel walls. The preliminary CFD model was generated to experiment with the model t/c ratio and the inlet and exit boundary conditions. Since the model is rather large compared to the size of the wind tunnel, the model blockage in the tunnel will affect the pressure distribution over the model. As a result, before the EDF system and inlet geometries were added, the baseline airfoil upper surface hump model was run in order to adjust the model t/c so as to best match the free air predicted pressure distribution on the model upper surface. This type of t/c adjustment is much easier without the added complexity of the inlet/EDF geometry.

Secondly, the simplified model allows more efficient optimization of the inlet and exit boundary OVERFLOW is notoriously slow to converge for internal flow problems, and tends to be fickle about boundary conditions for internal flows concerning the conservation of mass flow. The preliminary grid system used for the t/c and boundary condition study is shown in Figure 16.

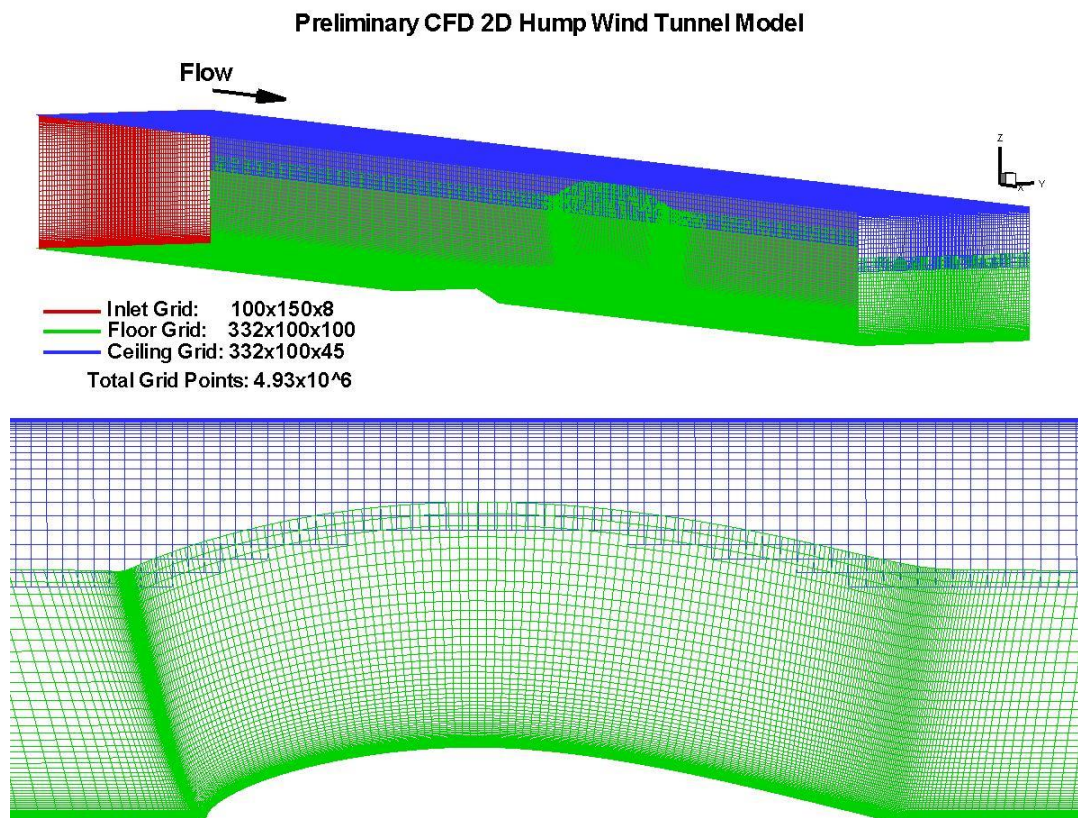


Figure 16: Preliminary wind tunnel 2D hump model CFD grid system.

From Figure 16, the height and width of the tunnel are an accurate representation of the wind tunnel test section and the hump geometry. Both the ceiling and floors are viscous walls. For the floor, a laminar boundary layer is prescribed upstream of the model which transitions to turbulent at the hump leading-edge. The ceiling boundary layer is treated in a similar fashion with transition occurring approximately 2 feet upstream of the floor hump leading-edge location. The actual wind tunnel side walls diverge slightly to account for the boundary layer growth on the walls. For the CFD model, the side walls are model as inviscid walls to mimic the spatial growth of the actual wind tunnel without having to diverge the actual grid walls.

Several inlet and exit boundary conditions, and boundary condition (BC) combinations were employed in an attempt to achieve good convergence of the solution and the correct, stabilized mass flow rate at the inlet and exit planes. The combination of BCs that were arrived at included a simple free-stream condition at the inlet coupled with a nozzle inflow condition that fixes total pressure and temperature and extrapolates mass flow, followed by a basic supersonic/subsonic inflow/outflow boundary condition at the exit.

After initial runs with the baseline $t/c=0.18$ model, the t/c was reduced to $t/c=0.158$ in order to match the XFOIL predicted free-air pressure distribution at $\alpha=0^\circ$. A comparison of the XFOIL predicted free-air pressure distribution and the baseline $t/c=0.18$ and reduced $t/c=0.158$ OVERFLOW wind tunnel hump pressure distributions is given in Figure 17.

Comparison of XFOIL Free-air and OVERFLOW Tunnel Hump Geom. Pressure Distributions

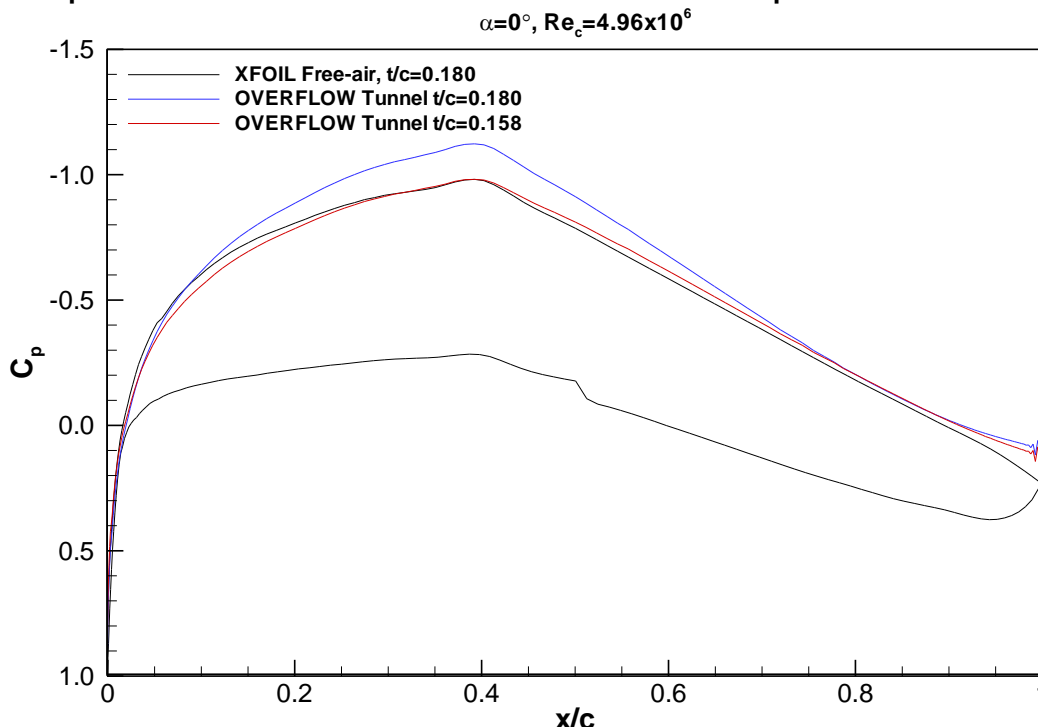


Figure 17: Comparison of XFOIL predicted free-air and OVERFLOW wind tunnel hump geometry pressure distributions, $\alpha=0^\circ, Re_c=4.96 \times 10^6$.

From Figure 17, the blockage created by the wind tunnel walls increases the effective flow velocity over the model, producing a higher than wanted negative C_p at the model maximum thickness. In order to replicate the boundary layer entering the EDF inlet to that of a free-air condition, the pressure distributions between the XFOIL predicted free-air and OVERFLOW hump geometry should match as closely as possible. As a result, the t/c of the OVERFLOW hump geometry was successively reduced. The final t/c chosen was $t/c=0.158$, approximately 12% lower than the $t/c=0.18$ baseline. As seen from Figure 17, the $t/c=0.158$ pressure distribution much more closely matches the XFOIL free-air predicted pressure distribution. A plot showing the tunnel centerline pressure contours and flowfield streamlines is shown in Figure 18.

The boundary layer velocity profile at $x/c=0.90$ was extracted from the OVERFLOW solution. The OVERFLOW predicted boundary layer thickness is approximately 1.5 inches, which compares fairly well to the XFOIL predicted free-air value of 1.38 inches ($\approx 8\%$ difference).

OVERFLOW Predicted Pressure Coefficient Contours For the Wind Tunnel Hump Geometry

$V_\infty = 163 \text{ ft/s}$, $Re_c = 4.96 \times 10^6$, $t/c = 0.158$

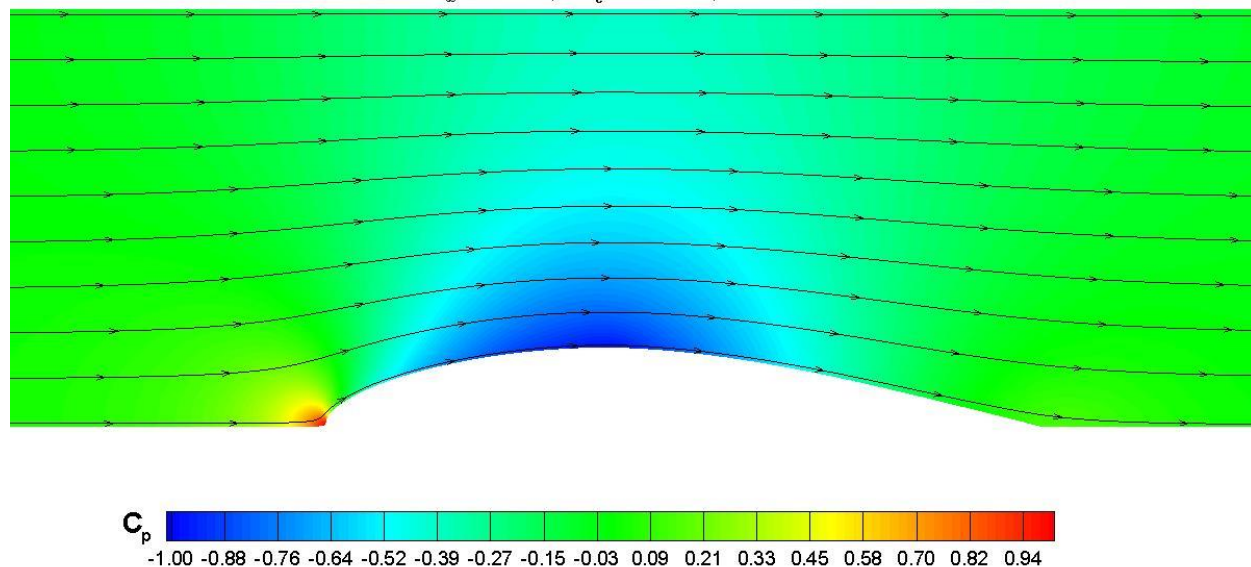


Figure 18: OVERFLOW predicted pressure coefficient contours for the wind tunnel hump geometry, , $\alpha = 0^\circ$, $Re_c = 4.96 \times 10^6$.

5.7.2 Full EDF Hump Model

After the preliminary CFD model of the basic airfoil pressure distribution in the tunnel was investigated, the full CFD model including the 3 inlets/fans were added to the basic airfoil geometry. A schematic of the airfoil upper surface with the EDFs and ducting system is shown in Figure 19.

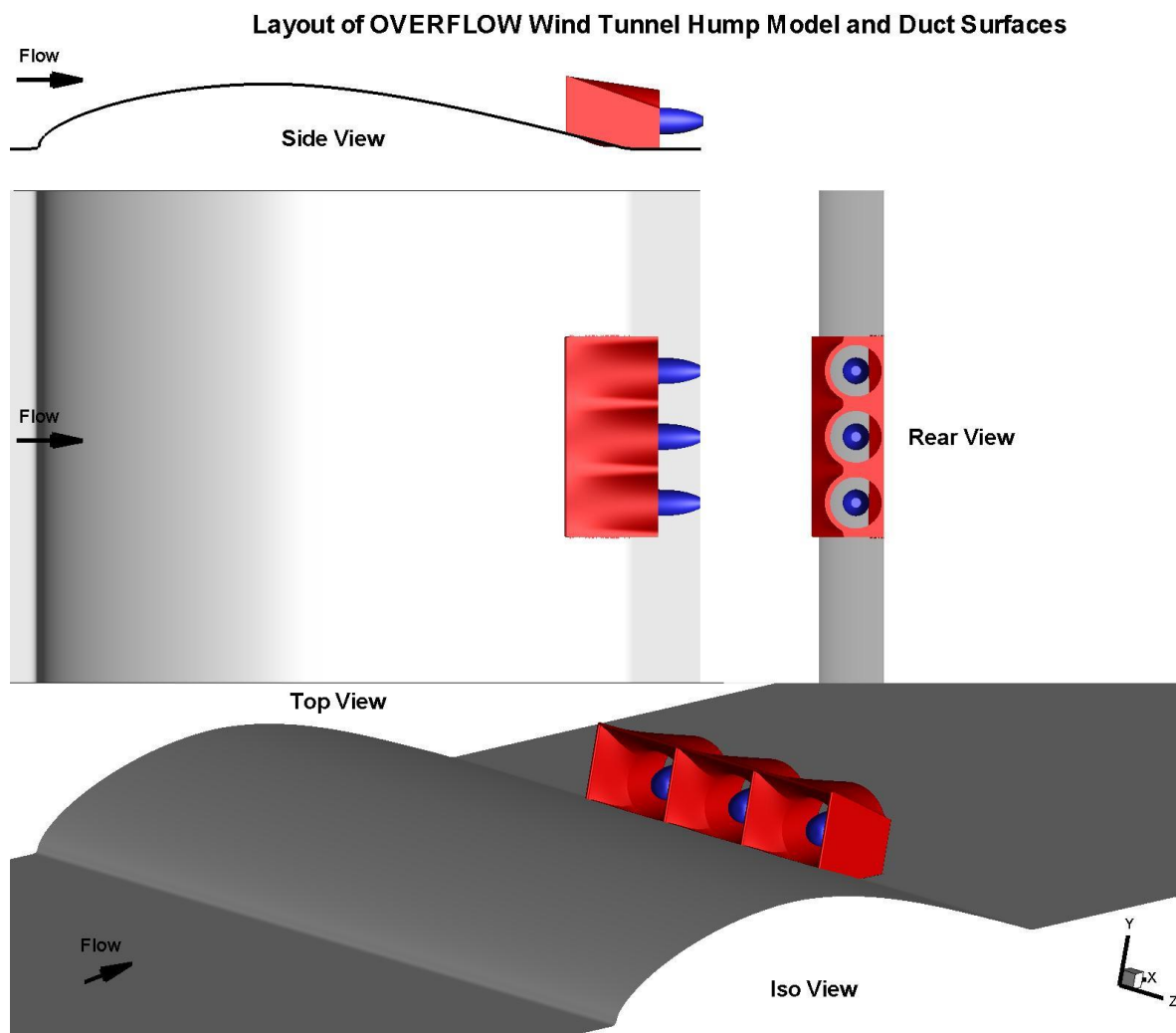


Figure 19: Overall layout of the OVERFLOW CFD model of the 2D wind tunnel hump model including the three inlet and EDF duct systems.

From Figure 19, the EDF duct system is shown in red. The center plugs for the individual fans are shown in blue. For the OVERFLOW CFD model, the individual fans are modeled using an actuator disk boundary condition. The boundary condition imposes a Δp at the fan disk location. The plug (shown in blue) represents the electric motor body present in the actual EDF and extends aft several inches from the EDF unit.

The overall grid system developed for the CFD model is shown in Figure 20. From Figure 20, the grid system is made up of 51 individual grids, totaling 32,460,914 points. The grid system was developed from the ProE CAD surfaces using chimera grid tools. A scripting system was set up to generate the surface grids based on facet files exported by ProE. All grid normal spacing begins with a y^+ of 1 or less. Upwinding with the Spalart-Almares turbulence model was used for all cases. Cases were run with and without the center plug geometry. All cases were run with a simulated free stream cruise velocity for the TG-14A of 97 kts (163.61ft/s). Three basic thrust levels for the fans were investigated. These included a full thrust available at

cruise, a thrust required at cruise, and a windmill case. For the full thrust at cruise, each fan was set to achieve a nominal thrust of 15 lbs based on an estimation of the mass flow rate through the duct. Since the thickness of the OVERFLOW boundary layer was not known prior to the run, nor the effect of the fan on the upstream pressure distribution, the mass flow estimate does not make an allowance for the ingested boundary layer. As a result, the thrust levels calculated from the solutions should be slightly larger due to the ingested boundary layer reducing the effective inlet velocity. For the cruise thrust case (thrust required at cruise), each fan was set to achieve a nominal thrust of approximately 6.65 lbs. For both of the thrust cases, mass flow in the fan duct was estimated and the Δp adjusted to achieve that mass flow. Thrust was then calculated based on the post run calculated duct mass flow, inlet velocity, and exit velocity. The inlet velocity is the average velocity over the inlet area for each duct/fan, which includes the effect of the boundary layer. For the windmill case, no Δp in the duct was specified with the resulting mass flow simply a result of the baseline flow through the system. Although the plug is present in the duct, the fan disk is not, and as a result the windmill case represents the most optimistic flow through case in terms of blockage.

OVERFLOW Wind Tunnel Hump EDF Model Grid System

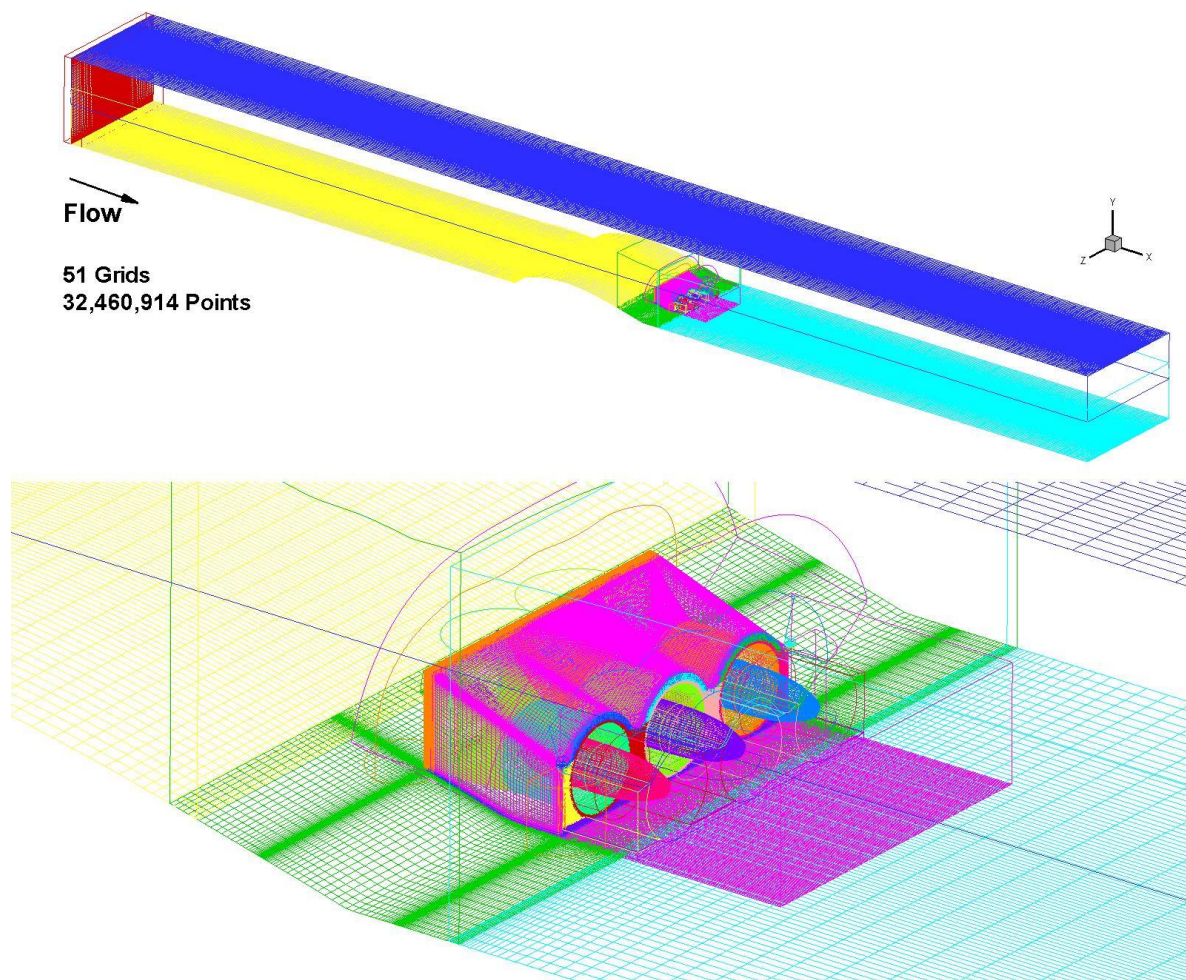


Figure 20: OVERFLOW grid system developed for the full 2D hump wind tunnel model including the three EDF units.

Table 3 shows the predicted mass flow rates for the two thrust cases, and the resulting calculated thrust numbers for all three cases. The thrust results shown in Table 3 were calculated by taking the mass flow calculated in the circular fan duct and multiplying by the difference in the average inlet and exit velocity. As discussed above, the actual thrust number is higher than the estimated thrust for a given mass flow due to the effect the ingested boundary layer reducing the effective inlet velocity. It should also be noted that after running several cases, it was noted that the pressure at the exit of the duct, where the average exit velocity was calculated, was slightly below the free-stream pressure. It is believed that the duct exit pressure not returning to free-stream at the duct exit is due to the constraining effect of the wind tunnel walls. Since the calculation of thrust using the mass flow and the difference between the exit and inlet velocity assumes that the pressure has returned to free-stream, the as-run pressure difference along with the exit area were used to calculate a pressure thrust to correct the mass flow based thrust. This pressure thrust reduced the mass flow based thrust by approximately 0.8 lbs for the full thrust case, and 0.15 lbs for the cruise thrust case. The thrusts shown in Table 3 reflect this correction. Accounting for this pressure thrust will allow a more direct comparison to a thrust balance reading during the wind tunnel test entry, as a fan mounted thrust balance would automatically take this pressure thrust into account.

Case	Est. \dot{m} (slugs/s)	Est. Thrust lbs	Calc. \dot{m} (slugs/s)	Avg. Inlet V (ft/s)	Avg. Exit V (ft/s)	Thrust (lbs)
Full T_a	0.08027	15	0.0808	153.72	358.22	15.7
Cruise T_r	0.0629	6.65	0.0627	119.91	271.61	9.4
Windmill	n/a	n/a	0.0402	87.78	166.16	3.1

** Free-stream $V_\infty = 163.61$ ft/s

Table 3: Estimated and calculated mass flows and resulting thrust numbers for the cases run.

Surface pressure distributions for the three cases are shown in Figure 21. The surface pressure distributions shown in Figure 21 were taken along the model center line, which is the middle of the center duct. From Figure 21, the full thrust pressure distribution most closely matches the free air and reduced thickness airfoil pressure distributions. The C_{ps} aft of $x/c=0.15$ are slightly more negative than the free air or reduced thickness $t/c=0.158$ cases. The estimate of the mass flow for the full thrust case was the mass flow used to size the duct inlets, and as a result the pressure distribution should most closely match the free air pressure distribution.

Comparison of XFOIL Free-air and OVERFLOW Tunnel Hump Geom. Pressure Distributions

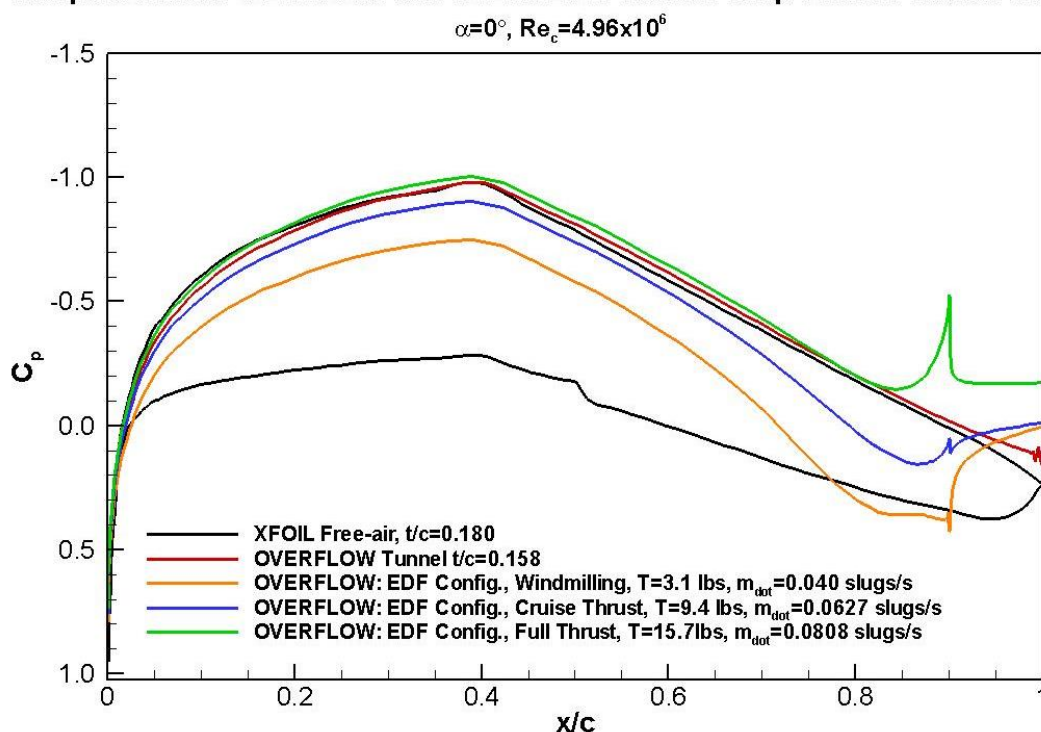


Figure 21: Comparison of center line surface pressure distributions for the baseline free-air airfoil, the reduced thickness airfoil section in the tunnel model, and the full and cruise thrust cases, and the windmill case.

For mass flows below the design mass flow, the fan/duct system produces some amount of blockage, or spillage. The blockage or spillage effect is clearly evident in the cruise and windmill thrust pressure distributions, and has a large effect on the overall pressure distribution of the airfoil. For the cruise thrust available case, the reduction in mass flow below the design mass flow creates blockage which reduces the velocity of the flow as it approaches the inlet, creating a more positive pressure coefficient. Due to the elliptical nature of the subsonic flow field, this reduction in flow velocity due to the increased blockage is felt far upstream on the airfoil. As the level of blockage, or spillage increases for the windmill case, these effects become more severe. For the full thrust case, the calculated thrust is 15.7 lbs, slightly larger than the estimated 15 lbs. The increase in thrust is a result of the ingested boundary layer lowering the effective inlet velocity. For the cruise thrust case, the difference between the predicted and as calculated thrust is much larger. This larger increase in the thrust for the cruise case is due to the reduced effective inlet velocity due to the increased spillage of the cruise thrust case. Recall that the thrust is equal to the mass flow through the duct times the difference between the exit and inlet velocity. As the effective inlet velocity decreases due to increased blockage, the effective thrust will increase. Although the thrust increases due to the spillage created by the increased blockage, the lift will clearly decrease, with an accompanying increase in drag. Due to the reduction in area of the duct and plug, the windmill case produces a thrust of 3.1 lbs. Since the blockage of the fan disk is not modeled, the blockage of the actual fan at windmill conditions will be larger.

Contours of Mach number and streamlines for a vertical cut plane taken through the center duct for the full thrust, cruise thrust, and idle cases are shown in Figure 22. From Figure 22, for the full thrust case, the flow through the duct looks fully attached and well behaved. No discernible or significant separation is observed on the top, outer portion of the duct inlet. Separation is present on the rear facing faces of the plug and inlet top. For the inlet top, a tear drop shape extending from the aft face of the duct will be included in the wind tunnel model as shown in Figure 14, but was not included in the CFD model. For the cruise thrust case, again the flow in the duct looks fully attached and well behaved. A low Mach number region on the top, outer portion of the duct surface denoting some local separation is present for the cruise thrust case. This separation on the duct outer surface is a result of the spillage created by the reduced mass flow in the duct moving the inlet highlight lip stagnation streamline more into the duct, creating a large adverse pressure gradient as the flow negotiates the outer duct inlet lip geometry. As the blockage is further increased for the windmilling case, the separation on the outer top surface of the duct increases significantly, and separation on the duct floor is also present.

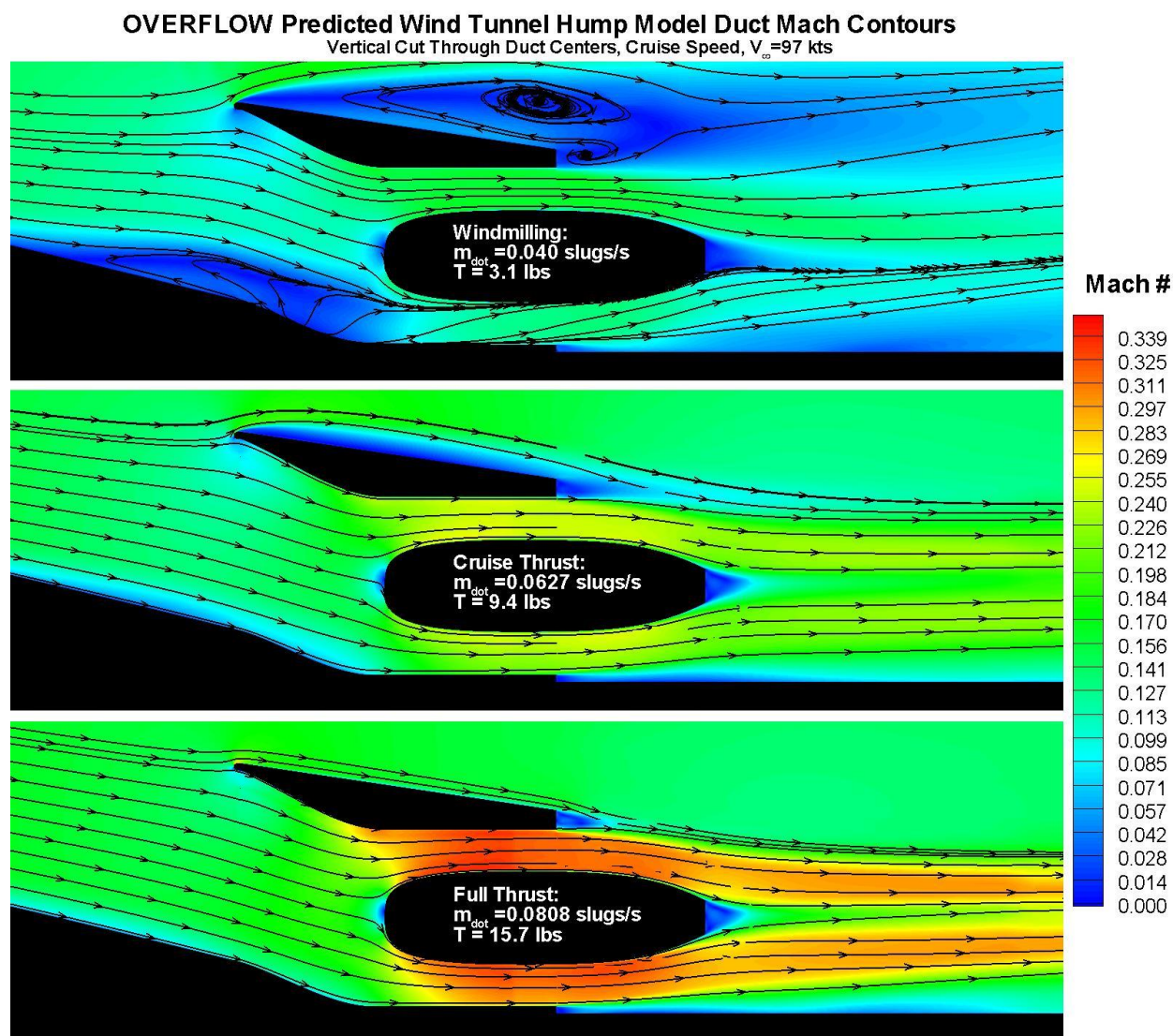


Figure 22: Mach contours and streamlines for a vertical cut plane through the center duct for the full thrust, cruise thrust, and idle cases.

OVERFLOW Predicted Wind Tunnel Hump Model AIP Total Pressure Recovery
Cruise Speed, $V_\infty = 97$ kts

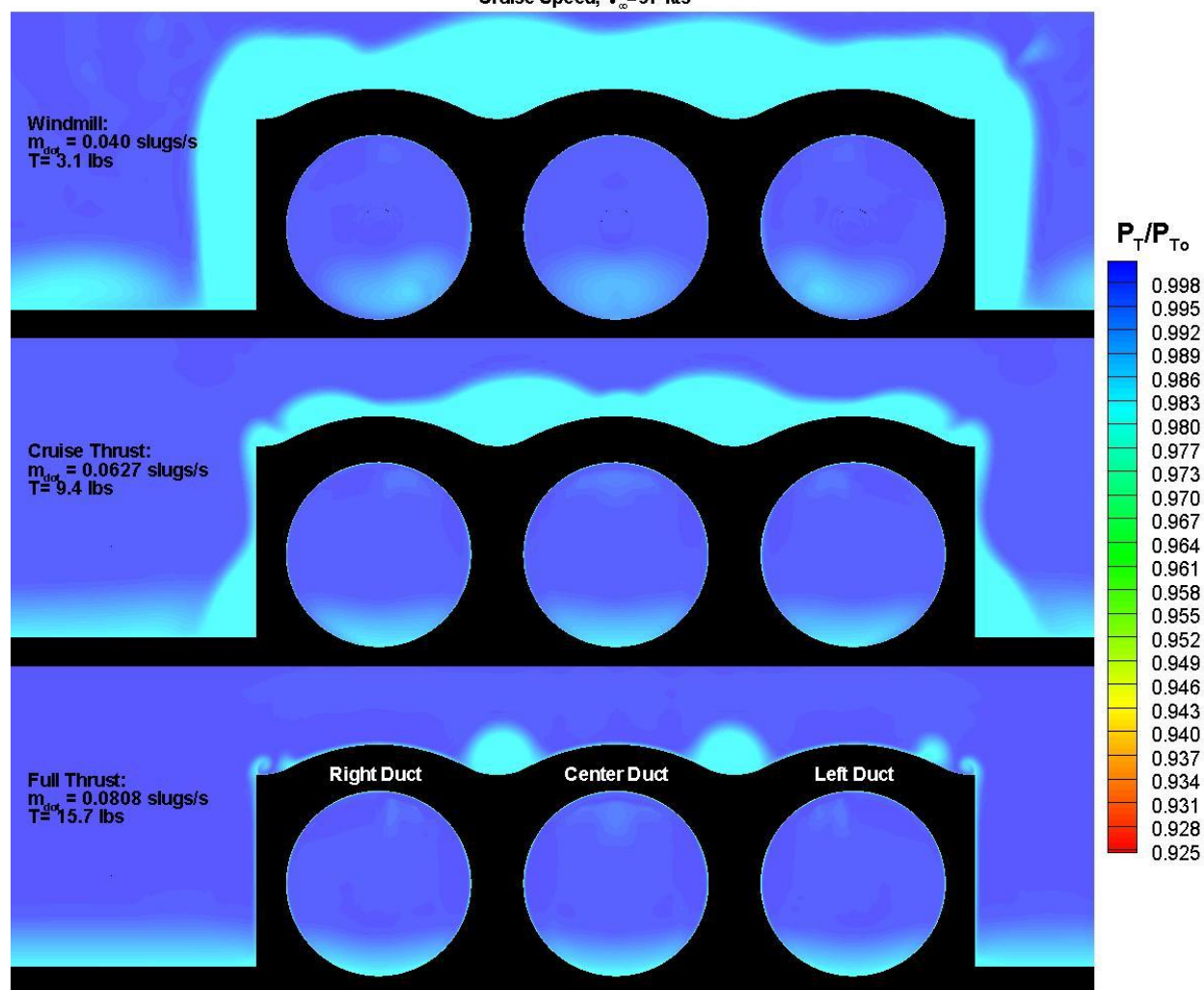


Figure 23: Contours of total pressure ratio for the three duct cases at a plane just downstream of the transition from the s-duct to the fan circular duct.

Contours of total pressure ratio for the three ducts for the cases at a plane just downstream of the transition from the s-duct to the fan circular duct are shown in Figure 23. The total pressures in Figure 23 are normalized by the free stream total pressure. From Figure 23, although the duct uses an aggressive $L/D \approx 1$, the fact that the duct is converging combined with the low free stream Mach number produces very little total pressure inlet distortion. For the full thrust case, the presence of the ingested boundary layer can be seen near the duct floor. The size of the boundary layer and its effect on the total pressure can be seen to increase as the mass flow through the fan decreases for the cruise and windmill case. Since the duct is converging, the flow accelerates into the fan duct, reducing the size and effect of the boundary layer. This can be seen by noting the total pressure deficit in the boundary-layer on either side of the duct structure. The total pressure deficit on the outer, external surface of the duct can also be seen to increase significantly for the idle case. Although somewhat harder to discern from the contours shown in Figure 23, close examination shows that while the contours for the center duct are symmetric about the duct center plane, the outer right and left ducts do show some slight asymmetry. This

asymmetry is more easily visible as the mass flow decreases. Total pressure contours for a cut plane taken at the fan face are shown in Figure 24.

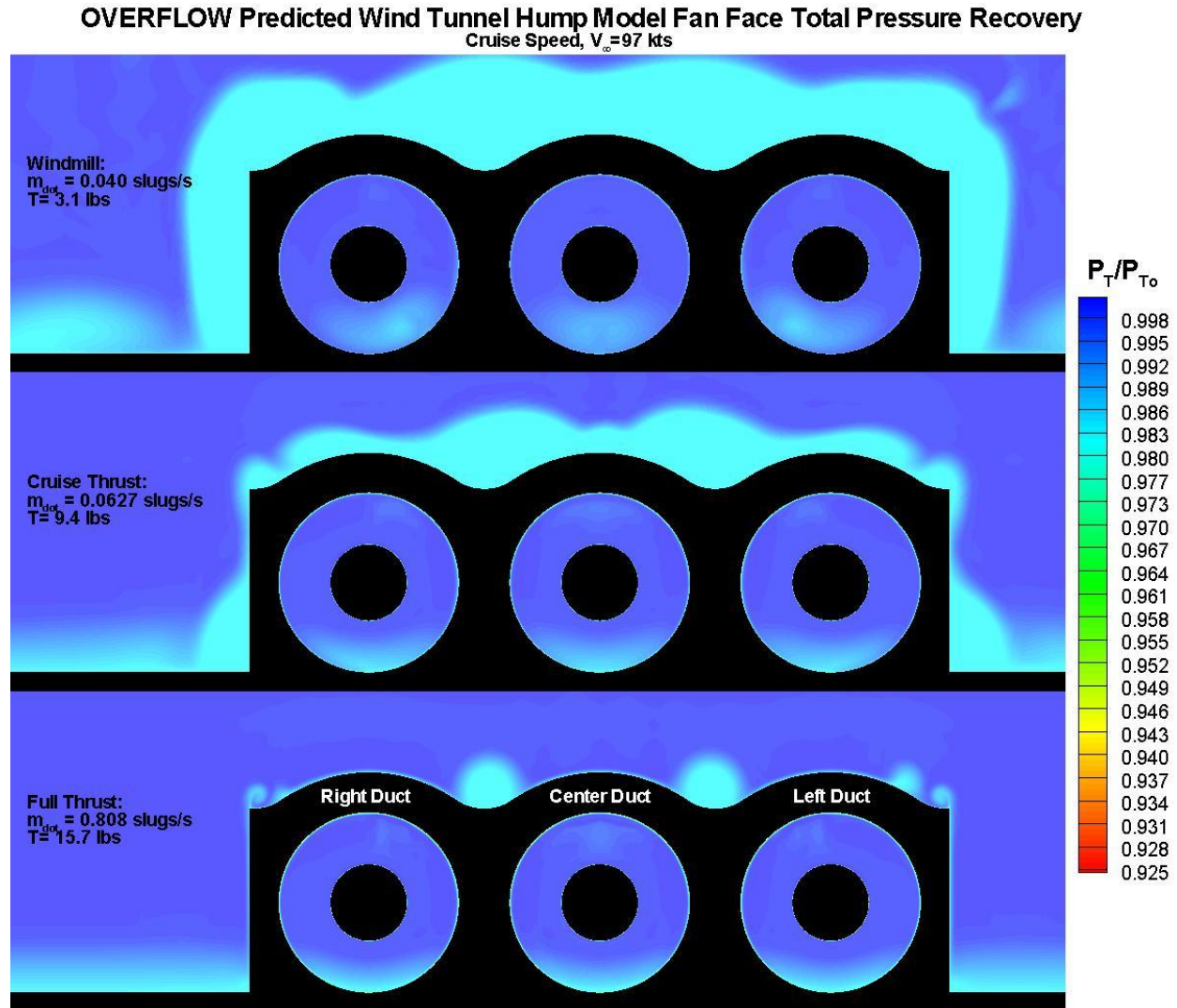


Figure 24: Contours of total pressure ratio for the three duct cases at a cut plane corresponding to the fan face.

From Figure 24, the presence of the boundary-layer on the duct floor is again clearly visible near the duct floor for all three cases. Again, however the total pressure inlet distortion appears to be very low, between $P_T/P_{To} \approx 1$ and 0.95. External flow features on the outer portion of the duct surface are more evident at this cut plane slightly further downstream of the plane shown in Figure 23. Although the solution is run steady state, the large separation on the duct top outer surface for the windmill case does show some asymmetry as the separation and shedding from the duct top outer surface is time dependent and fluctuates even in the steady state solution.

A plot showing the Mach contours for the fan face are shown in Figure 25. From Figure 25, a slight, but not insignificant variation in Mach number from the floor of the duct to the top of the duct is also present due to the ingestion of the boundary layer. The separation on the duct top

outer surface and its increasing progression with decreasing mass flow through the duct is also more visible in Figure 25. Surface pressure contours and surface streamlines for the full and cruise thrust cases are shown in Figure 26 and Figure 27 .

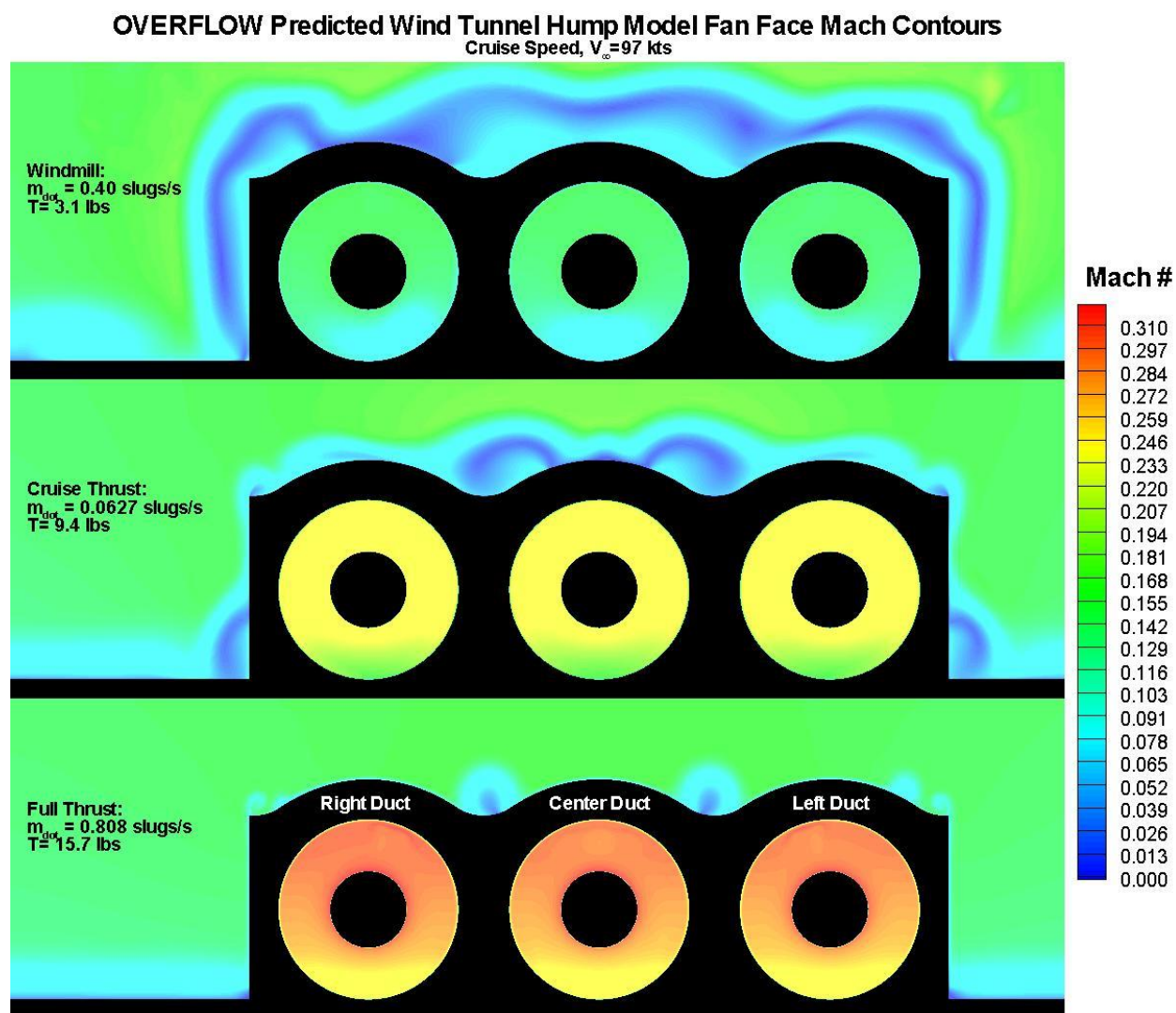


Figure 25: Contours of Mach number for the three duct cases at a cut plane corresponding to the fan face.

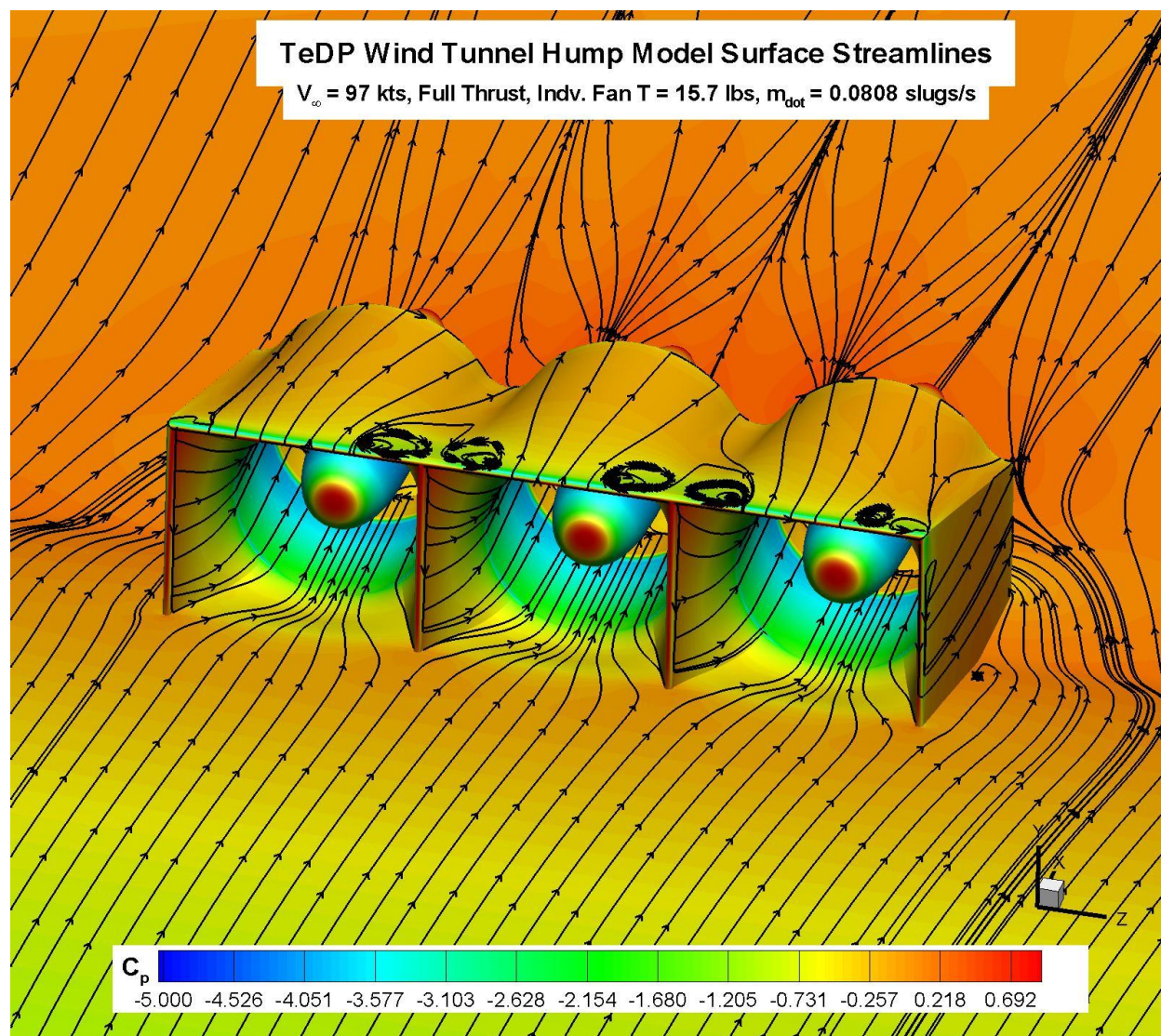


Figure 26: Surface pressure contours and surface streamlines for the full thrust case.

From Figure 26, the surface pressure contours and surface streamlines for the full thrust case show a well behaved flow internal to the ducts. A small region of low pressure where the duct transitions form the converging s-duct to the round fan duct is visible. The small low pressure region is due to a discontinuity in the 2nd derivative of the surface curvature at this intersection. Also visible in the surface streamlines are small areas of separation just downstream of the inlet lip on the vertical posts. These small separated regions are also due to a discontinuity in the surface curvature between the lip and duct entrance. Finally two small areas of separation on the duct top above the inlet right and left middle posts and the outer top corners is visible. This separation is small and does not extend up far from the surface, but is clearly discernible in Figure 26. As the mass flow is decreased for the cruise thrust case shown in Figure 27, the blockage created by the reduced mass flow is clearly visible in the surface streamlines. The flow is pushed out, around the ducts as compared to the design mass flow case shown in Figure 26. The increase in separation over the top of the duct is also clearly discernible in Figure 27.

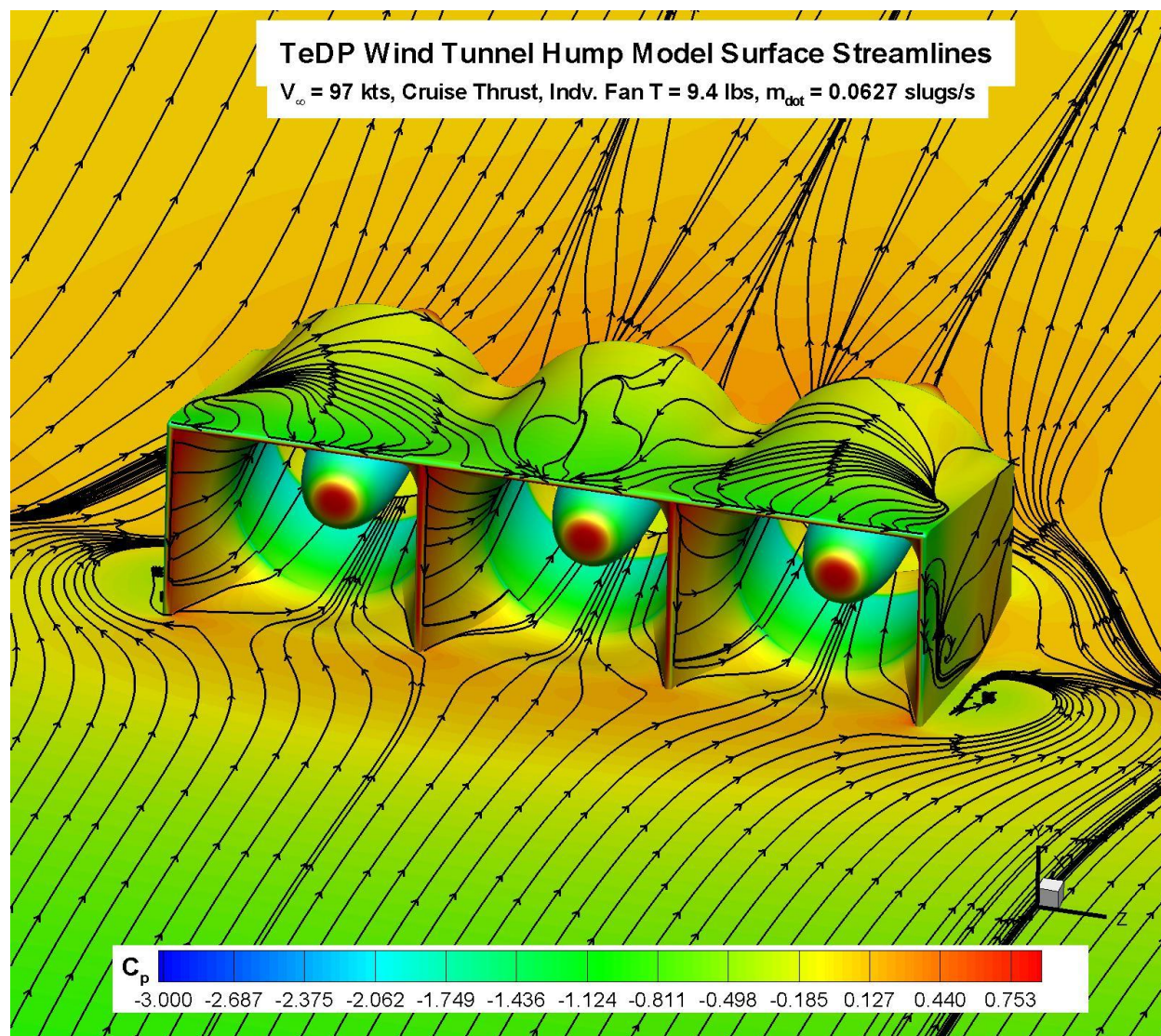


Figure 27: Surface pressure contours and surface streamlines for the cruise thrust case.

Finally, a plot showing Mach contours and streamlines for a horizontal cut plane at the duct center height showing the flow downstream of the ducts for the full thrust and cruise thrust cases is shown in Figure 28 and Figure 29. Figure 28 and Figure 29 show a well behaved flow field downstream of the ducts. Small regions of separation for the flat rear facing surfaces of the aft duct face are observed. As discussed above, although not modeled in the CFD, the wind tunnel model will have small tear-drop surfaces which extend aft from the duct surface rear face in an attempt to minimize or eliminate the rear facing surface separation. The increased spillage of the lower thrust cruise case shown in Figure 29 can also be seen as the streamlines are forced away from the duct structure. A full set of plots for each case investigated is provided in Appendix #1.

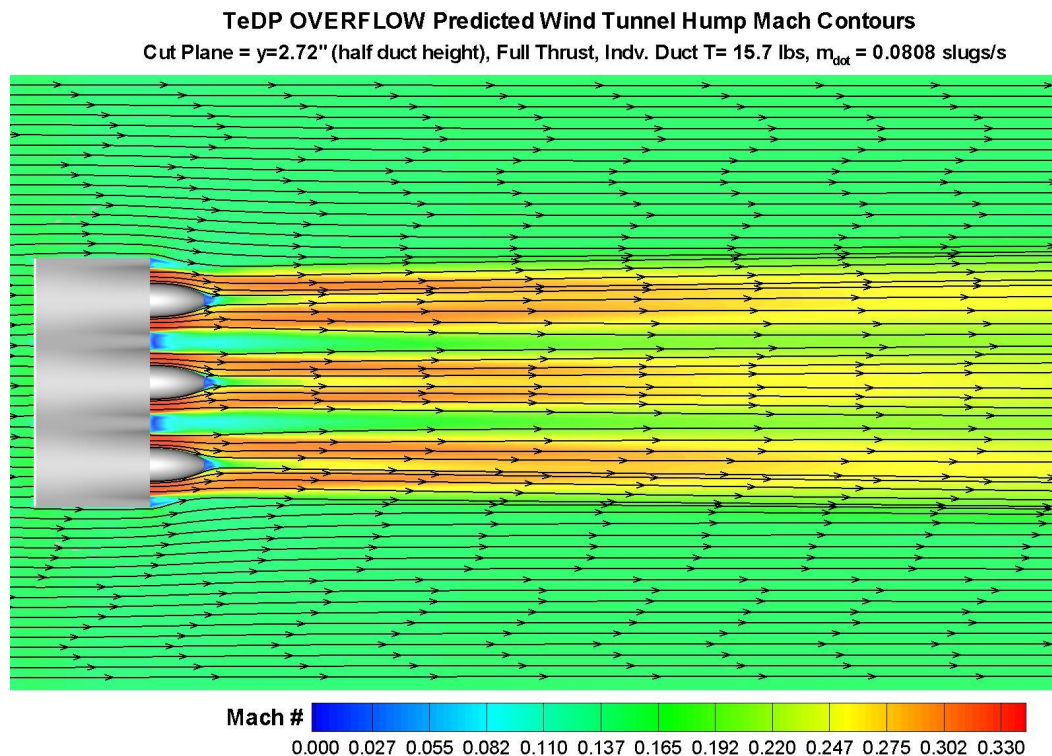


Figure 28: Mach contours and streamlines for a horizontal cut plane at the duct center height for the full thrust case.

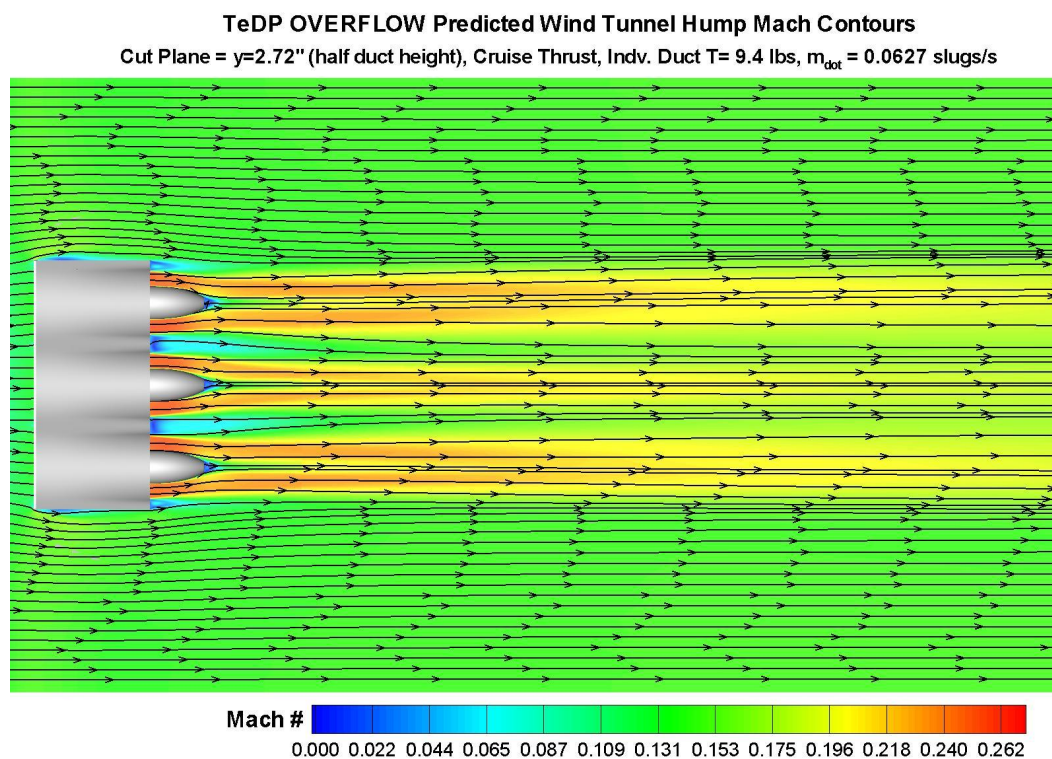


Figure 29: Mach contours and streamlines for a horizontal cut plane at the duct center height for the cruise thrust case.

5.7.3 Differential Thrust Results

In addition to the baseline runs with all of the fans at the same thrust level as discussed in the previous section, runs with one of the fans operating at a different mass flow/thrust levels were also run. The differential thrust runs were investigated to determine the effect a neighboring fans mass flow rate has upon the distortion and flow characteristics of the adjacent fan. For the differential thrust cases, the different cases will be identified by a percentage thrust level with full cruise thrust available denoted by 100%, cruise thrust required by 50%, and the windmill case by 0%. For a case where the left and center fans are at full cruise thrust available with the right fan at cruise thrust required, the identification would be 50%:100%:100%. The differential thrust cases were 50%:100%:100%, 0%:100%:100%, and 0%:50%:50%.

OVERFLOW predicted centerline pressure distributions for the all fans running full and cruise thrust cases and the differential thrust cases are shown in Figure 30. From Figure 30, for the 100%:100%:0% case, the pressures on the centerline of the model show reduced pressures upstream of the center fan as compared to the all fans running full thrust case. These reduced pressures (less negative) are due to the reduced mass flow of the outboard fan creating blockage which spills over to the center fan. The effect on the pressure distribution due to the neighboring fans reduced mass flow is significant, and extends all the way to the leading edge. Increasing the right fan from windmill to 50% thrust increases the pressures (more negative) as compared to the windmill case. The rise in the pressures places the distribution approximately halfway between the 0% windmill case and the full thrust case (100%:100%:100%). Similarly, the 0%:50%:50% pressure distribution also shows increased blockage in front of the center fan as compared to the cruise thrust case (50%:50%:50%).

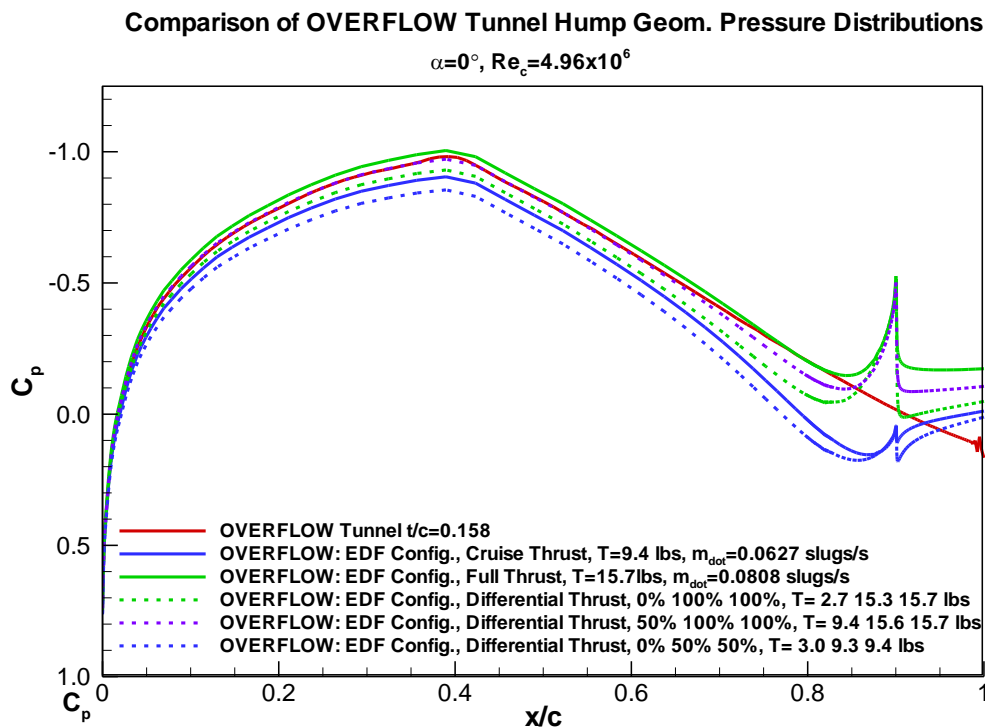


Figure 30: Comparison of centerline OVERFLOW predicted surface pressure distributions for the airfoil section in the tunnel model, the full and cruise thrust cases, and the differential thrust cases.

Also included in the legend of Figure 30 is the calculated thrust for each fan. For the 0:100%:100% case, the individual thrusts are 2.7lbs:15.3 lbs:15.7lbs. As compared to the 100%:100%:100%, the thrust of the centerline fan is reduced from 15.7 lbs to 15.3 lbs. One might expect that the thrust of the centerline fan would increase due to the reduced (more positive) pressures upstream of the centerline fan. The more positive pressures would indicate a lower effective inlet velocity for the centerline fan, producing a net thrust increase as compared to the 100%:100%:100% case. The thrust, however, of the centerline fan is slightly lower. Close inspection of the results show that the increased blockage of the neighboring fan has changed the effective sideslip angle on the vertical post lip between the right and center fans. This increased effective sideslip angle significantly increases the separation in the center fan inlet lip. A plot comparing the surface streamlines and surface pressure contours for the 100%:100%:100% full thrust case and the 50%:100%:100% and 0%:100%:100% differential thrust cases is shown in Figure 31.

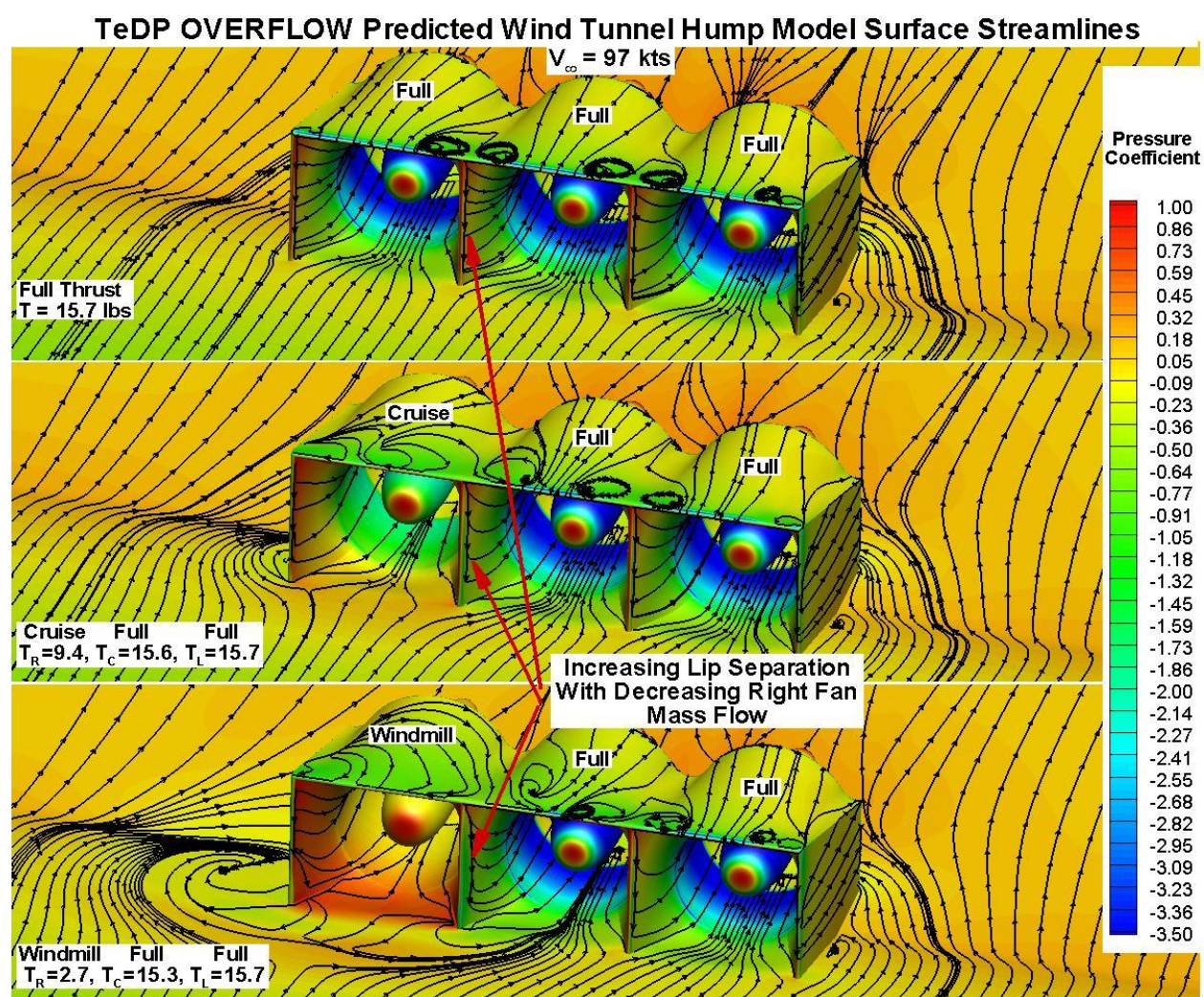


Figure 31: Surface pressure contours and surface streamlines for the 100%:100%:100% case, and the 50%:100%:100% and 0%:100%:100% differential thrust cases.

From Figure 31, the effect of reducing the thrust level and mass flow of the right outboard fan is apparent in the surface streamlines. The large amount of blockage for the 0%:100%:100% case

is clearly evident, and although much more subtle, visible in the 50%:100%:100% case. Also evident in Figure 31 is the increasing center fan lip separation with decreasing thrust/mass flow for the right fan. Losses due to the increasing lip separation are most likely the reason for the reduced center fan thrust even though one might expect an increase in thrust due to the effective increase in blockage in front of the center fan. The effect of the increasing lip separation with reducing outboard fan mass flow also correlates well with the reduction in thrust between the 50% and 0% right outboard fan cases. At 50% thrust on the outboard fan, the center fan thrust only decreases from 15.7 lbs to 15.6 lbs. For this case the center fan inlet lip separation is much smaller than the 0% case where the thrust drops to 15.3 lbs, with a visibly larger separation.

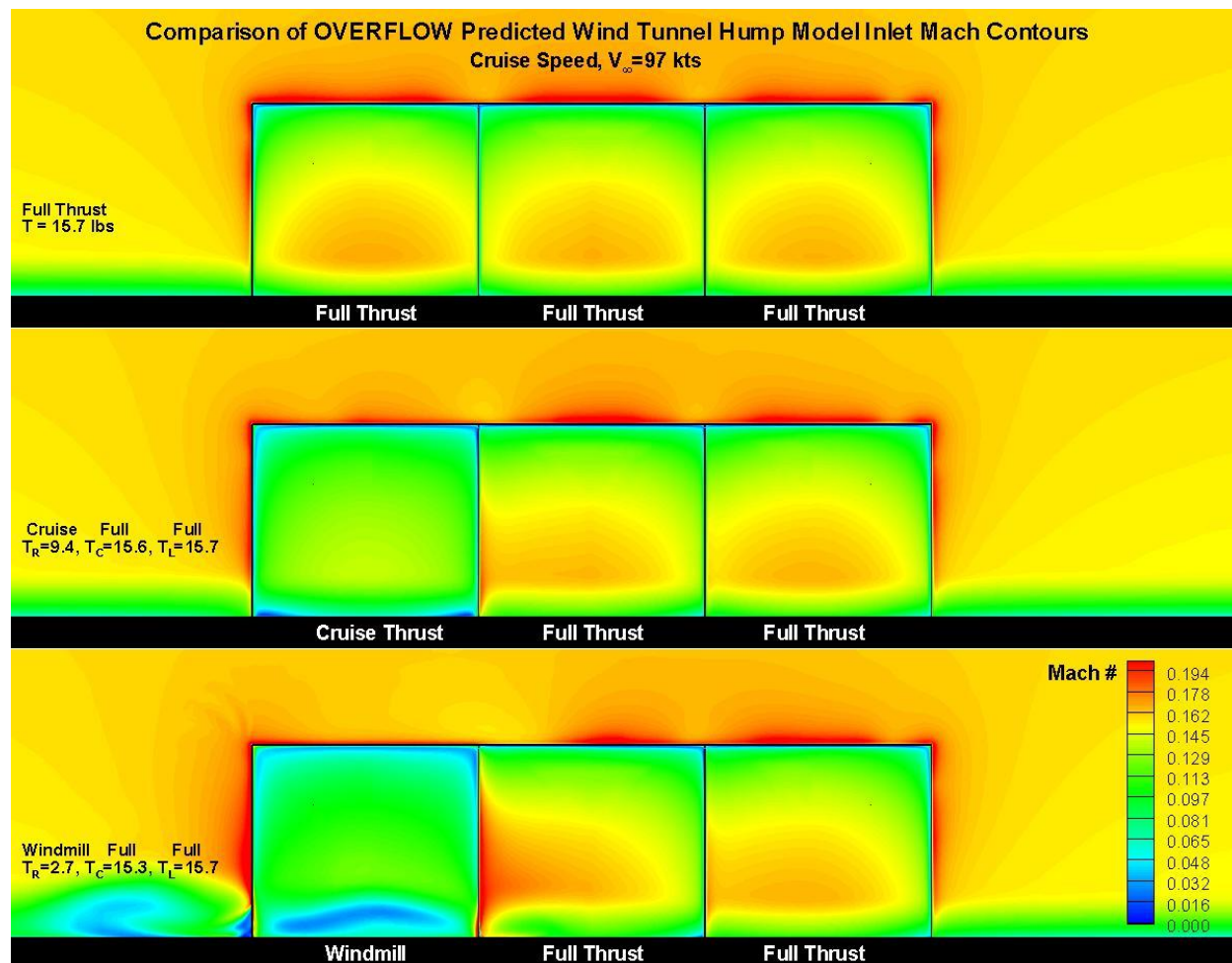


Figure 32: OVERFLOW predicted Mach contours at the inlet plane for the 100%:100%:100% case, and the 50%:100%:100% and 0%:100%:100% differential thrust cases.

Contours of Mach number at the inlet plane for the 100%:100%:100% full thrust case and the 50%:100%:100% and 0%:100%:100% differential thrust cases is shown in Figure 32. From Figure 32, the high Mach contours on the center inlet right lip are clearly evident on the windmill case, and denote the effective high sideslip angle on the inlet lip due to the spillage of the right fan. This change in effective sideslip angle and high Mach contours are also visible in the 50% thrust case, although to a lesser extent. The results shown in Figure 32 correlate very well with those shown in Figure 31 for the surface streamlines. Also of significance in Figure 32 is that

the effect on the inlet lip from the right fan increased spillage is not limited to the center fan. A change in Mach contours at the lip denoting a change in effective sideslip angle is also visible on the left inlet, although to a lesser extent.

Total pressure contours for the 100%:100%:100% full thrust case and the 50%:100%:100% and 0%:100%:100% differential thrust cases is shown in Figure 33. From Figure 33, as was observed for the cases where all of the fans were running, the overall total pressure loss is small due to the converging duct and low free-stream Mach number. The blockage induced separation on the outside of the fairing for the right fan is clear visible for both the 50% thrust and windmill case. Also, asymmetry in the total pressure contours for the windmill case is visible in the center fan contours.

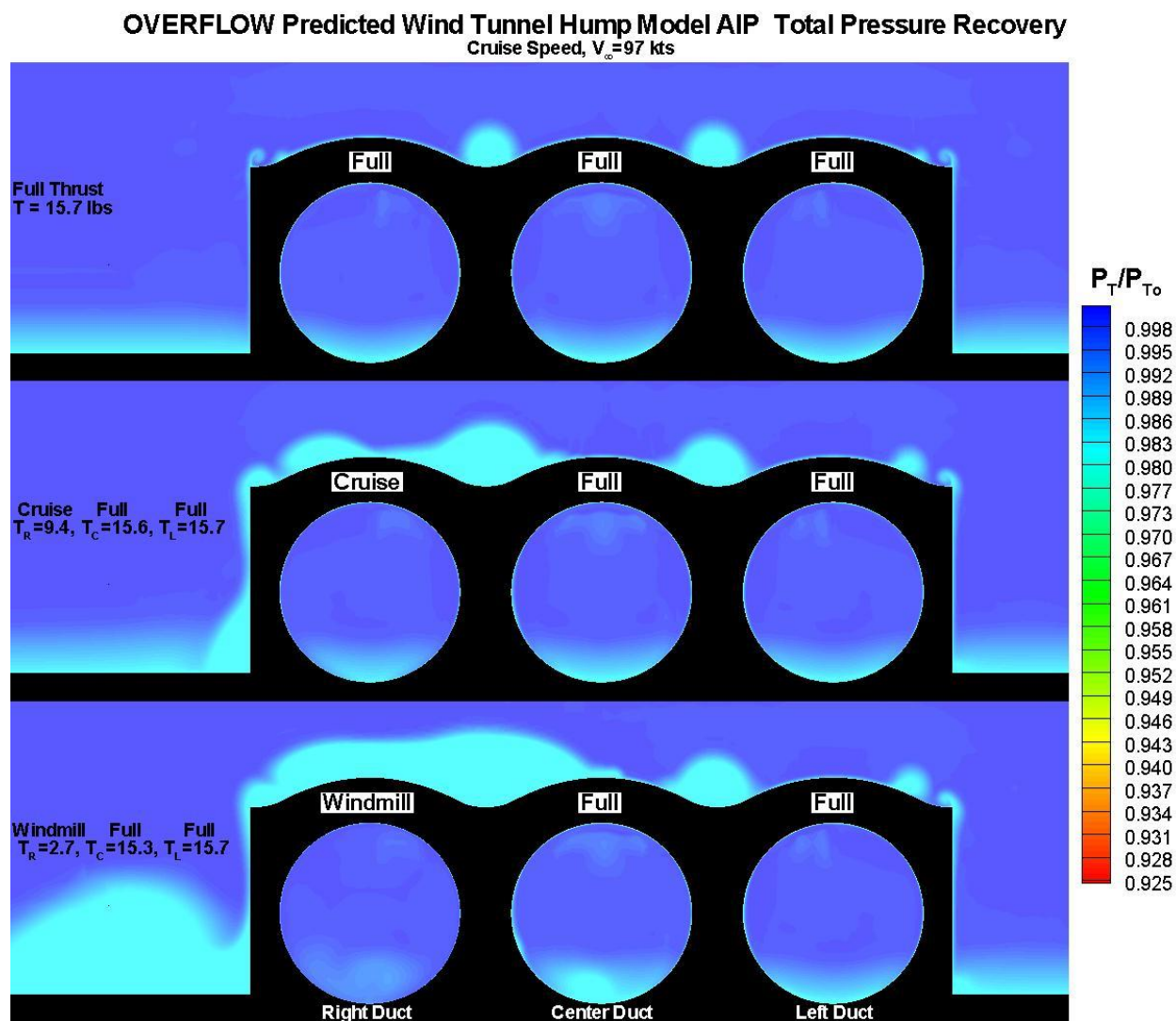


Figure 33: OVERFLOW predicted total pressure contours at the inlet plane for the 100%:100%:100% case, and the 50%:100%:100% and 0%:100%:100% differential thrust cases.

Finally, plots showing Mach contours and streamlines for a horizontal cut plane at the duct center height showing the flow downstream of the ducts for the 50%:100%:100 and 0%:100%:100% differential thrust cases are shown in Figure 34 and Figure 35. From Figure 34 the increased blockage of the right fan at cruise thrust is not as apparent at the center duct height as in the surface streamlines shown in Figure 31. The effect of the increased blockage for the windmilling right fan shown in Figure 35 is clearly evident as the streamlines are forced away from the right duct into the center duct and to the outside of the fairing. A full set of plots for each differential case investigated is provided in Appendix #2.

TeDP OVERFLOW Predicted Wind Tunnel Hump Mach Contours

Cut Plane = $y=2.72''$ (half duct height)

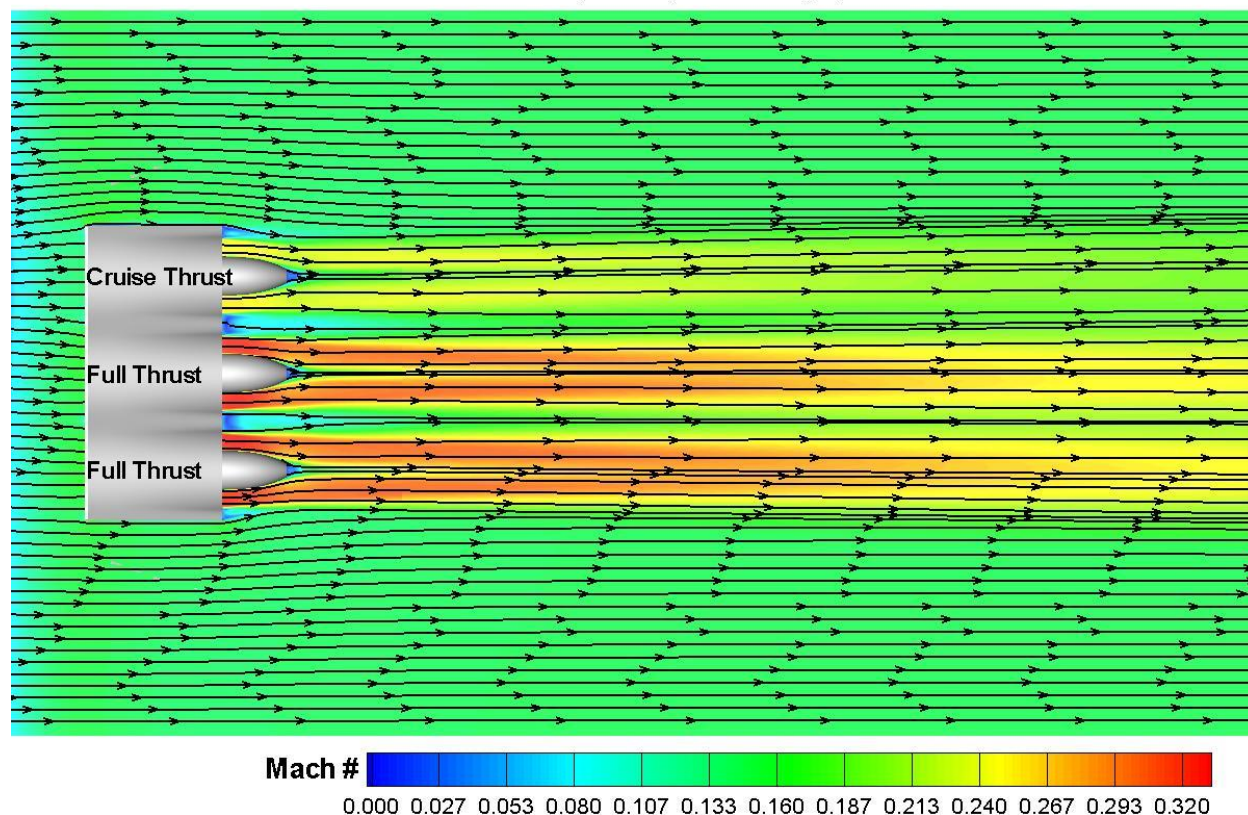


Figure 34: Mach contours and streamlines for a horizontal cut plane at the duct center height for the 50%:100%:100% differential thrust case.

TeDP OVERFLOW Predicted Wind Tunnel Hump Mach Contours

Cut Plane = $y=2.72''$ (half duct height)

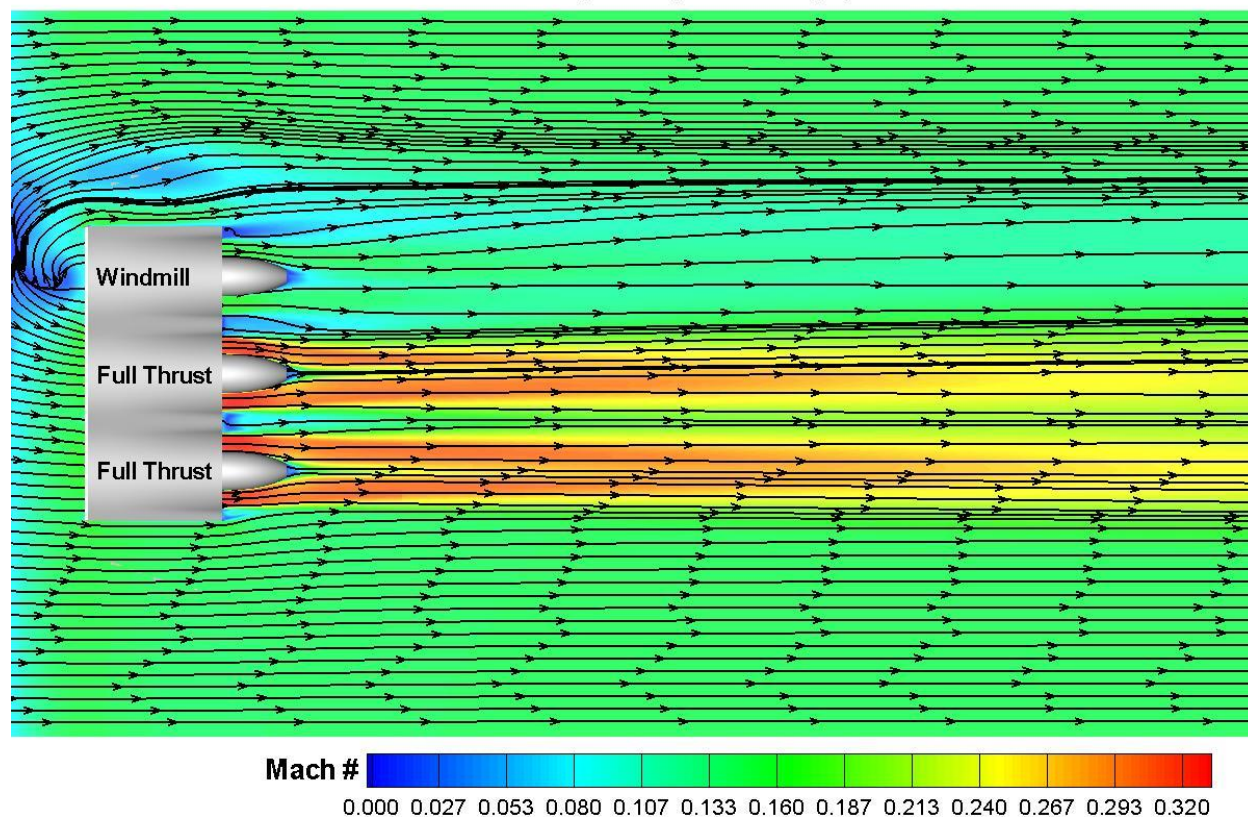


Figure 35: Mach contours and streamlines for a horizontal cut plane at the duct center height for the 0%:100%:100% differential thrust case.

5.7.4 CFD Results Summary

Results from the CFD study of the wind tunnel model and duct geometry show that for the thrust cases with all fans running, the inlets behave well with no internal separation, minimal secondary flows, and very little inlet distortion. The inlet lip and outer duct surface perform well for the design mass flow, but show increasing separation with mass flows below the design mass flow. The pressure distribution for the reduced mass flow cases showed the effect of increasing blockage caused by the below design mass flow spillage. The differential thrust cases showed the effect of an adjacent fans spillage affecting the neighboring fan blockage and effective inlet lip sideslip angle. The changes in effective lip sideslip angle were also seen to extend beyond the directly adjacent fan. The pressure distribution upstream of the adjacent fan was also affected by its neighbor. Each individual fan thrust level/mass flow has a global effect on the flowfield.

As a result of the CFD study, the inlet lip and the duct transition from the s-duct to the fan duct were redesigned prior to construction of the wind tunnel model. Based on the results to date, it appears that the duct inlet could most likely be reduced to provide better flow quality external to the duct surface at the cruise thrust available case. Whereas the current design is a point design

for the full thrust required at cruise, a multi-point design across multiple flight conditions is most likely more appropriate. Unfortunately, due to time and budget constraints, a redesign of the duct inlet area on the scale truly required was not possible. Also, a redesign of the inlet area for the flight vehicle would need to be performed on a full airfoil body with a lower surface. Thrust angle and flow exit angle would also be taken into account. For the wind tunnel test, the inlet surfaces were predicted to perform well.

5.8 Wind Tunnel Test

After the CFD study was complete and changes made to the s-duct inlet/exit and outer lip geometry, the wind tunnel model was manufactured. The 2D hump model was designed to be tested in the University of Illinois 3'x4' low speed, low turbulence wind tunnel. The tunnel is an open-return type with a rectangular 3-ft by 4-ft by 8 ft test section. The tunnel width expands in the streamwise direction through the test section to account for the wall boundary-layer growth. The maximum speed of the tunnel is approximately 235 ft/sec. The wind tunnel test was conducted from September 14th through September 27th.

5.8.1 Model Construction and Experimental Set-Up

The hump model was manufactured from high density urethane using CNC sculpting. The urethane was then coated with a hard polyester shell to provide some durability to the urethane and provide a smooth aerodynamic surface. The polyester coating used was Duratec 707-061. After sanding, the polyester coating was painted and a final wet sanding performed. The model was designed to span the width of the tunnel. In order to fit the model into the tunnel, the hump was manufactured in three pieces. The pieces were full chord length with two side pieces and a center piece. The width of the center piece matched the width of the three fan inlet system. The seams between the three hump pieces ran streamwise and were taped to prevent any flow through. The inlets and duct system were manufactured using stereo lithography. Photographs showing the model installed in the UIUC 3'x4' low speed, low turbulence wind tunnel are given in Figure 36 and Figure 37.

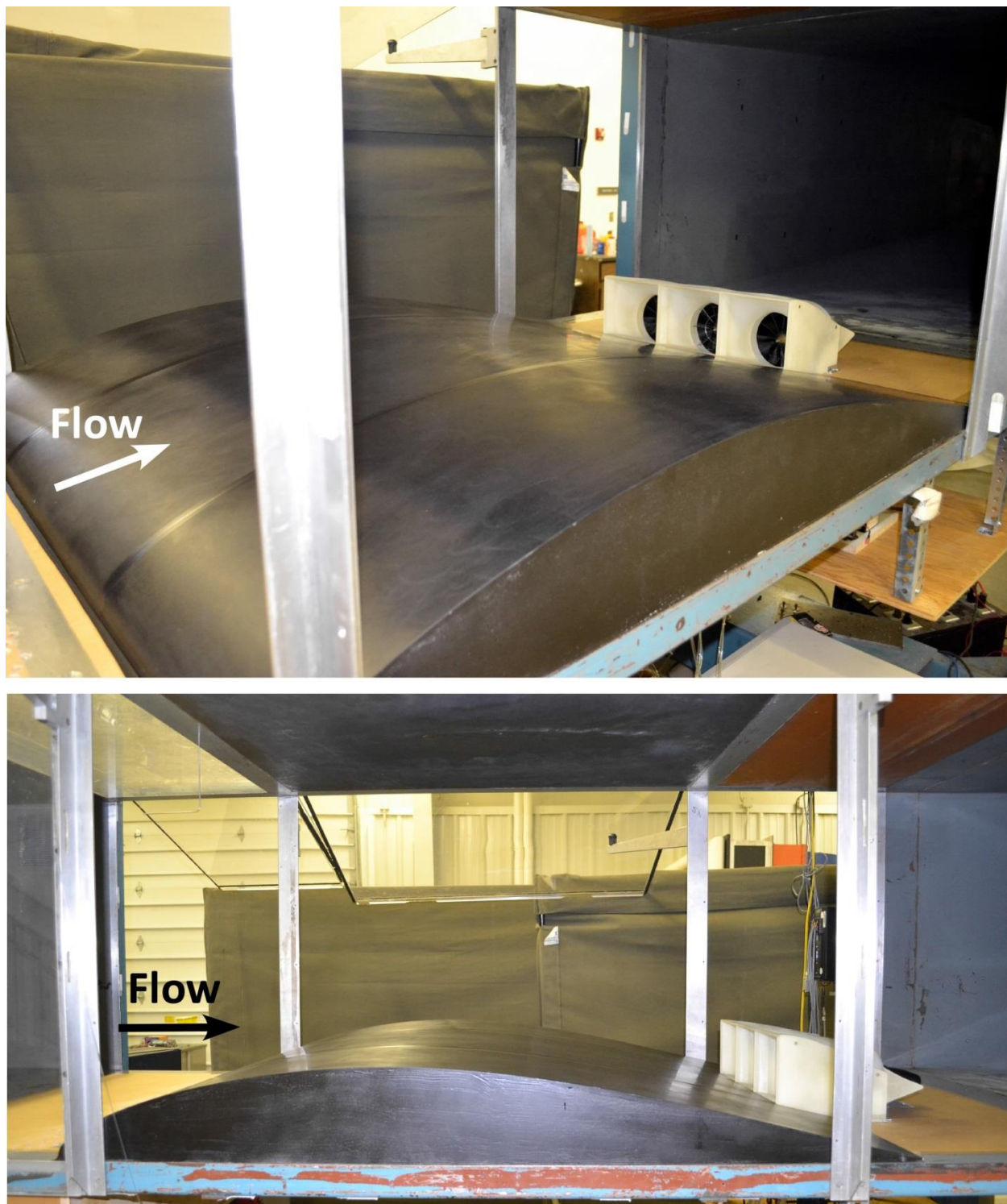


Figure 36: Photographs of the hump model with inlets and fans installed in the UIUC 3'x4' low speed wind tunnel.

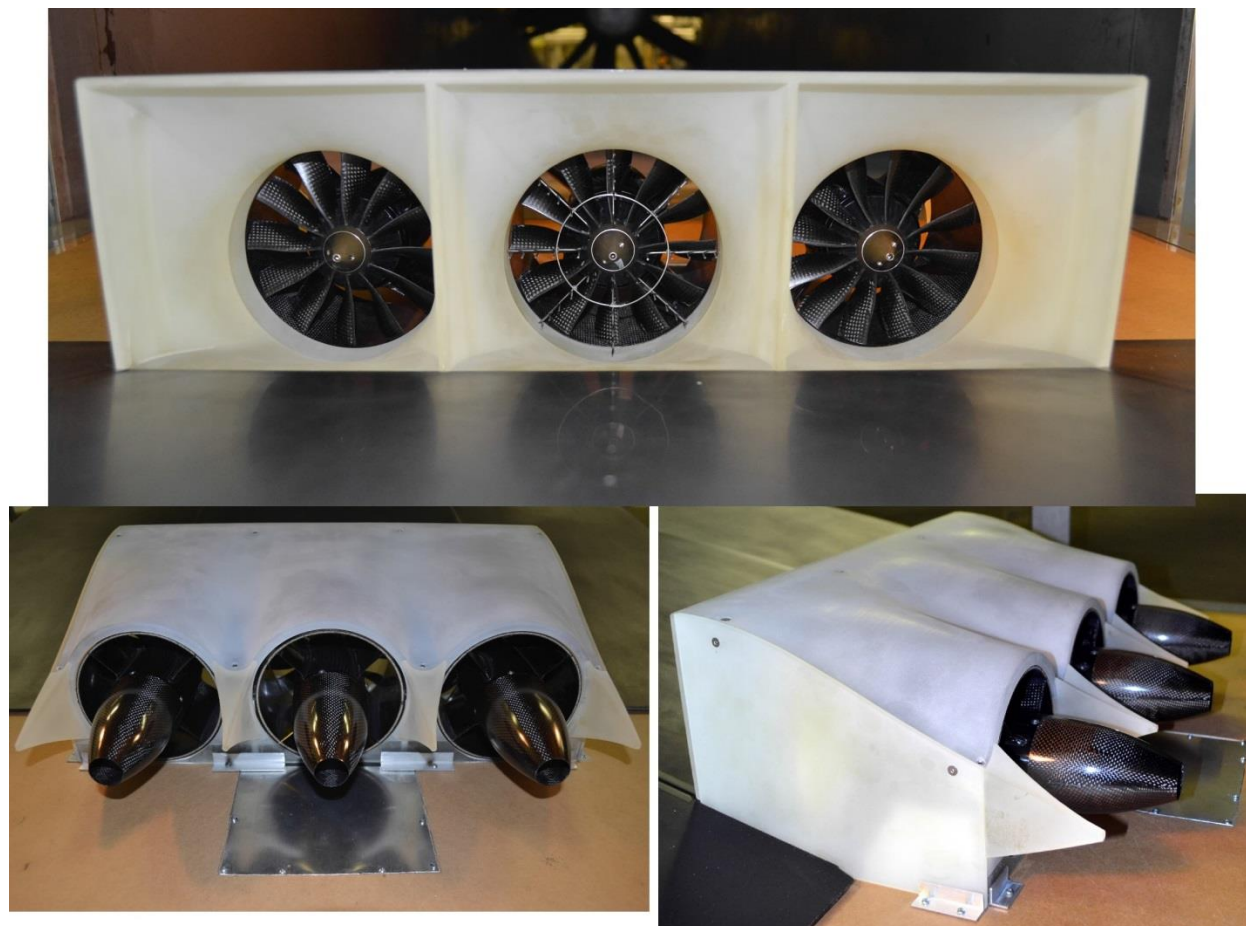


Figure 37: Photographs showing several different views of the inlets, fans, and outer duct covers for the model installed in the UIUC 3'x4' low speed wind tunnel.

5.8.2 Instrumentation

The primary parameters of interest for the wind tunnel test are the center duct/fan inlet distortion and the thrust produced by the centerline EDF unit. Other parameters of interest during the test are the mass flow rate in the off center EDF units, the boundary-layer thickness upstream of the EDF inlet location, surface static pressures along the model centerline, and individual fan voltage and amperage. Additionally, the motor temperature of the center fan was also measured.

In order to measure the centerline fan inlet distortion, a total pressure rake was designed and constructed. The total pressure rake conforms to the standards set forth in the SAE ARP1420 Rev. B Aerospace Recommended Practice publication for inlet flow distortion.¹⁰ The standard SAE inlet distortion rake consists of 40 total pressure probes arranged in eight equiangularly spaced rakes of 5 probes per rake location at the centroids of equal areas. The 40 individual pressure rake tubes were constructed from stainless steel hypodermic tubing with an OD of 0.042 inches and wall thickness of 0.004 inches. Based on information presented in AGARD-AR-245 on the "Recommended Practices for Measurement of Gas Path Pressures and Temperatures for Performance Assessment of Aircraft Turbine Engines and Components,"¹¹ the recommended

tube d/D for a tube inflow variation of $\pm 20^\circ$ should be at least $d/D=0.84$, with a tube inlet bevel angle of 10° to 20° , and a tube tip extension ratio, L/D of 3 to provide the largest range of inlet flow angles with minimal measurement error. A plot showing the to-scale inlet distortion rake design is given in Figure 38. The rake was manufactured by soldering the 5 probes of each rake location into a single unit. The 8 individual 5 port units were then mounted in a ring just upstream of the fan at a location defined as the aerodynamic interface plane (AIP). The AIP was defined as 0.7 inches upstream of the fan face and 0.3 inches downstream of the exit of the rectangular to circular s-duct. Photographs of the installed inlet distortion rake are given in Figure 39.

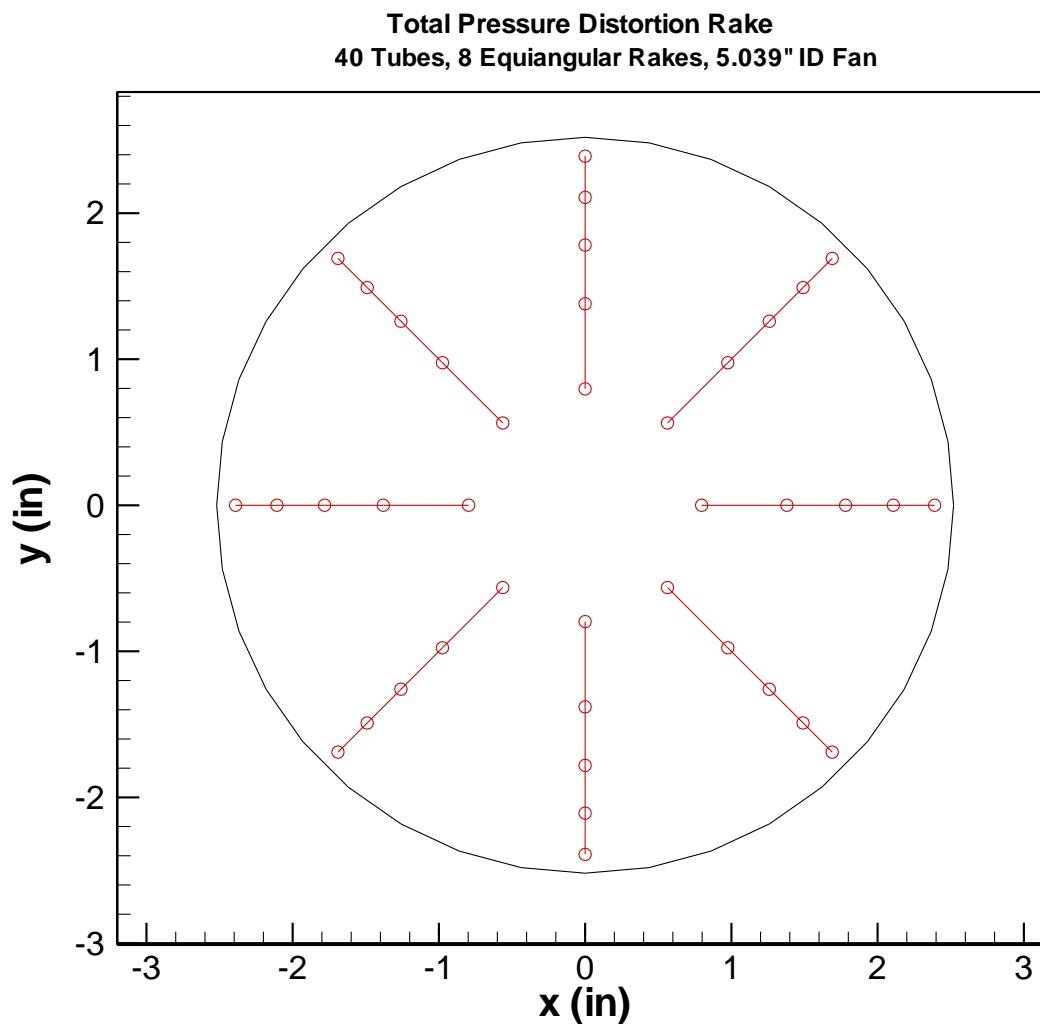


Figure 38: Inlet pressure distortion rake layout.



Figure 39: Photograph showing miniature 40 port center fan inlet distortion rake.

In addition to the 40 port inlet distortion rake, 4 static pressure ports were located at the AIP for each fan. The four static pressure ports were averaged to give a single static pressure. This static pressure was used to calculate the mass flow for the right and left fans. For the center fan, both the static and total pressures from the rake were used to calculate the center duct mass flow rate. The hump model was instrumented with 28 surface static pressure ports at x/c locations ranging from the model leading-edge to $x/c=0.89$, just upstream of the duct entrance along the model centerline. A plot showing the surface static pressure tap locations is given in Figure 40.

2D Hump Model Centerline Surface Static Pressure Tap Locations

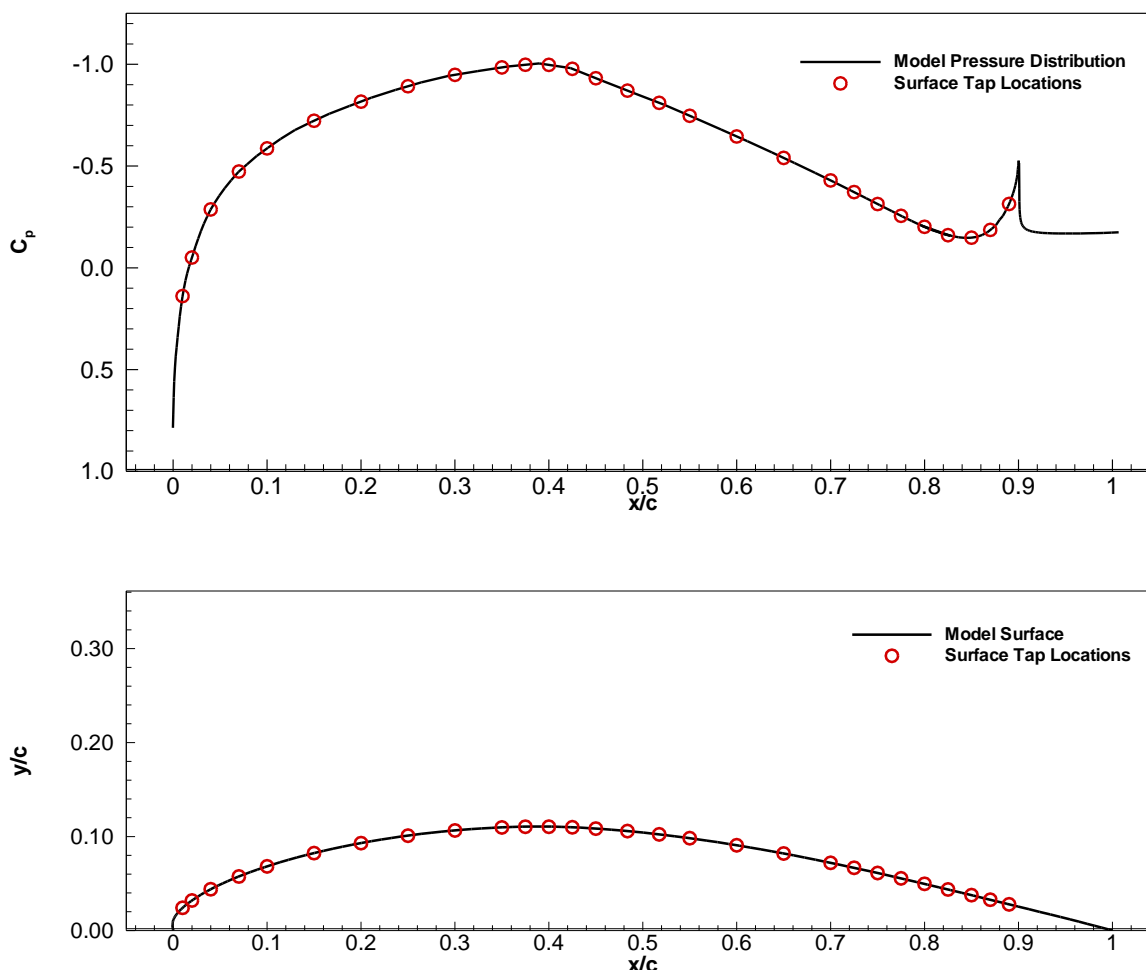


Figure 40: 2D hump model centerline surface static pressure tap locations.

Finally, the boundary-layer thickness and profile upstream of the inlet was also measured. The boundary layer profile was measured using a simple traversing total pressure tube. The tube was located so that the x/c location of the measurement was just off center line as close to the inlet entrance as possible at $x/c=0.85$. The probe was traversed up from the model surface using a simple stepper motor based linear actuator with a total travel of about 2 inches. All pressures were acquired using a Pressure Systems Inc. Initium digital pressure measurement system.

As discussed in Section 5.4.3, the thrust of the center fan was measured using a balance system mounted directly to the fan. The thrust balance designed utilizes a compact fan attachment structure that mounts to a 1D ultra-low friction linear slide. The slide allows the attachment structure and fan to move freely in the thrust/drag direction. A single load cell attached to the attachment fixture is used to measure the thrust. The load cell was manufactured by Transducer Techniques (model # MDB-25), with a capacity of 25 lbs. The stand was located in a pocket cut into the tunnel floor. The thrust balance was calibrated using a weight and pulley system attached to the fan mounting bracket. A plot of the fan calibration output is given in Figure 41 with photographs of the installed thrust stand shown in Figure 42. Sensitivity and repeatability

of the thrust stand output was found to be very good during the test, with run-to-run repeatability at approximately 0.1 lbs.

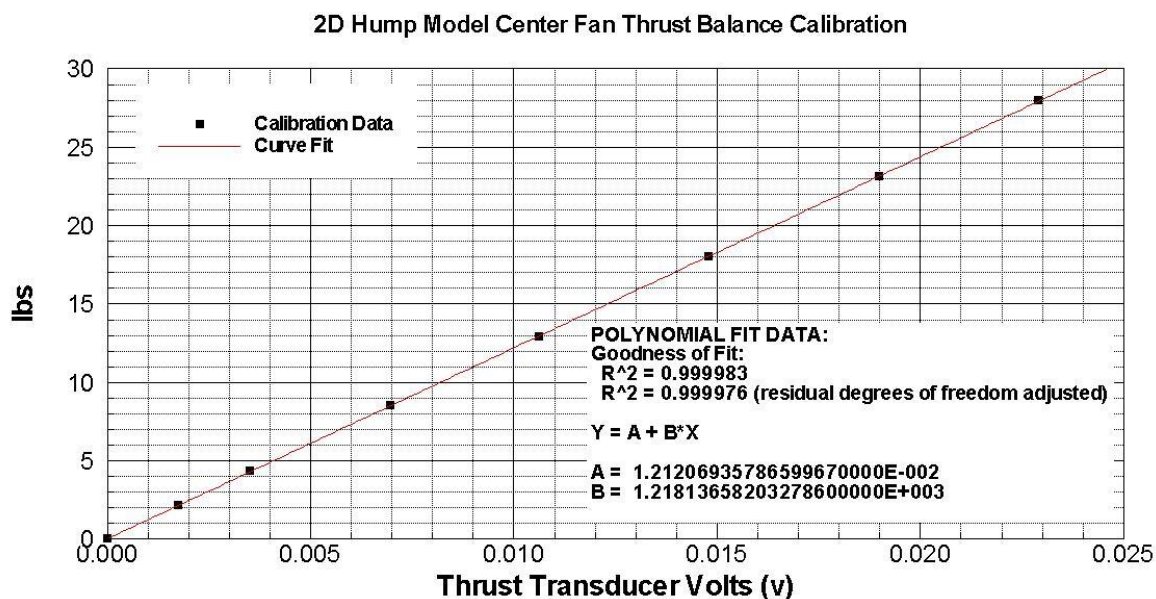


Figure 41: Center fan thrust balance calibration results.

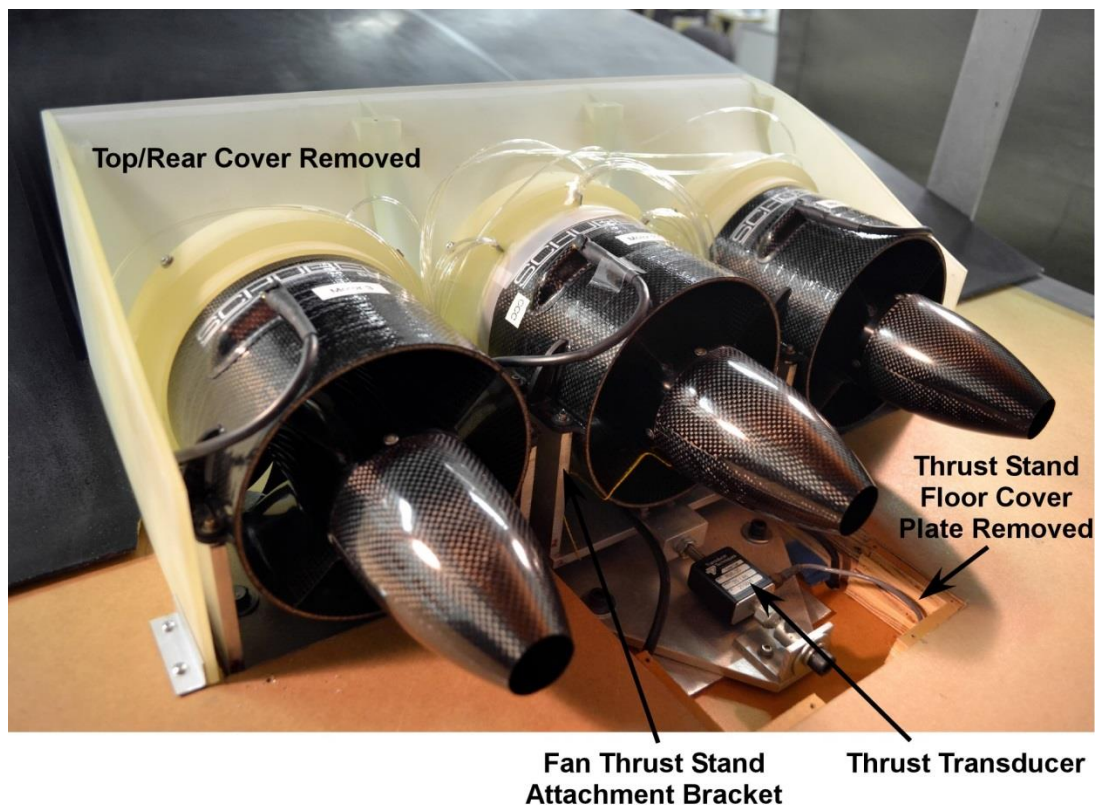


Figure 42: Photograph showing center fan thrust stand and transducer.

Voltage and amperage to each fan controller was also monitored. The voltage was determined using a simple voltage divider circuit to reduce the voltage to within the $\pm 10\text{V}$ range of the A/D board. Amperage was measured using a Hall effect current sensor manufactured by Tamura (model L03S300D15). Finally, the temperature of the center EDF unit motor was also monitored using a PRTD mounted directly to the motor internal main rotor bracket. All data acquisition, reduction, EDF unit, and tunnel control were accomplished using National Instruments LabVIEW software.

5.8.3 Wind Tunnel Test Results

After model installation and instrumentation calibration, testing was broken into three phases. The first phase tested the hump model in the tunnel with no EDFs or ducts, just the basic airfoil. For this phase, surface pressures and boundary layer profiles were obtained to make sure the basic flowfield matched the assumed baseline. After the baseline was verified, the next phase tested the model with all three of the fans operating at the same throttle setting, including 100%, 75%, and 50% throttle. Again, all data with the tunnel running were obtained at a free-stream velocity of approximately 172 ft/s, producing a chord based Reynolds number of $\approx 5.0 \times 10^6$ to match the TG-14A cruise conditions. In addition to the tunnel running cases, static thrust cases were also obtained. The next phase of the testing included investigating differential thrust effects. After obtaining all of the differential thrust results, the inlet distortion rake was removed from the center fan to determine the effect its distortion/blockage had upon the fan thrust level. At full thrust it was found that the distortion rake reduced the thrust level by approximately 6%. As a result, all of the thrust levels reported in the “All Fans Running” section (5.8.3.2), are for the distortion rake removed case, whereas the thrust levels reported in the differential thrust section (5.8.3.3) are with the distortion rake installed. Finally, the final phase of the test included smoke flow visualization. A run log of the test entry is given in Appendix #3.

5.8.3.1 *Hump Model Airfoil Alone*

Prior to installation of the EDF units and the inlets and ducts, the basic hump airfoil model was tested in the tunnel to provide a baseline of the basic airfoil flowfield and boundary layer and also to compare to the pressures and boundary layer predicted by the CFD. In order to replicate the basic airfoil in the tunnel, a small trailing-edge piece was manufactured and attached to the model center section that was occupied by the inlet/duct/fan structure.

After installation of the trailing-edge piece, baseline boundary-layer measurements were made using the traversing pitot probe at a model Reynolds number of $Re_c = 5 \times 10^6$. The measured boundary-layer thickness was approximately $\delta = 1.8$ inches. This baseline boundary layer thickness was 50% larger than anticipated. At $x/c = 0.85$ for $Re_c = 5 \times 10^6$, the predicted boundary-layer thickness is approximately $\delta = 1.2$ inches (See Figure 7). This boundary-layer thickness was significantly larger than expected and was a result of the boundary-layer growth on the wind tunnel inlet wall. Since the model was mounted on the tunnel floor, the model boundary-layer is a continuation of the tunnel floor boundary-layer. The model leading-edge was located approximately 15 inches downstream of the test section entrance. It was hoped that the favorable pressure gradient on the inlet contraction would keep the boundary-layer laminar and only transition at the model leading-edge. Apparently, the 7.5:1 contraction ratio of the inlet does not

provide a favorable gradient of sufficient magnitude to keep the boundary-layer laminar. As a result, a boundary-layer suction system upstream of the model leading-edge was implemented to remove the thick turbulent tunnel inlet boundary-layer.

The suction system consisted of a plenum box manufactured and affixed to the tunnel floor below the model leading-edge. Suction for the system was provided by three large-scale leaf blower motors. A similar side-wall suction system was developed for a high lift test in the same tunnel and the leaf blower motors were scavenged from that set-up. A photograph showing the suction system and suction grate upstream of the model is given in Figure 43.

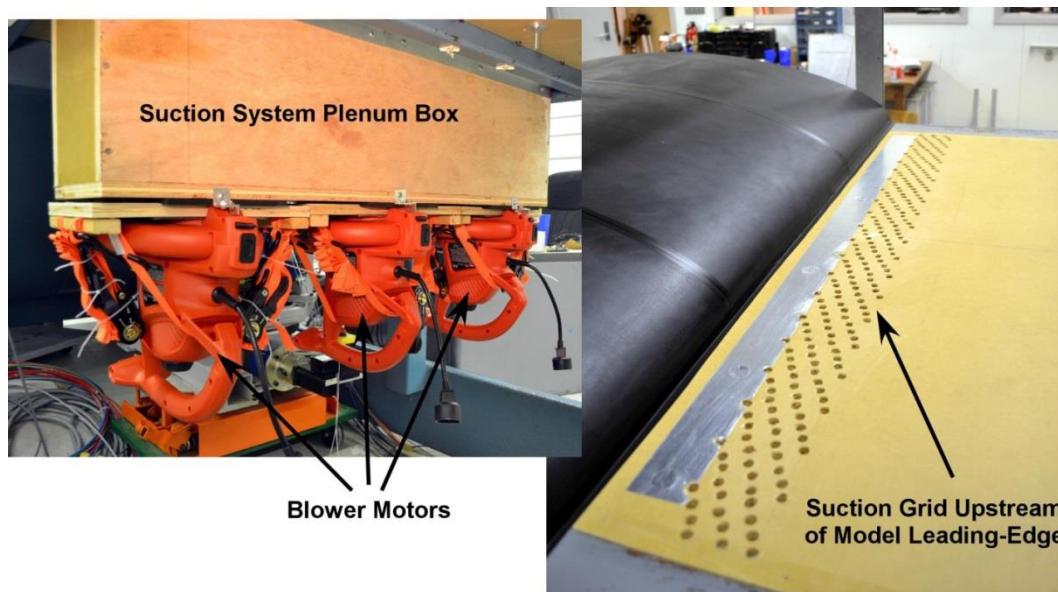


Figure 43: Photographs showing suction plenum box and suction grid upstream of the model leading-edge.

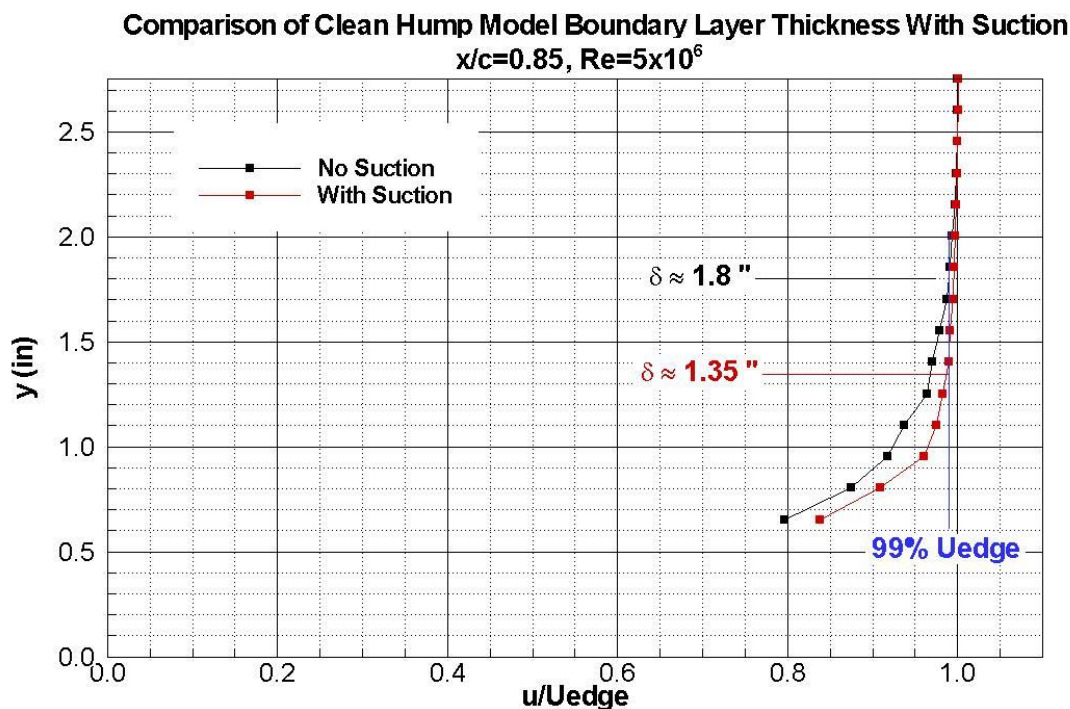


Figure 44: Comparison of boundary-layer profiles on the clean hump model with and without suction.

A plot showing boundary-layer profiles for the model with and without the suction system operating at $Re_c=5 \times 10^6$ is given in Figure 44. From the boundary-profiles, the boundary-layer thickness, δ was determined from the standard definition of the boundary-layer thickness being the height in the boundary-layer at which $u/U_{edge} = 0.99$. From Figure 44, due to the limited travel of the linear actuator, only the top portion of the boundary-layer profiles could be acquired. For the no suction case, the boundary-layer thickness was found to be approximately $\delta \approx 1.8$ inches. Again, the expected boundary-layer height at this chordwise location was approximately $\delta \approx 1.2$ inches. With the suction system on, the boundary-layer thickness is reduced to $\delta \approx 1.35$ inches. While still not as thin as the predicted thickness, the boundary-layer thickness with suction is only 12% above the predicted value, which is much better than the 50% above the predicted value for the no suction case. As a result, the suction system was used for all wind-on measurements.

XFOIL free-air, OVERFLOW predicted, and experimental pressure distributions for the clean hump model are shown in Figure 45. From Figure 45, the OVERFLOW and experimental pressure distributions for the clean hump model compare very well. These distributions also compare well to the XFOIL free-air distribution. From the results shown in this section, the baseline adverse pressure gradient and turbulent boundary-layer upstream of the inlet and duct system compare well with the initial predictions and assumptions used to size and design the inlet and duct systems.

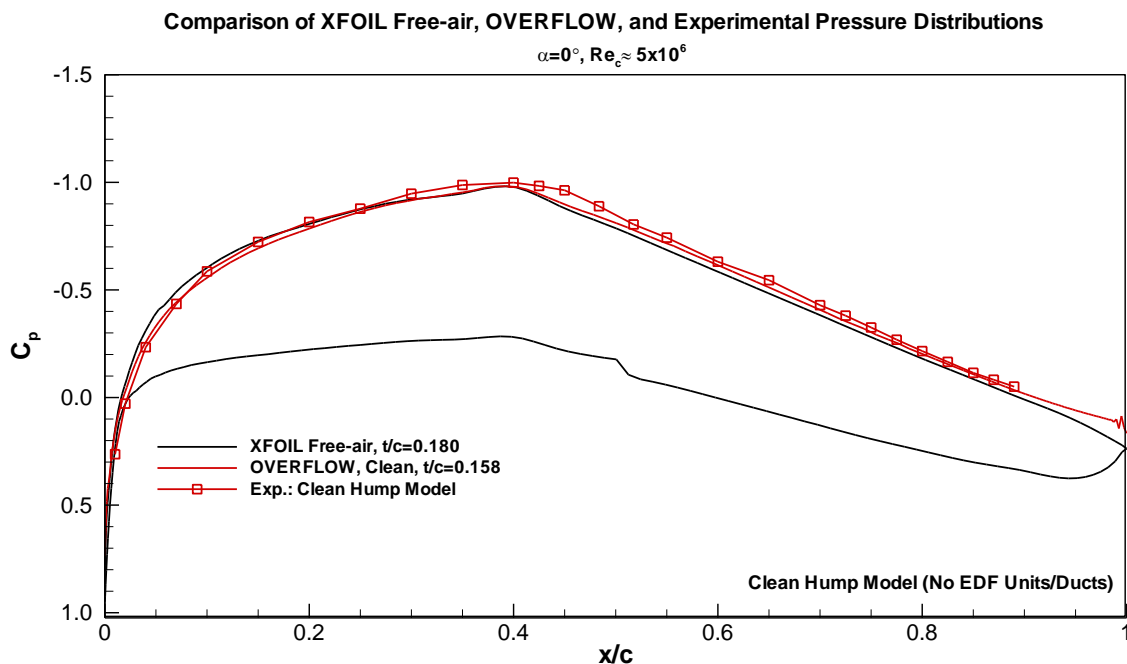


Figure 45: Comparison of XFOIL free-air, OVERFLOW, and experimental pressure distributions for the clean hump model.

5.8.3.2 All Fans Running Results

After confirming that the baseline pressure distribution and incoming boundary-layer were correct, the EDF units and ducting system were installed. The first phase of the EDF testing was conducted with all of the fans running at the same throttle position. Throttle settings included 100%, 75%, and 50% wind-on, and 100%, 75%, and 50% with the wind-off static thrust.

A comparison of XFOIL free-air, OVERFLOW, and experimental surface pressures for the 100%, 75%, and 50% throttle setting at $Re_c = 5 \times 10^6$ is shown in Figure 46. Also included in Figure 46 are the measured centerline fan thrust level versus throttle setting and input power. From Figure 46, the experimental pressures compare relatively well with the OVERFLOW predicted pressures. For the 100% throttle case, the experimental pressures compare well with the XFOIL and OVERFLOW predicted pressures until near the fan inlet. Aft of $x/c \approx 0.75$, the experimental pressures are slightly more positive than the OVERFLOW predicted pressures, indicating more blockage and less mass flow through the fan than predicted. This less than predicted mass flow is a result of the batteries not being able to deliver the power required by the fan to operate at its fully rated thrust level. For fully rated thrust, the fan requires 9.75 kW of power, whereas the batteries used for the test could only provide 6.8 kW (50 V at 136 amps), a 31 % reduction. The 6.7 kW observed at the tunnel, was slightly less than that observed on the test stand at RHRC (see Section 5.4.4). The thrust level recorded for the 100% throttle case was 14.25 lbs, 0.75 lbs below the hoped for 15 lbs. It is believed that if the full 9.8 kW were applied to the fan, a thrust level above the hoped for 15 lbs would be achieved. At the 50% throttle setting, the pressures just upstream of the fan compare well to the OVERFLOW predicted

pressures. One difference noted between the OVERFLOW and experimental pressures, however, is that upstream of the model maximum thickness at $x/c \approx 0.38$, the effect of increased blockage at fan mass flows below the design mass flow are not observed in the pressures. Where the OVERFLOW predicted pressures show the blockage effect extending all the way to the leading-edge of the model, the experimental pressures show an effect only up to the model maximum thickness. It is believed that this discrepancy between the computational and experimental results is due to the manner in which the CFD tunnel and experimental tunnel conditions were set. Thrust for the 75% and 50% throttle case was 9.3 lbs and 3.3 lbs, respectively.

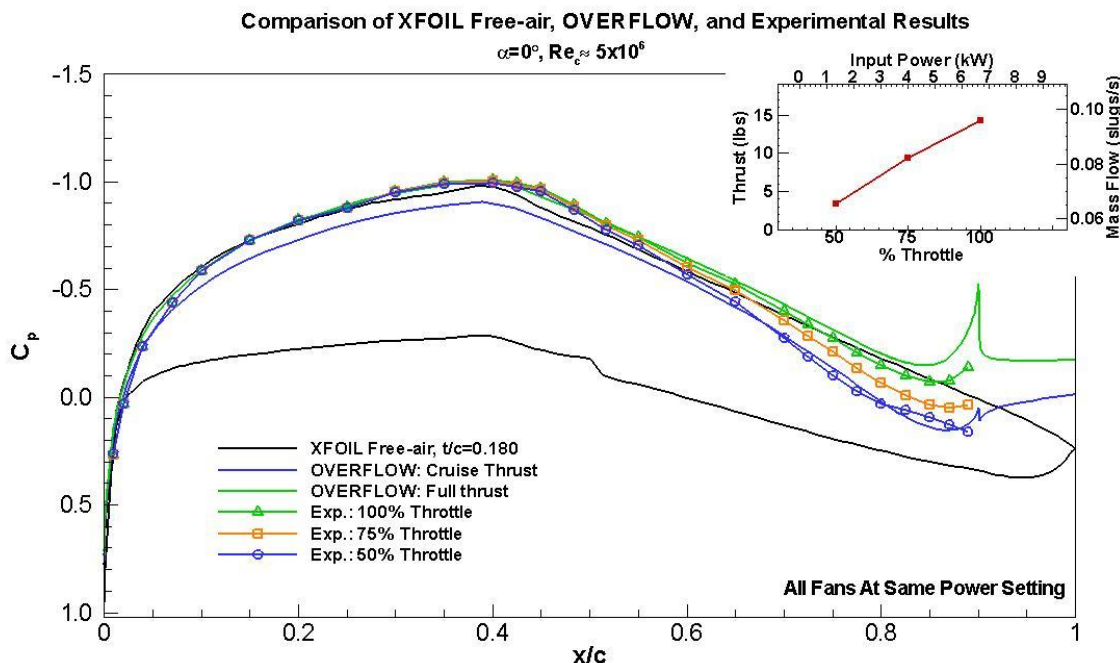


Figure 46: Comparison of XFOIL free-air, OVERFLOW, and experimental pressures for various throttle settings with all the fans at the same power level, and experimental thrust versus input power and throttle setting.

It should be noted that the mass flows measured for the center fan are slightly higher than predicted in the CFD. For the 100% throttle case, for example, the CFD mass flow was 0.0808 slugs/s, whereas the experimentally measured mass flow was 0.0957 slugs/s, or 18% higher. This higher mass flow rate is a result of the fact that for the actual fan unit, a small amount of flow is passed through the motor itself to help cool the motor. Close inspection of the motor trailing cone in Figure 42 shows that the motor plug end is open. This opening allows flow to pass from a small annular opening at the fan face through the motor windings and out the tail cone to help cool the motor. From the PRTD mounted on the internal fan main rotor bracket, the temperature observed was rise with increasing throttle setting and run time. The maximum observed temperature, however, was rather low at 107 °F.

Center fan distortion rake total pressure contours for the three throttle settings are shown in Figure 47. Also included in Figure 47 are the calculated SAE inlet distortion parameters for both the experimental and OVERFLOW CFD predictions. The SAE parameters include the average rake total pressure divided by the free-stream total pressure (P_{T2}/P_{T0}), the average circumferential

distortion descriptor ($DPCP_{avg}$), and the maximum radial distortion descriptor ($DPRP_{max}$). The total pressure contour range is set to the same range as the OVERFLOW predicted total pressure contours shown in Figure 23. From Figure 47, as was observed for the CFD results, the total pressure contours show little recovery loss. A small increase in distortion with decreasing throttle setting is observed in the contours. Again, the small distortion levels are a result of the converging duct coupled with the low free-stream Mach number ($M=0.154$). The experimental contours compare well to the OVERFLOW predicted contours. For the SAE pressure recovery (P_{T2}/P_{T0}), the experimental and CFD results compare well, and do not show much effect of thrust level, again as would be expected due to the converging duct and low free-stream Mach number. The average circumferential and maximum radial distortion descriptor levels are extremely low. Acceptable distortion levels for these descriptors are generally considered to be below a range from 0.04 to 0.05.¹² The measured distortion values are 10 times smaller than these levels. For the circumferential parameter, the experimental levels are approximately double the OVERFLOW predicted values. A small increase in the circumferential descriptor is observed to occur with a decrease in the thrust level. For the radial descriptor, the experimental and OVERFLOW predicted levels compare better, with a decrease in the maximum radial distortion with decreasing thrust level. Again, the measured SAE distortion descriptor values are very small, approximately 10 times smaller than levels generally considered to be acceptable.¹²

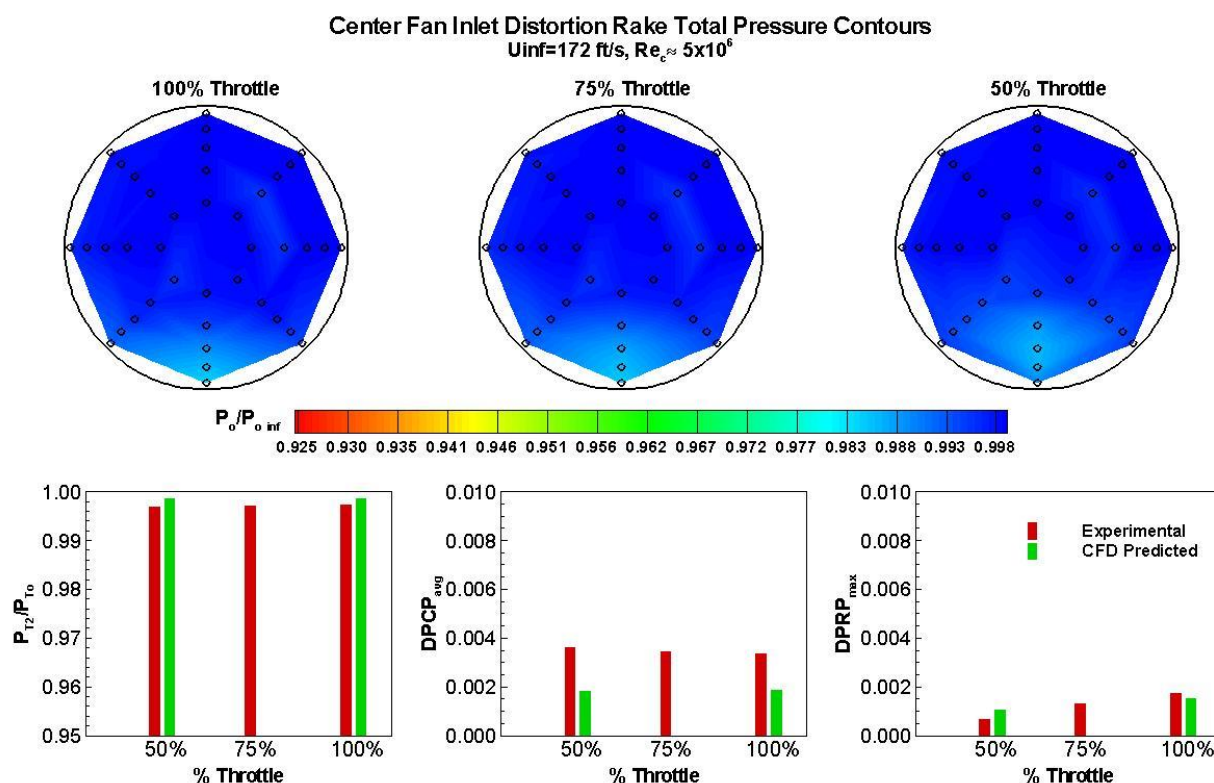


Figure 47: Center fan inlet distortion rake contours and SAE parameters for various throttle settings with all the fans at the same power level, $U_{inf}=172 \text{ ft/s}, Re_c=5 \times 10^6$.

Static thrust as a function of throttle setting and fan power required is shown in Figure 48. Also included in Figure 48 are the thrust and power required results for the wind-on case as were shown in Figure 46. From Figure 48, recalling the preliminary static thrust stand results shown in Figure 13 (Section 5.4.4), the 100% throttle static thrust results are extremely low, 16.5 lbs as

compared to the 26 lbs for the static thrust test stand results. While the thrust does decrease between the wind-on and static cases, the overall static thrust levels are much lower than expected.

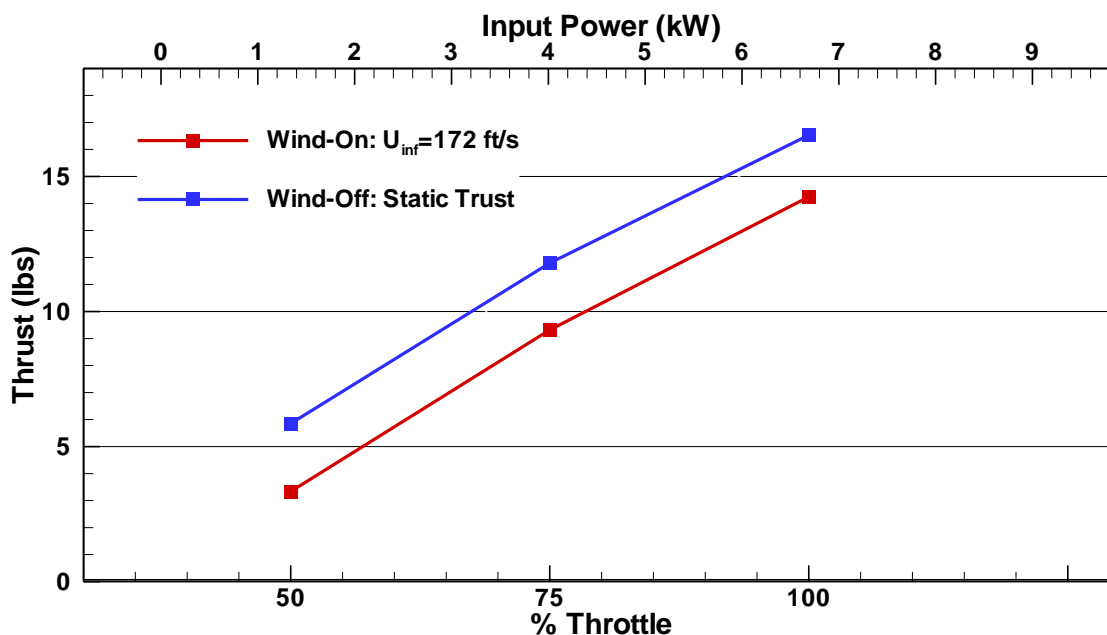


Figure 48: Comparison of thrust and fan power versus throttle setting for wind-on and wind-off static thrust cases.

Total pressure contours for the static thrust case along with the SAE distortion descriptors are shown in Figure 49. From Figure 49, unlike the wind-on cases, instead of the distortion being located at the bottom of the duct, the distortion is at the top of the duct and decreases with reducing throttle position. The SAE distortion parameters mimic the distortion characteristics observed in the total pressure contours. The results shown in Figure 49 indicate that the reason the static thrust levels are so low are because the inlet upper inlet lip is separating. The inlet and duct were designed for the full thrust setting at cruise, wind-on. For the wind-off static case, the mass flow provided by the incoming flow stream is missing, as a result, the inlet tries to pull additional mass flow from the surrounding fluid, creating a large effective negative angle-of-attack on the top inner lip surface. This large negative angle-of-attack on the lip causes the flow to separate into the fan, reducing the static thrust. As the required mass flow decreases with decreasing throttle setting, the separation and resulting distortion decrease.

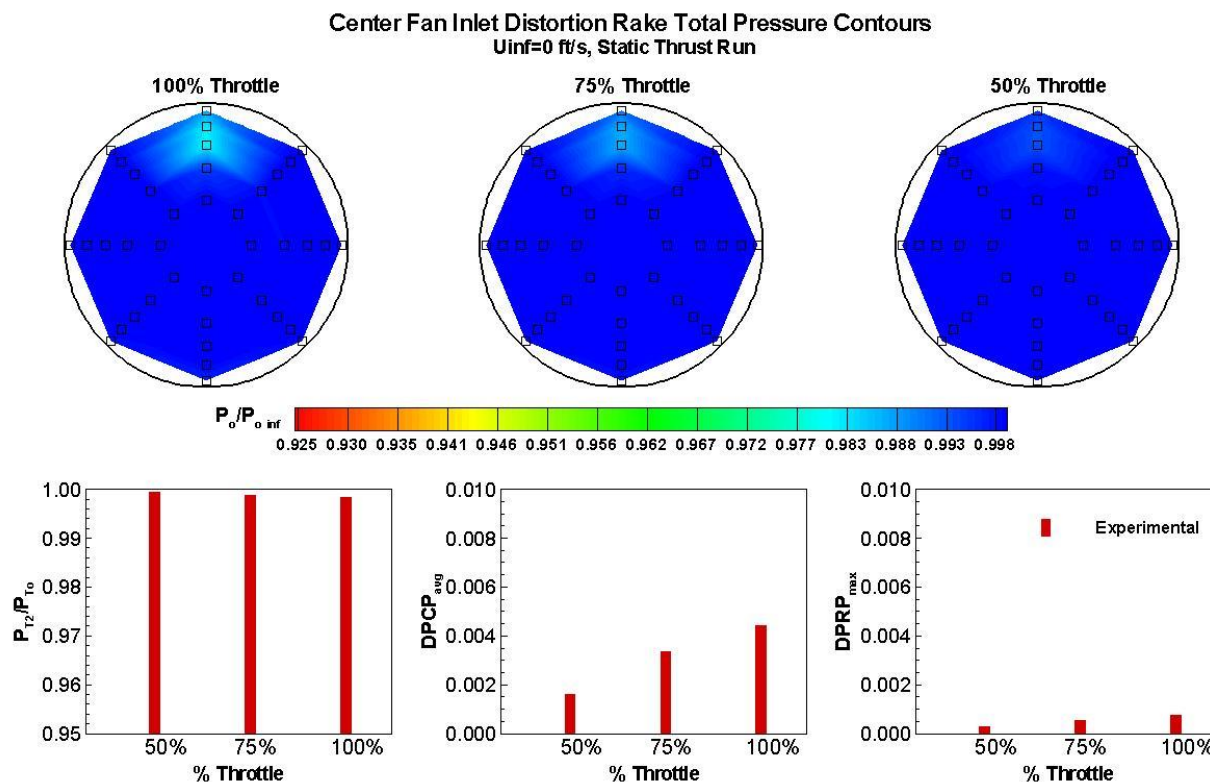


Figure 49: Center fan inlet distortion rake contours and SAE parameters for various throttle settings with all the fans at the same power level, $U_{inf}=0$ ft/s, static thrust case.

5.8.3.3 Differential Thrust Results

After running the cases where all of the fans were at the same throttle level, the differential thrust cases were investigated. The differential thrust cases were run to examine the effect an adjacent fans thrust and mass flow level had upon the neighboring fan's distortion and thrust level. From the CFD results shown in Section 5.7.3, the spillage induced blockage of an adjacent fan can have a significant effect upon the neighboring fan's flowfield. The differential thrust cases investigated had the center fan at 100% throttle and varied the adjacent fans from 100% to 50% and windmilling. The individual cases included a 100%:100%:50%, 100%:100%:0%, 50%:100%:50%, and finally 0%:100%:0%. A plot showing the surface pressures and thrust levels for the differential thrust cases is given in Figure 50. From Figure 50, the experimental and OVERFLOW predicted pressures compare well with each showing a reduction in centerline pressures with increased blockage due to the spillage for the right or left fan at decreased mass flow. From the pressures, the case with the most blockage is the 0%:100%:0% as would be expected. Again, the discrepancy between the OVERFLOW pressures feeling the blockage up to the leading-edge and the experimental pressures only to the airfoil maximum thickness is observed. A bar plot showing the thrust level for each differential case is also shown in Figure 50. From the bar plot, as the blockage due to the adjacent fan(s) spillage increases, the centerline fan thrust was observed to increase. The increase in thrust appears to be proportional to the increase in neighboring blockage. The blockage from the neighboring fan is essentially reducing the effective inlet velocity of the center fan, increasing its thrust. This increase in thrust was not

observed for the CFD cases. From the CFD, for the differential thrust cases, changes in the effective inlet lip sideslip angle produced increasing levels of separation in the inlet. As a result, the inlet lip-to-duct transitions were modified prior to the wind tunnel test. It is believed that these modifications significantly reduced or prevented the separation observed in the CFD results, allowing the thrust increases to be observed.

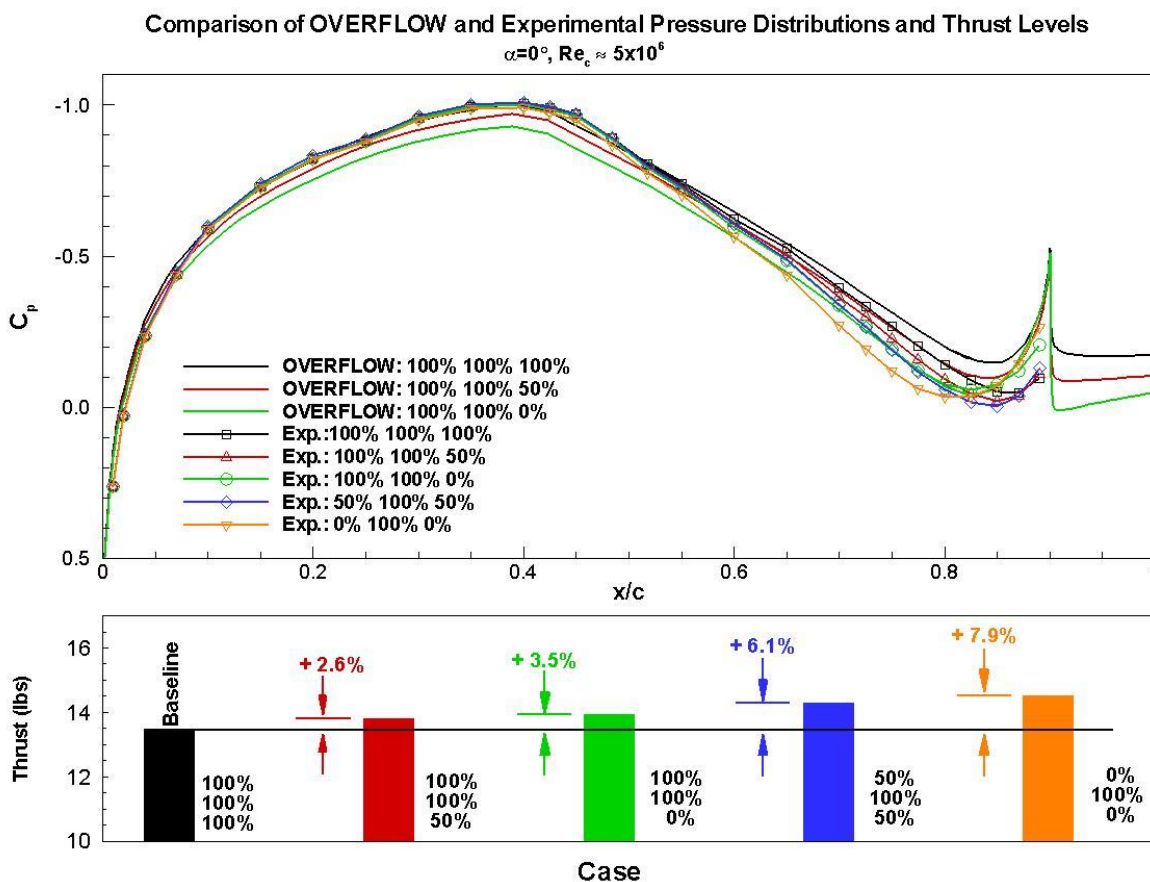


Figure 50: Comparison of OVERFLOW predicted and experimental pressures and thrust levels for the differential thrust cases, $U_{inf}=172$ ft/s, $Re_c=5 \times 10^6$.

A plot showing the center fan inlet total pressure contours and calculated SAE distortion parameters for the differential thrust cases is given in Figure 51. From Figure 51, from the total pressure contours, the distortion in the center fan was observed to increase with increasing spillage from the neighboring fans, with the 0%:100%:0% case showing the largest effect as would be expected. Two of the three calculated SAE parameters also show increased distortion in the center fan with increased spillage from neighboring fans. The average total pressure ratio and circumferential descriptors clearly show increased distortion proportional to increased spillage from the outer fans. The maximum radial descriptor does not show a clear trend with increasing spillage. Much like the cases with all of the fans at the same power level, or the static thrust cases, although the distortion was shown to increase with increasing spillage from neighboring fans, the overall levels are small.

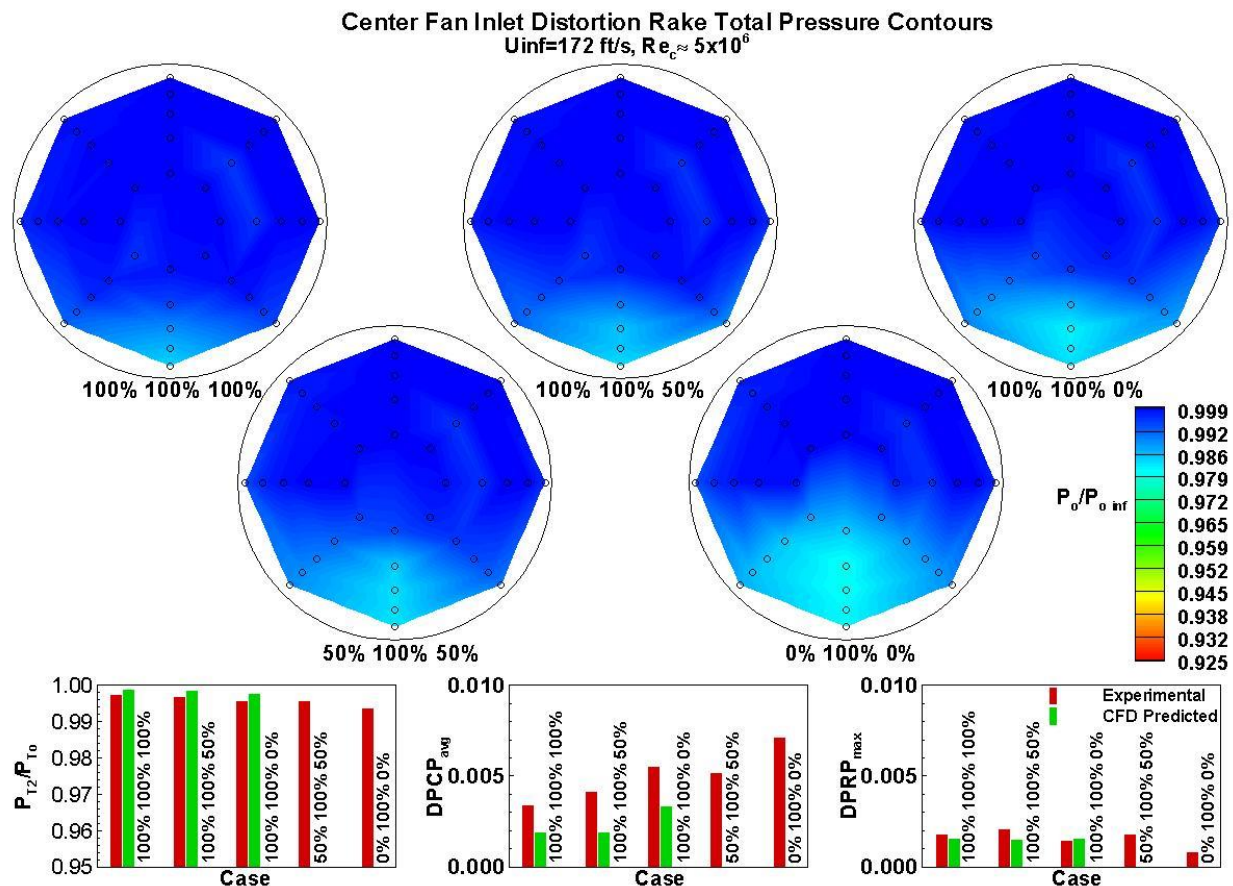


Figure 51: Center fan inlet distortion rake contours and SAE parameters for various differential thrust throttle settings, $U_{inf}=172 \text{ ft/s}$, $Re_c=5 \times 10^6$.

The unsteadiness of the center fan thrust time histories were also investigated to determine if the increased distortion due to the differential thrust settings also increased the unsteadiness in the fan thrust reading. The center fan thrust measurements were acquired at 1 kHz for 5 seconds. The standard deviation of the center fan thrust time history was calculated in order to gage the unsteadiness in the baseline 100%:100%:100% case and how it changed with the various differential thrust settings. The standard deviation is a measure of how much variation, or deviation from the mean exists in a signal. The equation for standard deviation is given as:

$$\text{Standard Deviation, } \sigma = \sqrt{\frac{1}{N} \sum_{i=1}^N (x_i - \bar{x})^2} \quad \text{Equation 8}$$

The standard deviation for the baseline 100%:100%:100% case and the differential thrust cases are shown in Figure 52. For the baseline 100%:100%:100% case shown in Figure 52 with the distortion rake installed, the center fan thrust was $T=13.5 \text{ lbs}$. From Figure 52, the standard deviation for the baseline case was $\sigma = 0.53 \text{ lbs}$, or about 4% of the average thrust level. For the 100%:100%:50% case, the standard deviation drops slightly from $\sigma = 0.53 \text{ lbs}$ to $\sigma = 0.52 \text{ lbs}$,

which is probably in the repeatability of the measurement. For the 100%:100%:0%, 50%:100%:50%, and 0%:100%:0% cases, the standard deviation increases, from $\sigma = 0.57$ lbs for the 50%:100%:50% up to $\sigma = 0.69$ lbs for the 0:100%:0% case. From the baseline to the largest recorded standard deviation for the 0:100%:0% case, the difference is $\Delta\sigma = 0.16$ lbs, a relatively small number. On a percentage basis, however, the difference does equate to a 30% increase in σ . It should also be noted that the differences in standard deviation between the cases did not correlate directly to the thrust increases shown in Figure 50. While the maximum standard deviation did correspond to the largest distortion and center fan thrust increase case, the intermediate cases are less clear.

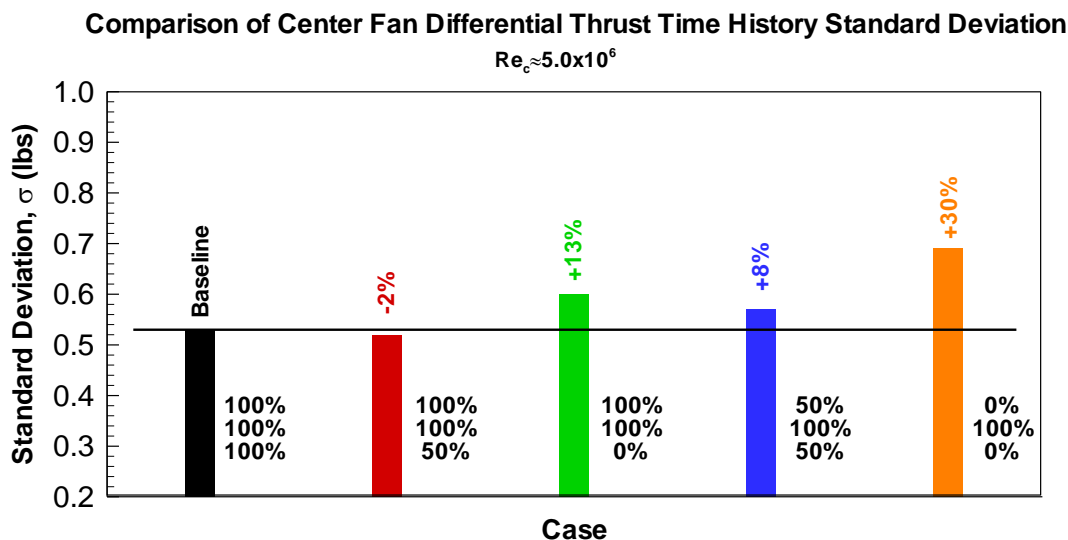


Figure 52: Comparison of the center fan differential thrust time history standard deviation.

5.8.3.4 Smoke Flow Visualization Results

Smoke flow visualization was also performed in order to attempt to visualize the flow field and separation patterns associated with the fans and inlet system. Due to the nature of smoke flow visualization, the maximum free-stream velocity attainable with good visualization of the smoke was approximately 30 ft/s. At higher free-stream speeds, the smoke disperses beyond a point where good visualization is possible. In order to best match the higher speed test condition run ($U_\infty \approx 172$ ft/s), the free-stream to duct speed was matched (≈ 290 ft/s). For a free-stream speed of 30 ft/s, the throttle setting was basically at the minimum allowable throttle setting, or 19%. This gave the appropriate speed ratio. Smoke flow visualization cases included all fans windmilling, all fans at 19% throttle, and a differential thrust case of 0:19%:19%. Side, top, and front quartering views were obtained. High definition video of the results were obtained and still were taken from the video.

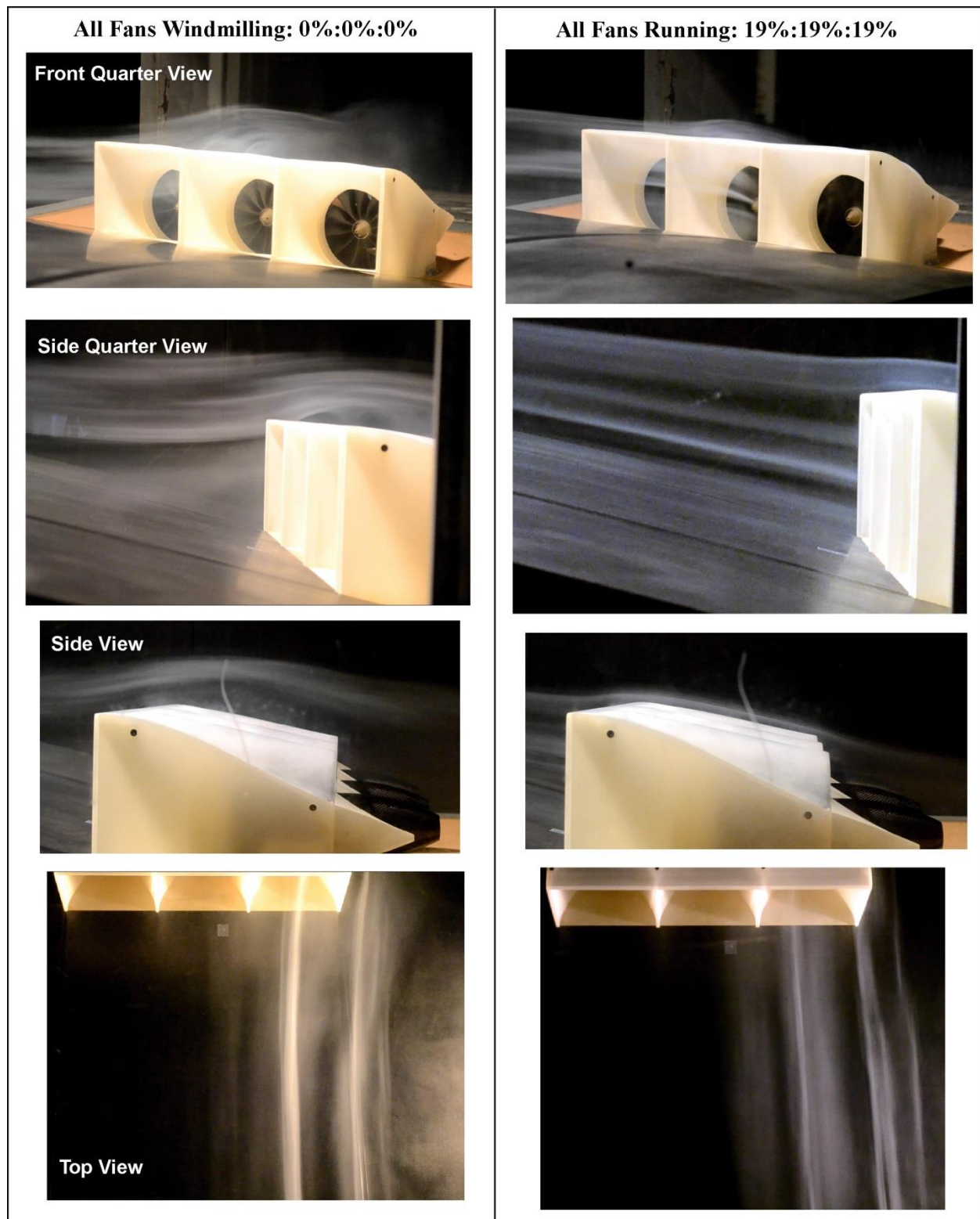


Figure 53: Comparison of smoke flow visualization with all fans windmilling and with all fans running.

Figure 53 shows a comparison of the smoke flow visualization results for the windmilling case versus all of the fans running. For the windmilling case, the large amount of blockage created by

the windmilling fans is readily apparent as the flow attempts to negotiate out and around the inlet. The side and front quarter views show a large amount of separation on the top outer portion of the ducts. The top view shows the streamlines curving to the outside as the flow again tries to move out of the way of the duct system. The case with all the fans operating at the same power level shows a strikingly different flowfield. The photographs show no apparent separation for the all fans running case. The streamlines into and around the duct system are straight and appear to follow the duct contours.

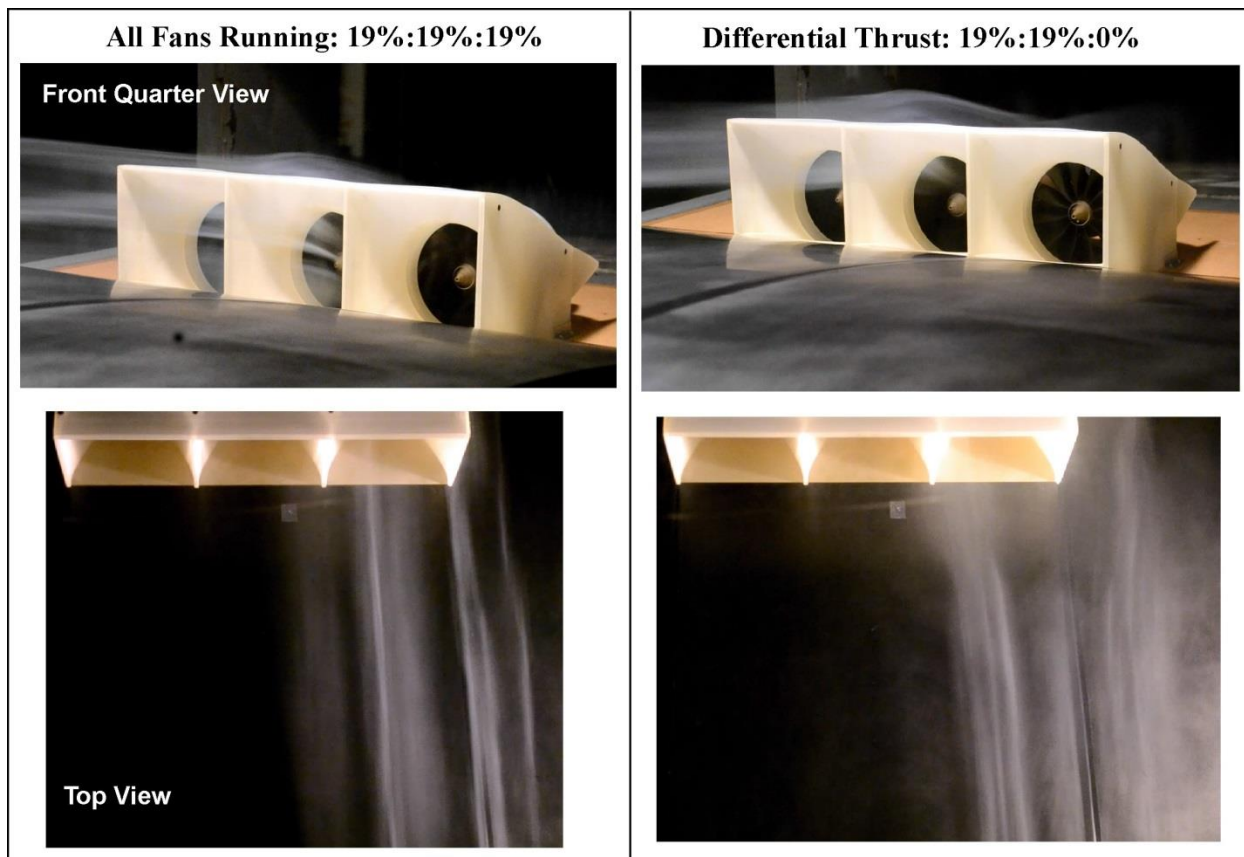


Figure 54: Comparison of smoke flow visualization with all fans running and a differential thrust case where the left fan is windmilling.

Smoke flow visualization was also performed for a differential thrust case. For the differential thrust case, the left fan throttle was set at 0%, or windmilling where the center and right fan were running at the scaled full throttle (19%). For the differential thrust case, the side views were not taken since the differences between the center and left fan could not be discerned. Only the front quartering and top view were obtained. Figure 54 shows a comparison between the all fans running and the differential thrust flow visualization results. From Figure 54, for the differential thrust case front quarter view, the added blockage from the left fan windmilling can be seen in the center fan streamlines showing increased curvature over the top of the center duct. The top view shows the streamlines coming into the left fan getting pushed towards the center fan and out, away from the duct structure.

Overall, the flow visualization results show that for the case where all the fans are operating at the same power level, the flow appears to be well ordered and there is not apparent separation external to the duct system. For the windmill case, or the differential thrust case, the blockage created by the windmilling fan(s) causes a significant disturbance to the flowfield. For the all fans windmilling case, the blockage was observed to cause significant separation external to the duct system. Qualitatively, the smoke flow visualization results compare well to the CFD predicted streamlines shown in Figure 26 through Figure 29, and Figure 31.

5.8.3.5 *Wind Tunnel Test Summary*

The wind tunnel test results were very positive. The data set produced is a very unique and has already provided insights into the complex TeDP flowfield. Generally, the experimental results compared well to the CFD predictions. The thrust level at the design point was 14.24 lbs, approximately 8% below the predicted value of 15 lbs. The lower thrust was a result of the inadequate battery power. It is believed if the full 9.75 kW were available to the motor instead of the 6.8 kW provided by the batteries, the 15 lbs thrust target would have easily been achieved.

Unfortunately no boundary layer profiles were obtained with the duct system installed. Boundary layer profiles with the duct system installed were attempted on the final day of the test entry. After reinstalling the traversing pitot probe system, the first attempt at obtaining a boundary layer profile was unsuccessful as the pitot tube was not attached to the ESP pressure module. The second attempt also met with issues as the tygon tube leading from the pitot probe to the ESP module became pinched in the mounting fixture. Since each run required a total of 4 hours to recharge the batteries, approximately 10 hours were used trying to obtain the profiles. Since flow visualization results were also deemed important, in the remaining time it was decided to forgo the boundary layer profile measurements with the ducts in place in favor of obtaining the smoke flow visualization results.

For the cases with all the fans running at the same power level, as was observed in the CFD predicted pressures, significant blockage effects on the experimental surface pressures were observed at fan mass flows below the design mass flow. The increased blockage effects were observed to reduce surface pressures upstream of the duct and increase inlet distortion levels. Also, the increased blockage upstream of the fans were shown to increase thrust levels (as compared to predicted) due to the reduction in effective inlet velocity. A movable inlet lip would help to minimize the off-design mass flow effects. While changes in inlet distortion were observed, the overall levels were very small, approximately 10 times smaller than generally acceptable distortion levels.

Differential thrust levels were also observed to have significant effects on the adjacent fan performance. Spillage for the reduced thrust level fan was observed to affect the adjacent fan incoming pressure distribution, creating a more diffusive environment upstream of the adjacent fan and reducing the inlet velocity. This reduction in inlet velocity produced an increase in the adjacent fan thrust. For the largest differential thrust case (0%:100%:0%), the adjacent fan thrust was shown to increase by approximately 8%. The increase in thrust with a neighboring fans reduction in thrust could have significant implications for use of differential thrust in trim and

yaw control. Increasing the inlet lip radius would help to better account for changes in the effective inlet lip sideslip angle due to neighboring fan spillage.

The smoke flow visualization results qualitatively compared well to the CFD predicted streamlines for all three cases investigated, windmilling, all fans operating at the same power level, and a differential thrust case. The smoke flow visualization results helped to provide a good understanding of the overall duct flowfield under differing operating conditions.

6 SUMMARY AND CONCLUSIONS

In order to meet future goals for aircraft efficiency proposed large reductions in fuel burn, emissions, and noise, next generation aircraft will have to employ new technologies. One configuration which shows significant promise is the Hybrid Blended Wing Body (HBWB) coupled with a turboelectric distributed propulsion (TeDP) system. The HBWB provides high cruise L/D. With pylon mounted ultra high bypass ratio (UHB) engines, the HBWB provides a possible 52% fuel burn reduction. The revolutionary TeDP propulsion concept uses electric motor driven fans to provide propulsive thrust, with the gas turbine generators providing electric power for the system and can reduce fuel burn another -18% to -20%, for a total combined fuel burn reduction of -70% to -72%.

The TeDP concept has several distinct advantages. These include boundary layer ingestion (BLI), re-energizing the wake of the airframe with the fan thrust stream, decoupling the propulsion from the power source, a very high effective bypass ratio, ultimate redundancy for increased safety, and differential thrust control for directional stability, trim, and possible yaw control. There are also significant challenges associated with TeDP, including increased inlet distortion due to BLI. The TeDP concept also leads to strong coupling between the aerodynamics and propulsion of the airframe. Significant interactions exist between the sectional aero performance and thrust level. Changes in thrust level and mass flow through the fan can affect circulation, spillage induced blockage, and stagnation point movement, producing significant changes in sectional lift and moment.

A successful TeDP implementation poses significant challenges. RHRC proposes the development of a distributed propulsion system for a small test bed aircraft. The development of a flying demonstrator for TeDP concepts, systems, and technologies allows early investigation of complex aerodynamics, propulsion, and systems vital to the success of a TeDP configuration. The flying demonstrator reduces development risk of a larger, dedicated TeDP configuration by testing concepts, performance, and technologies at a smaller, and relatively cheaper scale. The subscale test bed can be used to study the effects of BLI, aerodynamic/thrust coupling, angle-of-attack, differential thrust effects on adjacent fan performance and distortion, inlet area design, and power generation topology.

The key to the successful implementation and use of the test bed is to study and focus on technologies which will scale appropriately to the full scale transport aircraft. Although the subscale test bed is significantly smaller in size, thrust level, Reynolds number, and cruise speed, key technologies and concepts scale well from the test bed to the full scale aircraft.

Technologies which scale well include BLI effects, aerodynamic and propulsive coupling effects, inlet lip geometry effects, and power distribution topology. Areas that do not scale well include the inlet duct shape, the electric power levels generated and required, and the effects of possible transonic shocks upstream of the inlets. Since the test bed aircraft operates at low subsonic speeds, the inlet is a converging s-duct, and not a diffusing s-duct required by transonic fans. Other than the transonic shock effects, aerodynamics external to the inlet and fan should scale well, while those internal to the fan do not.

The main goal of the Phase I program was to design and test a multi-fan, boundary layer ingesting model based on a conceptual test bed aircraft TeDP installation. The wind tunnel test measured installed fan thrust, inlet distortion, model surface pressures upstream of the inlet, boundary layer profiles, and required fan power for a three fan model based on a full scale test bed aircraft design. The test examined the effects of adjacent fan thrust level on neighboring fan performance and distortion. All proposed tasks and milestones for the Phase I program were met and achieved, including identification of an appropriate test bed aircraft already in NASA's inventory, design of a notional TeDP system to replace the aircraft's IC/propeller based propulsion system, selection of an available electric ducted fan, design of a model, inlet and s-duct for the fan, development of a 3D CFD model, and finally construction and wind tunnel testing of the multi-fan model. Although only a single fan model was proposed in the original program, the scope of the effort was increased to examine multiple fans. This increase in scope was pursued as it significantly increased the immediate usefulness and applicability of the Phase I results to the full scale TeDP effort.

The test bed aircraft identified for the project is one of NASA Dryden's TG-14A motor gliders. The TG-14A was chosen for a combination of factors including aerodynamic performance, available space for batteries and instrumentation, maximum take-off gross weight, and ease of modification. A TeDP system was designed to replace the TG-14A's 100 HP Rotax 912 engine. The TG-14A's Rotax 912 and propeller produces approximately 550 lbs static thrust, with 270 lbs available at a cruise speed of 97 kts. The TeDP system was designed to replicate the static thrust and the thrust available at cruise. The electric ducted fan chosen was the Schuebeler DS-94-DIA HST DSM6745-700. The DS-94-DIA HST DSM6745-700 has a fan ID of 5.04 inches with a fan swept area of 14.57 in², producing a static thrust of 29 lbs with a power input of 9.75 kW. Eighteen individual fans would be required to replace the TG-14A baseline Rotax power plant.

After examining several test model set-ups, a set-up was chosen and model designed where a three fan/duct system was mounted in a 2D wind tunnel floor mounted hump model that approximates the upper surface of the TG-14A root chord airfoil. The floor mounted hump geometry allows a full size chord model, duct, and fan. The test can be conducted at full flight Reynolds numbers. The disadvantage lies in being unable to varying the incoming boundary-layer by changing the angle-of-attack and not being able to get sectional lift and moment characteristics. The use of the full scale fan hardware, coupled with the correct boundary-layer and flight Reynolds numbers made the hump model design the most attractive.

After designing the 3 fan hump model, a full 3D CFD model was developed of the wind tunnel set-up. The OVERFLOW CFD code was used to generate a complete model of the wind tunnel

test set-up, including tunnel walls, the hump model, inlets, ducts, and fan/motor plugs. The CFD model was used to gain a better understanding of the TeDP flowfield and the impact of varying fan mass flows and differential thrust effects. Results from the CFD study of the wind tunnel model and duct geometry showed that for the thrust cases with all fans running at the same mass flow, the inlets designed behaved well with no internal separation, minimal secondary flows, and very little inlet distortion. The inlet lip and outer duct surface performed well for the design mass flow, but showed increasing separation with mass flows below the design mass flow. The pressure distribution for the reduced mass flow cases showed the effect of increasing blockage caused by the below design mass flow spillage. The blockage induced effects upon the sectional pressure distribution were significant. The differential thrust cases showed the effect of an adjacent fans spillage affecting the neighboring fan blockage and effective inlet lip sideslip angle. The changes in effective lip sideslip angle were also seen to extend beyond the directly adjacent fan. The pressure distribution upstream of the adjacent fan was also affected by its neighbor. Each individual fan thrust level/mass flow had a global effect on the flowfield.

After the CFD study was complete the wind tunnel model was manufactured and tested in the University of Illinois 3'x4' low speed, low turbulence wind tunnel. The hump model was manufactured from high density urethane using CNC sculpting. The inlets and duct system were manufactured using stereo lithography. The wind tunnel test measured the center duct/fan inlet distortion and the thrust produced by the centerline EDF unit. Other parameters measured during the test included the mass flow rate in the off center EDF units, the boundary-layer thickness upstream of the EDF inlet location, surface static pressures along the model centerline, and individual fan voltage and amperage. Additionally, the motor temperature of the center fan was also measured.

The wind tunnel test results were very positive. The experimental results generally compared well to the CFD predictions. The thrust level measured at the design point was 14.24 lbs, approximately 8% below the predicted value of 15 lbs. The lower thrust was a result of the inadequate battery power. Due to battery limitations, the maximum power available to the individual motors was 6.8 kW instead of the required 9.75 kW. It is believed if the full 9.75 kW were available to the motor, the 15 lbs thrust target would have easily been achieved.

For the cases with all the fans running at the same thrust level or mass flow, significant blockage effects on the experimental surface pressures were observed at fan mass flows below the design mass flow. The increased blockage effects were observed to reduce surface pressures upstream of the duct and increase fan inlet distortion levels. Also, the increased blockage upstream of the fans were shown to increase thrust levels due to the reduction in effective inlet velocity. While changes in inlet distortion were observed, the overall levels were very small, approximately 10 times smaller than generally acceptable distortion levels.

Differential thrust levels were also observed to have significant effects on the adjacent fan performance. Spillage for the reduced thrust level fan was observed to affect the adjacent fan incoming pressure distribution, creating a more diffusive environment upstream of the adjacent fan and reducing the effective inlet velocity. This reduction in inlet velocity produced an increase in the adjacent fan thrust. For the largest differential thrust case the adjacent fan thrust was shown to increase by approximately 8%.

Results from the Phase I investigation were very encouraging. A very unique CFD and experimental data set was generated for a distributed array of boundary-layer ingesting propulsors. Overall the CFD and experimental results compared well. The results show significant coupling between the aerodynamics of the section and the fan thrust/mass flow, specifically the effect of increased blockage at reduced mass flows. Differential thrust results show that an adjacent fan(s) thrust/mass flow level will affect the neighboring fan inlet behavior and thrust level, increasing thrust for reduced mass flows. The increase in thrust with a neighboring fans reduction in thrust could complicate the use of differential thrust for trim or yaw control. Increasing the inlet lip radius would help to better account for changes in the effective inlet lip sideslip angle due to neighboring fan spillage. Lessons learned from these aerodynamic/propulsive coupling results are applicable to the larger, full scale transport version.

7 PHASE II OBJECTIVES

Based on the Phase I results and lessons learned, the overall objective of the Phase II program will be to test a pseudo 3D wind tunnel model with a set of 5 BLI electric ducted fans mounted on a 2D straight wing. The test will examine multi-fan effects on aerodynamic/propulsive coupling, BLI, and multi-fan circulation effects. Specifically, the effect of thrust levels and mass flow on both the overall wing and sectional aerodynamic characteristics including lift, drag, and pitching moment will be studied. The test will also focus on the effect of different thrust levels on the aerodynamics of approach and landing configurations, especially high angle-of-attack, approach to stall, and stall. The effects of spanwise differential thrust, specifically the effect of changing mass flow and spillage on adjacent fan thrust, performance, and distortion will also be studied. Finally, the effect of inlet lip size and inlet height will also be studied.

The program will begin with a 2D CFD study to investigate thrust angle effects on aerodynamic/propulsive coupling in order to minimize coupling effects with changes in thrust/mass flow. After basic design of the new 2D straight wing wind tunnel model, a full 3D CFD model of the proposed test article will be developed using OVERFLOW. The 3D CFD model will be used to study, optimize, and better understand the multi-fan TeDP flowfield, including aero/propulsive coupling, circulation and angle-of-attack effects, and help guide the wind tunnel model design. The detailed CFD model will be instrumental in the understanding and successful final wind tunnel test of the proposed model. After the CFD study, the wind tunnel model will be built and tested in the University of Illinois 3 ft x 4 ft low speed wind tunnel. The model will have 5 BLI electric ducted fans. Each fan will be instrumented for thrust, voltage, amperage, and rpm. The center three fans will have individual chordwise pressure measurements for sectional lift and pitching moment. Sectional drag will be computed with a traversing wake rake. Additionally, a floor mounted balance will measure overall lift, drag, and pitching moment. The set-up will also be designed so that boundary layer parameters upstream of each inlet can be measured. The Phase II program will produce an extremely unique and comprehensive data set for multi-fan TeDP BLI configurations that currently does not exist. The aero/propulsive coupling and multi-fan interaction results can be scaled for use on the proposed test bed aircraft and full scale transport aircraft.

A Phase II option will also be proposed which will use CFD to perform a detailed scaling study between the subscale test bed and the full scale transport configuration. The CFD based scaling study will investigate how the aero/propulsive coupling scales between the subscale and transport configurations and how the different wing planforms (straight wing versus HBWB) might affect the coupling. The scaling study will also be used to investigate inlet design, converging versus diverging ducts and their effect upon the flowfield,

8 REFERENCES

¹ Felder, J. L., private communication, Oct. 2013.

² Felder, J. L., Tong, M. T., Chu, J., “Sensitivity of Mission Energy Consumption to Turboelectric Distributed Propulsion Design Assumptions on the N3-X Hybrid Wing Body Aircraft,” AIAA 2012-3701, paper presented at the 48th AIAA/ASME/SAE/ASEE Joint Propulsion Conference and Exhibit, 30 July – 01 August, 2012, Atlanta, Georgia.

³ Felder, J. L., Brown, G. V., Kim, H. D., paper ISABE-2011-1340, 2011.

⁴ White, F., *Viscous Fluid Flow*, 2nd. Ed., McGraw-Hill, Inc., New York, 1991, pp. 242-244.

⁵ Schlichting, H., *Boundary-Layer Theory*, 7th Ed., McGraw-Hill, New York, 1987, pp. 296-209.

⁶ Schetz, J., *Boundary Layer Analysis*, Prentice Hall, New Jersey, 1993, pp. 241.

⁷ Drela, M., and Giles, M., “Viscous-Inviscid Analysis of Transonic and Low Reynolds Number Airfoils,” *AIAA Journal*, Vol. 25, No. 10, October 1987, pp. 1347-1355.

⁸ http://en.wikipedia.org/wiki/Peukert%27s_law

⁹ Jespersen, D., Pulliam T., Buning, P., “Recent Enhancement of OVERFLOW,” AIAA Paper 97-0644, 1997.

¹⁰ “Gas Turbine Engine Inlet Flow Distortion Guidelines,” SAE ARP 1420, Rev. B, 2011.

¹¹ “Recommended Practices for Measurement of Gas Path Pressures and Temperatures for Performance Assessment of Aircraft Turbine Engines and Components,” AGARD advisory report No. 245, June 1990.

¹² Berrier, B. L., Morehouse, M. B., “Evaluation of Flush-Mounted, S-Duct Inlets With Large Amounts of Boundary-Layer Ingestion,” Paper presented at the Symposium on Vehicle Propulsion Integration; Warsaw; 6-9 Oct. 2003; Poland.

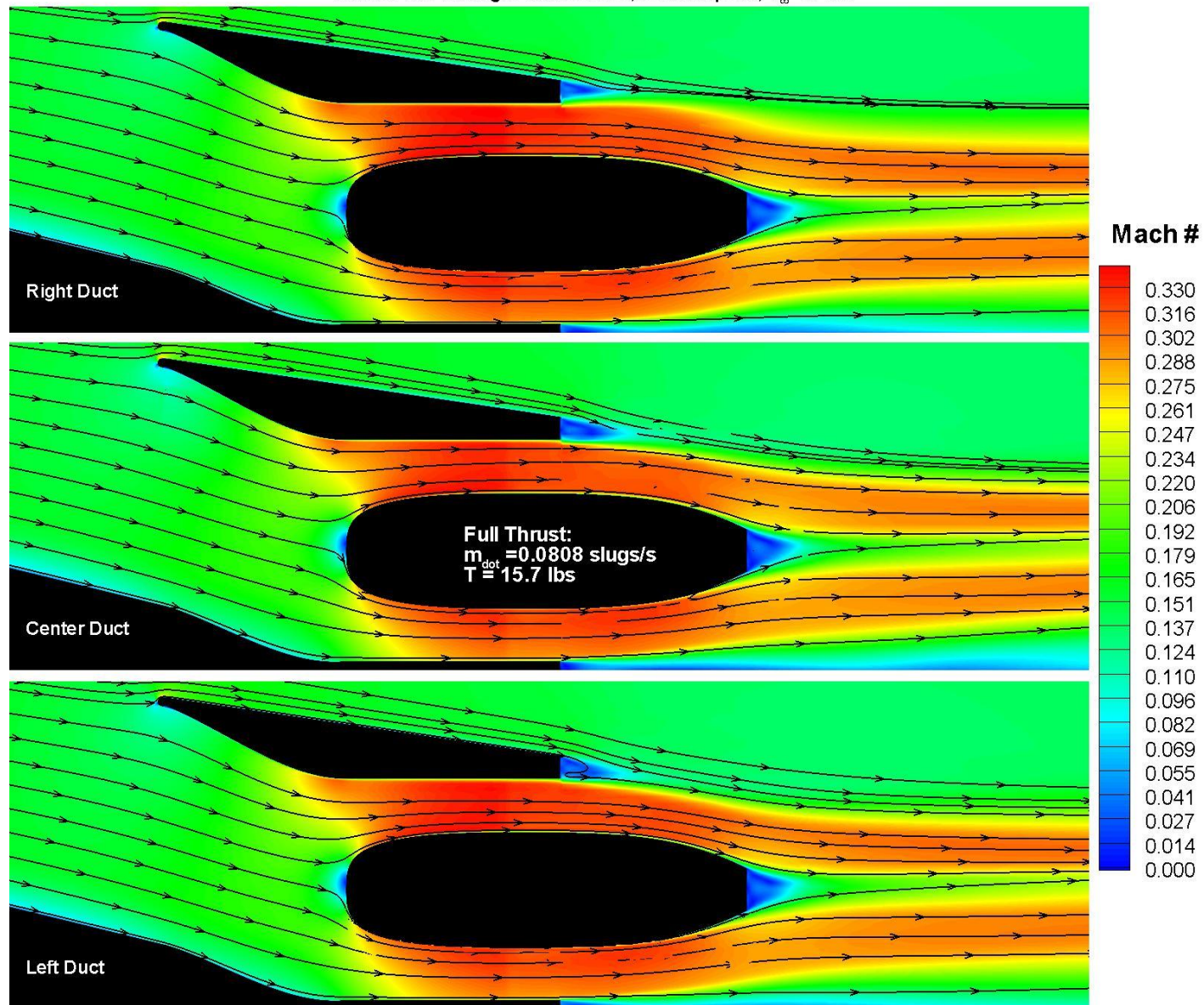
9 APPENDIX #1

All Fans Running At Same Power Level CFD Plot Summary

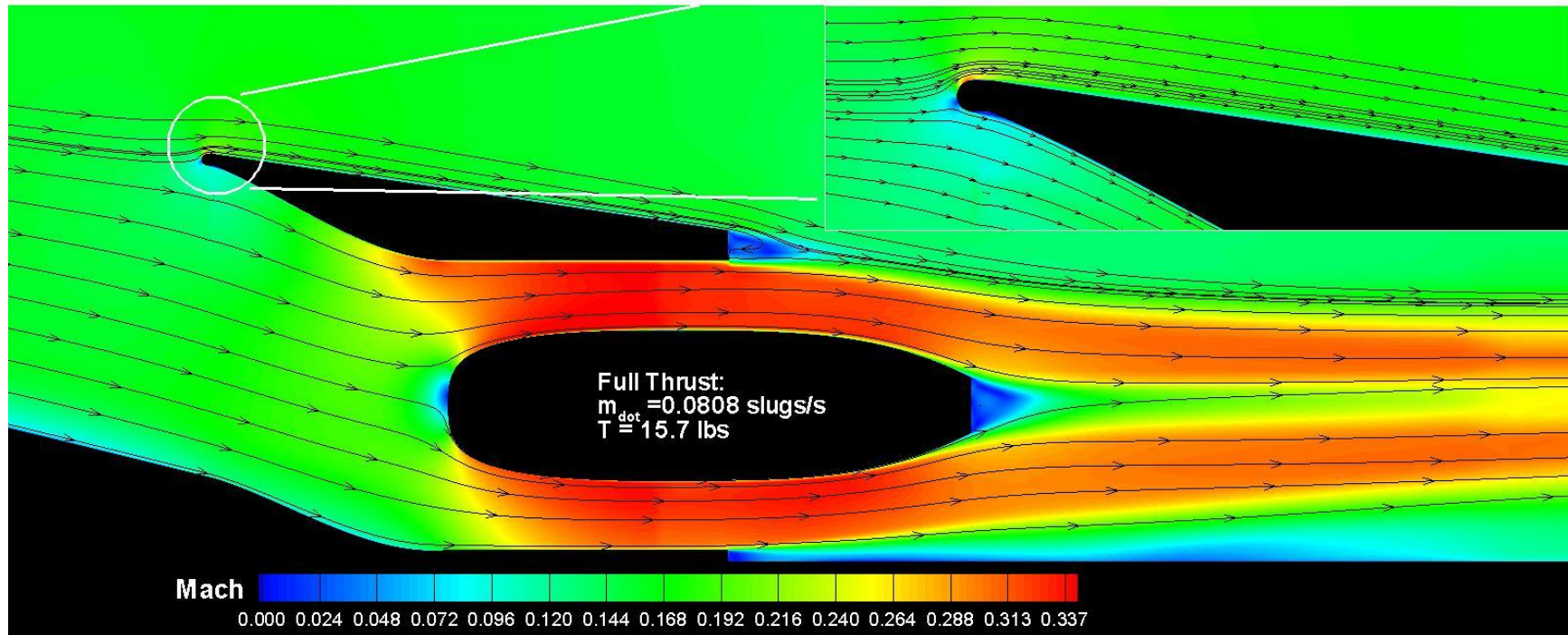
with suction

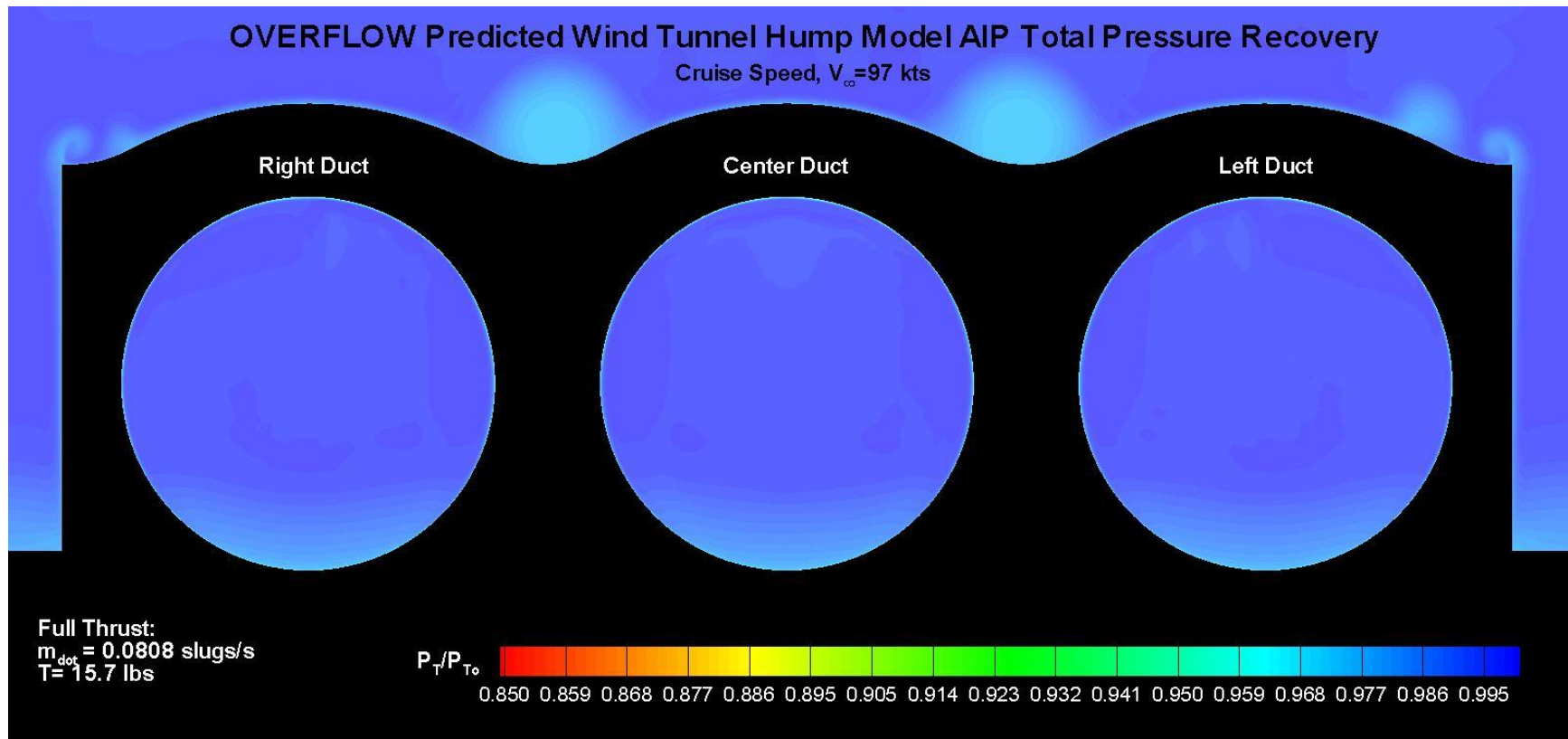
Full Thrust Case

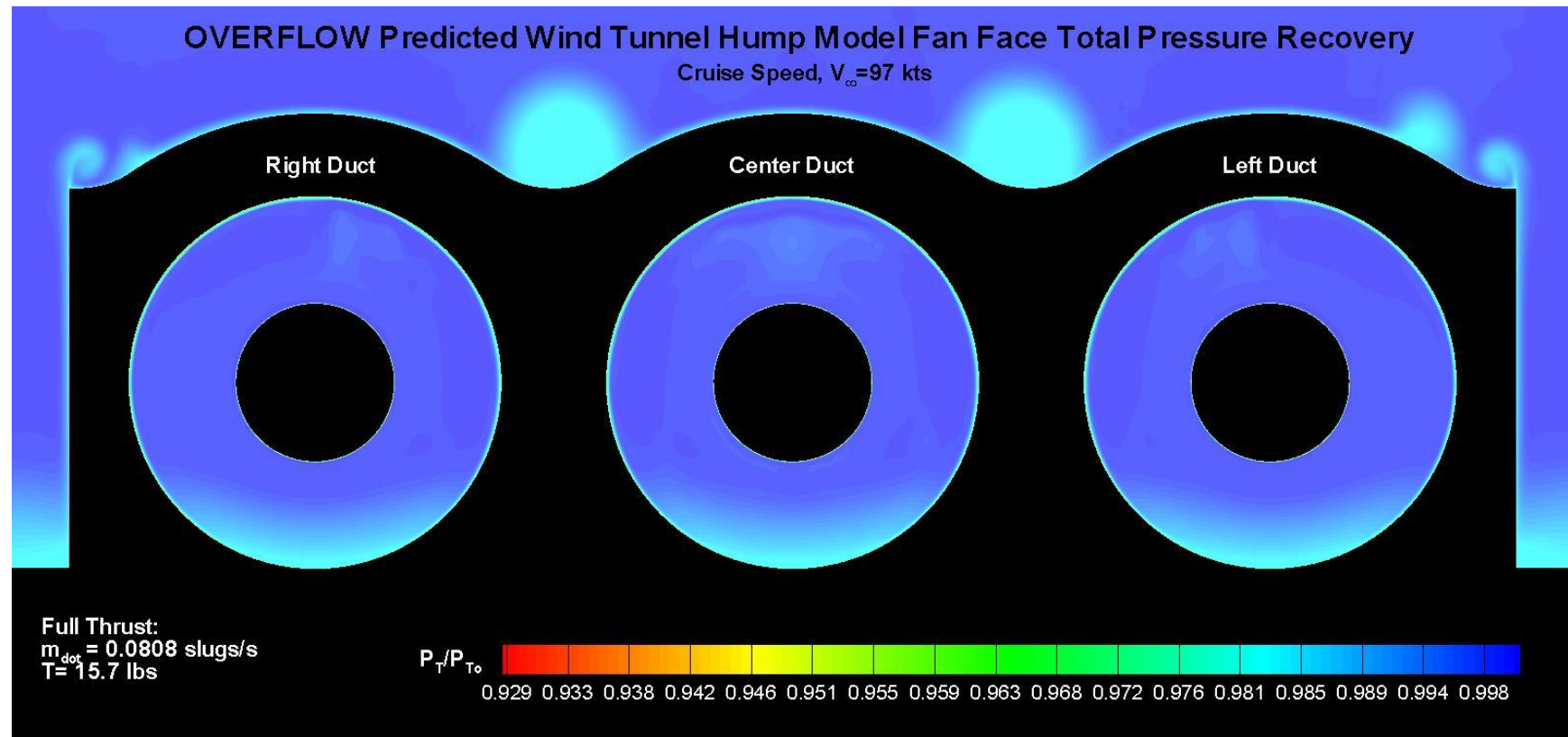
OVERFLOW Predicted Wind Tunnel Hump Model Duct Mach Contours
Vertical Cut Through Duct Centers, Cruise Speed, $V_\infty = 97$ kts

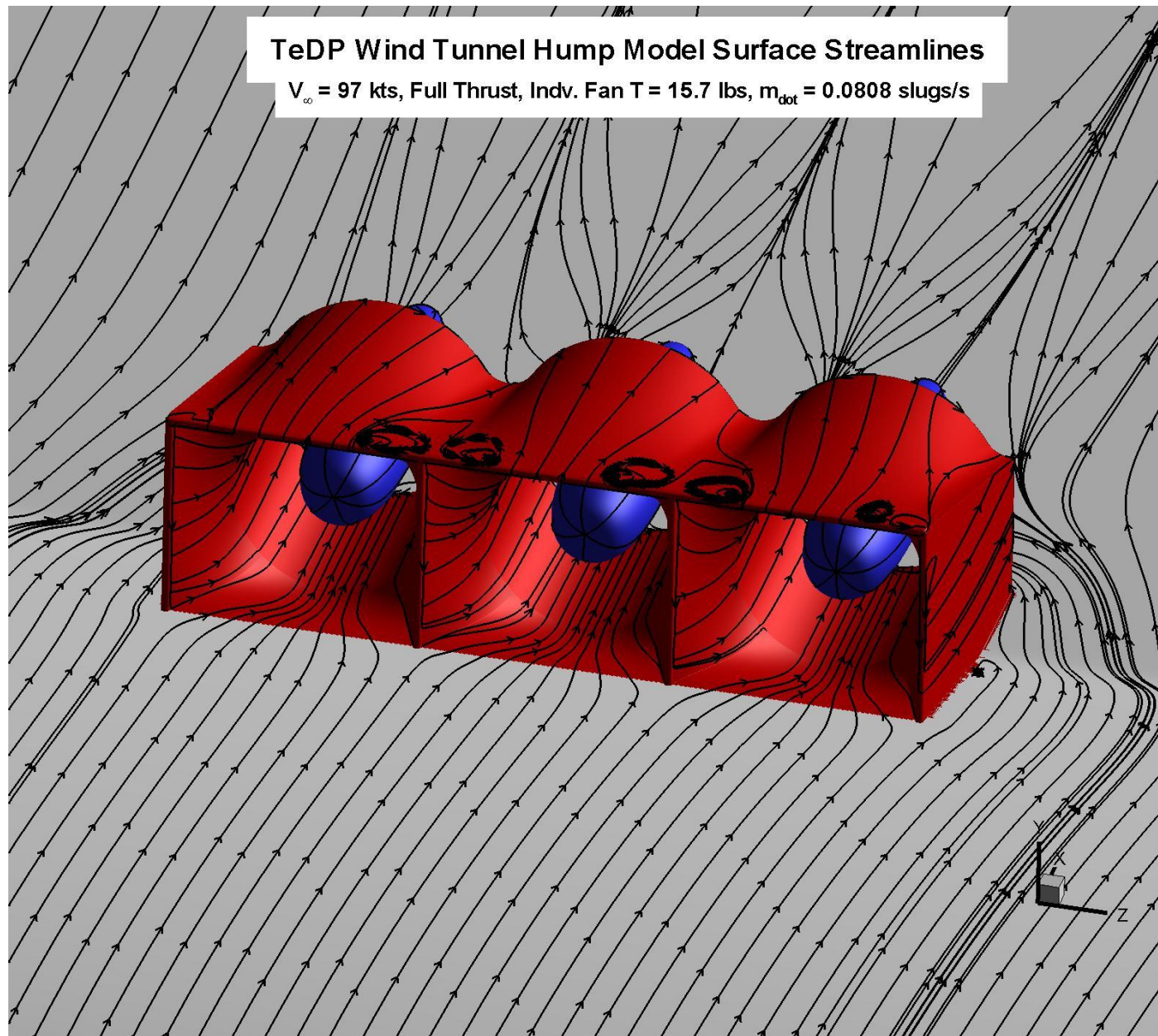


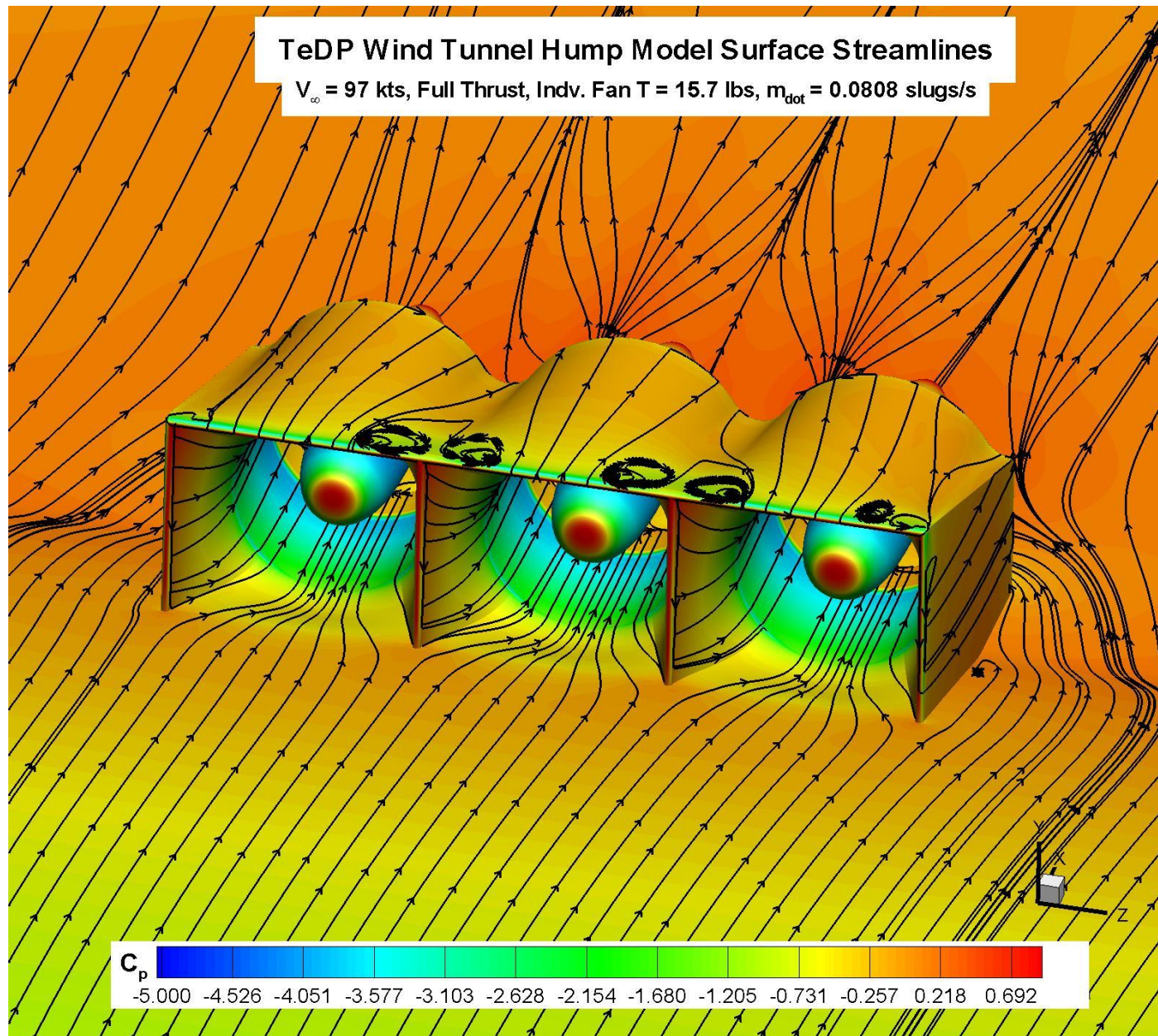
OVERFLOW Predicted Wind Tunnel Hump Model Center Duct Mach Contours
Vertical Cut Through Duct, Cruise Speed, $V_\infty = 97$ kts





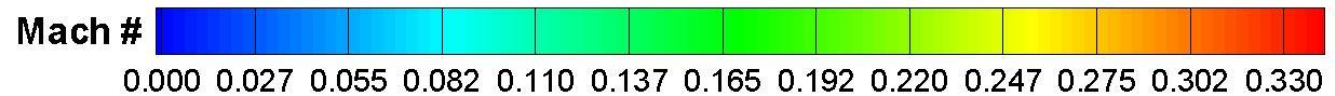
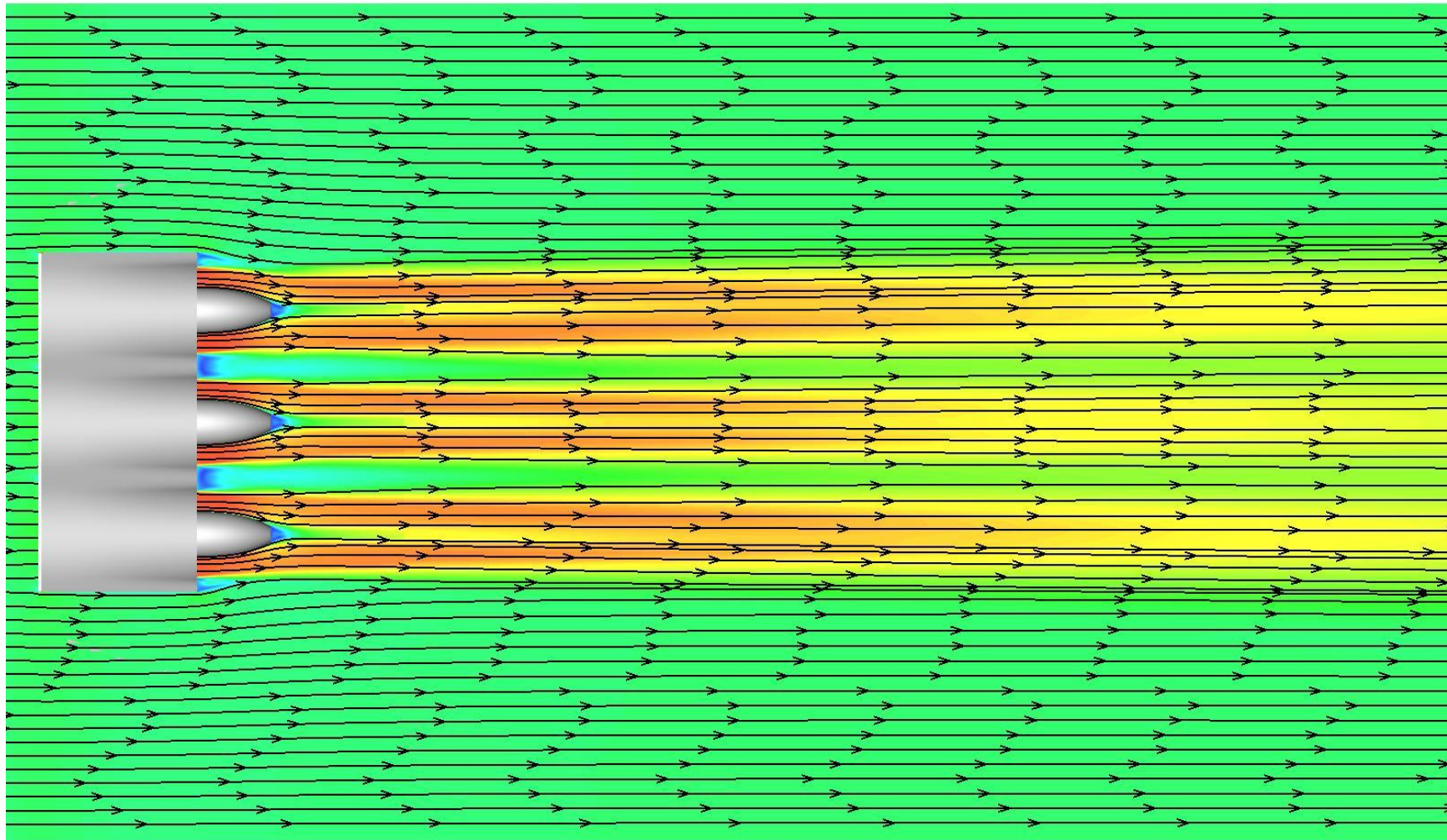






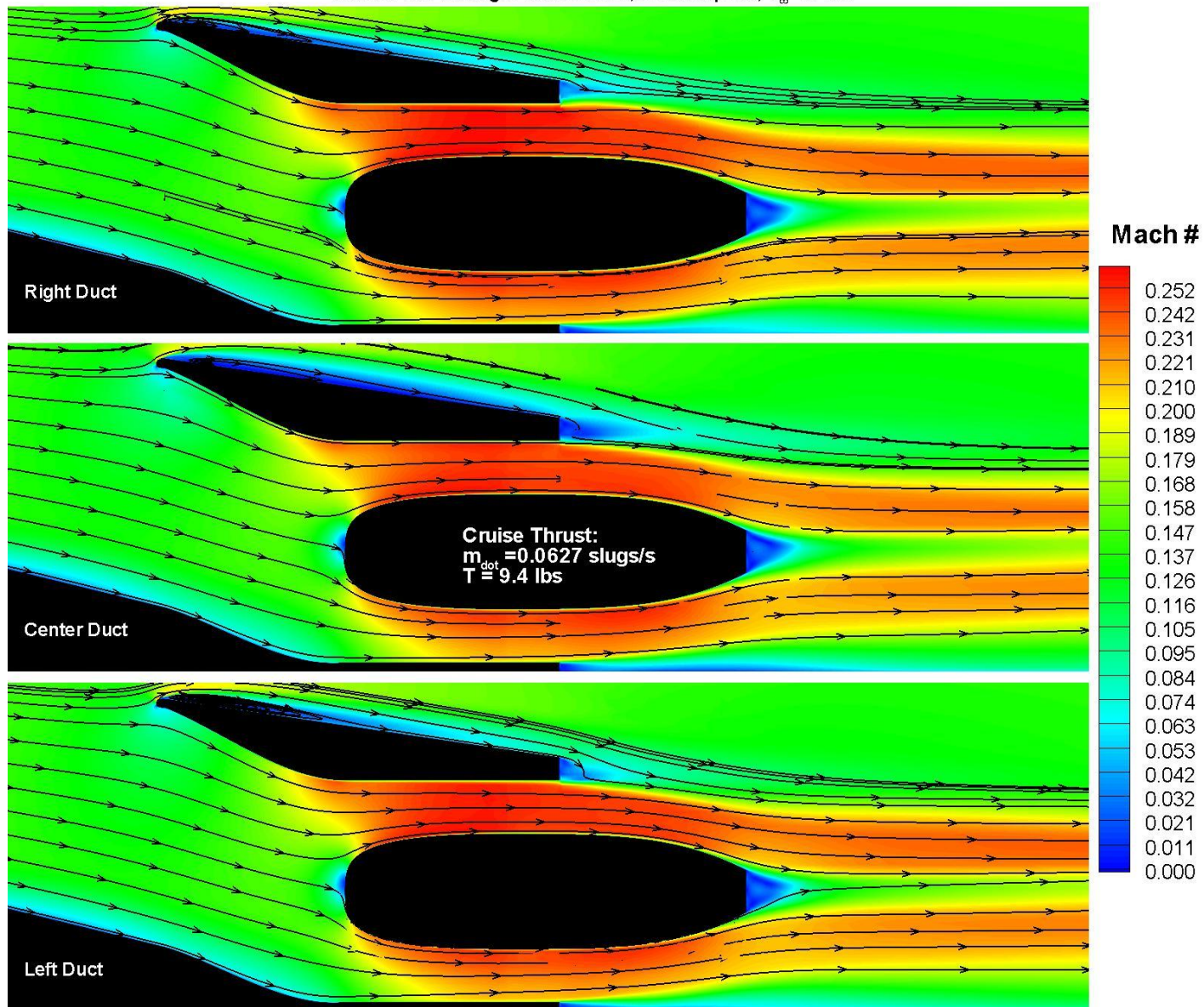
TeDP OVERFLOW Predicted Wind Tunnel Hump Mach Contours

Cut Plane = $y=2.72''$ (half duct height), Full Thrust, Indv. Duct $T=15.7$ lbs, $m_{dot}=0.0808$ slugs/s

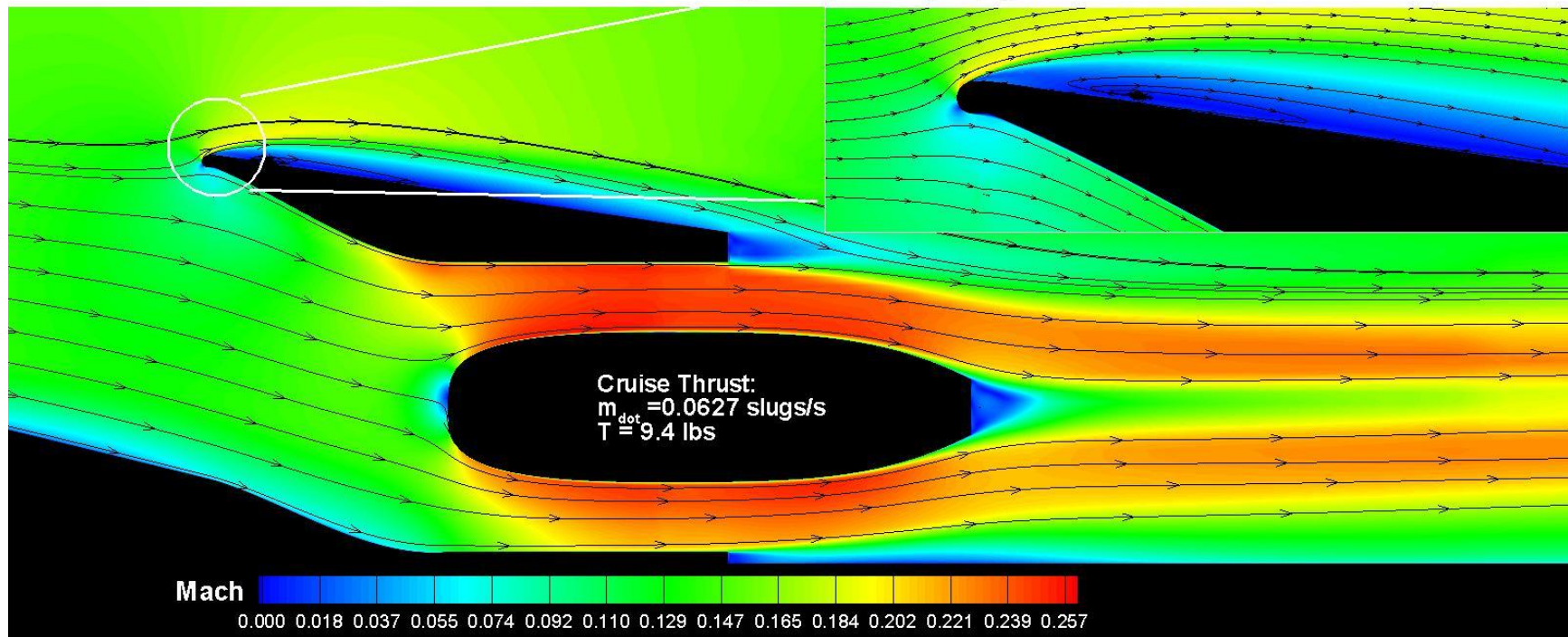


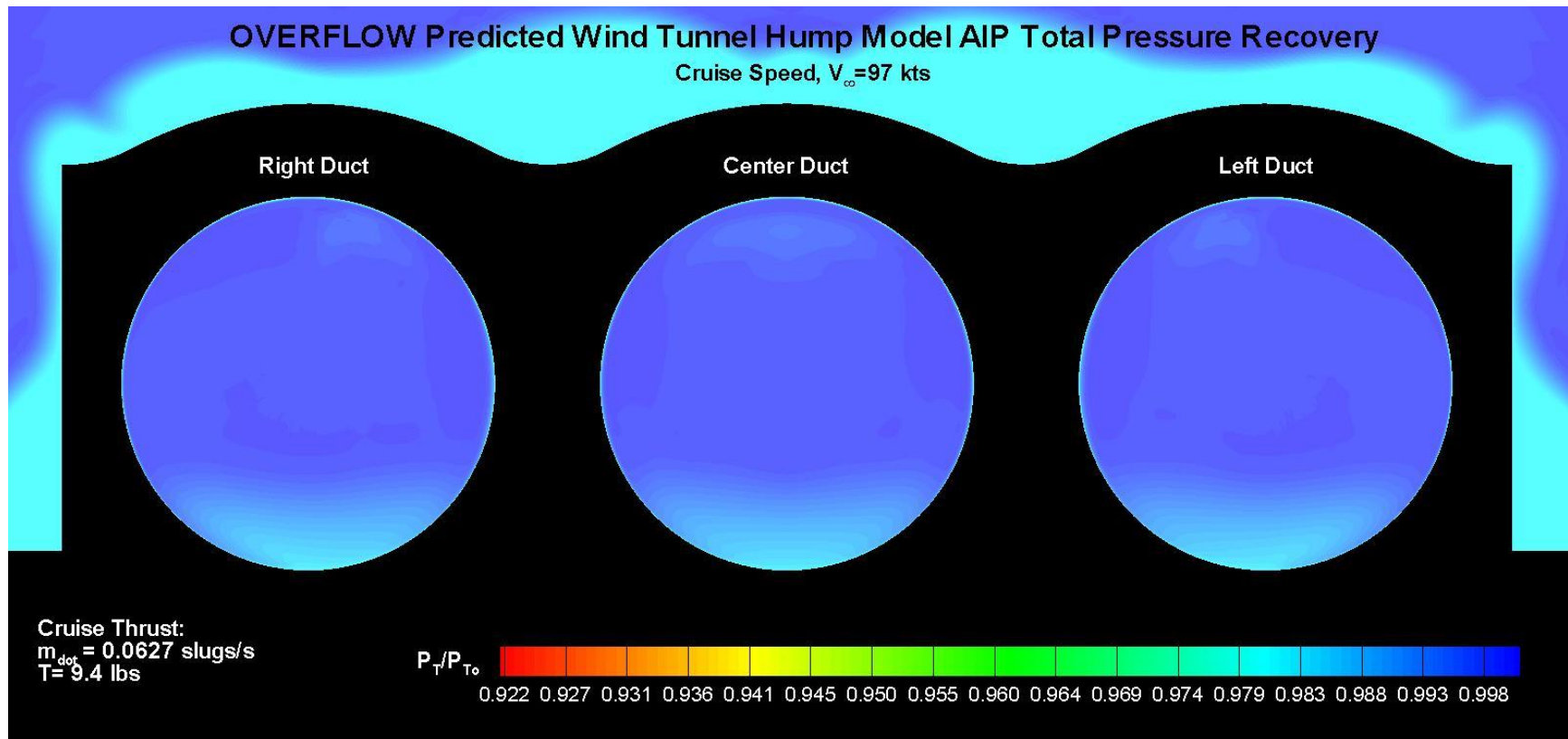
Cruise Thrust Case

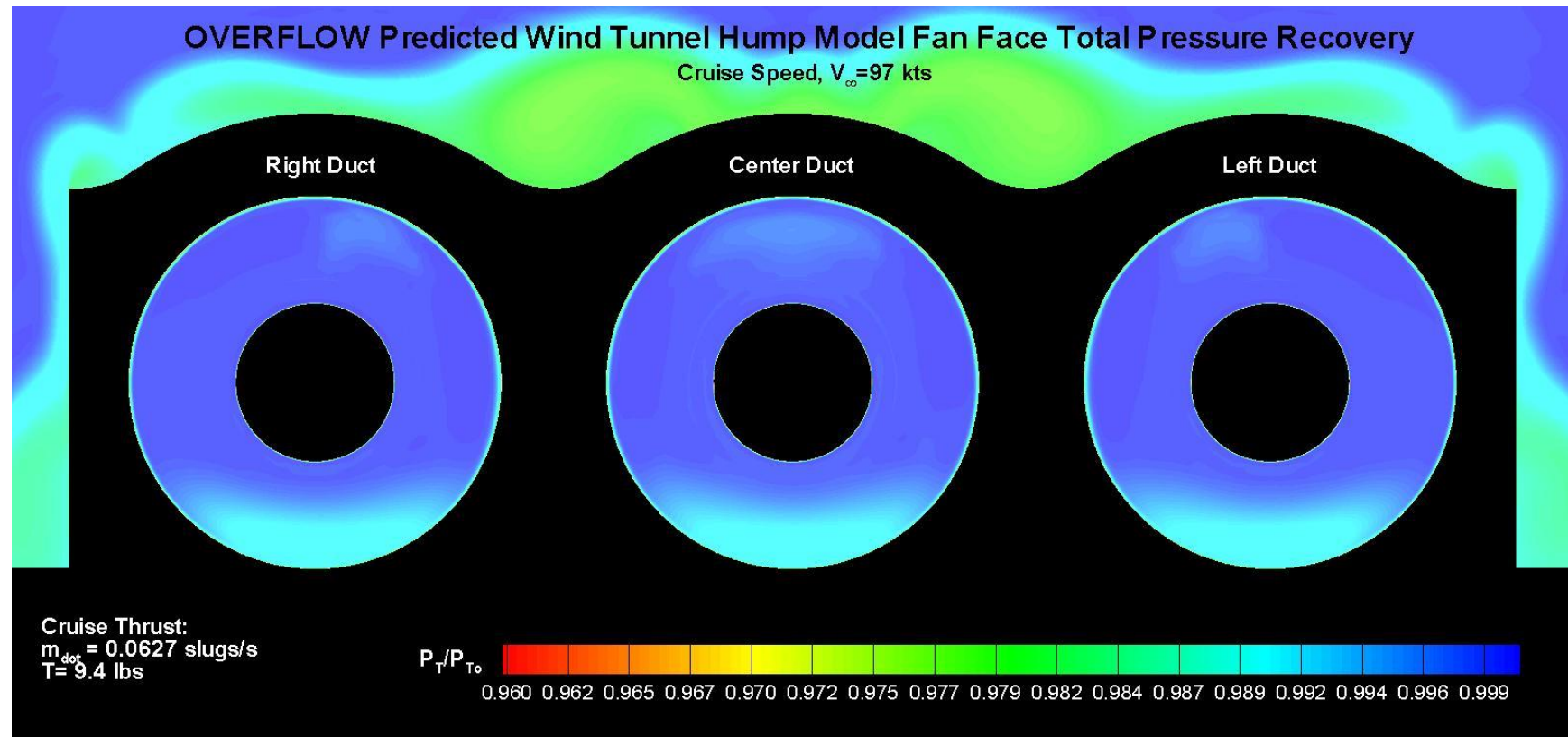
OVERFLOW Predicted Wind Tunnel Hump Model Duct Mach Contours
Vertical Cut Through Duct Centers, Cruise Speed, $V_\infty = 97$ kts

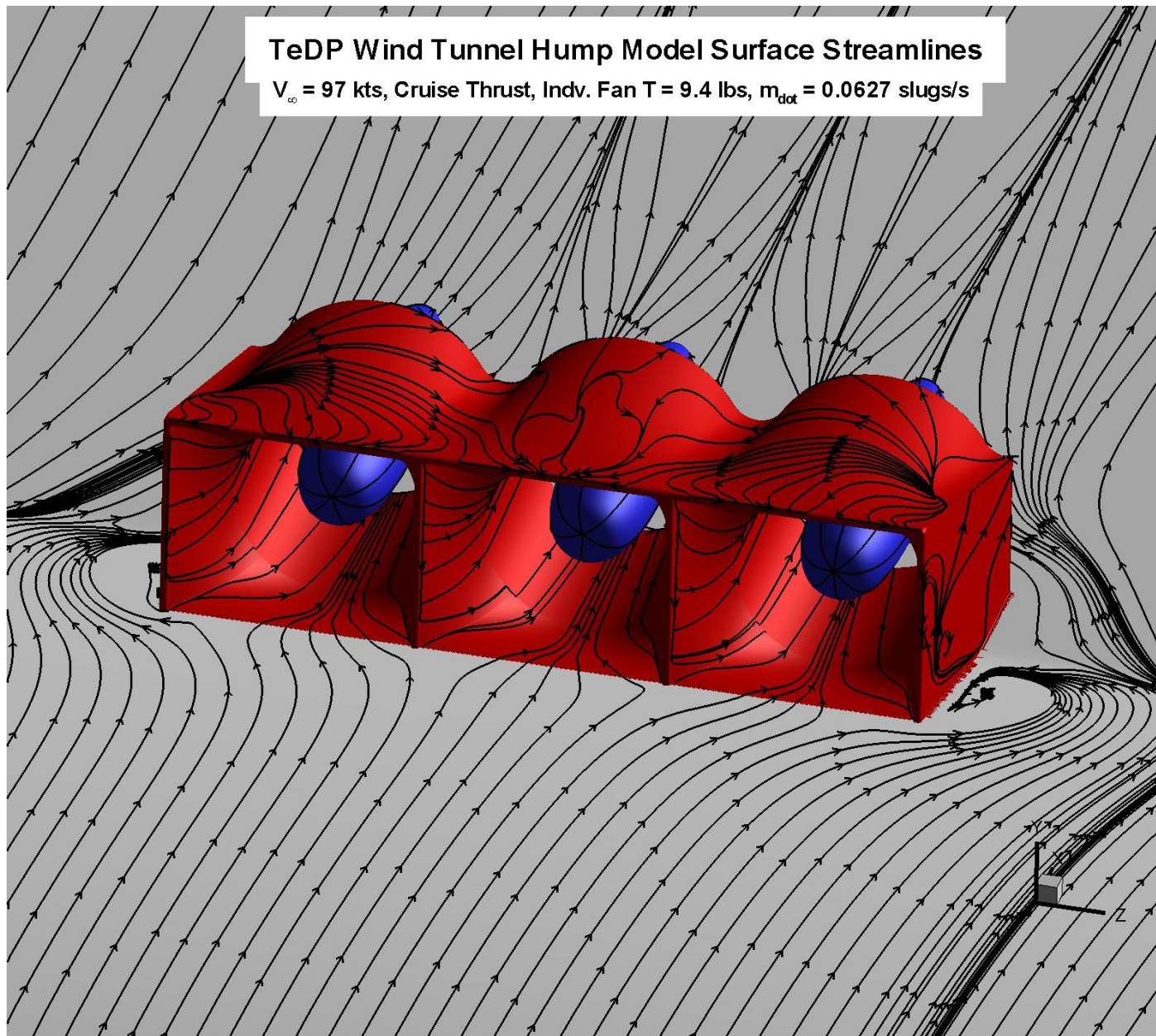


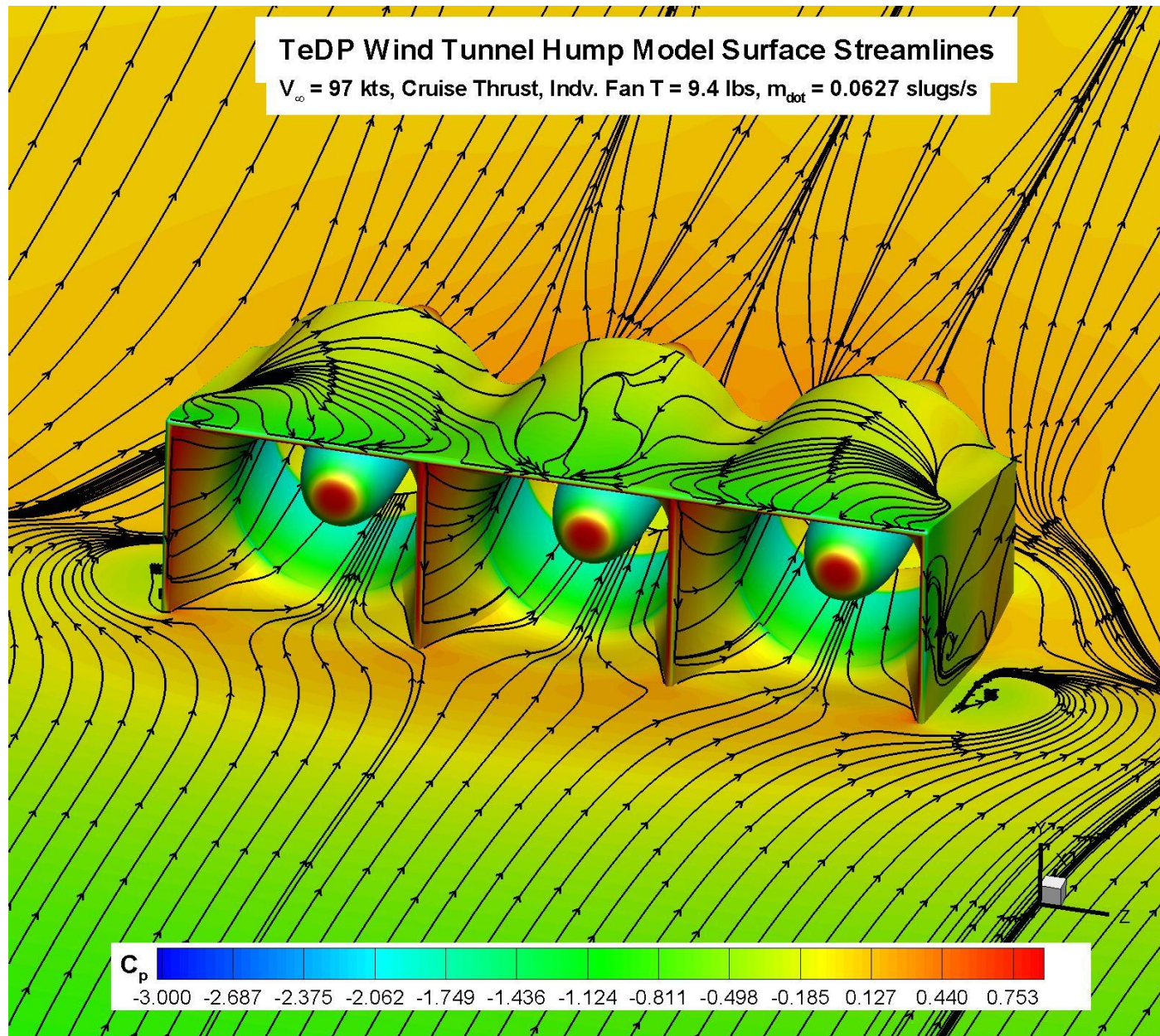
OVERFLOW Predicted Wind Tunnel Hump Model Center Duct Mach Contours
Vertical Cut Through Duct , Cruise Speed, $V_\infty = 97$ kts





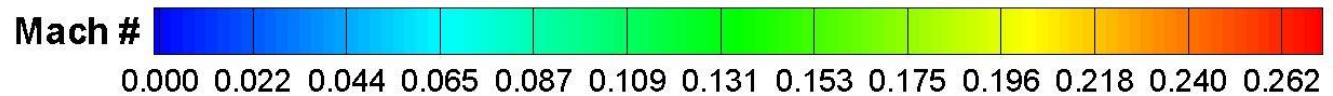
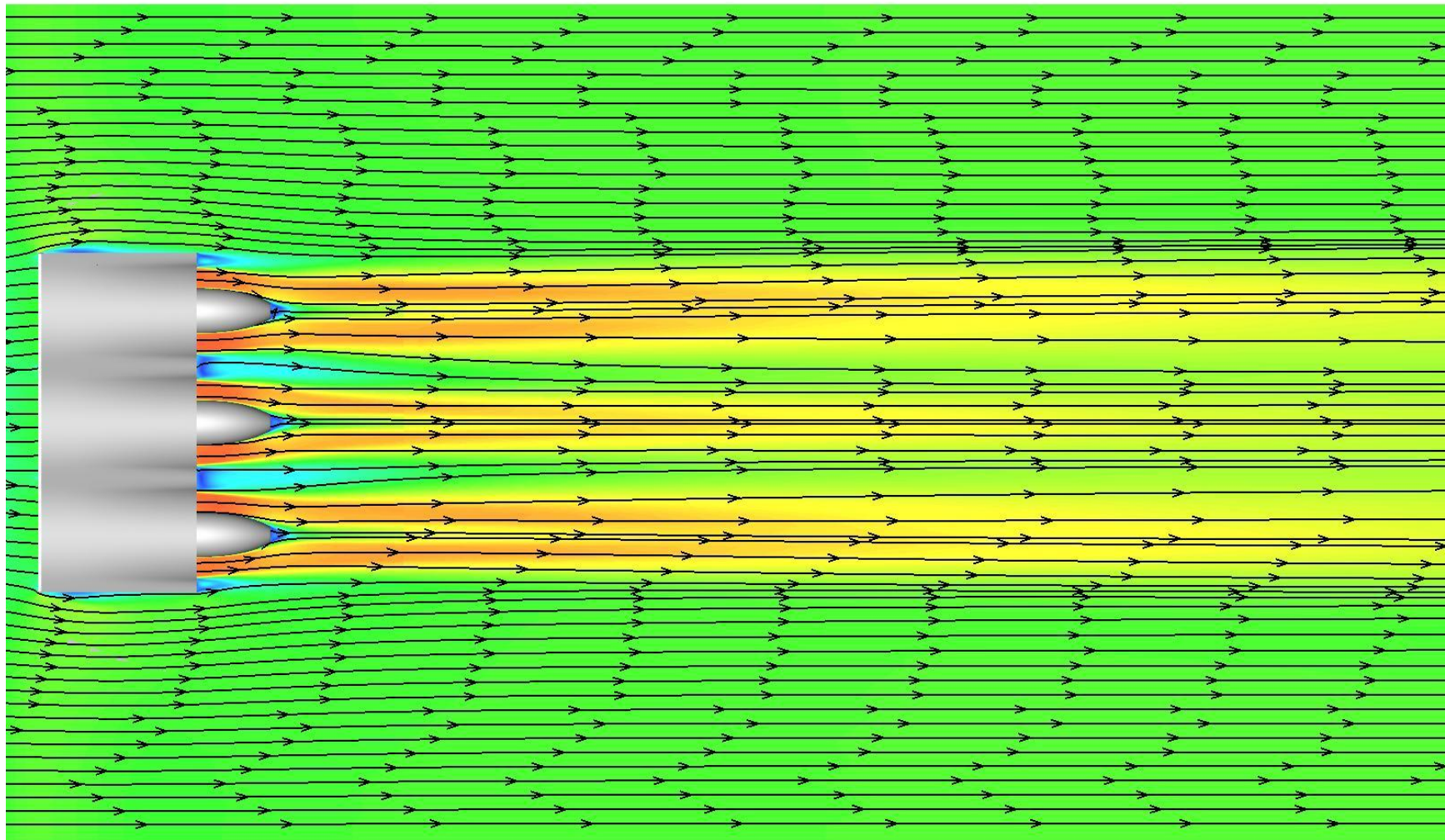






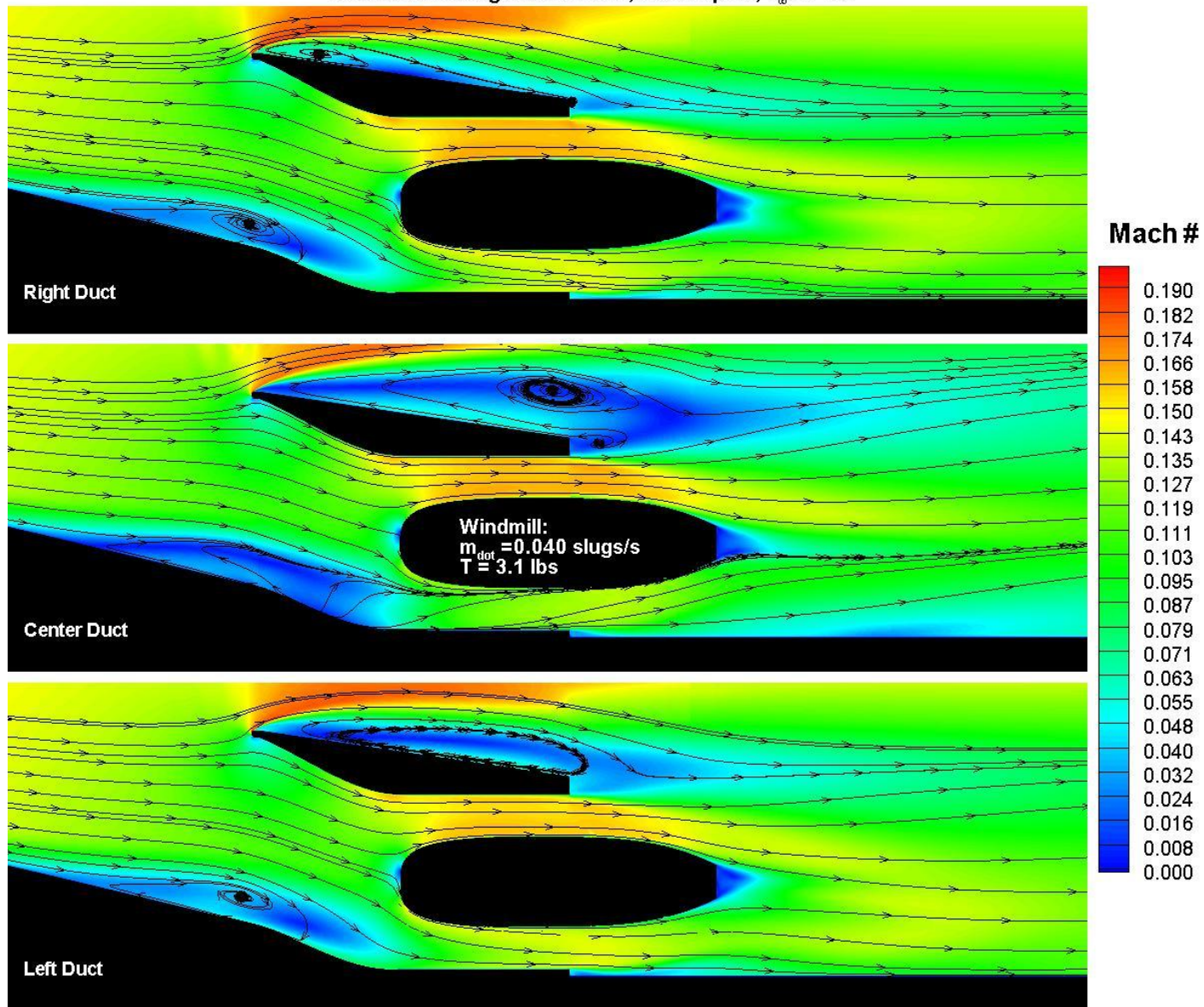
TeDP OVERFLOW Predicted Wind Tunnel Hump Mach Contours

Cut Plane = $y=2.72''$ (half duct height), Cruise Thrust, Indv. Duct $T=9.4$ lbs, $\dot{m}_{\text{dot}} = 0.0627$ slugs/s



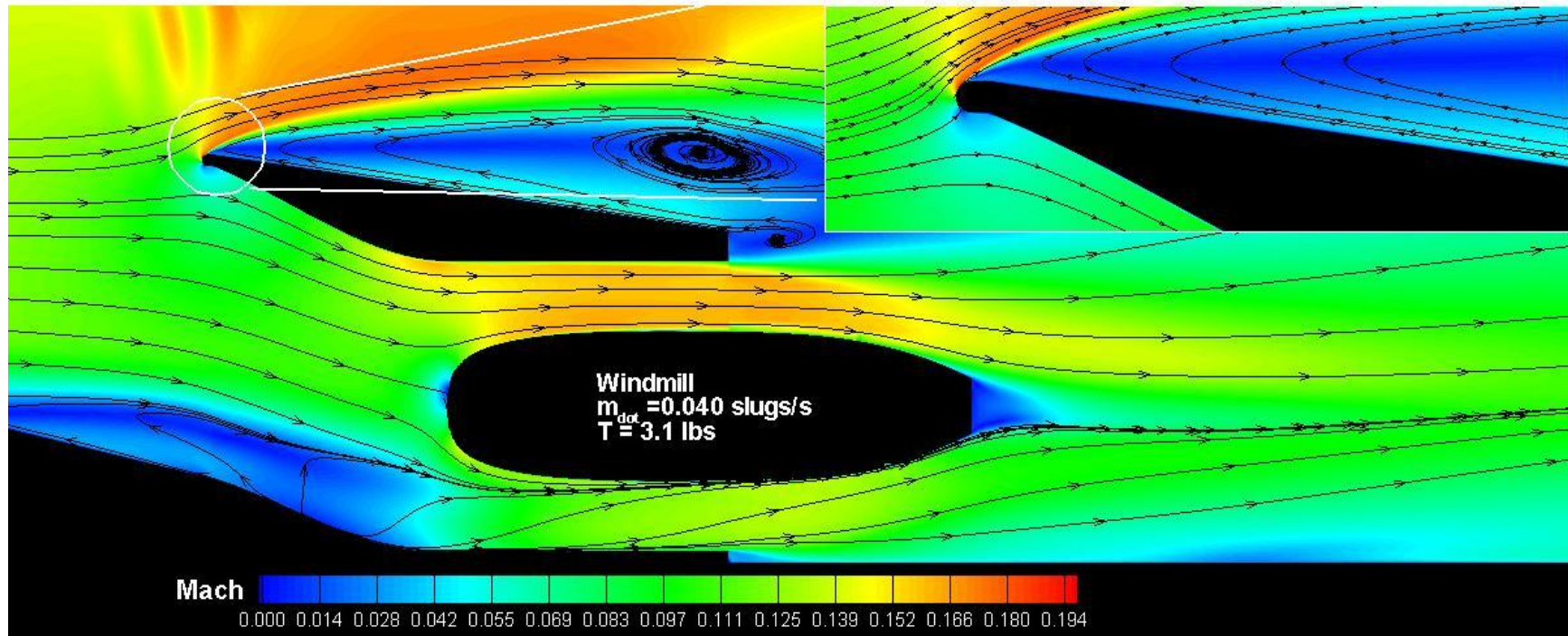
Windmill Case

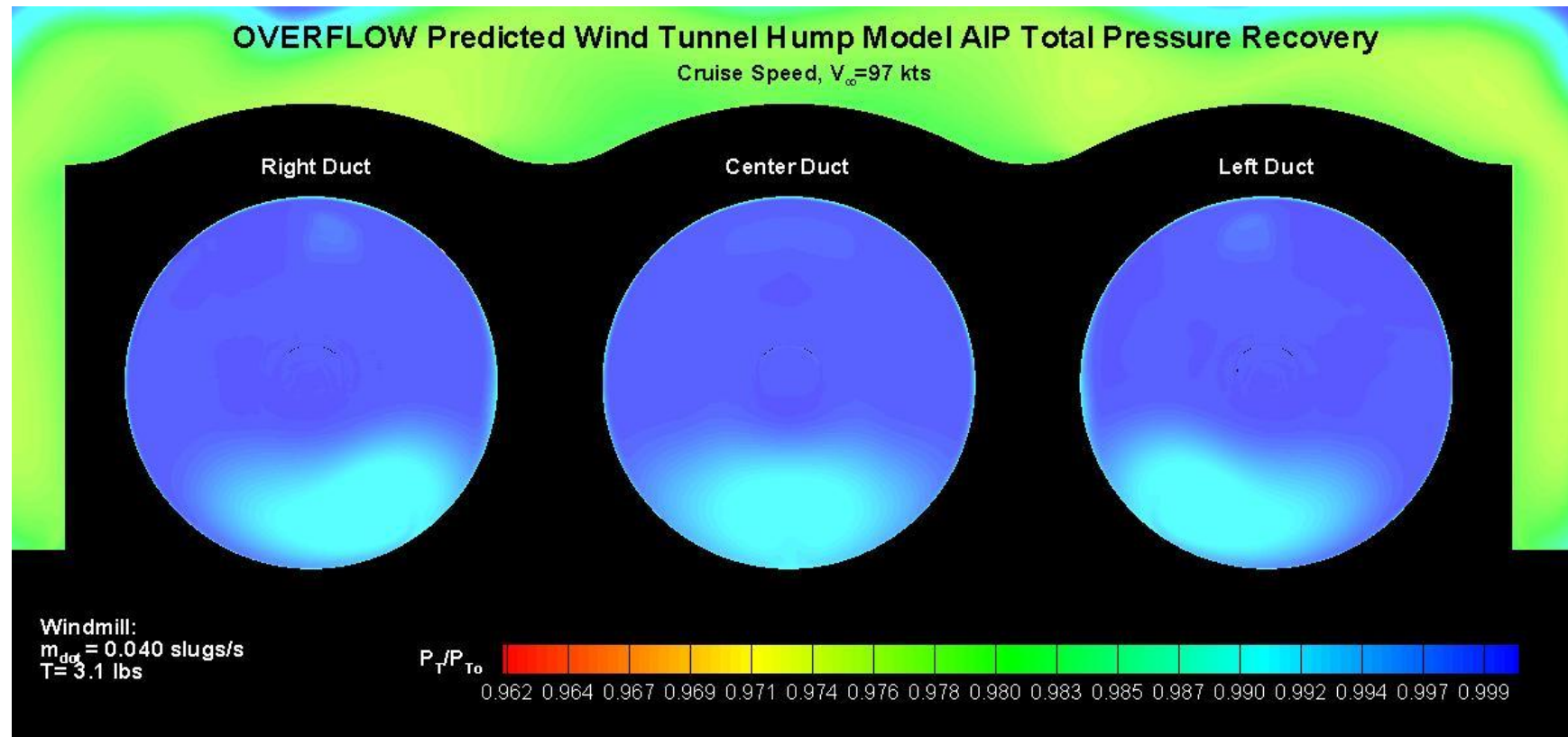
OVERFLOW Predicted Wind Tunnel Hump Model Duct Mach Contours
Vertical Cut Through Duct Centers, Cruise Speed, $V_\infty = 97$ kts

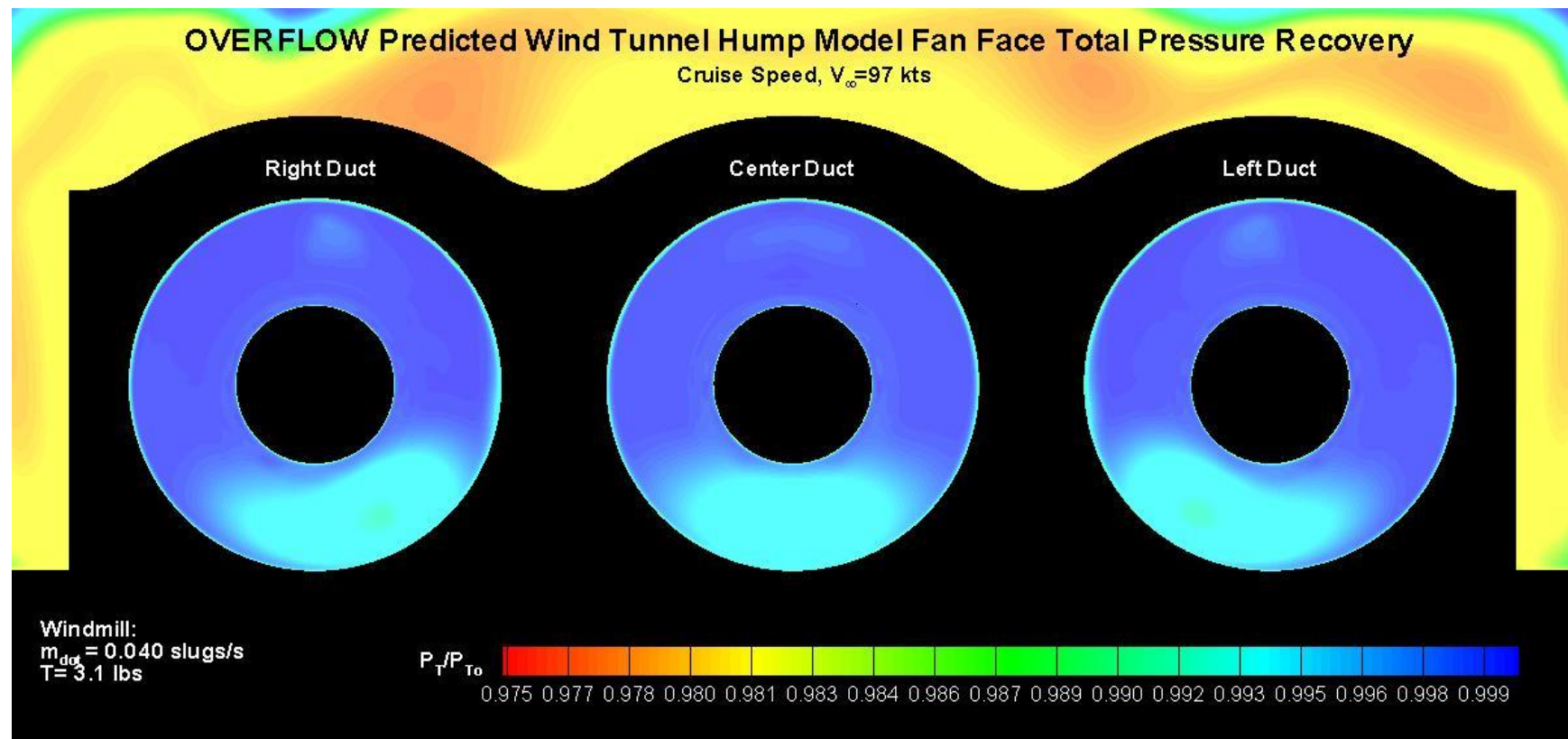


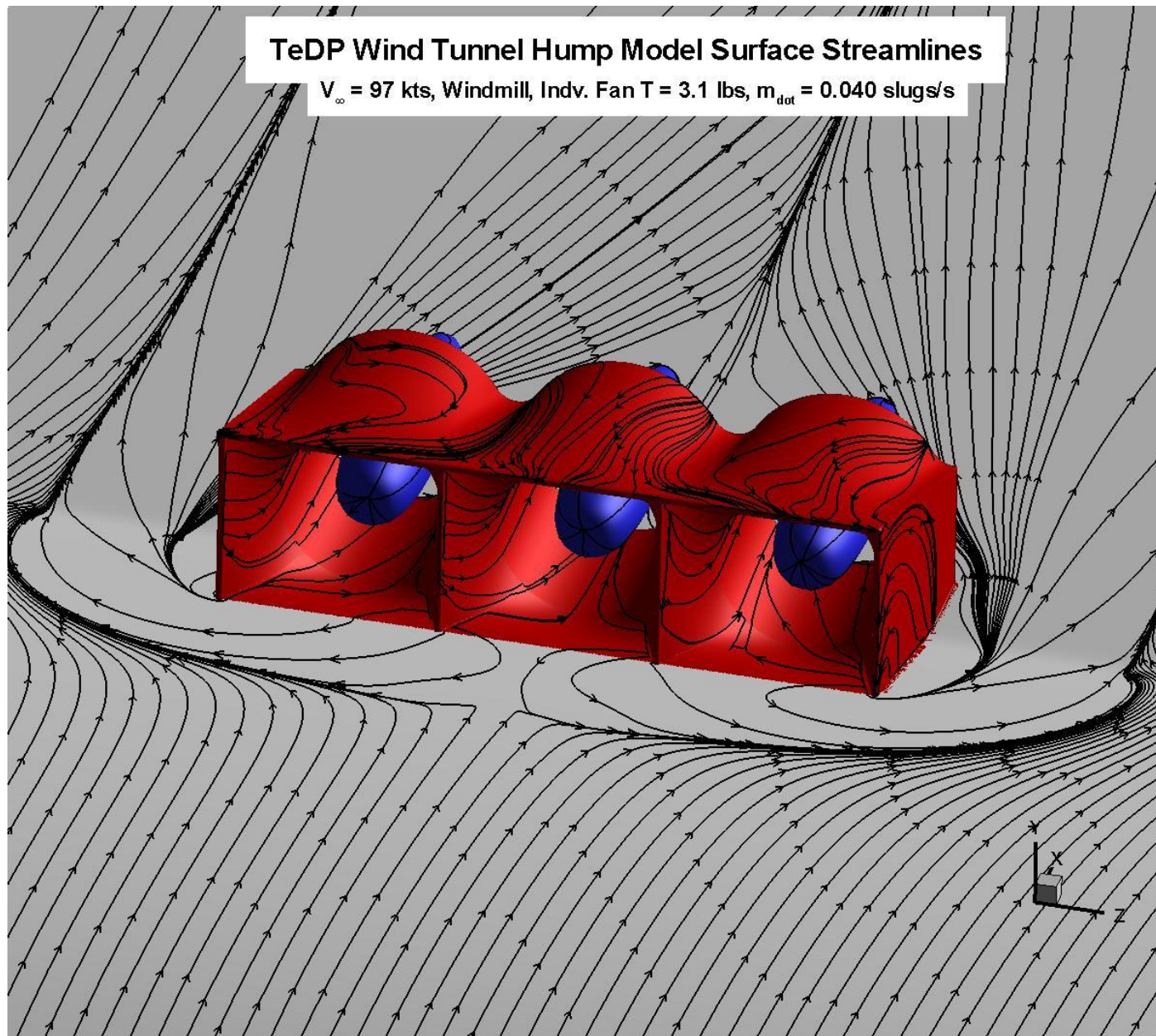
OVERFLOW Predicted Wind Tunnel Hump Model Center Duct Mach Contours

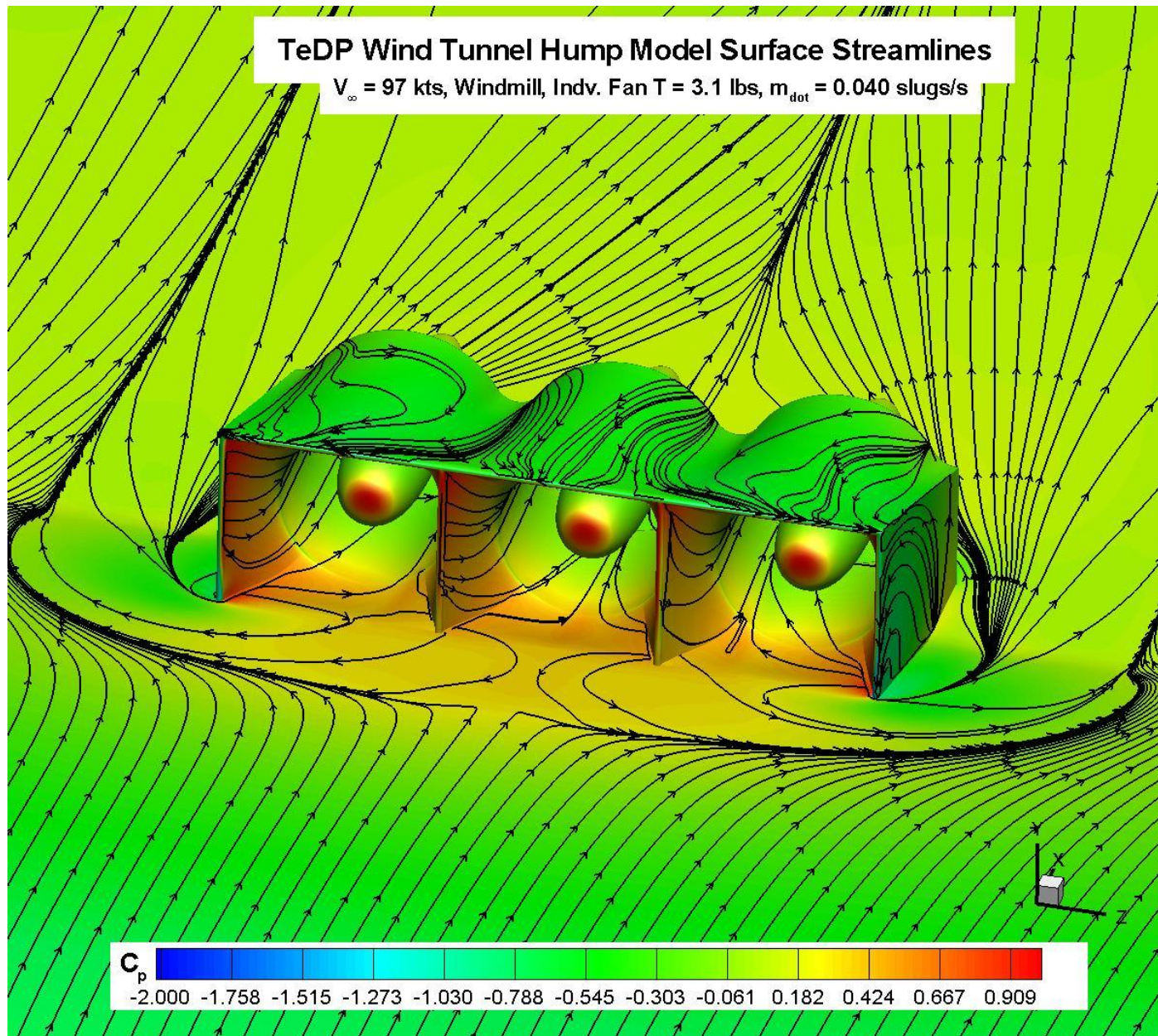
Vertical Cut Through Duct, Cruise Speed, $V_{\infty}=97$ kts





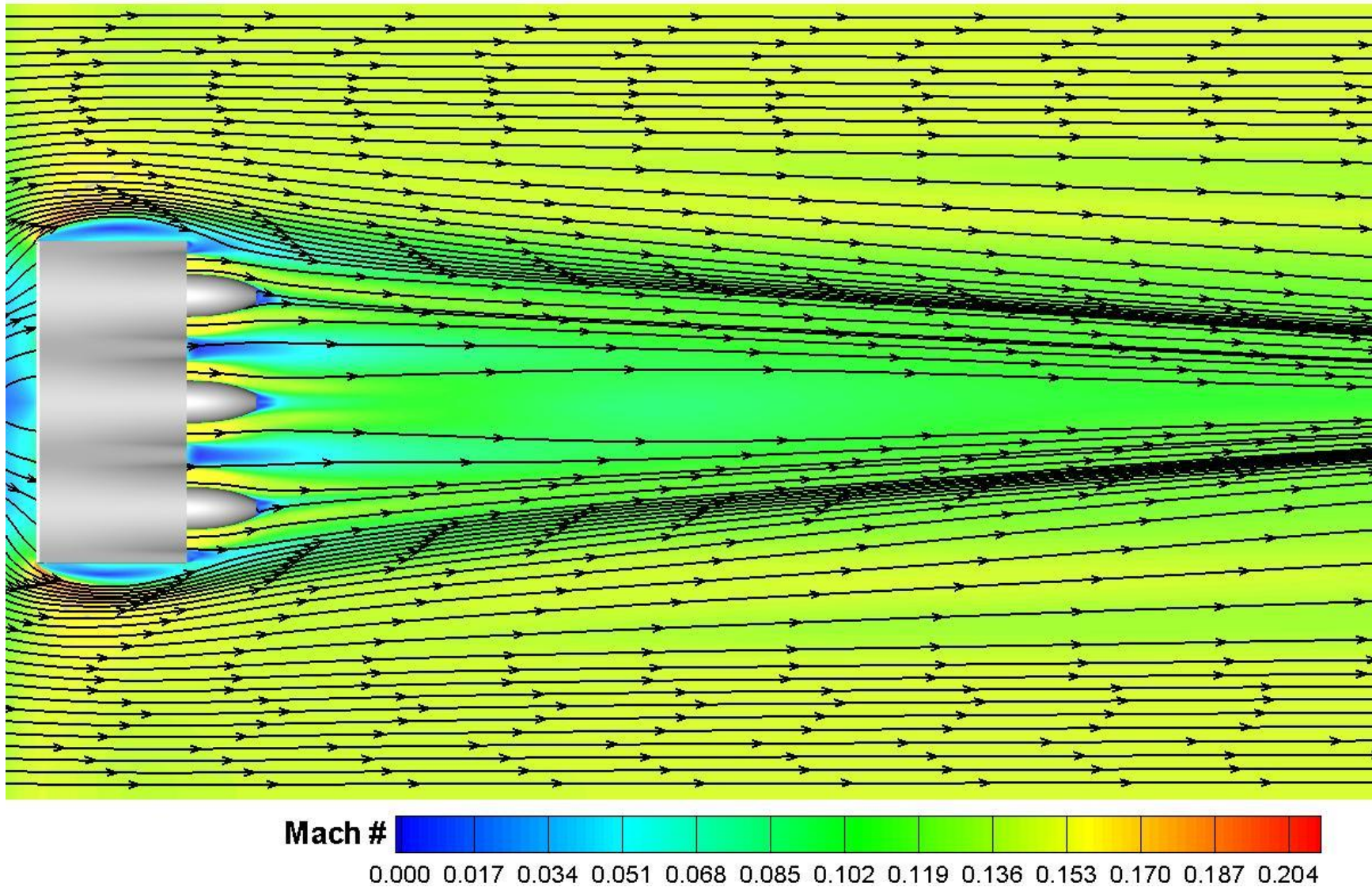






TeDP OVERFLOW Predicted Wind Tunnel Hump Mach Contours

Cut Plane = $y=2.72''$ (half duct height), Windmill, Indv. Duct $T=3.1$ lbs, $\dot{m}_{dot} = 0.040$ slugs/s

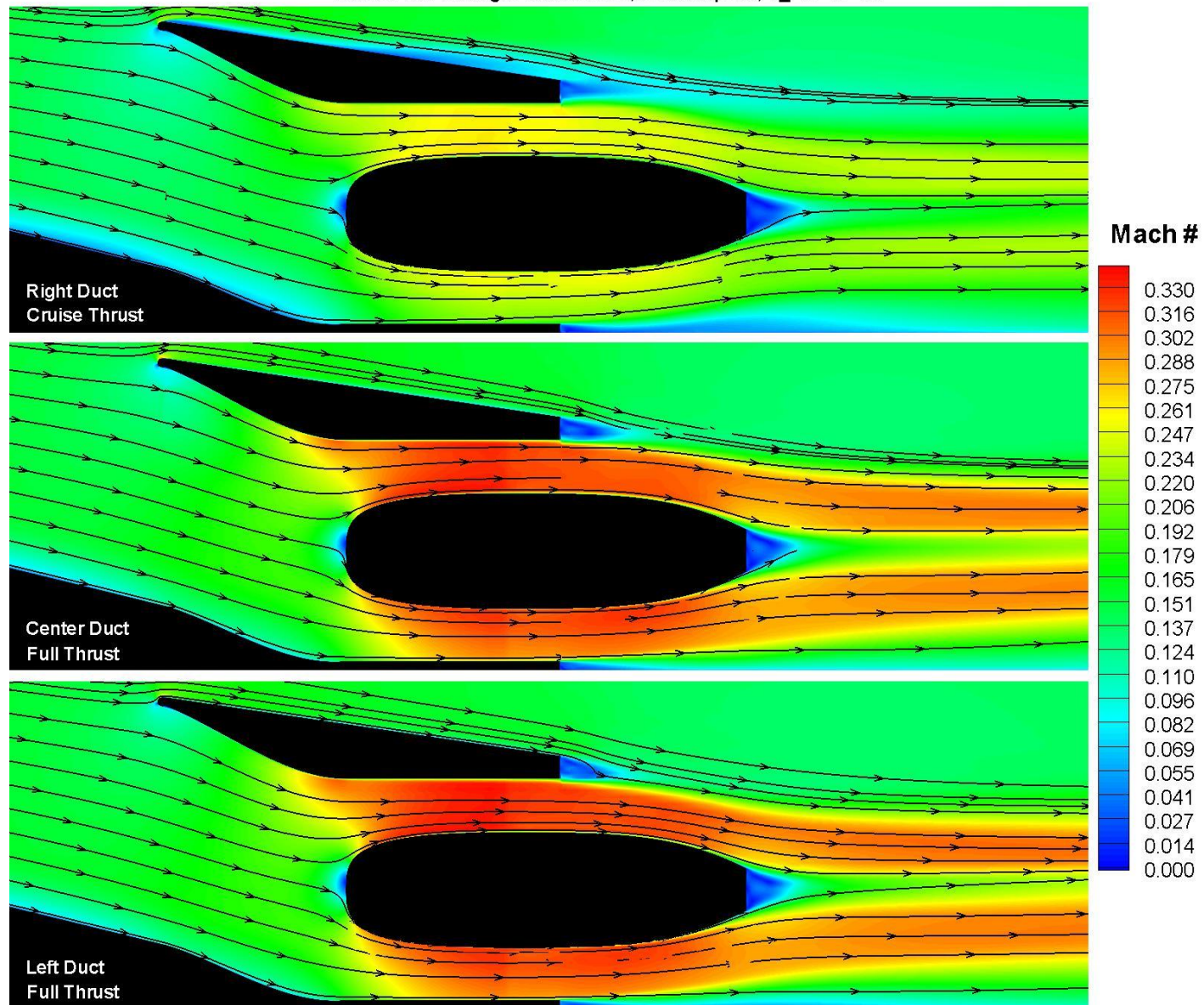


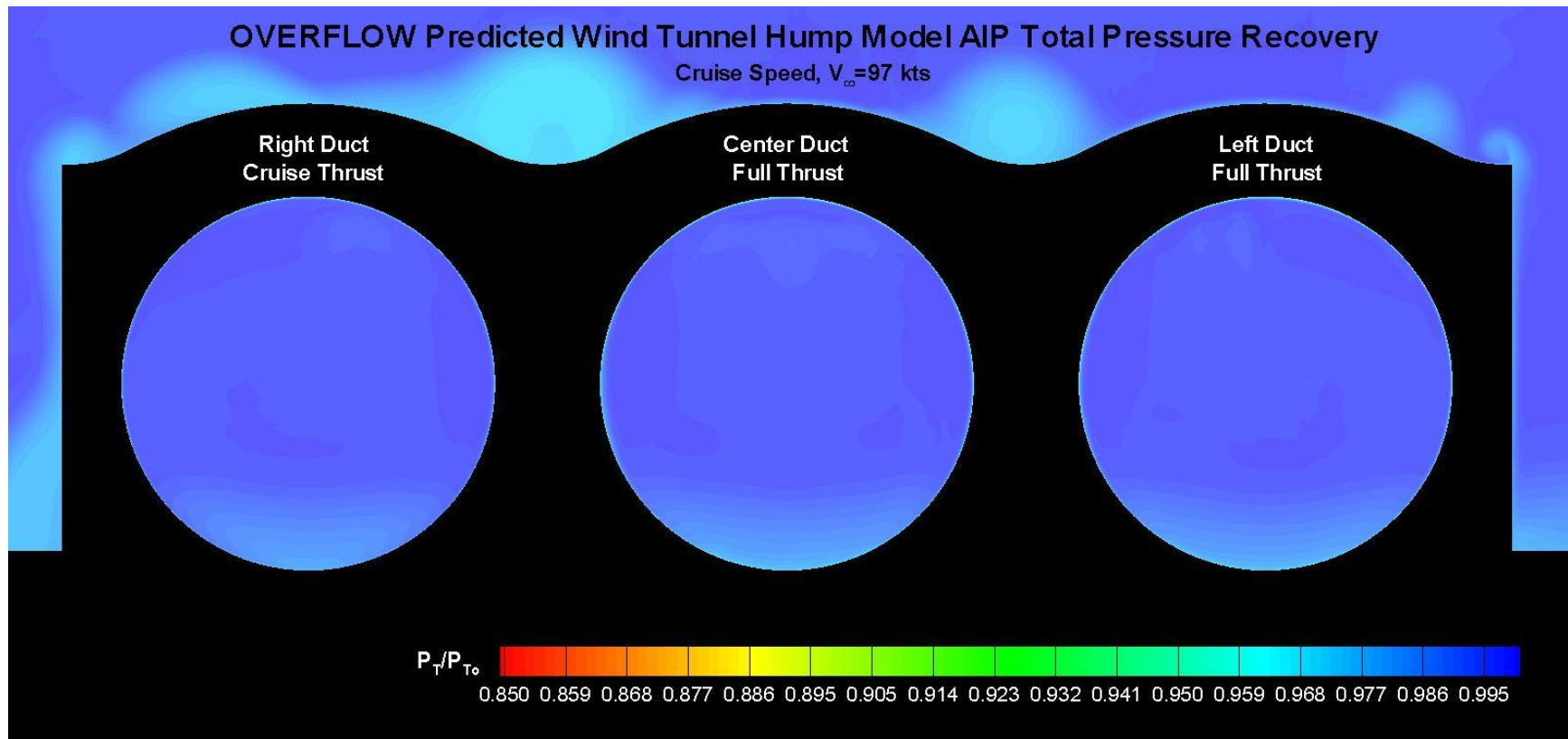
10 APPENDIX # 2

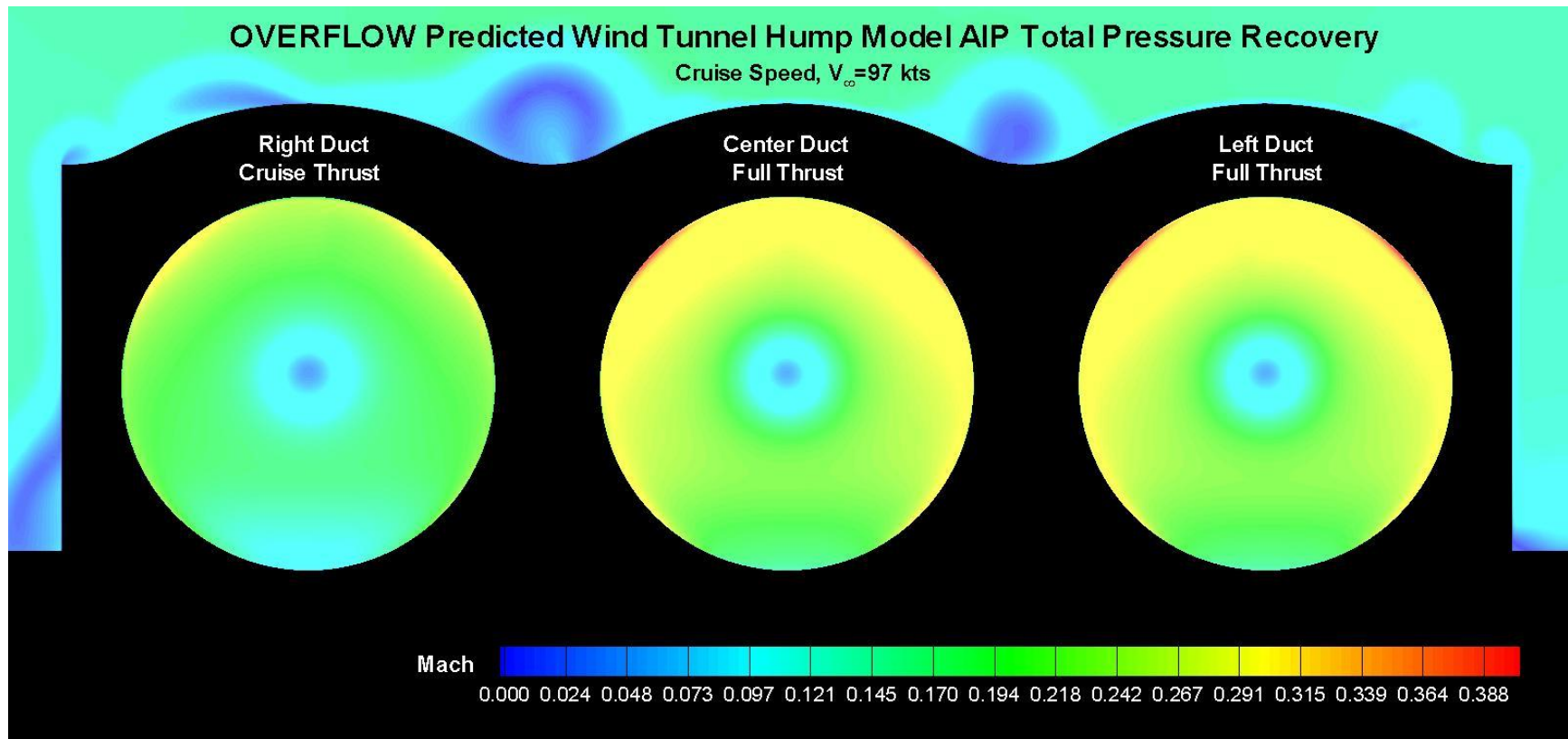
Differential Thrust CFD Plot Summary

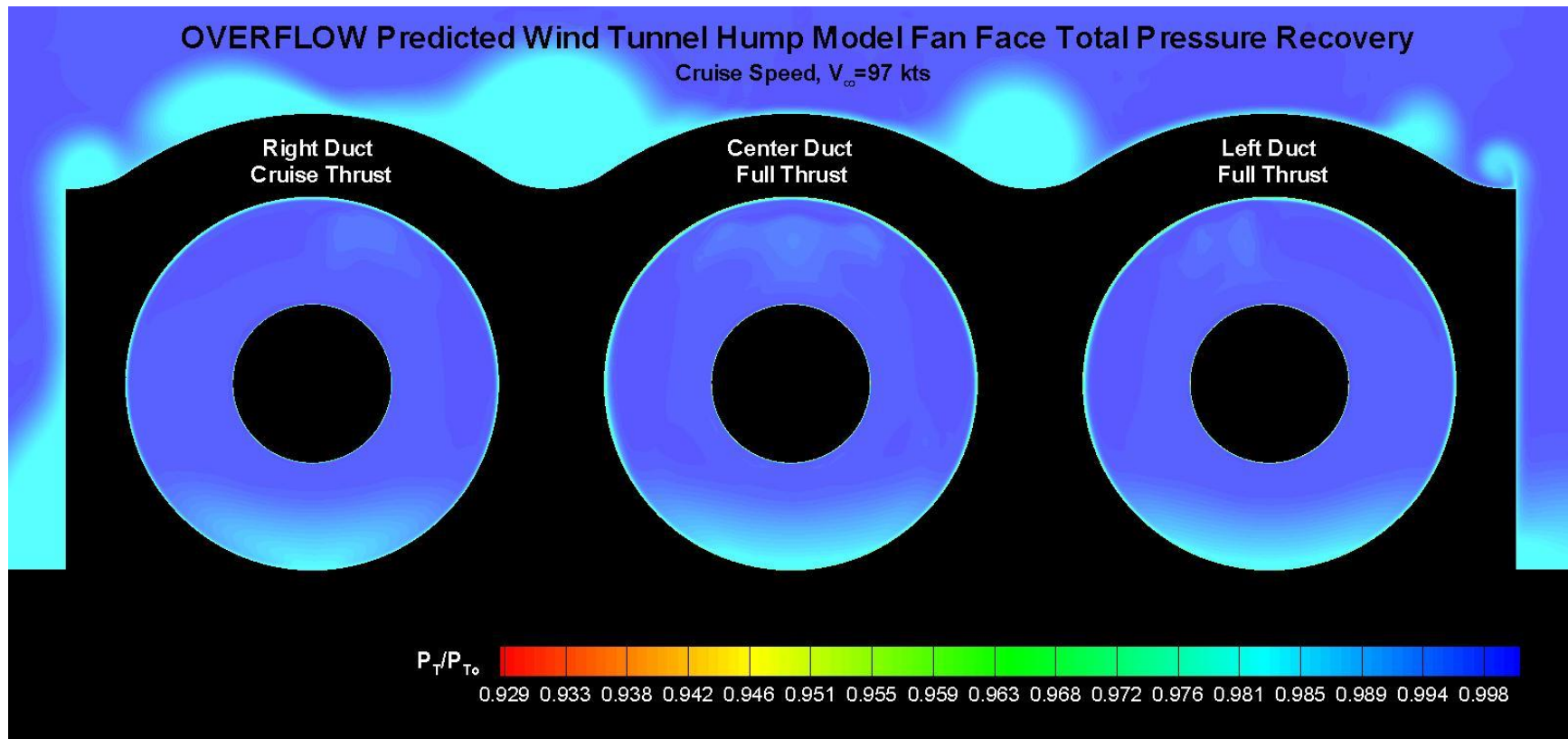
50% 100% 100% Different Differential Thrust Case Thrust Case

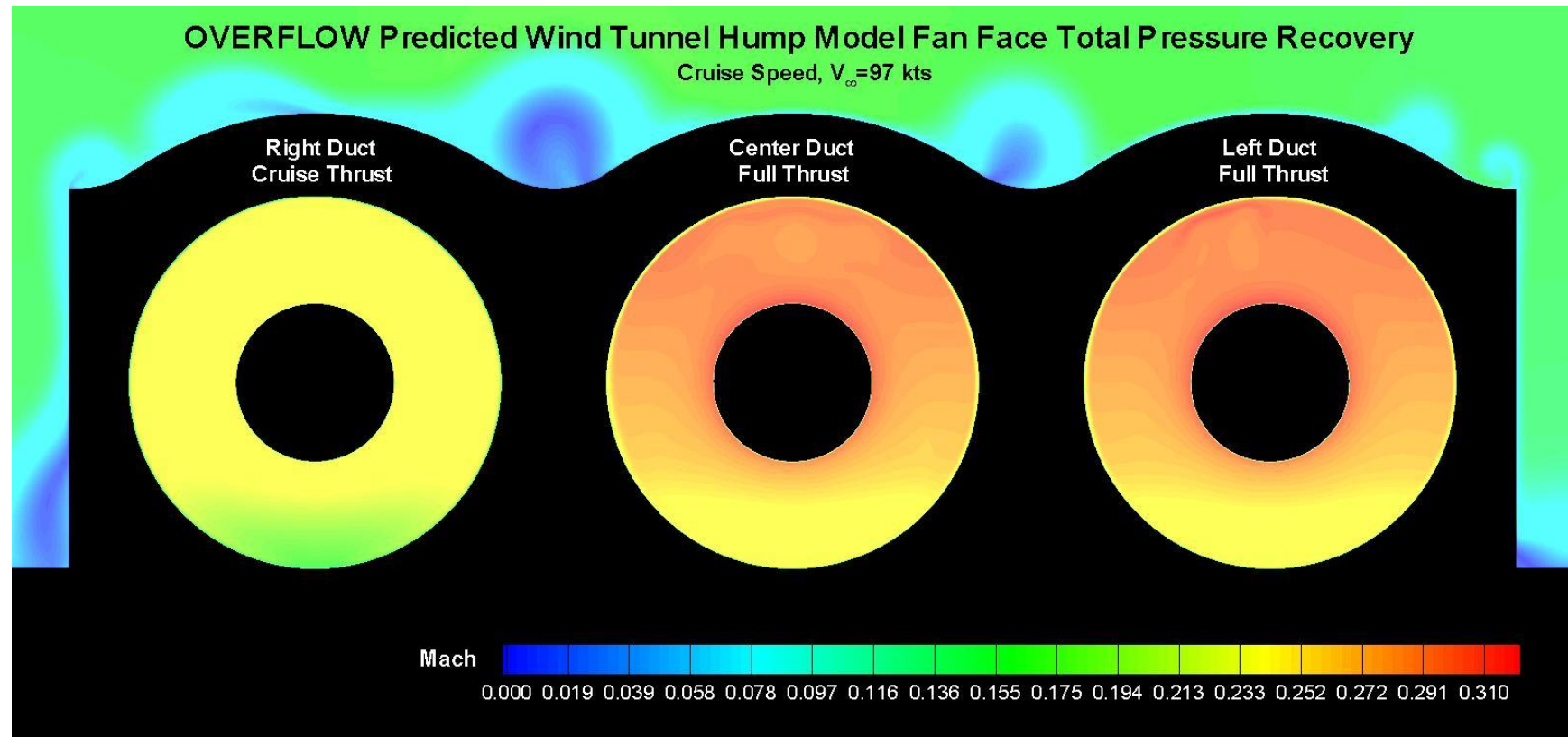
OVERFLOW Predicted Wind Tunnel Hump Model Differential ThrustDuct Mach Contours
Vertical Cut Through Duct Centers, Cruise Speed, $V_{\infty} = 97$ kts

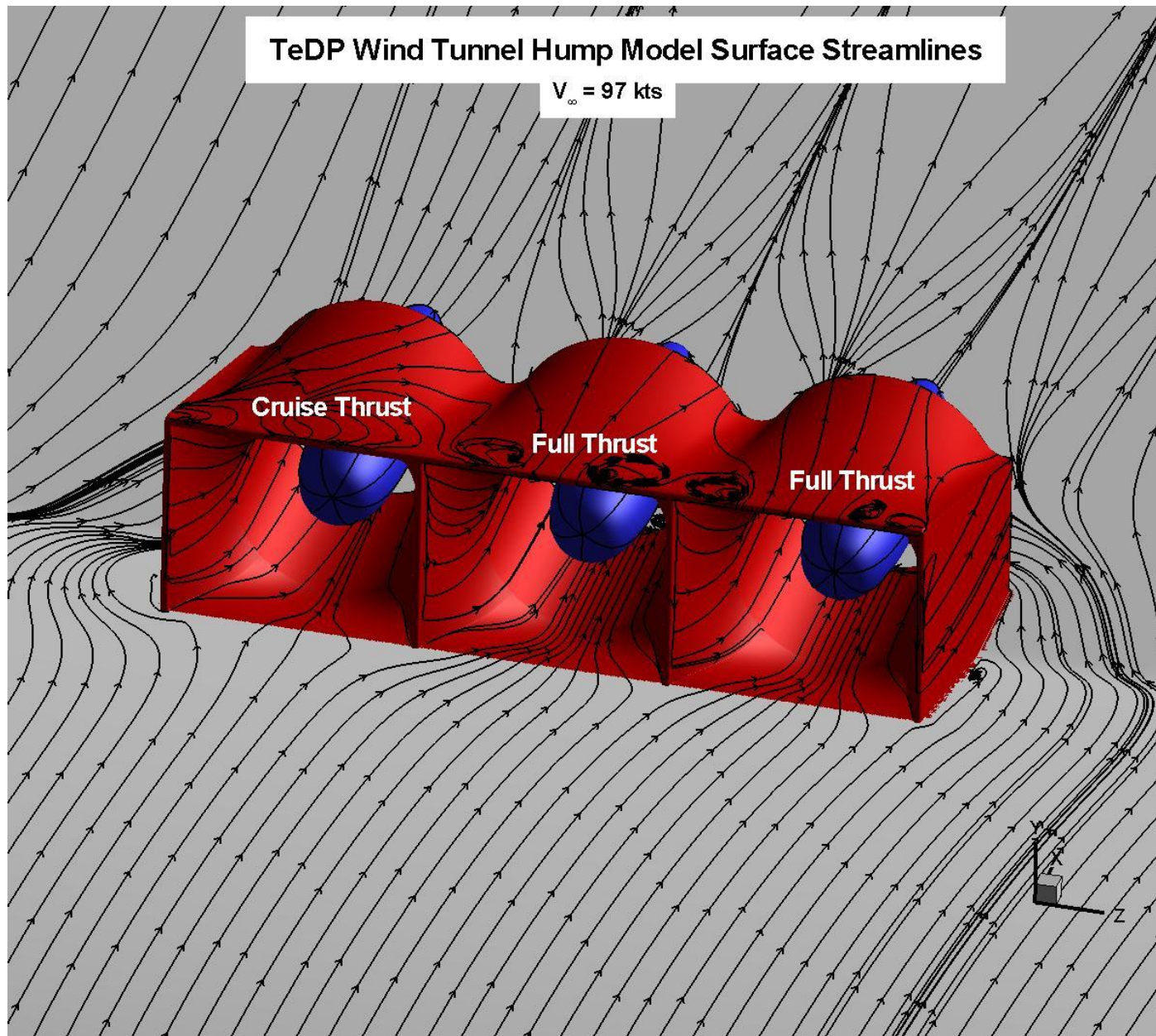


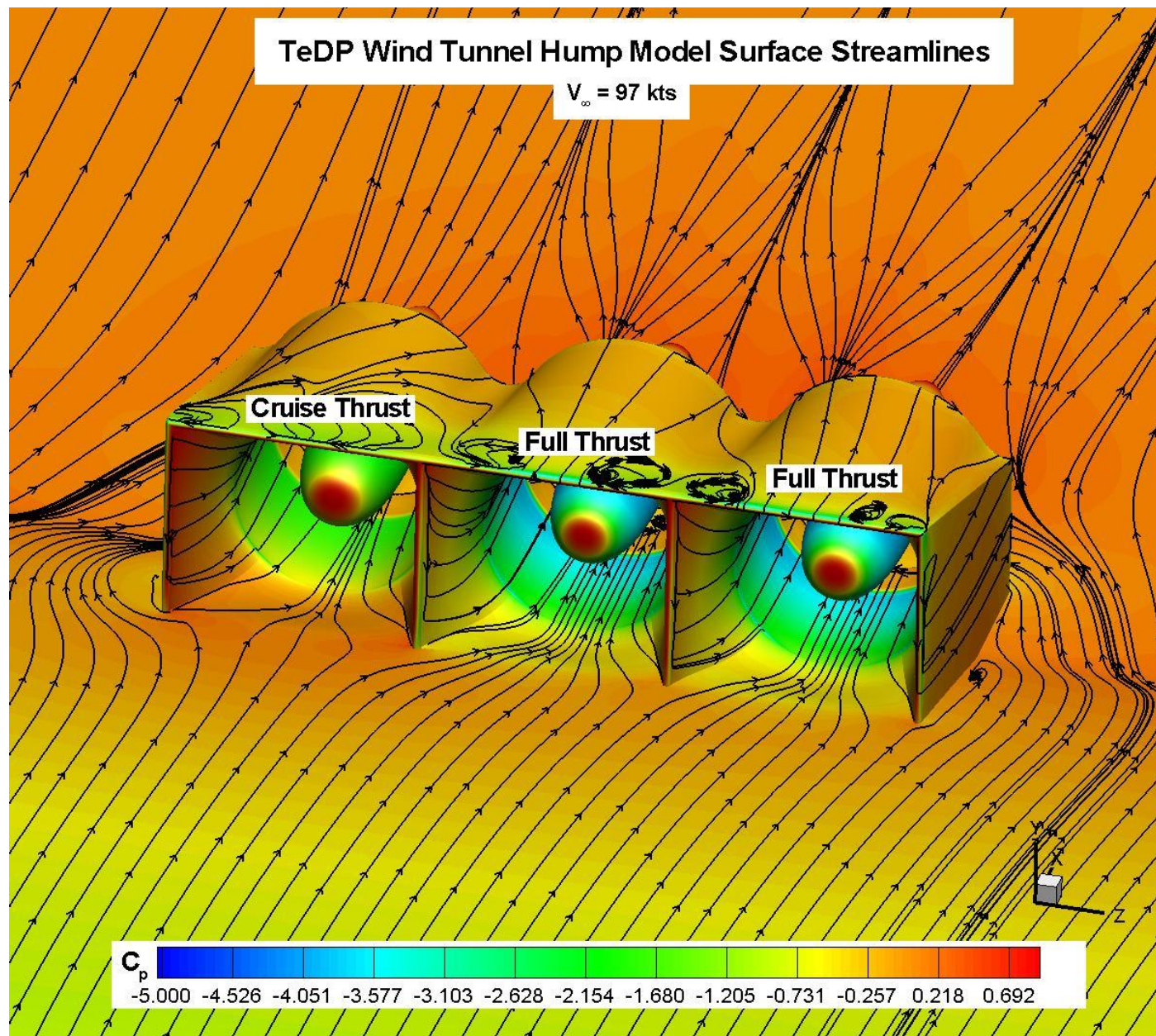






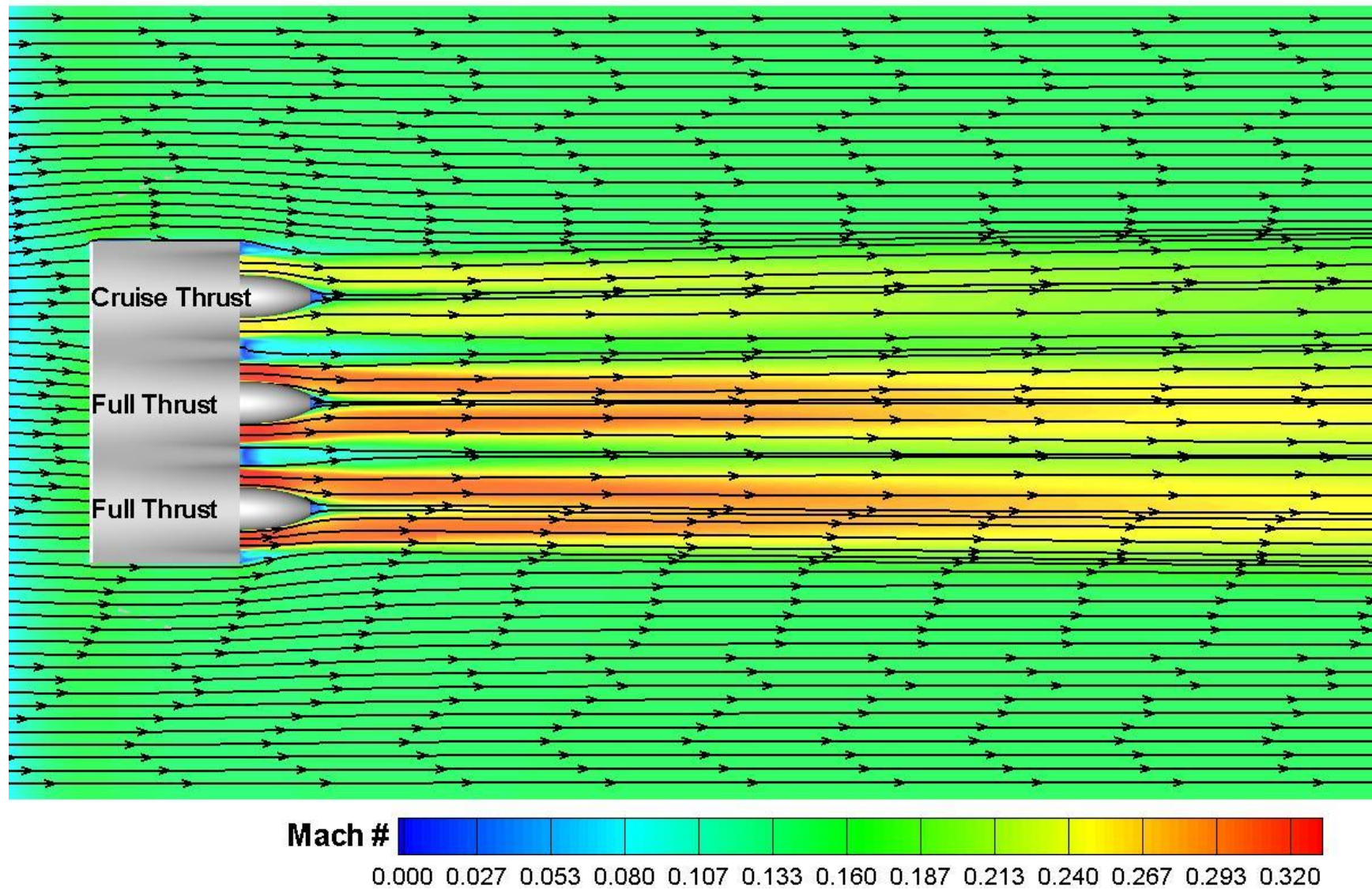






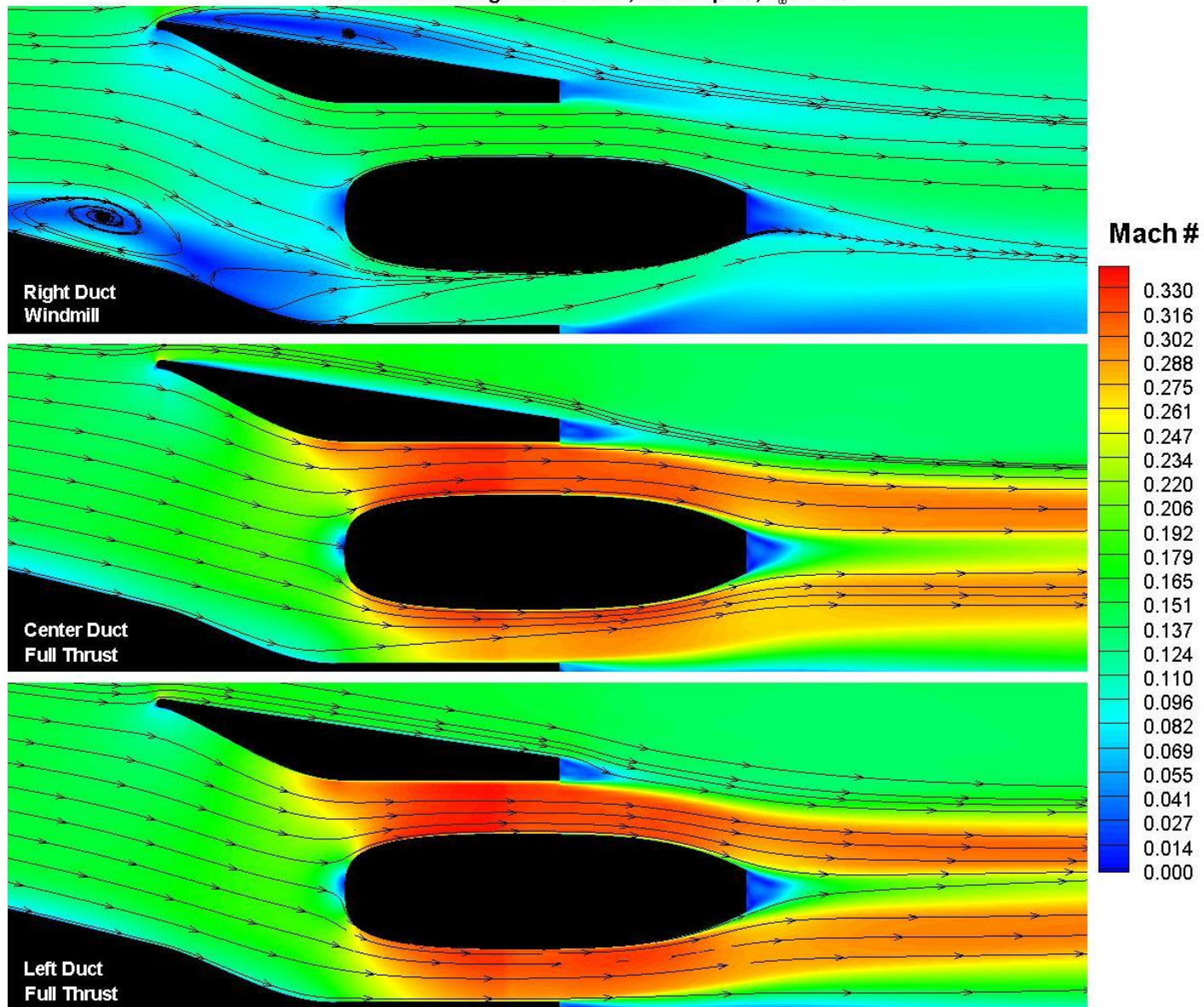
TeDP OVERFLOW Predicted Wind Tunnel Hump Mach Contours

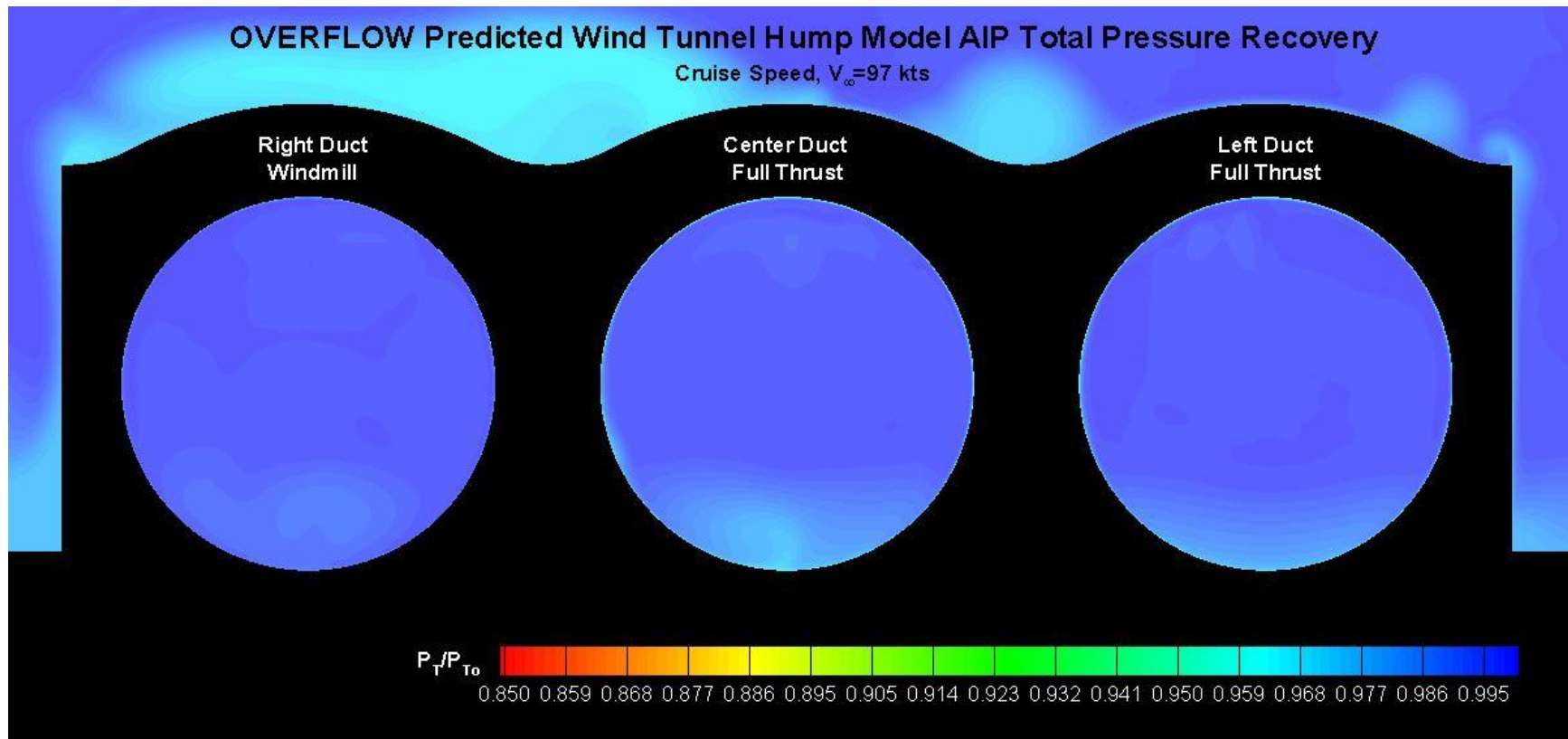
Cut Plane = $y=2.72''$ (half duct height)

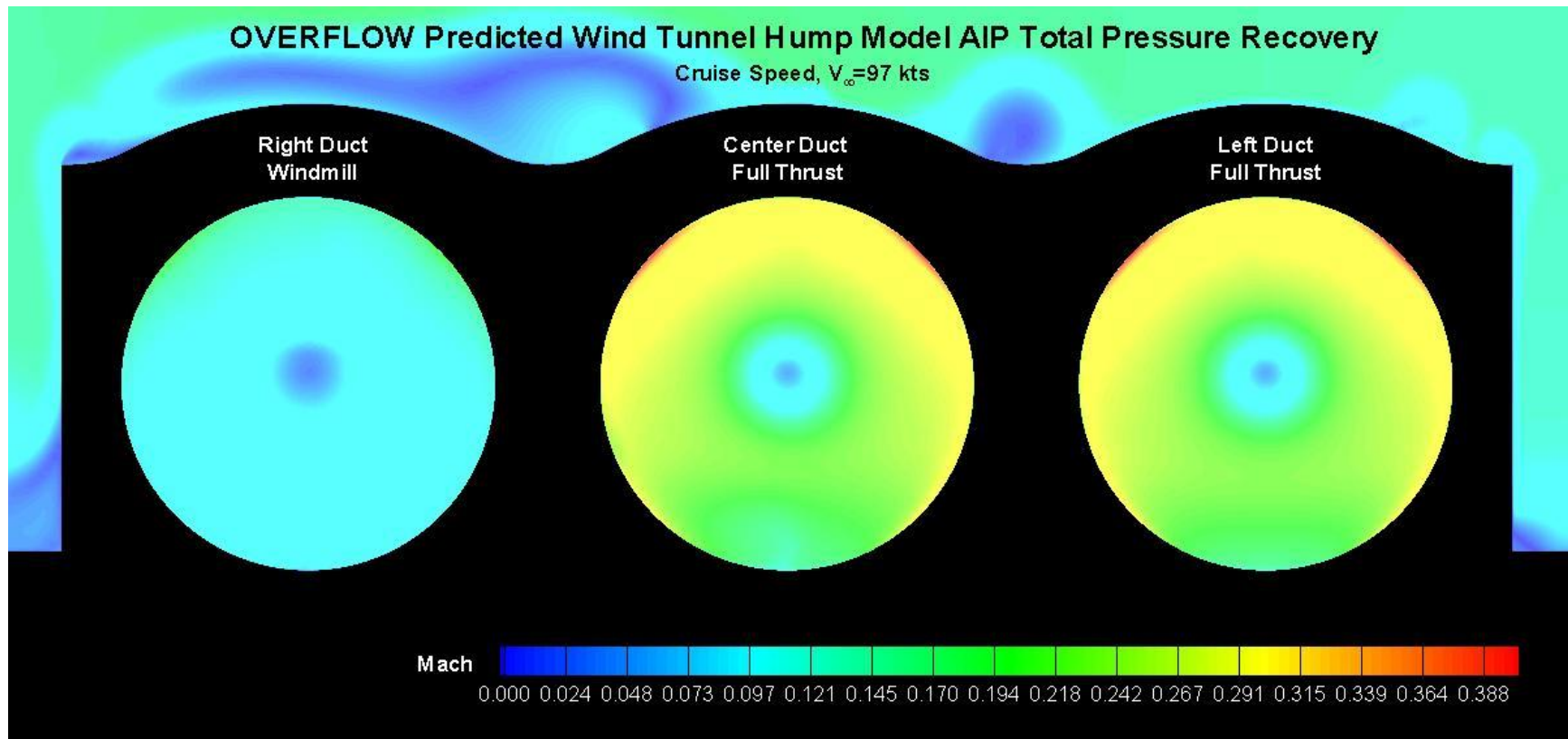


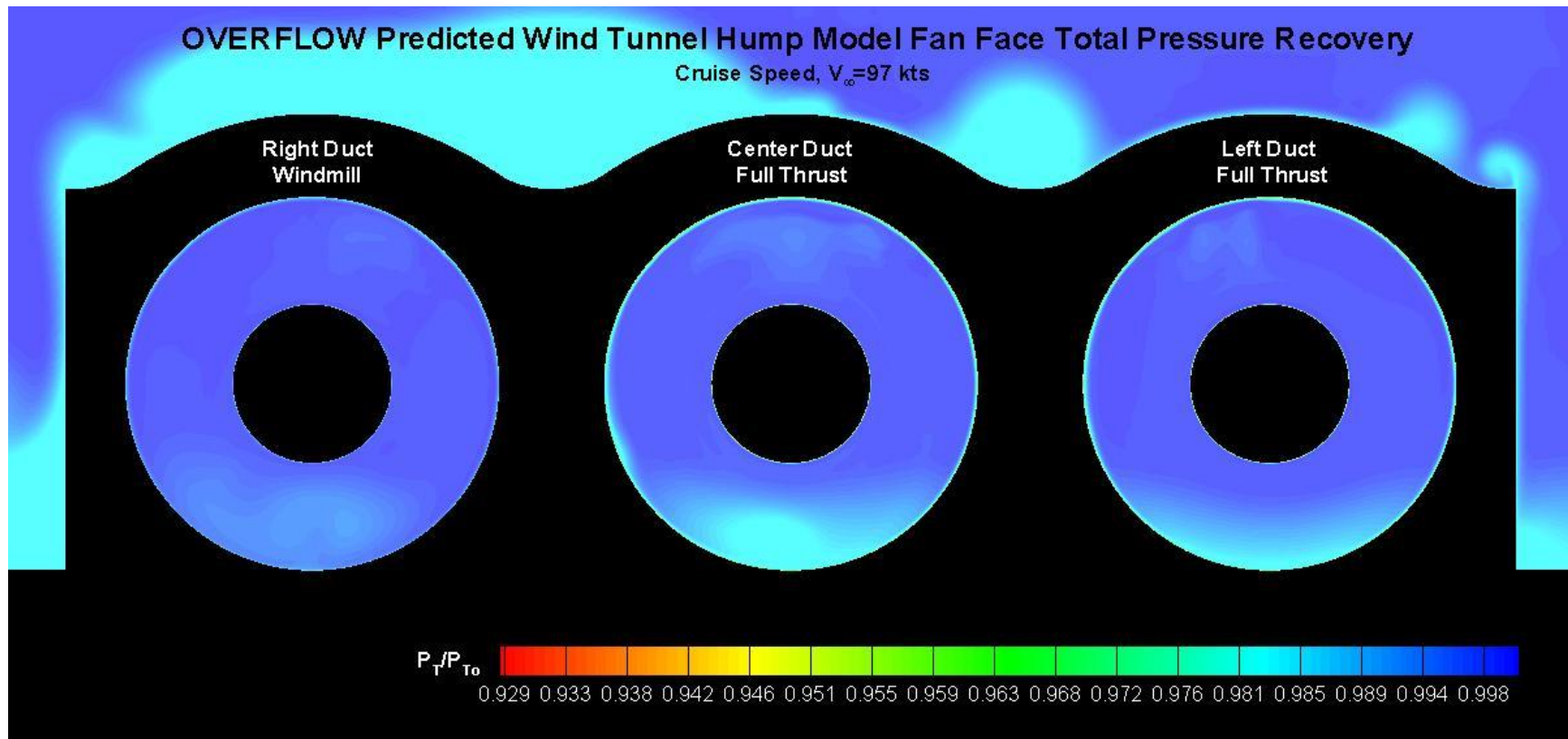
0% 100% 100% Different Differential Thrust Case Thrust Case

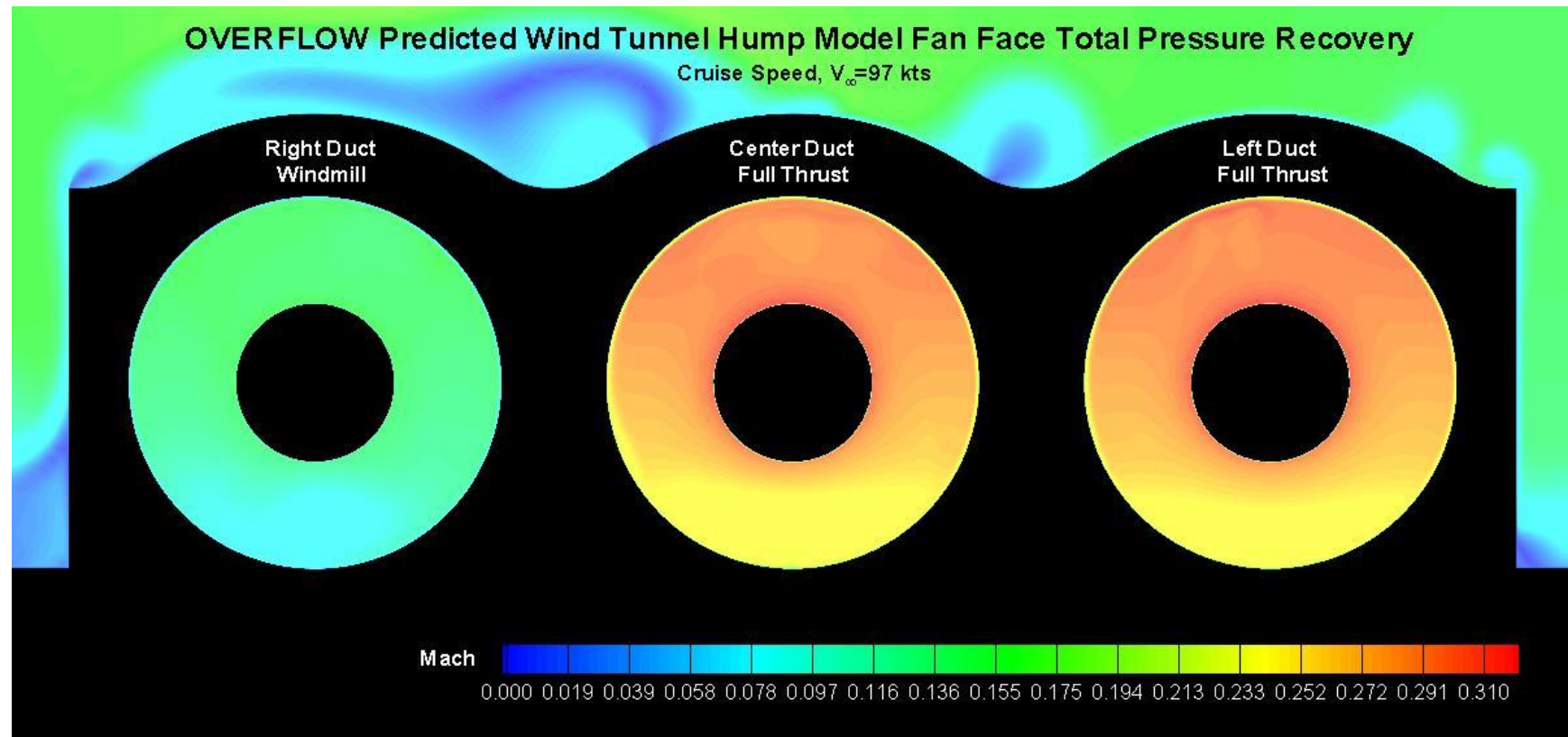
OVERFLOW Predicted Wind Tunnel Hump Model Differential ThrustDuct Mach Contours
Vertical Cut Through Duct Centers, Cruise Speed, $V_{\infty} = 97$ kts

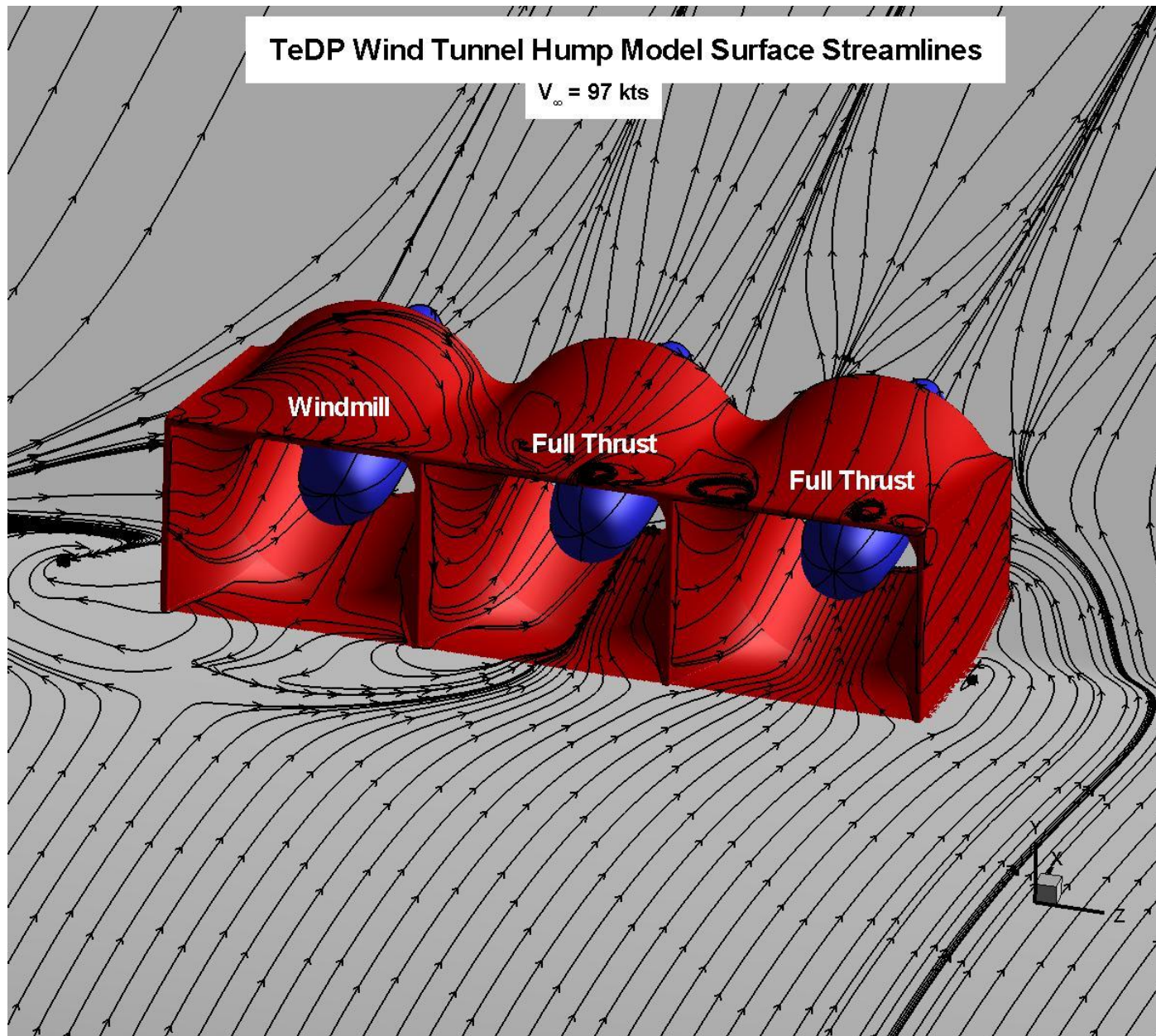


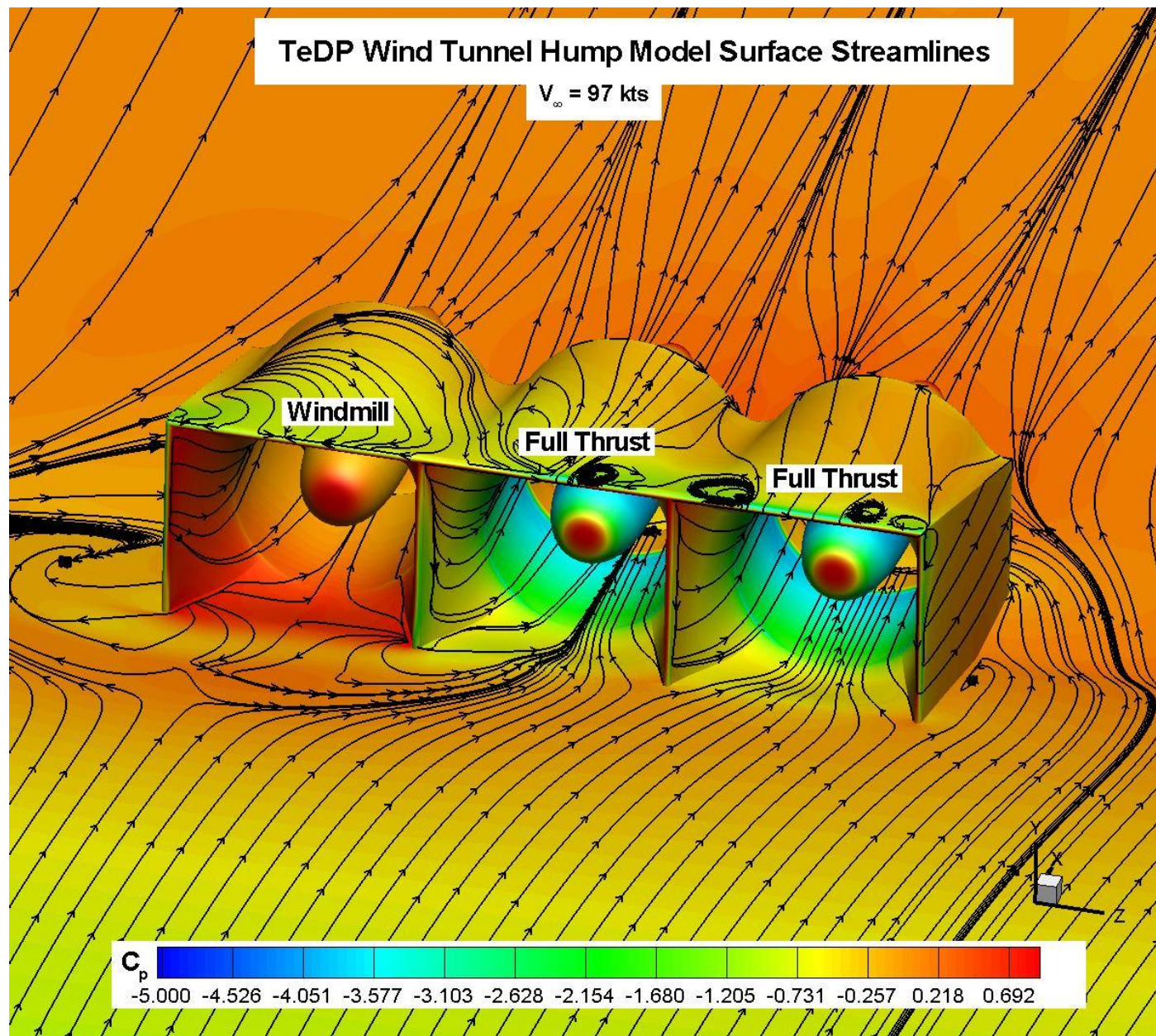






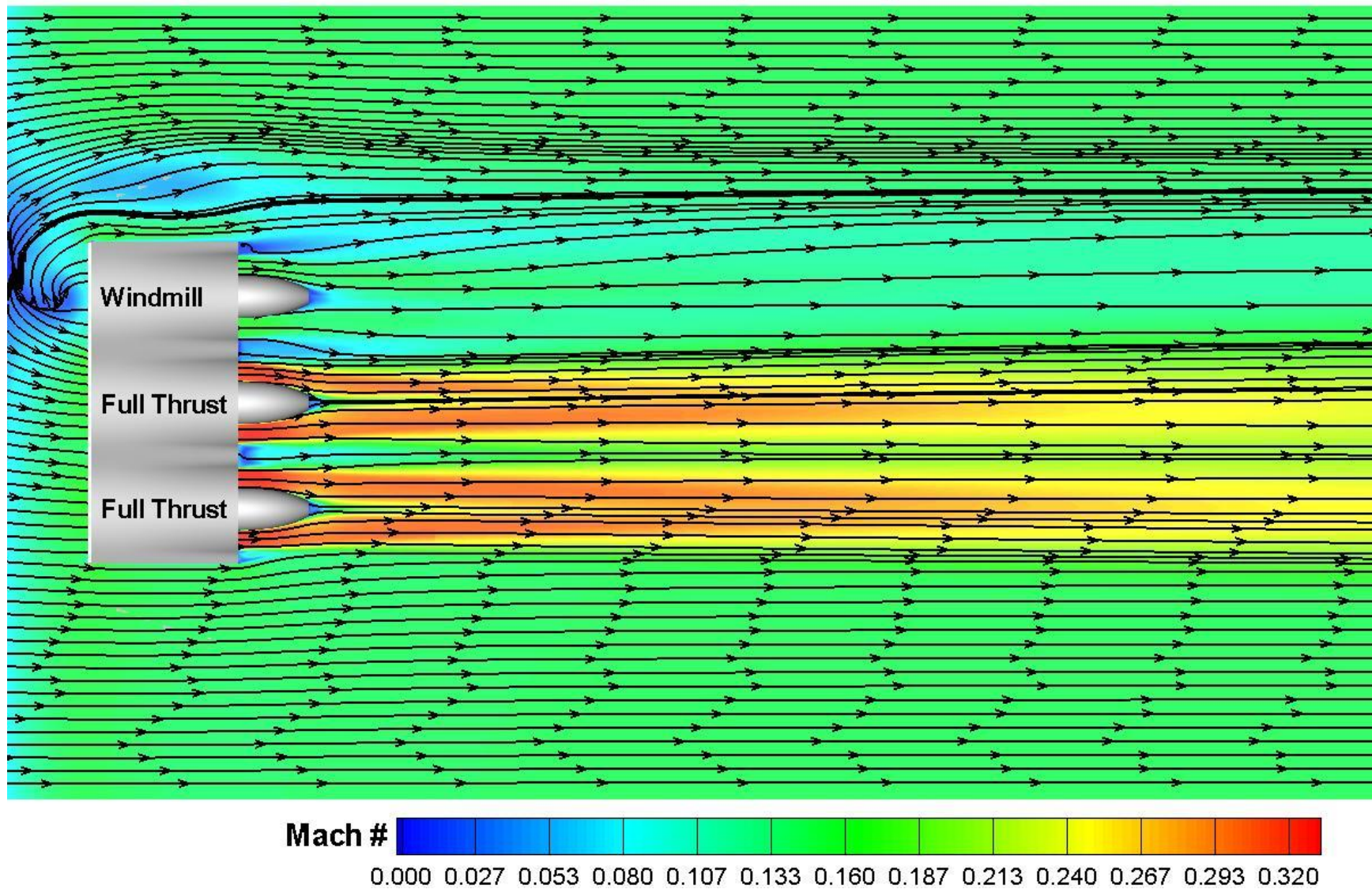






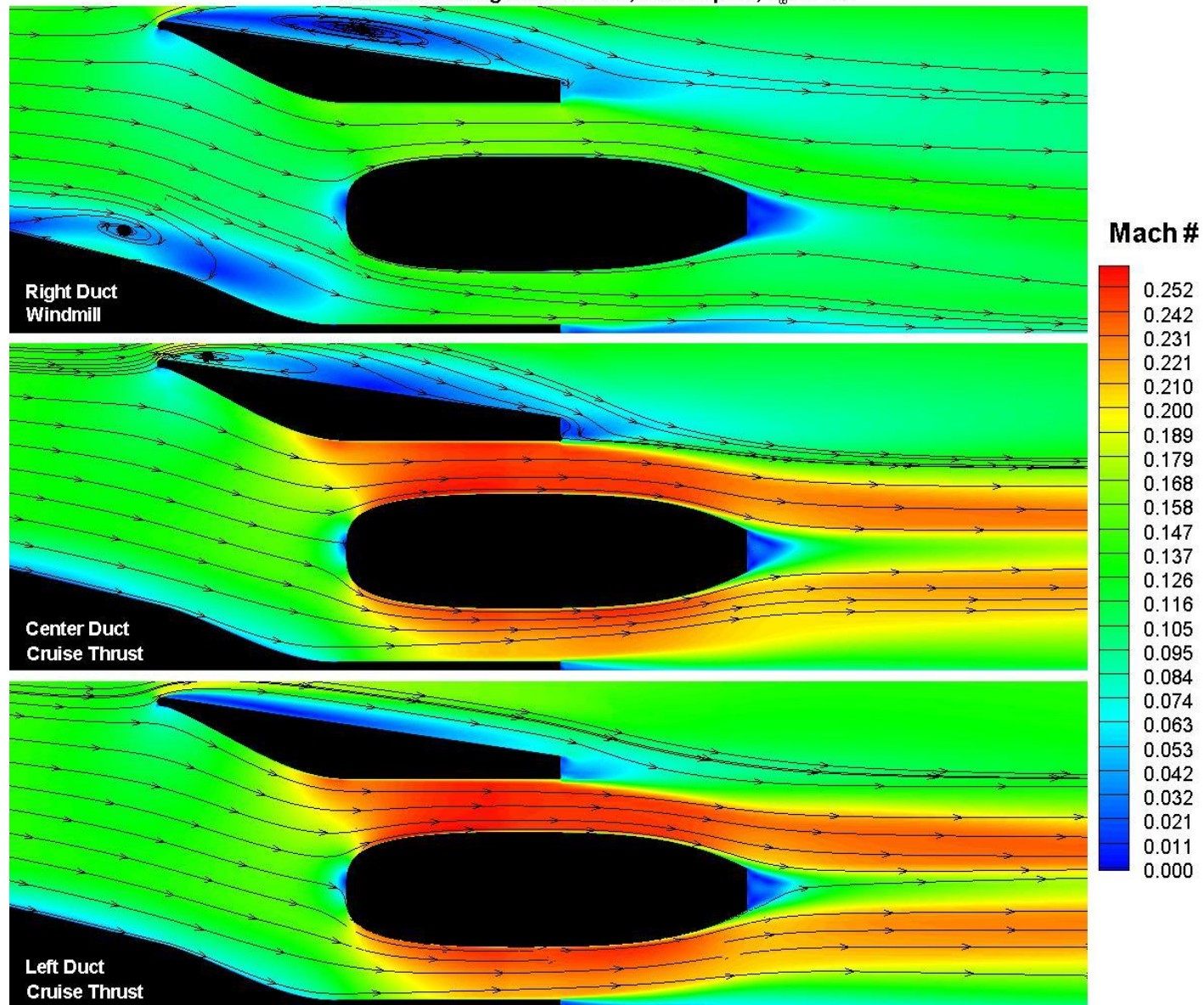
TeDP OVERFLOW Predicted Wind Tunnel Hump Mach Contours

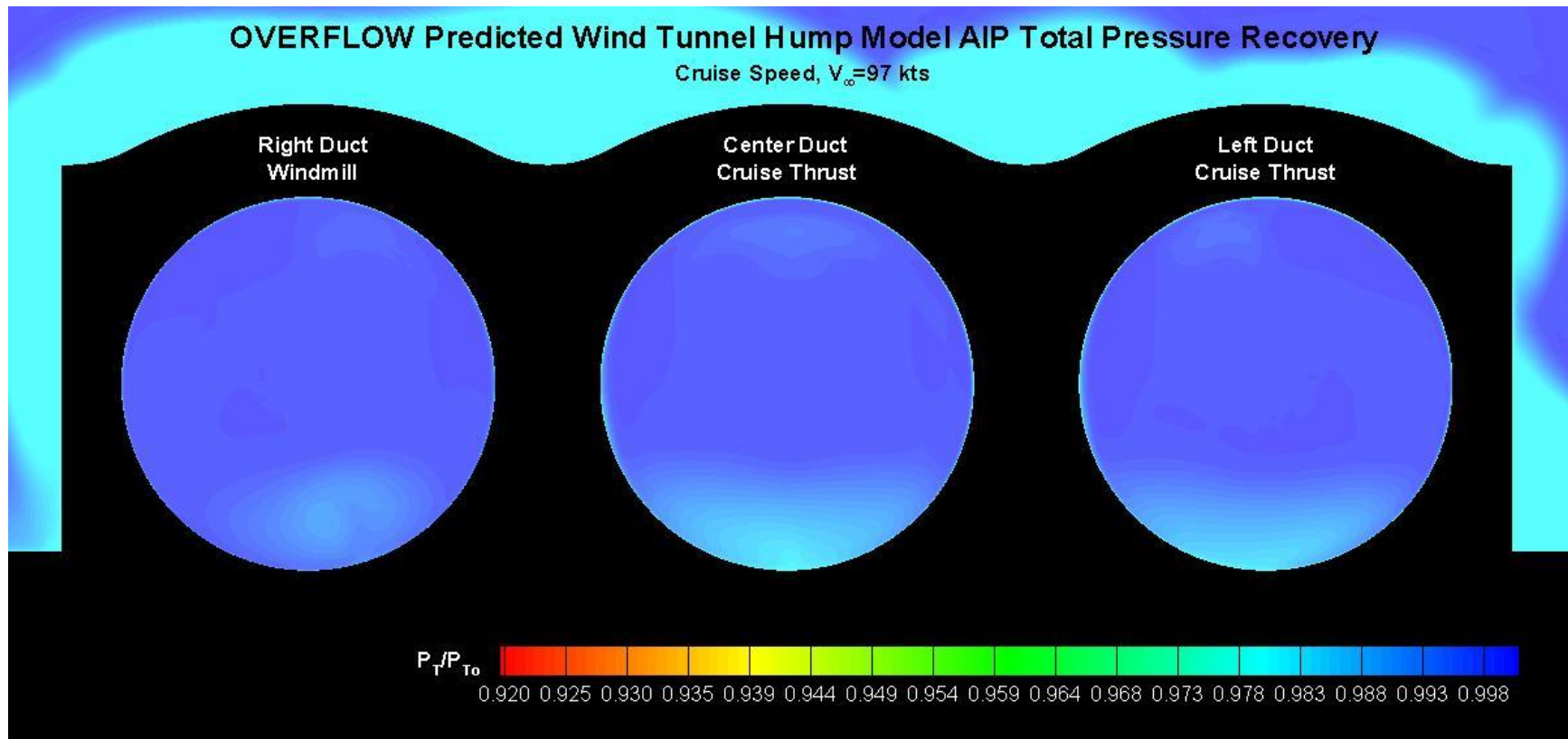
Cut Plane = $y=2.72''$ (half duct height)

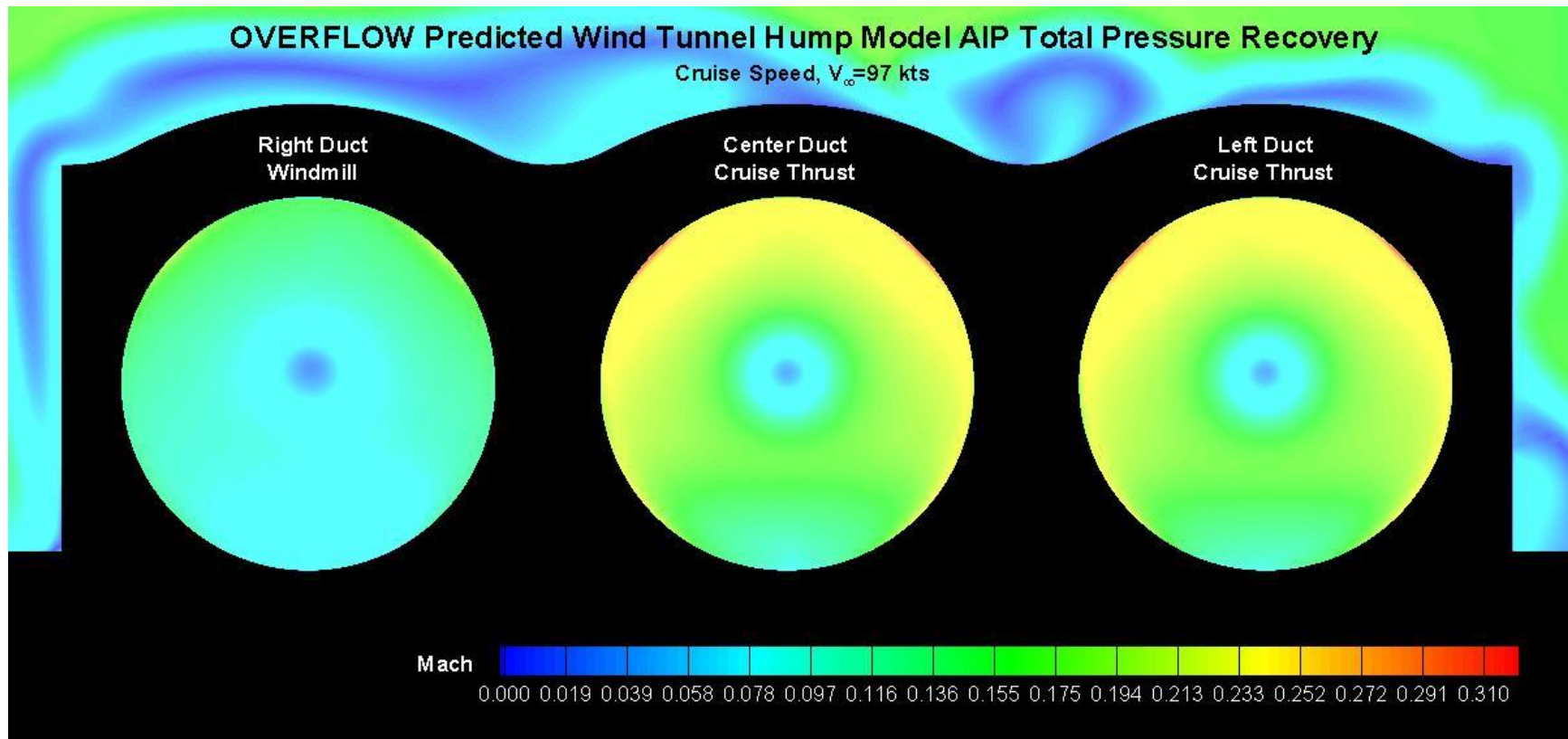


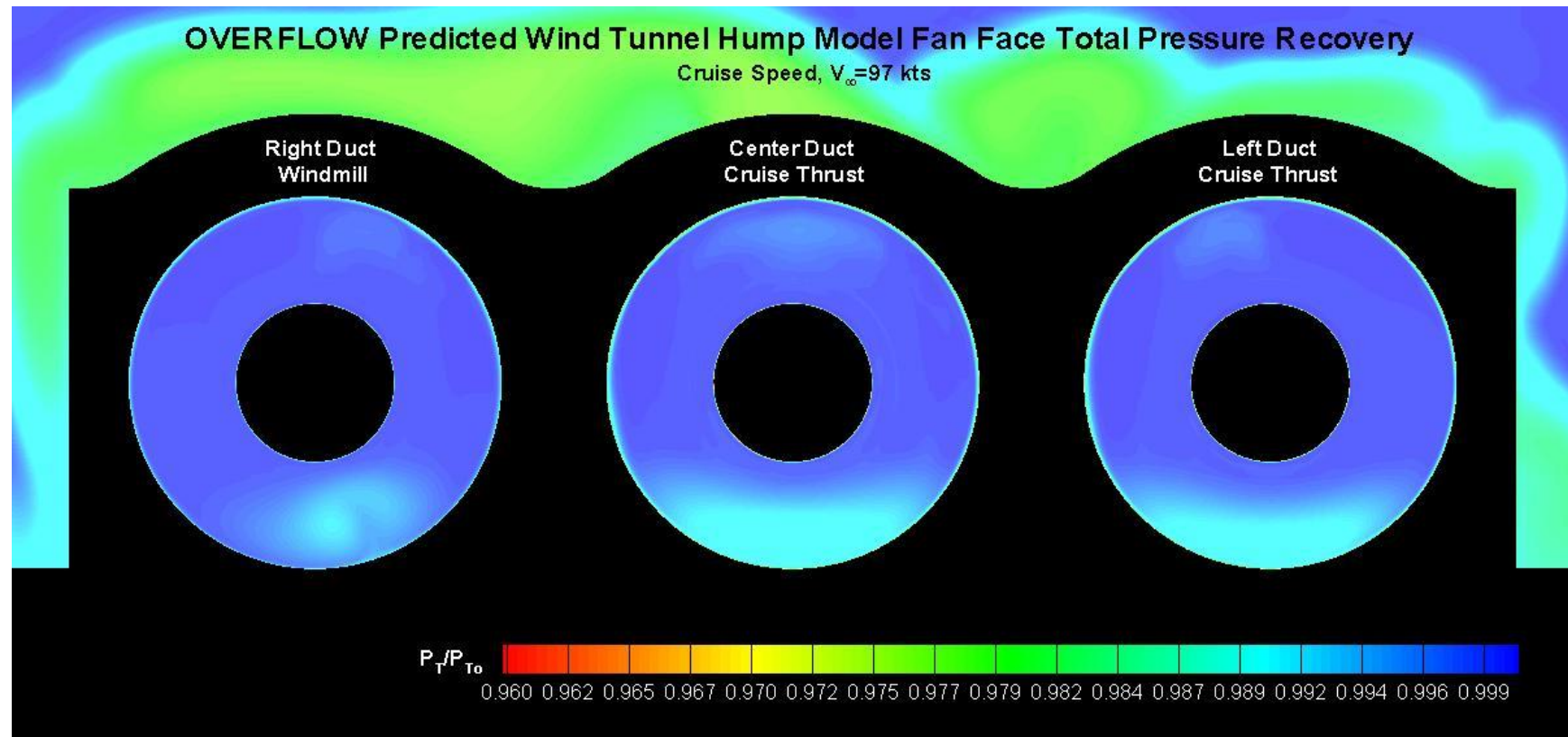
0% 50% 50% Different Differential Thrust Case Thrust Case

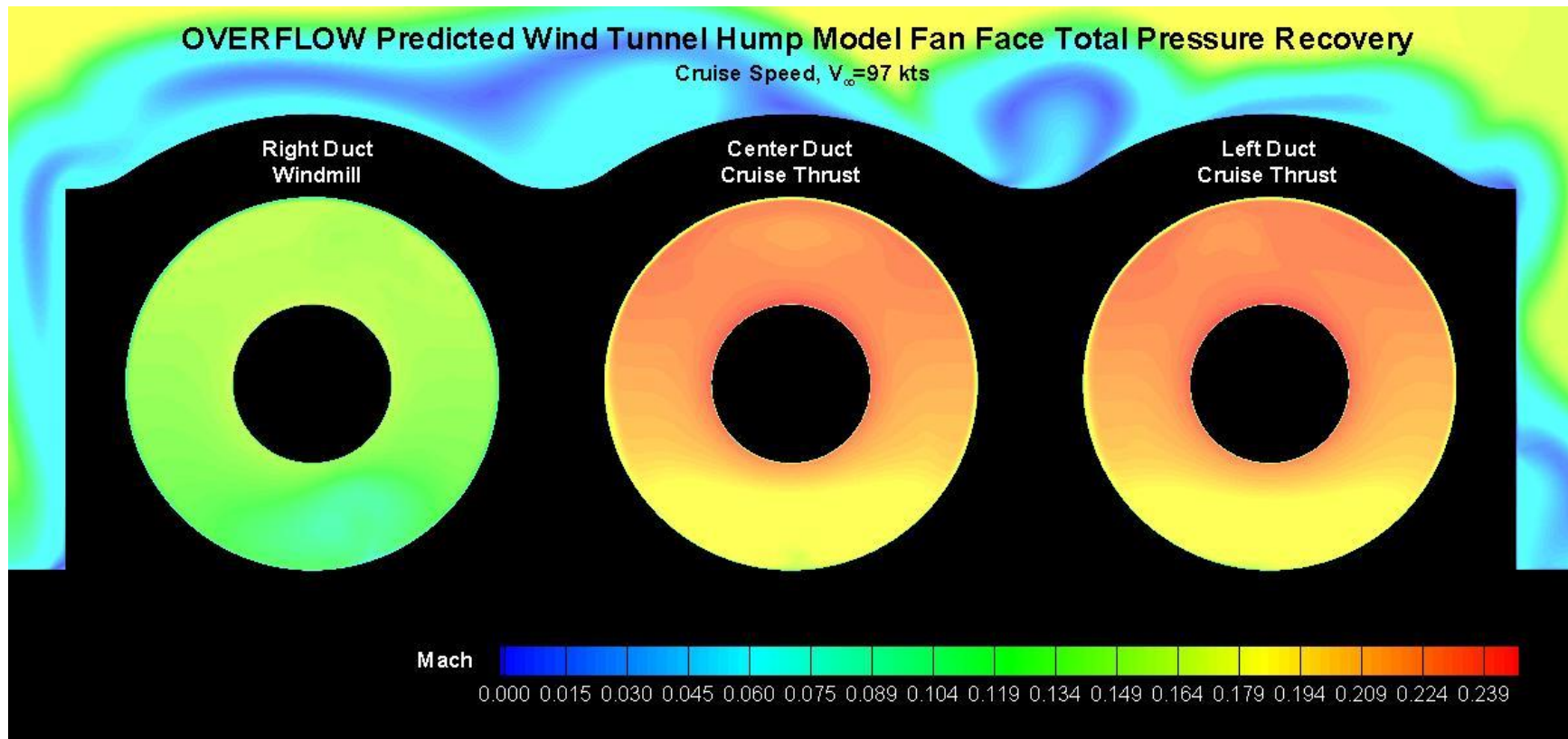
OVERFLOW Predicted Wind Tunnel Hump Model Differential ThrustDuct Mach Contours
Vertical Cut Through Duct Centers, Cruise Speed, $V_{\infty} = 97$ kts

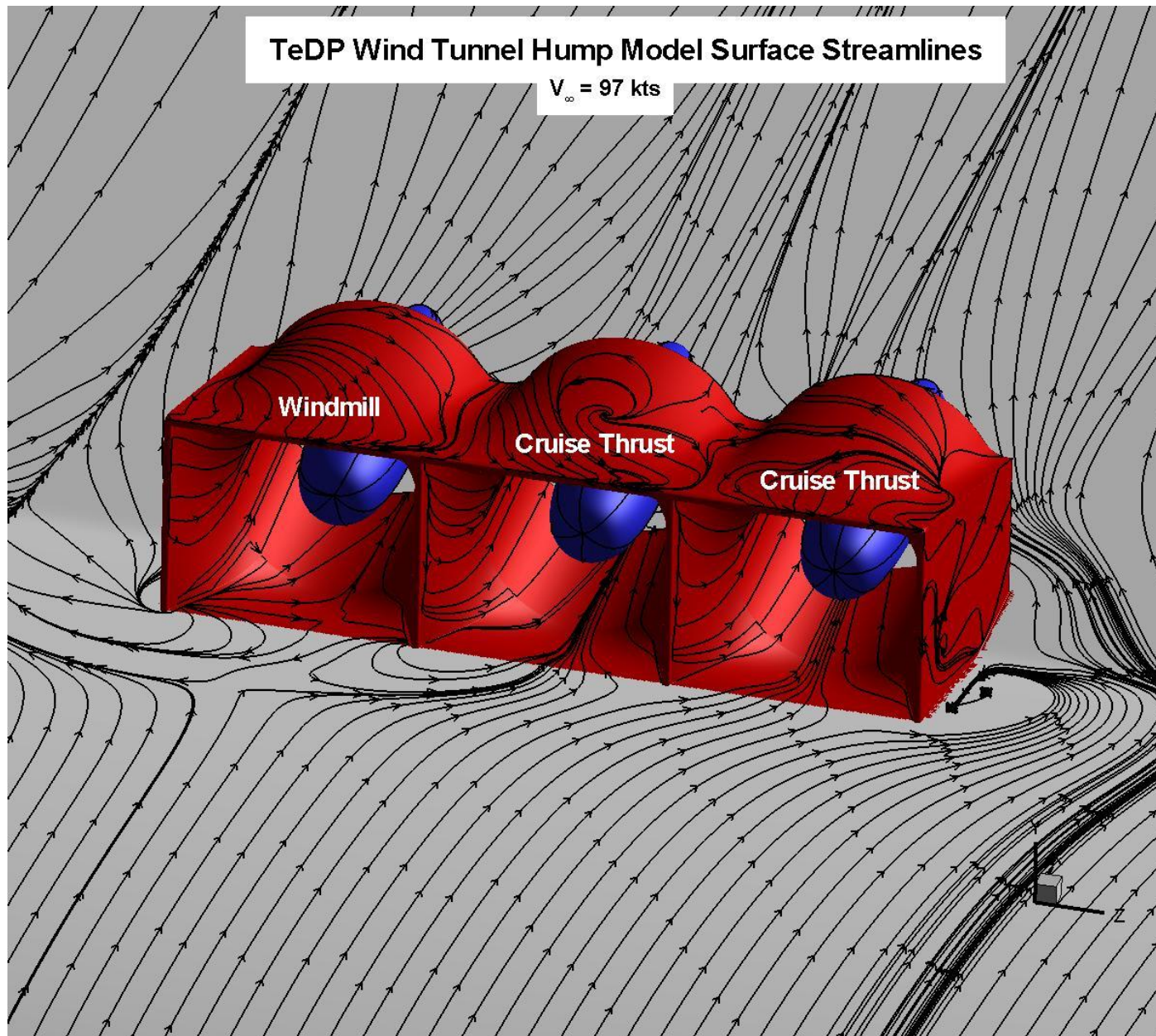


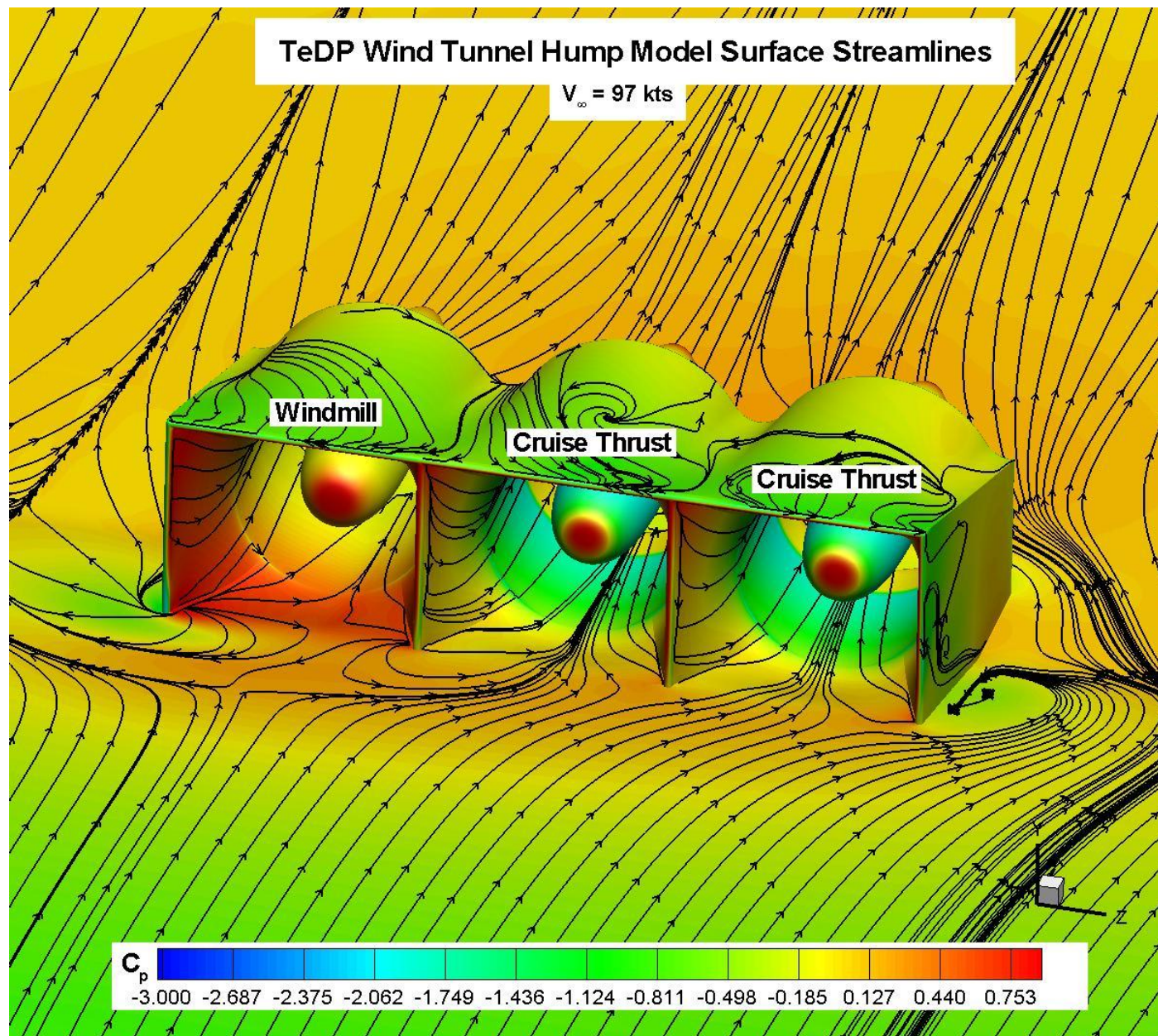






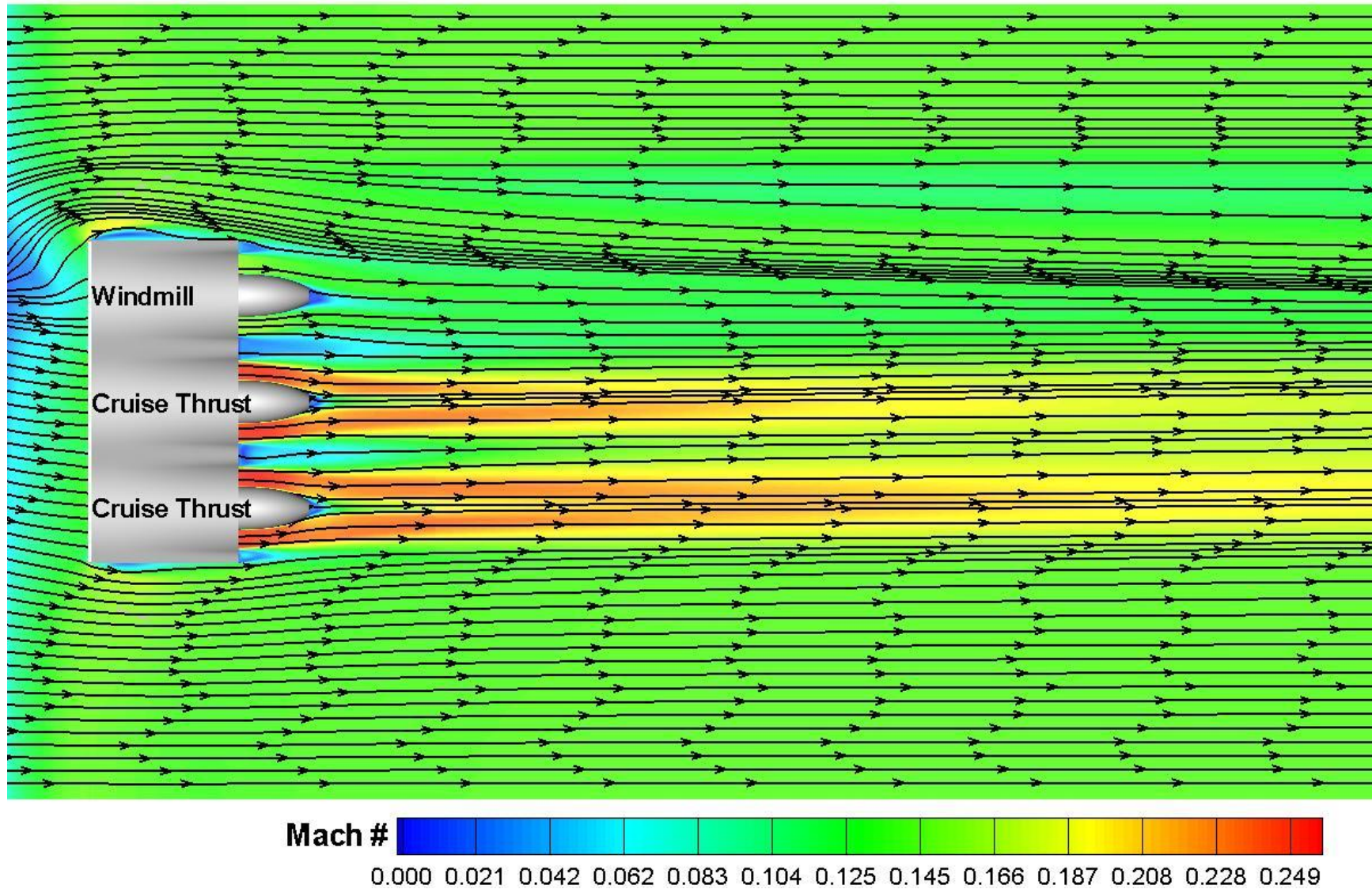






TeDP OVERFLOW Predicted Wind Tunnel Hump Mach Contours

Cut Plane = $y=2.72''$ (half duct height)



11 APPENDIX #3

Wind Tunnel Test Run Log

TeDP Illinois Run Log

Date	Time	Run #	Filename	Re	RPM	Uinf (ft/s)	PSI Cal	Model Config	Fan Throttle %			Distortion Rake	Comments
									Right	Center	Left		
9/19/2013	10:10am	1	clean.airf.1.bl.dat	4.96x106	930	172	Yes	Clean					Clean Airfoil, no ducts, baseline bl profiles
	10:25am	2	clean.airf.2.bl.dat	4.96x106	930	172		Clean					
	10:30am	3	clean.airf.3.bl.dat	4.96x106	930	172		Clean					
	10:40am	4	clean.airf.4.bl.dat	4.96x106	930	172		Clean					
	10:45am	5	clean.airf.5.bl.dat	4.96x106	930	172	Yes	Clean					
	10:55am	6	suction.airf.6.bl.dat	4.96x106	930	172	Yes	Clean					Clean Airfoil, no ducts, with suction bl profiles (changed wait time between pts from 3 to 5 seconds)
	11:10am	7	suction.airf.7.bl.dat	4.96x106	930	172		Clean					
	11:20am	8	suction.airf.8.bl.dat	4.96x106	930	172		Clean					
	11:27am	9	suction.airf.9.bl.dat	4.96x106	930	172		Clean					
	11:50am	10	suction.airf.10.bl.dat		930	172		Clean					
9/23/2013	9:40pm	11	idle.nosuction	4.96x106	930	161	Yes	Fans	0	0	0	Yes	Fans Installed On Model, Idle Condition, No BL Traverse, 5 repeat points
	9:55pm	12	idle.suction.12	4.96x106	930	161	Yes	Fans	0	0	0		With suction
	10:00pm	13	idle.suction.13	4.96x106	950	165	Yes	Fans	0	0	0		With Suction, Slightly Higher RPM
9/24/2013	10:25am	14	static.thrust.14.1	0	0	0	Yes	Fans	30	30	30	Yes	Static Thrust Run
			static.thrust.14.2						50	50	50		
			static.thrust.14.3						75	75	75		
			static.thrust.14.4						100	100	100		
	1:30pm	15	static.thrust.15.1	0	0		Yes	Fans	100	100	100	Yes	Reduced Fan Gap Slightly, relieved possible motor wire interference on cowl top
			static.thrust.15.2						75	75	75		
			static.thrust.15.3						50	50	50		
	4:45pm	16	suction.thrust.16.1	4.96x106	1000	172	Yes	Fans	100	100	100	Yes	Tunnel On, Full, 3/4, and 1/2 thrust rpm settings, all three fans running
			suction.thrust.16.2						75	75	75		
			suction.thrust.16.3						50	50	50		
	8:00pm	17	suction.thrust.distort.17.1	4.96x106	1000	172	Yes	Fans	100	100	50	Yes	Tunnel On, 1st set 100 100 50, second set 0 100 0
			suction.thrust.distort.17.2						0	100	0		
9/25/2013	8:40am	18	suction.thrust.distort.18.1	4.96x106	1000	172	Yes	Fans	100	100	0	Yes	Tunnel On, 100 100 0
		19	suction.thrust.distort.19.1	4.96x106	1000	172		Fans	50	100	50	Yes	Tunnel On, 50 100 50
	3:00pm	20	suction.test.20	4.96x106	1000	172	Yes	Fans	0	0	0	No	Idle Fans 0 0 0, removed distortion rake, duct static pressure check
	3:10pm	21	suction.thrust.21.1	4.96x106	1000	172	Yes	Fans	100	100	100	No	Tunnel On, 1st Set 100 100 100, 2nd Set 75 75 75, 3rd Set 50 50 50
			suction.thrust.21.2						75	75	75		
			suction.thrust.21.3						50	50	50		
	6:20pm	22	static.thrust.22.1	0			Yes	Fans	100	100	100	No	Static Run, No Distortion Rake, 1st Set 100 100 100, 2nd Set 75 75 75, 3rd Set 50 50 50
			static.thrust.22.2						75	75	75		
			static.thrust.22.3						50	50	50		
9/26/2013	6:00pm	23	Flow Vis		200	30		Fans	0	0	0	No	Smoke Flow Visualization, Fans Idle
	10:00pm	24	Flow Vis		200	30		Fans	19	19	19	No	Smoke Flow Visualization, Fans 19 19 19
	10:30pm	25	Flow Vis		200	30		Fans	19	19	0	No	Smoke flow Visualization, Left Fan Off